

Langmuir Probes in the Wendelstein 7-X Test Divertor Unit

Inauguraldissertation

zur

Erlangung des akademischen Grades eines
Doktors der Naturwissenschaften
(Dr. rer. Nat.)

der

Mathematisch-Naturwissenschaftlichen Fakultät

der

Universität Greifswald

vorgelegt von
Lukas Rudischhauser

Greifswald, 25.06.2021

Dekan Prof. Dr. Gerald Kerth

1. Gutachter Prof. Dr. Thomas Sunn Pedersen

2. Gutachter Prof. Dr. Holger Kersten

Tag der Promotion: 15.10.2021

Abstract

This thesis describes how the data of the Langmuir probes in the Wendelstein 7-X (W7-X) test divertor unit (TDU) were evaluated, checked for consistency with other diagnostics and used to analyse plasma detachment.

Langmuir probes are an electronic diagnostic, and were among the first to be used in plasma physics to determine particle fluxes, potentials, temperatures and densities. W7-X is a large, advanced stellarator, magnetic confinement fusion experiment, operated at the Max-Planck Institute for Plasma Physics (IPP) in Greifswald, Germany. Its TDU is an uncooled graphite component, shaped and positioned to intercept the convective heat load of the plasma. Detachment describes a desirable operation state of strongly reduced loads on this component.

The evaluation of Langmuir probe data relies heavily on models of the sheath, formed at the interface between plasma and a solid surface, to infer plasma parameters from the directly measured quantities. Multiple such models are analysed, generalised, and adapted to our use case. A detailed comparison is made to determine the most suitable model, as this choice strongly affects the predicted parameters. Special attention is paid to uncertainties on the parameters, which are determined using a Bayesian framework.

From the inferred parameters, heat and particle fluxes are calculated. These are also indirectly measured by two other, camera-based diagnostic systems. Observations are compared to test the validity of assumptions and calculations in the evaluation of all three diagnostics by checking their results for consistency.

The first comparison, with the infrared emission camera system, shows good agreement with theoretical predictions and reported measurements of the sheath transmission factor, for which we derive and measure a value in W7-X. Parameter dependencies in the quality of this agreement hint at remaining issues.

The second comparison, with the H_α photon flux camera system, shows significant discrepancy with expectations. These are argued to originate from systematic differences in the measurement locations, which are quantified and related to the magnetic topology.

Langmuir probe observations of individual discharges are analysed to discuss conditions under which detachment occurs, transition into that state and fluctuations observed prior to and during it. A spatial parametrisation of the data is developed and used to facilitate this. These observations contribute to the larger aim of understanding particle balance control and fusion plasma edge processes.

Contents

Abstract	iii
1. Introduction	1
1.1. Nuclear Fusion Requirements	2
1.2. Plasma confinement	6
1.3. W7-X	20
1.4. Thesis outline	23
2. Divertor Langmuir probes in W7-X	25
2.1. Langmuir probe principles	25
2.2. Probe hardware	27
2.2.1. Probe tips	27
2.2.2. Cabling	31
2.2.3. Electronics	32
2.3. Langmuir models	37
2.3.1. Simple Langmuir model (SL) derivation	39
2.3.2. Motivation for expansion to advanced models	42
2.3.3. Consideration of sheath	42
2.3.4. Consideration of magnetic pre-sheath	45
2.3.5. Consideration of current return path	47
2.4. Considerations for evaluation	50
2.5. Parameter uncertainty estimation	56
2.6. Comparison of models	62
2.6.1. χ^2 method	63
2.6.2. Normalisation of residuals	65
2.6.3. Normalisation of χ^2	66
2.6.4. Results	68
2.6.5. Avenues for extension of work	73

3. Heat flux comparison	75
3.1. Introduction	75
3.2. Theory	76
3.3. Langmuir probe (LP) measurement of heat flux	83
3.4. IR measurements of heat flux in W7-X	88
3.5. Calculation of sheath transmission coefficient	89
3.6. Results	91
3.7. Summary	103
3.8. Appendix	104
4. Particle flux comparison	105
4.1. Introduction	105
4.2. H_{α} -light observation	106
4.3. S/XB derivation	107
4.4. Results	109
4.4.1. Low-density discharge 20181010.010	109
4.4.2. High-density discharge 20180814.025	113
4.5. Discussion	122
4.6. Further work	125
5. Langmuir probe measurements of plasma detachment in W7-X127	
5.1. Outline	129
5.2. Reduction and parametrisation	130
5.3. Strike line (SL) position and movement	132
5.4. Inter-shot comparison of detachment	134
5.4.1. Open questions for further work	151
5.5. Transition into detachment	152
5.6. Fluctuations prior to detachment transition	156
5.7. Unstable detachment	158
6. Summary	169
Bibliography	177
Acronyms	191
List of Symbols	197

List of Figures	201
List of Tables	205
A. Appendix	207
B. Publications	211
C. Acknowledgements	213
Statutory declaration	215

1

Introduction

[The] fusion chamber of a stellarator and the magnets that surround it look like something Gaudí might have imagined: a mess of twists, turns and asymmetries.

(The Economist, Stellar work, Oct 24th 2015)

[...] 50 6-tonne magnet coils, strangely twisted as if trampled by an angry giant.

(Science, The bizarre reactor that might save nuclear fusion, Oct 21st 2015)

The €1billion 'pretzel' that could save planet Earth!

(Daily Mail, 13th December 2015)

The stellarator W7-X is often described as strange. While it is undeniably complex, it is a logical solution of a process to simultaneously meet a set of requirements. This set is generated by tracing a path from simple and easily stated requirements at the root of a decision tree through choices at the branches to solutions at the leaves. At each branching decision point, benefits are weighed against additional requirements which must be taken into account. This chapter will contextualise the topic of this thesis by following a single path through the tree, leading from fusion energy generation to W7-X and the task of its divertor Langmuir probes. Side branches will be mentioned, but not explored. The Langmuir probes themselves, the main topic of this thesis, will be introduced in the next chapter.

1.1. Nuclear Fusion Requirements

The root of the decision tree are the requirements of nuclear fusion. The probability of a nuclear reaction occurring depends on the strength of the electrostatic repulsion keeping the positively charged nuclei apart and the stability of the reaction's products. Inside nuclei, the short-ranged strong nuclear force competes with the comparatively weaker, but long-range, Coulomb force. For small nuclei, more strong force interactions mean that enlarging the nucleus provides more stability, as long as a balance of neutrons and protons is maintained. Large nuclei become more unstable as their size grows to the range of the strong nuclear force. This behaviour can be seen in the binding energy per nucleon in Figure 1.1. A reaction of two light nuclei thus tends to fuse them to produce one larger nucleus, with the binding energy no longer required to maintain stability converted to kinetic energy. If we can induce these reactions by accelerating light nuclei so that the probability of them overcoming the Coulomb repulsion and fusing increases, we can convert their otherwise inaccessible internal energy to accessible kinetic energy. The reaction probability for various light nuclei fusion processes, measured by the cross-section σ , is shown in Figure 1.2. To maximise the reaction probability, we focus on the process and energy which minimises the difference between the Coulomb and the reaction cross section σ , i. e. the fusion of the hydrogen isotopes deuterium (${}^2_1\text{H} = \text{D}$) and tritium (${}^3_1\text{H} = \text{T}$) at $\approx 100 \text{ keV}$. This reaction is described by the equation



or in nuclear reaction notation



Because ${}^4\text{He}$ is an especially stable nucleus¹, substantially more energy is released than was necessary to bring the hydrogen nuclei to the energy of the cross-section peak. By transferring some of the released energy to the fuel, the process can therefore be energetically self sustaining while still releasing energy in an accessible form. This transfer can happen through collisions in a macroscopic system of many particles and will tend to distribute their

¹Due to its 'double magic' configuration of a fully filled quantum state with even proton and neutron numbers.

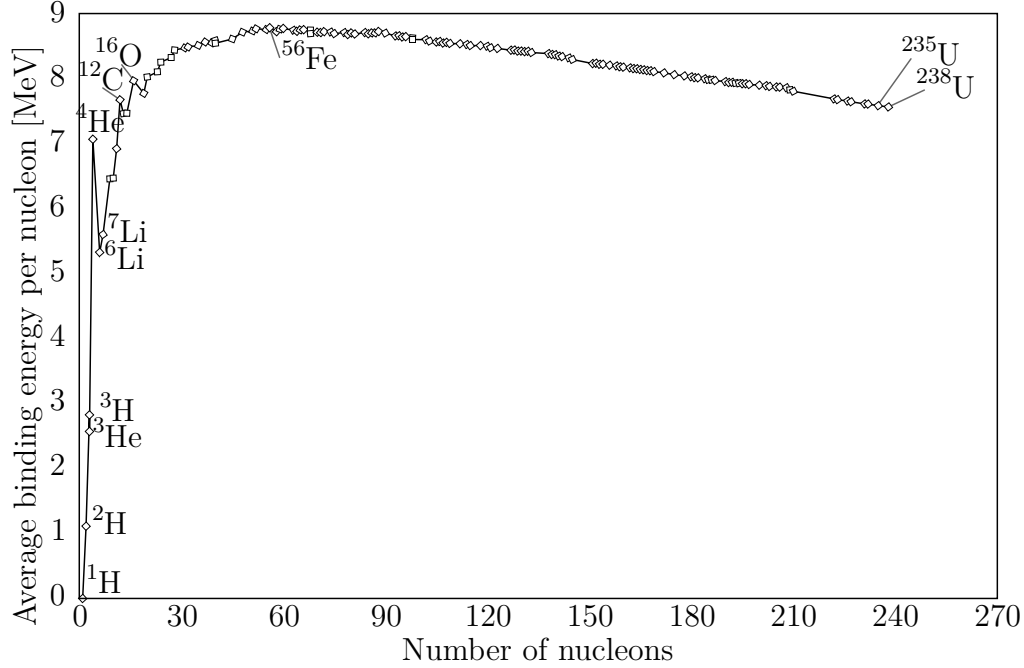


Figure 1.1.: Binding energy per nucleon. Only stable nuclei shown. Fusion generally exothermic up to iron (^{56}Fe), fission favoured above.

energy according to a Maxwellian distribution. Assigning this distribution a temperature T_i in units of energy [eV], we can calculate the reactivity $\langle\sigma\nu\rangle$, an average over the particle velocity distribution ν and reaction cross-section σ . Varying the temperature, we find that the optimum is reduced to around 67 keV, as shown in Figure 1.3. This is due to the asymmetric shape of the Maxwellian in which many particles have higher energies than the characteristic temperature.

Already at particle energies in the eV range, material will be gaseous and atoms stripped of their electrons. These conditions describe a plasma: A macroscopic ensemble of unbound ions and electrons, with negligible net charge and charge inhomogeneity shielded over the Debye length scale, which for cold ions is

$$\lambda_D = \sqrt{\frac{\epsilon_0 T_e}{e^2 n_e}}. \quad (1.3)$$

In this expression, T_e is the electron temperature in units of [eV], n_e the

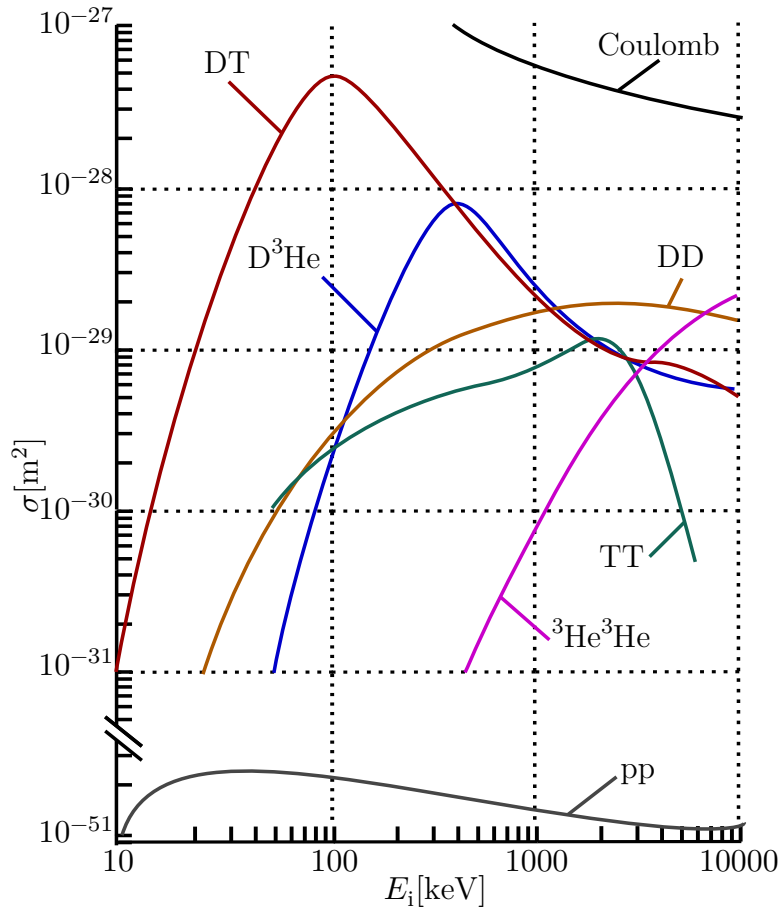


Figure 1.2.: Fusion cross sections of light-nuclei processes. DT peaks at the lowest energy of approximately 100 keV. Tunnelling still required to overcome more likely Coulomb repulsion. The pp-reaction dominant in the sun is unfeasible for terrestrial energy generation (note broken axis). Figure courtesy of D. Böckenhoff.

electron density in units of $[m^{-3}]$, ϵ_0 the permittivity of free space and e the electron charge.

For a DT fusion reaction in a plasma to be energetically self sustaining, the energy generated from reactions and distributed through collisions must exceed the energy lost to the environment. The collision cross-section for neutrons in the plasma is small, which implies that the generated fusion α

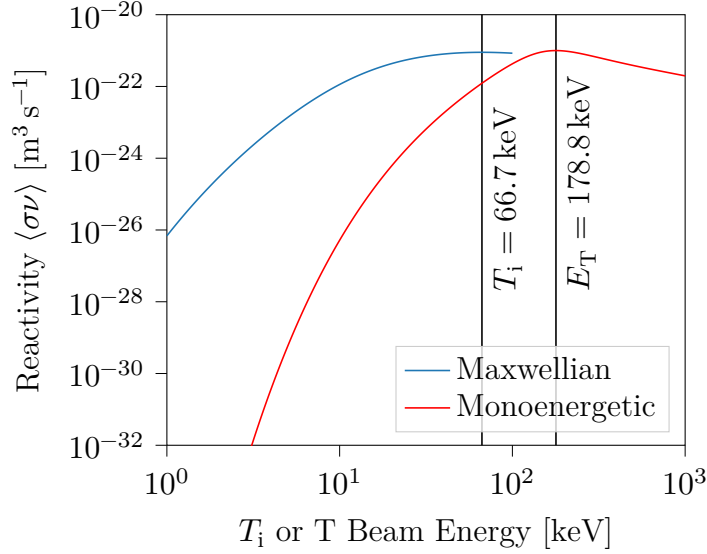


Figure 1.3.: Reactivity of the DT reaction. Rates from parametric model of Bosch and Hale [1] shown only within their validity ranges. Code courtesy of J.-P. Koschinsky.

particle heat P_α alone must compensate the transport and bremsstrahlung radiation losses P_t & P_b :

$$P_\alpha = P_t + P_b \quad (1.4a)$$

$$\frac{n_i^2}{4} \langle\sigma\nu\rangle E_\alpha = \frac{3n_e T_e}{\tau_E} + C n_e^2 T_e^{1/2} Z_{\text{eff}} \quad (1.4b)$$

We assume in this and the following expressions equal densities of tritium and deuterium, equal ion and electron temperature and negligible dilution by impurities. $E_\alpha = 3.5\text{ MeV}$ is the energy of the α particles. Transport losses are modelled by an energy density divided by an effective energy confinement time τ_E . Bremsstrahlung depends on the weighted sum of the average charge of each species $Z_{\text{eff}} = \frac{\sum_i n_i \bar{Z}_i}{n_e}$ and is scaled by a constant $C = 5 \times 10^{-37} \text{ Wm}^3/\sqrt{\text{keV}}$. The requirement for self-heated, 'ignited' fusion can thus be formulated as

$$n_i \tau_E \geq \frac{12T_e}{\langle\sigma\nu\rangle E_\alpha - 4CT_e^{1/2} Z_{\text{eff}}}, \quad (1.5)$$

a condition known as the Lawson criterion [2]. This can be reformulated by multiplying with T_i and evaluating the reactivity at the minimum of $\frac{T_i^2}{\langle\sigma v\rangle} = 14 \text{ keV}$. We thus obtain a useful figure of merit for fusion, the triple product:

$$n_i T_i \tau_E \gtrsim 3 \times 10^{21} \text{ keV s m}^{-3}. \quad (1.6)$$

It is not necessary for the reaction to reach this condition to generate power economically, since we did not account for the power of the neutrons. This is converted and can be partially used as auxiliary heating power, while maintaining a power amplification $Q > 1$. Achieving this condition in an economical way and harnessing fusion would represent a safe, sustainable method of accessing the energy of nuclear reactions.

The requirements are thus set out.

- We need to generate a dense plasma,
- heat it to some tens of keV,
- replenish it with deuterium and tritium, and crucially,
- limit the loss rate τ_E of energy to the environment.

Provision of tritium

Replenishing the particles fused to helium requires that deuterium and tritium are provided and can be injected into the plasma. Deuterium is abundantly available in nature and commercially extracted. Tritium radioactively decays with a half-life of 13.6 years and does not naturally occur in concentrations viable for extraction. It can be bred by capturing the fusion neutrons in lithium and splitting it as ${}^6\text{Li} + n \longrightarrow {}^4\text{He} + \text{T} + 2.75 \text{ MeV}$ or ${}^7\text{Li} + n \longrightarrow {}^4\text{He} + \text{T} + n - 2.47 \text{ MeV}$. The complex realisation of these breeding blankets branches off from the path we follow in this introduction and is discussed elsewhere [3].

1.2. Plasma confinement

The loss of both particles and energy must be prevented. The former to maintain the plasma density, the latter initially to achieve the necessary

reaction temperature and then to retain self-heating conditions. This can either be achieved using the mass of the plasma particles or their charge in the three confinement types outlined below.

Gravitational confinement

In stars, gas is compressed by its own gravity, causing it to heat and degenerate into plasma. Within the core, the Lawson criterion is fulfilled and fusion occurs, mostly through the proton-proton (p-p) reaction chain with low power density due to its small cross section (see Figure 1.2). In our sun, a star with low metallicity $Z = \sum_{i>\text{He}} \frac{m_i}{M_\odot} = 0.0122$ [4], proton-proton reactions contribute 99.2% of generated power. The large density in the core and radiative zone prevents convection, resulting in good energy confinement. Such densities are obviously unattainable on earth, so this confinement is of no practical interest for fusion power generation.

Inertial confinement

When rapidly compressed and heated, a solid can temporarily reach the requirements of the Lawson criterion in Equation (1.5). The fusion reaction will force the solid apart again, but this motion is inhibited by the inertia of the plasma particles, giving this confinement approach its name. Inducing fusion reactions in this way is attempted by directing powerful lasers or particle beams at a DT fuel target to heat and compress it. This can be done directly or indirectly by vaporising a hohlraum to generate a homogeneously radiating plasma, which in turn compresses the pellet, not unlike the Ulam-Teller design for a hydrogen bomb. The difficulties lie in achieving a uniform compression and eventually making a destructive process economical. Inertial confinement is another branch we will not explore.

Magnetic confinement

The Lorentz force will restrict a single charged particle to spiral about magnetic field lines at the Larmor radius

$$\rho = \frac{mv_\perp}{|q|B} \tag{1.7}$$

where q and m are the particle's charge and mass, B is the magnetic field strength and v_{\perp} is the particle's velocity perpendicular to that field. For strong fields and non-relativistic velocities this radius is small, $\rho_1 = 5$ mm for $E = 10$ keV, $m = m_{\text{H}}$, $q = e$, $B = 2.5$ T, such that we only consider the guiding centre of the motion moving along \vec{B} . If guiding centres always followed field lines it would be sufficient to construct a configuration with closed field lines to perfectly confine single particles. External forces due to gravity or electric fields, and changes of the magnetic field in direction or magnitude however cause guiding centre drifts in the $q\vec{F} \times \vec{B}$ direction.

These can, for example, be observed in particles trapped between two regions of strong field in a magnetic well due to the conserved constant of motion $\mu = \frac{mv_{\perp}^2}{B}$. This is the cause of the azimuthal precession of particles in the dipole field of the earth as they bounce between the poles. An ion travelling north over the equator experiences a downwards radial force to keep it on the curved field line and thus drifts westwards. Guiding centre drifts can never be avoided as field lines must be curved due to the inavailability of effective parallel confinement and size limitation on any practical device.

Dipole, magnetic well field configurations and pinches are considered for fusion plasma confinement, but we will not explore these branches further. Instead we turn to toroidal topologies in equilibrium. In these, guiding centre drifts orientated in opposite directions for ions and electrons imply a charge separation, which in turn causes a collective motion radially outwards, leading to a loss of particles. This can be countered by superposing a poloidal field onto the toroidal one, making it helical. Since the motion along the field is much faster than the drift velocities perpendicular to it, guiding centre drifts average out over many toroidal orbits.

Twisted toroidal fields

To better understand some properties of toroidal and helical fields, let us examine a single field line. A line on the surface of a torus subtends an angle with the toroidal direction $\hat{\varphi}$, the so called pitch angle ϑ , for which we will examine four cases and their consequences. These relate to the number of periods a FL makes in toroidal and poloidal direction around the torus. This also depends on the aspect ratio ϵ , where $\epsilon = \frac{\text{Major radius } R}{\text{Minor radius } r}$. The pitch

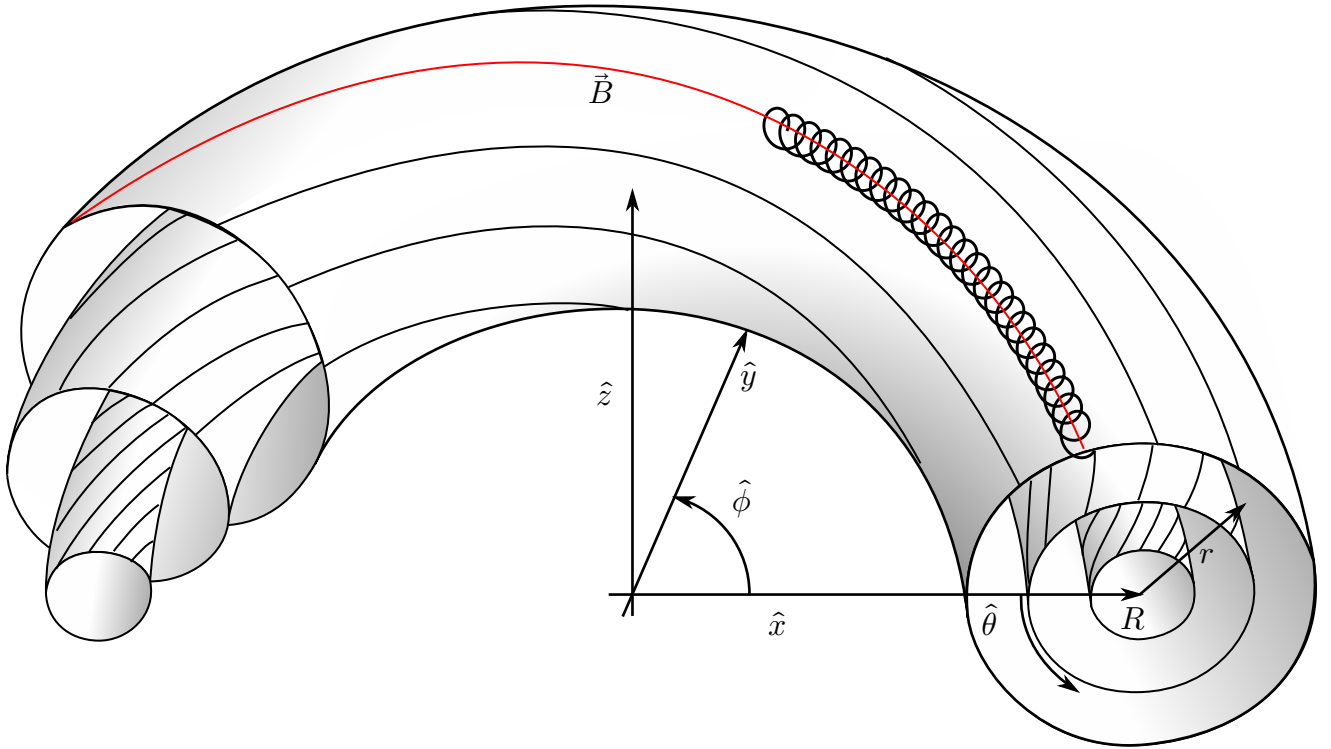


Figure 1.4.: Schematic of nested toroidal flux surfaces. A single field line (FL) is highlighted in red. The guiding centre of the particle gyration follows it. In addition to Cartesian coordinates $\hat{x}, \hat{y}, \hat{z}$, the torus can be described by major radius R , minor radius r , poloidal angle $\hat{\theta}$ and toroidal angle $\hat{\phi}$. Figure courtesy of D. Böckenhoff.

angle can be

- $\vartheta = 0$ such that the direction is purely toroidal and the field line closes on itself after one toroidal turn;
- $\vartheta = \pi/2$ such that the direction is purely poloidal and the field line closes on itself after one poloidal turn, but would never do so in toroidal direction;
- $\vartheta \times \epsilon \in \mathbb{Q} : \vartheta \times \epsilon \in n/m$ for $n, m \in \mathbb{N}$ such that the field line closes on itself after n toroidal turns, having done m poloidal turns; or

- $\vartheta \times \epsilon \in \mathbb{I} : \mathbb{R} \setminus \mathbb{Q}$. In this case the field line never closes on itself, infinitely circling the torus and coming arbitrarily close to any point, covering the entire surface.

As the relative strengths of the toroidal and poloidal field components vary continuously across the torus' minor radius r , so does the pitch angle. As each flux surface is defined by a pitch angle, which can never have two values in one place, those surfaces will necessarily be nested into each other. The particular case relevant to us, in which the variation of ϑ is monotonic, is shown in Figure 1.5.

Obviously, arbitrarily close to any irrational ϑ , there will be rational ϑ values. If flux surfaces are formed by irrational values, but not by rational ones, it seems paradoxical and hard to understand why twisted toroidal fields generate surfaces at all. This can be resolved by results from dynamic system theory, observing that magnetic field line flow is a Hamiltonian system and flux surfaces are therefore stable to small perturbations, according to Kolmogorov–Arnold–Moser (KAM) theory. A clear explanation of this deep, but abstract insight is given by Hudson *et al.* [5].

Instead of a single field line and an angle, it is beneficial to express the field in magnetic coordinates

$$\vec{B} = \nabla\psi \times \nabla\theta + \nabla\varphi \times \nabla\chi. \quad (1.8)$$

In this expression φ is again the toroidal direction and θ the poloidal direction, so that \vec{B} is decomposable into these two components. ψ and χ are defined to be constant on surfaces of constant pressure and vanish on the axis. Instead of the illustrative pitch angle, it is more common to use the rotational transform ι or safety factor q , where

$$\iota = \frac{d\chi}{d\psi} = \frac{1}{q} \quad \iota = \frac{\iota}{2\pi} \quad (1.9)$$

Derivations of these quantities and relations can be found in Reference [6]. Furthermore, we will redefine the minor radius as the distance from the central extremum of ι , normalise it to the last closed flux surface (LCFS) and label this quantity ϱ . The LCFS is the radially outermost closed flux surface not intersected by wall components. At $\varrho = 0$ the surface degenerates into a closed line, the magnetic axis. These definitions will be useful when magnetic axis and flux surfaces deviate from symmetry in toroidal coordinates.

Helical field lines balance guiding centre drifts. Certain field configurations, including those of tokamaks and W7-X which will be introduced below, also minimise the time-averaged radial drift of particles trapped in magnetic wells. The guiding centres move from one end of the well to the other on different paths, but the average radius varies only slowly over many cycles. As we will see below, common methods of generating these imply nested flux surfaces and therefore shear, which is furthermore beneficial to the magnetohydrodynamic (MHD) stability of plasma equilibria (Section 1.2). Yet such a field does not perfectly confine particles. Losses arise from four groups of effects:

Classical drifts Collisions between particles can displace them by distances up to ρ . This is unavoidable, but plays a minor role because ρ is small.

Neoclassical drifts Even when trapped particles stay at the same radius on average, they temporarily make radial excursions much larger than ρ . If they collide on these, the associated displacement is correspondingly larger. Loss rates thus depend on collisionality, bounce orbit width, and trapped particle fraction.

Equilibrium and stability effects The plasma fluid modifies the magnetic field. Collective movements of the plasma can self-reinforce by modifying the flux surfaces or stochasticise them by changing ϵ . This can lead to flux surfaces contacting the wall or being destroyed.

Anomalous drifts This group encompasses all other effects and is dominated by turbulence. It can easily be seen how, in a fluid picture of the plasma, gradients of plasma pressure are a source of free energy to turbulent instabilities, which flatten these gradients by transporting energy 'downhill'.

How best to describe a plasma depends on which scale of effect is to be investigated. Analogous to the four points above, it may be suitable to use single particle, velocity distribution (kinetic), fluid descriptions or a mixture, both for mathematical analysis and computational simulation. While theoretically everything could be simulated by many single particles, this is in practice prohibited by the computational effort necessary to trace $\mathcal{O}(10\text{ m}^3 * 1 \times 10^{21}\text{ m}^{-3})$ particles. Understanding the dynamics of a smaller

number however, is not sufficient, as most plasma properties are examples of emergent behaviour [7].

The relative importance of the transport effects in a device depends on properties of the magnetic field and distribution of plasma quantities, e. g. pressure gradients. While the latter establish self-consistently with transport processes, the former can be chosen and designed for by us. Toroidal field can be generated through coils in a closed circular solenoid configuration. A poloidal field can be superimposed in two ways. Either through a current flowing in the plasma — which as a cloud of free charges, in field direction only inhibited by collisions, has excellent conductivity — or through external coils.

These methods of generating poloidal field define the following two branching solutions to our confinement requirements.

Tokamaks

The approach using only internal plasma current for the poloidal field defines a tokamak, the Russian acronym for toroidal magnetic chamber. The field is ideally the same at each toroidal cross-section^{II}. Identical toroidal field coils are densely spaced to reduce field ripple. The toroidal current is induced by a central solenoidal transformer in the spindle of the torus. In addition to providing the poloidal field, the current also heats the plasma and initiates the gas break-down avalanche for plasma start-up. Further current to sustain the poloidal field is provided through the bootstrap current I_{bs} , which establishes itself due to differences in collisionality at different minor radii. A benefit of the tokamak design is the toroidal symmetry which simplifies engineering and reduces the complexity of simulation. Toroidal symmetry also implies omnigeneity, meaning radial guiding-center drifts average to zero as described in Section 1.2 [8]. Strong zonal flows at the edge can furthermore shear turbulent eddies, weakening this otherwise dominant mode of transport [9].

Using an internal plasma current to form the field however, brings with it several difficulties. A tokamak plasma is inherently self-organised and in a marginal equilibrium state. Instabilities can cause the plasma to be displaced, potentially bringing it into contact with the plasma vessel wall and

^{II}i. e. for each radial-poloidal plane

'disrupting' the plasma current. The lack of current leads to a breakdown of the equilibrium flux surfaces and loss of confinement. Furthermore, the inductive current can not be sustained indefinitely. Monotonic action of the transformer is limited by the current limits of the power supply, but a current reversal causes a reorganisation of the field and loss of confinement. Running a tokamak fully with non-inductively driven current has proven challenging and pulsed operation is the norm.

Many issues addressed in this work concern all toroidal magnetic confinement devices, but we focus on the Stellarator, only referring to the tokamak branch of designs for comparison.

Stellarators

Providing some of the rotational transform through external coils, reduces the reliance on, and problems associated with, a strong plasma current, but at the cost of toroidal symmetry and its benefits. Devices with externally generated rotational transform differ in their design and there are, correspondingly, different names for various solutions such as heliotron, torsatron, and stellarator. The concept was first laid out by Spitzer [10]. All concepts have in common that they are not toroidally symmetric, because they generate their field through a combination of internal current, torsion of the magnetic axis and rotation of the magnetic cross section. Depending on the number of rotations, the field has a number of symmetric periods. As the field is externally determined and controlled, a desirable field configuration can be found through optimisation and a machine and coil system built to generate it. This optimisation is indeed necessary because the neoclassical transport in a classical stellarator scales unfavourably towards a reactor: Neoclassical transport coefficients increase $\propto T_e^{7/2}$, requiring an unfeasibly large machine to ensure confinement at the required temperatures. We will consider optimisation targets and properties for W7-X in Section 1.3.

The wall

Common to all confinement concepts are problems of the inner wall of a fusion device. It is subject to heat flux from different channels.

If the DT reaction is to be used, generated fast neutrons will penetrate deep into the wall and heat it volumetrically. This is desirable for a power

plant as the volume can be cooled more easily than the surface and the neutron energy can thus be passed to a circulating coolant. Collisions should especially occur with lithium to breed tritium in the breeding blanket mentioned above. Simultaneously, a high neutron-collision cross-section layer will shield the coils and environment from energetic neutrons. In most current experimental devices, the fusion reaction rate R , and therefore also the neutron wall load, are negligible.

Each point in the plasma radiates isotropically at different wavelengths, depending on the rate and type of processes occurring. While bremsstrahlung dominates in the fully ionised core, line radiation from partially stripped ions can play an important role at the edge. As a first approximation for this purpose we can consider the plasma an axisymmetric torus, as most energetic radiation will come from near the magnetic axis. The variation of the heat flux from radiation, which different parts of the wall receive, is therefore mostly dependent on their distance to that axis. In simulations of W7-X at 8 MW radiated power, exceeding the currently available input power, the radiation heat flux is on the order of 100 kW m^{-2} [11].

The most important contribution to the heat flux in present devices is the load from charged particles. Particles are lost from confinement through transport as described above, but still follow field lines. They may be channelled to specific areas of the wall, depending on the field configuration. Here they deposit energy and momentum and recombine to neutrals. These three aspects of plasma wall interaction (PWI) are crucial to the operation of a fusion experiment and are of utmost importance to practical fusion power generation. What happens in a particle and fluid picture of the plasma at the wall will be discussed in Chapter 3. At this point, we will give a qualitative picture.

Energy deposition must be handled by sufficiently robust materials and cooling. To allow for long term operation, no deformation or major changes of physical properties must occur. Solutions like spacecraft heat shields, which experience similar heat loads on re-entry, but ablate in the process, are therefore not suitable. The most developed solutions are currently using solid beryllium, carbon or tungsten tiles with coolant pipes carrying water [12]. Different coolants are being considered, as well as the use of a flowing liquid, such as a lithium-lead alloy, as plasma facing material and coolant simultaneously [13].

The motivation for using the materials mentioned above is the considera-

tion of erosion and release of impurities into the plasma. Particles impinging on the surface can mechanically 'knock' other atoms out of the material (physical sputtering) or give them enough energy to overcome the work function of the lattice (chemical sputtering). Since the work function and particle energy are typically well in excess of the strength of molecular bounds, only elementary pure materials can be used as plasma facing components. Mixtures and compounds would rapidly change their composition and properties. Atoms thus sputtered will be ionised in the plasma, radiate energy and dilute it. To avoid excessive radiative energy losses, there are two strategies, based either on reducing the density of impurities or their radiation efficiency, roughly proportional to the square of charge for fully charged impurities. Tungsten has a low sputtering yield, but high atomic number, whereas beryllium and carbon have a higher sputtering yield, but lower atomic number. Other factors have to be taken into consideration such as hydrogen retention, mechanical properties, and neutron interaction.

Recombined neutrals must be collected and pumped away, such that an excessive gas pressure at the edge of the plasma is avoided. Otherwise, the plasma may radiate and cool quickly, potentially causing it to completely recombine in a scenario called radiation collapse. Furthermore, the increasing density may cause a loss of the electron cyclotron resonance heating (ECRH) resonance condition and thus prevent heating. In addition to the particle flux from the plasma, gas is released as the initially saturated wall gets heated and the gas diffusivity inside the material increases. In W7-X, baking of the vessel to 150 °C removes most of the absorbed gas before experiment operation. A gas balance steady state in W7-X is expected to be reached for discharge lengths on the time scale of minutes and with cryogenic pumps. Presently, much more gas is pumped from the machine during and after a discharge than was added as a pre-fill providing particles to a plasma. Nevertheless the influx from the wall can temporarily be greater than the pumping capability and discharge length limited not by the allowable energy input, but by gas pressure control [14].

To have a defined interaction region of the plasma and wall, as well as a location of neutral gas concentration, two strategies are used: Tiles can be inserted to directly **limit** the plasma, define a LCFS and intercept fluxes, or fluxes can be **diverted** into separate \vec{B} -field phase space volumes.

Limiters

A component intersecting the field and defining a LCFS is called limiter. Using a limiter constructed from a suitable first-wall material offers considerable benefits over letting field lines end on the vacuum vessel, such as concentrating neutrals for pumping. Limiters are however not suitable for high power operation because of excessive heat loads and impurity release.

Field lines (FLs) ending on the limiter will collect particles through perpendicular transport from closed flux surfaces. The longer the connection length between opposite ends of an intersected FL, the larger the heat flux at those ends. More limiters with a larger extent therefore reduce the heat load density q . For q to be evenly distributed among multiple surfaces, they must all be tangential to the same flux surface, which is difficult to achieve in the face of plasma equilibrium changes and finite manufacturing and placement precision. In addition to the high heat flux on limiters, their drawback is the release of impurities into the closed flux surface region of the plasma. Limiters by definition are in contact with the LCFS and impurities sputtered from the surface will penetrate into the core. Keeping impurities away from the core, where they would be fully ionised and radiate strongly, is imperative to achieve high plasma temperatures. This is especially problematic in Stellarators where electric fields tend to move impurities inwards unless flushed out by turbulence [15]. A solution in which the plasma wall contact happens 'far' from the LCFS, separated by a field region in which impurities can ionise and travel along the field back to the wall, is needed.

Divertors

Separating plasma-wall interactions from the core plasma can be achieved by diverted field configurations. This is done in tokamaks by introducing one or multiple toroidal current loops in addition to the induced current at the magnetic axis, effectively creating additional magnetic axes. When the LCFS is pictured as a loop of string, each additional axis with counter-directed current adds a loop to that string by twisting it. Loops may then be intersected by targets and impurities released from them caught in that loop, rarely reaching the new LCFS and core plasma beyond it. The self-intersection points of the poloidal flux component are called X-points, whereas the axes of the islands are called O-points.

Divertors not only prevent impurities from reaching the core plasma, but can also aid pumping by compressing neutrals and reducing their flow away from the target. This is achieved by baffles, not intercepting the field lines directed at the divertor targets, but closing paths away from them along which neutrals might travel. Material intersections form a perfect sink for the plasma, while the crossing of the LCFS into the scrape-off layer (SOL) can, from a divertor point of view, be considered the source. To a good approximation, all ions recombine to neutrals at the target and are lost to the plasma fluid. There exists therefore a sonic flow, i. e. at the plasma fluid sound speed c_s , of particles to the nearest divertor targets which drags neutrals reflected from them along with it [16].

In tokamaks the connection length along the field from an 'upstream' position at the LCFS to the 'downstream' contact with the target is shorter than in stellarators. This reduces the importance of cross-field transport, while emphasising the role of magnetic flux expansion. For this reason, advanced divertor configurations such as 'Super-X' and 'Snowflake' aim to bring X-points closely together and extend the length of the divertor flux boundary legs. Generally, tokamak experiments have converged on a common divertor design, exploring parameters such as x-point height and flux expansion for further improvement [17–19].

Stellarator divertor concepts have not converged on a single design and each realisation is less thoroughly explored. The design considerations for the retention of neutrals, i. e. pumping and baffling, do not differ from tokamaks. Reduction of heat fluxes can be achieved in different ways. Approaches which have been developed into divertor concepts are listed in Table 1.1. We focus on the first branch, including the design chosen for W7-X.

Island divertor

On flux surfaces with rational values of ι , perturbations of the magnetic field can resonantly interfere, similar to constructively superpositioned waves. The relative strength of this effect depends on the order of the rational value, as shown in Figure 1.5. The field of W7-X reaches a low-order rational iota value at the edge of the designed confinement volume, as can be seen in that figure for the standard configuration with $\iota = \frac{5}{5} = 1$ at normalised radius $\varrho = 1$. Deliberately set, resonant components of the field cause islands

Table 1.1.: Physical mechanisms of heat flux diffusion and corresponding divertor concept realisations.

Effect causing heat flux spreading	Realisations
Long connection lengths of field lines within magnetic islands due to their flat ι -profile	(Local) Island divertor — W7-X [20], Wendelstein 7-AS (W7-AS) [21], large helical device (LHD) [22]
Diffusion in ergodic layers of the magnetic field	Helical divertor — LHD [23]
Increased cross-field transport through stochastic regions at high-curvature 'ridges' of the field	Non-resonant divertor — Helically Symmetric Experiment (HSX) [24]

to form. Their width (extent in effective radius r_{eff}) depends on the value of ι , its local gradient (shear s) and the relative strength of the resonant component through the formula in [6]

$$\delta r = 4 \sqrt{\frac{rR \delta B_r}{ns B_\phi}}. \quad (1.10)$$

The above equation is valid only for the special case of large aspect ratio ϵ and circular cross section, but highlights the important influences. Island width δr is dependent on the relative strength of resonant components of the radial magnetic field δB_r to the poloidal magnetic field B_ϕ . This is scaled by minor and major radius r and R , shear s and the number of poloidal field periods n . High shear thus reduces island size, but requires the ι profile to traverse more resonances, as can be seen by comparing W7-X and LHD in Figure 1.5.

Phenomenologically characterising higher order islands, they can be described as chains of lenticular shapes in Poincaré diagrams with x- and o-points lying on the rational surface. Around their centres (o-points), flux surfaces form with very small shear. This can be understood in two, non-rigorous, complementary ways: The rational surface, at which the island forms, is split in two to contain a volume, but can still be identified as that

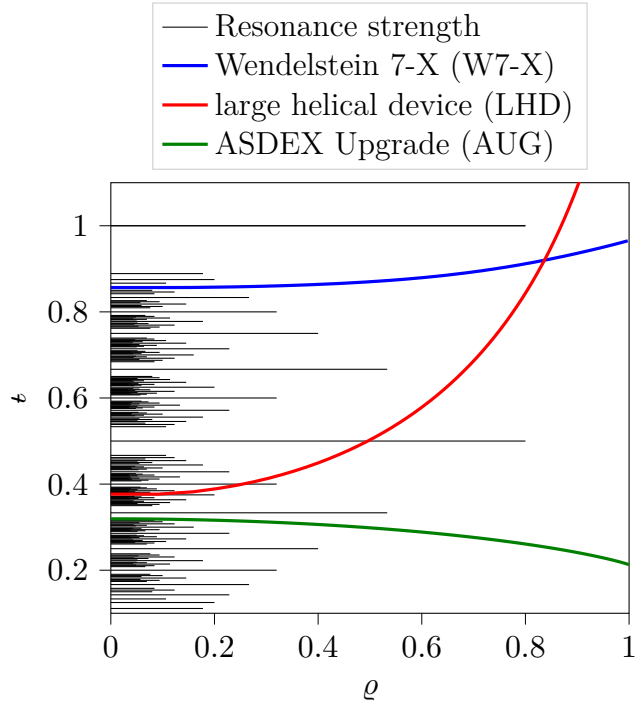


Figure 1.5.: Schematic t -profile of multiple devices over normalised radius. Strength of island resonances indicated on arbitrary scale by horizontal extent.

same surface, characterised by a single t value, at the x-points. The variation on both sides of the o-point must thus be sufficiently small for the field to stay connected. Additionally, following a field line on the 'inner' island surface, one may pass through the x-point onto the 'outer' island surface. Fast parallel transport implies that the pressure at the two locations will be very similar, and since pressure contours and flux surfaces are intimately linked, the rotational transform must also be similar everywhere along the field. Because of this low shear, connection lengths for field lines within the island are very long compared to those in the SOL outside the islands, and notably when compared to tokamaks. The opposite of what we said for tokamak divertors is therefore true: Flux expansion plays a relatively small role, while perpendicular transport is important for heat flux spreading [25].

1.3. W7-X

W7-X is an advanced stellarator built to assess the fusion relevance of the stellarator concept by demonstrating steady state operation near reactor plasma pressures and confinement [26]. Overviews of the progress towards these goals can be found in References [27–29]. Its field is optimised according to the following physical and technical criteria [30]:

Low neoclassical transport by minimising the geodesic curvature in regions where particles are trapped in magnetic wells;

Low bootstrap current to avoid dynamic changes to the field and thus achieve a controllable steady state;

Small effects of plasma pressure to prevent stochastisation and Shafranov shift of flux surfaces, which reduce the volume of good confinement;

Good MHD stability to allow operation at 5% normalised plasma pressure β ;

Good fast particle confinement necessary for scaling to an α -heated reactor;

Good flux surfaces with small islands inside the LCFS;

Good modular coil feasibility to allow construction of the machine and access ports.

W7-X plasmas have average major and minor radii $R \approx 5.5$ m and $r = 0.5$ m respectively, for a comparatively large aspect ratio of $\epsilon = 11$.

The resultant magnetic system of the torus is shown in Figure 1.6. It consists of 70 superconducting NbTi coils, arranged in five symmetric modules (five-fold rotational symmetry), with 14 coils of seven types in each. Modules are in themselves symmetric about a radial line from the torus centre (so called *stellarator symmetry*), such that each can be further divided into two half-modules. The technical challenges in the construction of W7-X are described by Bosch *et al.* [31].

For W7-X, steady state is defined as all physics and machine operation processes reaching equilibrium [32]. From this equilibrium requirement follow the choices of superconducting coils and ECRH using continuously operating

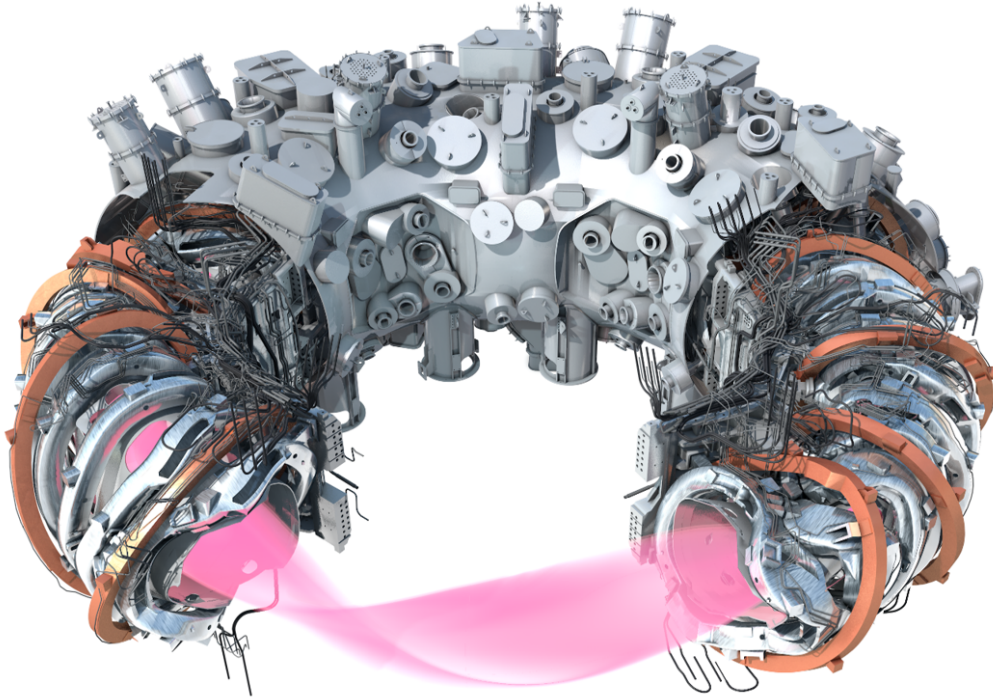


Figure 1.6.: Partial computer-aided design (CAD) view of the magnetic and vacuum system of the W7-X torus. Modules and layers have been cut away for visibility. Plasma shape is shown schematically in pink, surrounded by the inner vacuum vessel, the coil system in silver and copper colours. Coils are attached to central support ring and enclosed by the outer cryostat, with ports for instrumentation and infrastructure access.

gyrotrons as main heating system [33], whereas neutral beam injection (NBI) and ion cyclotron radiation heating (ICRH) are supporting heating systems for profile shaping and fast particle generation.

The coil system allows for flexibility in the field configuration by individually controlling the currents in each coil type, as well as fine-tuning with the aid of 15 room temperature copper coils. Nine reference configurations have different weighting of the above optimisation criteria.

All configurations share a shallow, i.e. low shear profile of rotational transform ι which crosses a low rational value at the edge, where therefore

large, stable magnetic islands are formed [34]. The W7-X divertor uses these islands as inherent diverted sections of the plasma to provide a phase space separation between closed flux surfaces and the SOL [35]. Each island flux tube wraps around the plasma helically and is periodically cut by a target plate. This results in a complex divertor geometry in which different sections of each island are cut at different angles, at different toroidal positions. The divertor is constructed to provide a wide heat load spread below critical values for nine reference configurations, spanning the configuration space permissible by the coil system. Each of the ten stellarator-symmetric divertor sections is composed of target modules, in turn constructed from fingers, subdivided by castellations [36]. Fingers and castellations reduce mechanical stresses due to thermal expansion of the divertor segments and surface.

Other plasma facing surfaces can be grouped by the heat load placed on them during an experiment. Weakly loaded areas are covered with stainless steel panels, more exposed ones with graphite tiles while the highest loads are borne by the graphite divertor.

Before installation of the water cooled high heatflux divertor (HHFD) [37] the machine operated with a massive graphite divertor identical in size and shape, the TDU [38]. The LP system discussed in this thesis and introduced in the next chapter is embedded into these divertor plates and diagnoses the plasma conditions there.

While the divertor is built to withstand heat loads of up to 10 MW m^{-2} , it is still preferable to operate the divertor under detached conditions to limit erosion and reduce the problem of SL movement (see Chapter 5). During detachment, a neutral gas cloud forms in front of the divertor targets and intercepts the heat flux. It has been reached and stably maintained in W7-X for up to 28 s [39]. Because atomic and molecular processes play an important role for detachment and process rates are highly sensitive to plasma conditions, separate and precise T_e and n_e measurements are particularly necessary. Providing these was the strongest motivation and aim of this thesis and hence our observations and analysis of detachment are its keystone achievement.

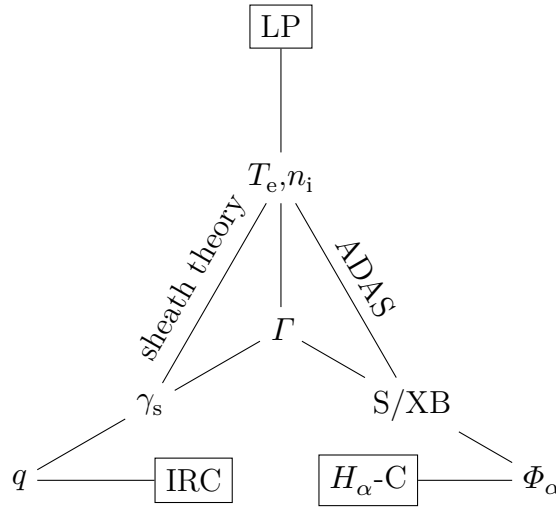


Figure 1.7.: Measurement network of heat flux q and particle flux Γ diagnostics. Through scaling factor values predicted by theory and experiment, physics quantities can be inferred from different sources. Abbreviations refer to Langmuir probe (LP), Infrared-Camera (IRC) and H_α -Camera (H_α -C). Details and relations will be explained in Chapter 3 and Chapter 4.

1.4. Thesis outline

The content of this thesis is organised as follows: In Chapter 2 we will introduce the LP system and discuss its evaluation. Special focus will lie on the comparison and use of different physics models of the LPs. Parameter values and uncertainties inferred from these models will be the basis of all further investigations.

In Chapter 3 and Chapter 4, the measurements of two key divertor quantities, the heat flux q and the particle flux Γ made by the LPs will be compared to those of other diagnostics. Figure 1.7 shows how these sources of information connect to form a network which can be used to complement measurements, check theoretical and simulation predictions and point to problems of diagnostics. LP values of T_e and n_e are inputs to equations and databases for scaling factors γ_s and S/XB to link LP, Infrared-Camera (IRC) and H_α -Camera (H_α -C) measurements.

Finally Chapter 5 will describe LP measurement observations of detach-

Chapter 1. Introduction

ment in the W7-X TDU, attempt to interpret them and explain some of the phenomena.

2

Divertor Langmuir probes in W7-X

Before describing the physics of Langmuir probes (LPs) and quantitatively analysing our measurements, the following section will give a short qualitative introduction and overview of the chapter to guide the reader.

2.1. Langmuir probe principles

Generally, LPs are objects in contact with the plasma to measure its electrical properties, such as the current drawn when a voltage is applied to the probe. Different pictures and descriptions of LPs are useful for understanding different aspects and in different contexts, so we will refer to the most instructive one in each case later.

In a simple and intuitive picture, bias voltage V_{LP} applied to the probe causes electrons to be attracted and ions repelled or vice-versa. Using a two-fluid model in which both plasma species are thermalised through frequent collisions, they have temperature-dependent Maxwellian energy distribution such that for continuously varying voltage the measured current at the probe I_{LP} is a smooth function of V_{LP} , the so called Current-Voltage characteristic (IV-characteristic). As we will see, the particle flow speeds in such a fluid model are limited, and thus the maximal currents are limited and saturate to I_{sat} and $I_{e,sat}$ respectively.

A sheath forms in front of an object in contact with plasma. The necessity for such a sheath is clear when considering that electrons flow much faster

than ions due to their lower weight. This initially causes a current from the surface to the plasma and the surface to charge up negatively, or conversely the plasma to become positively charged if the surface is grounded. The potential difference balances further particle flow until the net current is zero. Slowly biasing a LP amounts to changing the boundary condition of this electrostatic problem. We will make use of this picture when deriving LP evaluation models.

We will describe the process of LP evaluation and simultaneously introduce some further quantities and definitions: From the **raw data**, the measurements of applied probe voltage V_{LP} and measured probe current I_{LP} , some **intermediate derived quantities** can be obtained, such as the ion saturation current I_{sat} and the floating potential V_f . By fitting the raw data to a **Langmuir model** or transforming it the **inferred plasma quantities** temperature T_e and densities n_i & n_e are obtained. This requires auxiliary quantities such as the probe collection area A_{coll} and knowledge of plasma parameters such as ion charge Z .

To limit systematic errors in T_e & n_e by design, we will consider the effect the construction of the probe hardware has on the uncertainty in A_{coll} and saturation of I_{sat} .

The shape of the tips in contact with the plasma is special to Wendelstein 7-X (W7-X). Its faceted tips combine defined magnetic field angles with acceptable heat loads in all field configurations, but necessitate a re-consideration of analysis procedures. The reasoning behind the design and its details will be explained in Section 2.2. Next, the raw data measurement system will be described in Section 2.2.3. The reuse of an existing electronics system from Wendelstein Experiment in Greifswald für die Ausbildung (WEGA) required corrections of the collected data, accounting for a common mode, capacitance effects and interference between measurement channels. The most substantial part of this chapter will examine the interpretation of the LPs' IV-characteristics. First, we introduce existing LP models in Section 2.3 and discuss what we mean by 'model', important for the later comparison. Each model provides valuable elements which can be independently combined, such as expansion of the sheath along the perimeter of the projected area, predictions for sheath thickness and consideration of the current return path in a virtual double probe model. From these elements, six models are constructed. Section 2.4, describes in detail how they are evaluated to infer parameter values. It is shown how continuous data streams are

divided into discrete IV-characteristics and that multiple averaging methods for the parameters robustly obtain the same results. Least-square (LS), maximum likelihood (Max- \mathcal{L}) and Bayesian methods to obtain parameter uncertainties are considered in Section 2.5 and the `Minerva` framework is introduced. It is through this framework that the W7-X LPs are routinely analysed and their results saved. In Section 2.6 models are compared using the χ^2_ν method. Using an algorithm we developed to determine expected deviations from I_{mod} in the special situation of an incomplete model, we show that in attached plasma conditions all models perform equally well whereas in the cold plasma conditions of special interest to us, a modified version of Weinlich and Carlson’s model [40] performs best. This structure follows our *Review of Scientific Instruments* paper [41], but expands on a number of points both in breadth and depth.

2.2. Probe hardware

2.2.1. Probe tips

Observing the divertor plasma in W7-X with LPs is a challenge because of the spatial complexity of the plasma-wall interaction. Where should the probes be placed? The toroidally changing cross section adds a dimension of variation compared to constant-cross section configurations such as tokamaks or heliotrons. This is exacerbated by the experimental flexibility in operating the coil system, necessitating a divertor design that is not optimally fitted to one configuration but built to accommodate multiple. Furthermore, despite the symmetries of the ideal (as-designed) field, small deviations in construction of the (as-built) components [42] and especially plasma drifts [43] cause a variation of plasma contact between divertors in different machine half-modules. Since the asymmetry between modules can be reduced by fine-tuning of the configuration [44], and because the toroidal variation of the strike line (SL) is mainly a function of the (known) target plate positioning and angling, these dimensions were considered ignorable in the selection of observation positions for the LP system. The poloidal and up-down variation are covered by two arrays of probes, in divertor module HM50TM3h (Lower divertor (LD)) and HM51TM3h (Upper divertor (UD)) respectively. The toroidal position of the probes are defined by

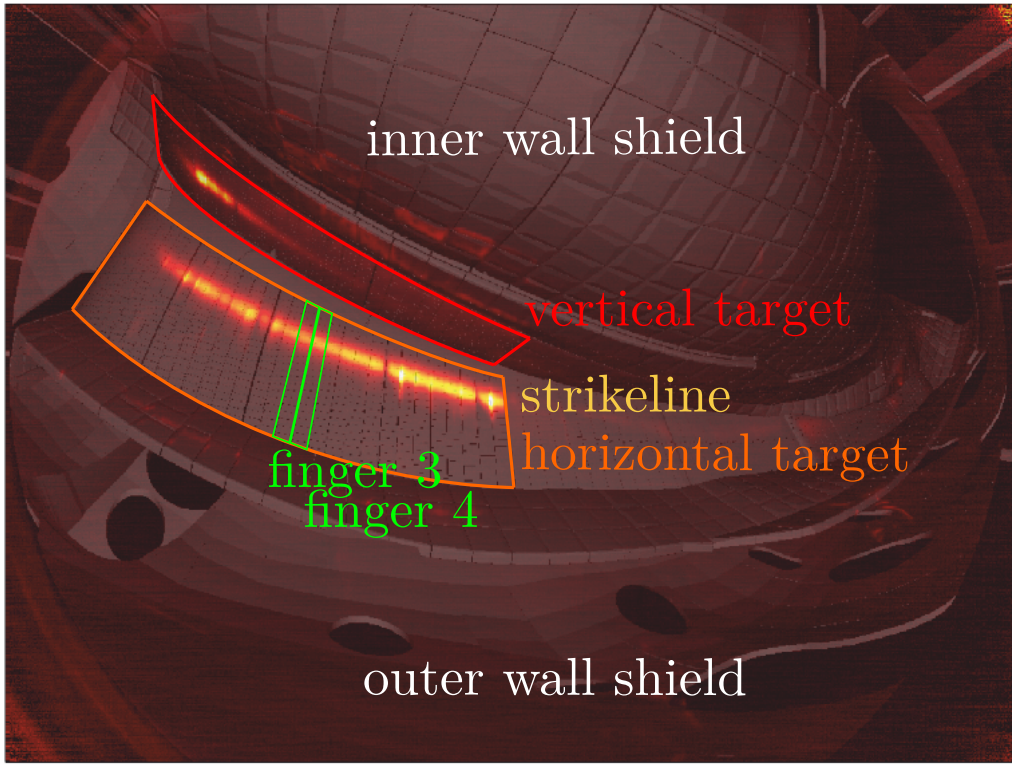


Figure 2.1.: View of one divertor module from the Infrared-Camera (IRC) [45] with overlaid CAD model. Two lines of ten probes are embedded into two adjacent Target Elements (TEs) 3 & 4 (fingers) in the horizontal target as indicated. The Heat load is visible especially at the strike lines on horizontal and vertical target as well as on the inner wall shield. Additional target elements not labelled. Figure courtesy of Peter Drewelow, adapted from Reference [45].

two stellarator-symmetric cross-sections intersecting the horizontal targets. These were chosen as SLs of configurations in the medium- and low-iota regions of configuration space lie in this region of the divertor. For operation phase (OP) 2, an additional array at toroidal positions on the high-iota target is installed.

The situation of the LPs in the machine can be seen in Figure 2.1.

Ideally the poloidal range of LP positions would span the entire divertor target at the selected cross section, i. e. from the edge of both the horizontal

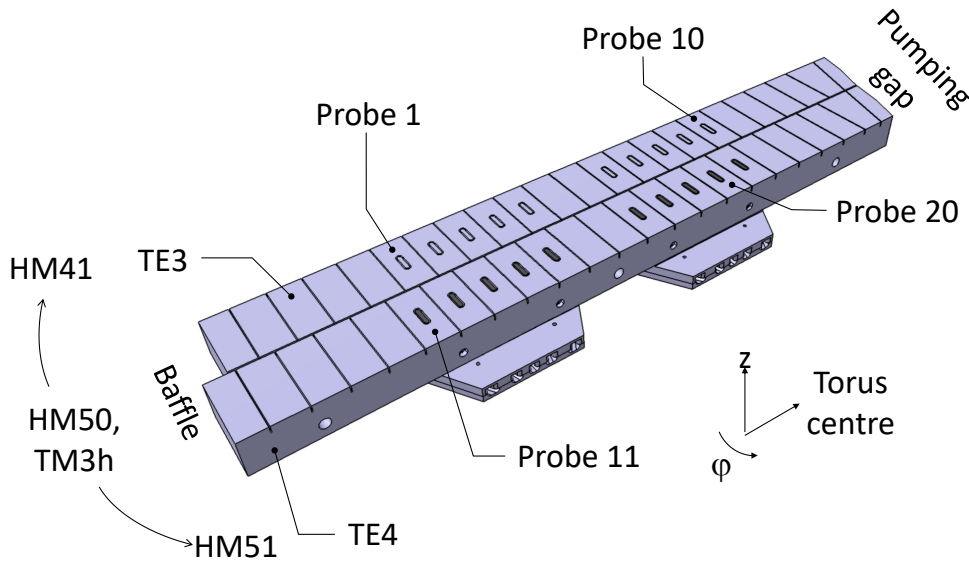


Figure 2.2.: Probe numbering and naming of components.

and vertical target to the Pumping Gap (PG). Placing probes in the vertical target was not possible because the space behind, necessary for cabling, is extremely limited. On the horizontal target, probes do not reach up to the PG in either the inertially cooled test divertor unit (TDU) in OP 1.2 or the water cooled high heatflux divertor (HHFD) in OP 2, because in both components sub-divertor space is limited by support structures or vacuum pumps.

To accommodate thermal expansion of the divertor surface, each module is constructed from castellated elements called 'fingers'. The distance of these castellations defines the toroidal spacing of the probes, 25 mm apart. To achieve the desired density of the LP array, probes arrays were placed on two adjacent fingers which are poloidally shifted 10 mm with respect to each other [46]. A computer-aided design (CAD) drawing of the two divertor fingers of the TDU with LPs, TM3hTE3 and TE4, is shown in Figure 2.2.

Just as the target plates must make a shallow angle with the field to reduce the heat flux, the probes must be prevented from eroding. Surfaces perpendicular to the field must therefore be avoided. It has long been known that flush mounted LPs are less well understood and their analysis more uncertain (see References in Section 2.3). It is therefore desirable to use the

largest field incidence angle compatible with expected heat loads, thermal contact and permissible erosion rate. As the expected heat load will vary with magnetic configuration and plasma conditions, a conservative choice must be made.

A further consideration is the size of the probes. Here we must make a trade-off between spatial resolution, reduced when probes tips are large, and relative importance of sheath effects, increased when tips are small. The latter refer to the increase of the current collection area A_{coll} due to the extension of the sheath from the probe surface which we will discuss in Section 2.3. An extreme example of this trade-off is the Doublet III-D (DIII-D) rail probe [47]. Using the axisymmetry of the tokamak, these probes are extended for 40 cm in the toroidal direction, thus having a large projected probe area negligibly impacted by the sheath. Such a design is of course not feasible in the non-toroidally symmetric field of W7-X.

Here therefore, an elongated faceted design was chosen, with tips 3 mm by 15 mm in size and a rounded rectangular shape shown in Figure 2.3. Rounding the edges is necessary to prevent sharp corners where arcing due to locally concentrated electric fields would be more likely. For the long and short axis of the probes respectively, the tip forms a wedge such that for the most critical field configuration the allowable heat load is not exceeded. Most probes always receive flux from the same direction and are fabricated with two wedges. Those tips for which the field incidence direction changes have four faces. Using facets rather than rounded surfaces makes the incidence angle uniform across each face. The field incidence angle, wedge angles, and area & perimeter of the probe projection are defined in Figure 2.5.

The tips are milled from the same graphite material as the surrounding target to avoid problems due to differential heat expansion [46].

To prevent overload to the divertor regions near the pumping gap with lower heat load handling capability during transient iota changes due to evolving toroidal currents, an additional divertor component was tested in OP 1.2 ([48] and References therein). The two test divertor unit scraper element (TDUSE) intercept field lines that might otherwise lead to a local overload of the divertor. One was equipped with eight cut-cylinder shaped LPs. Their data has not been analysed yet and will not be discussed in this thesis.

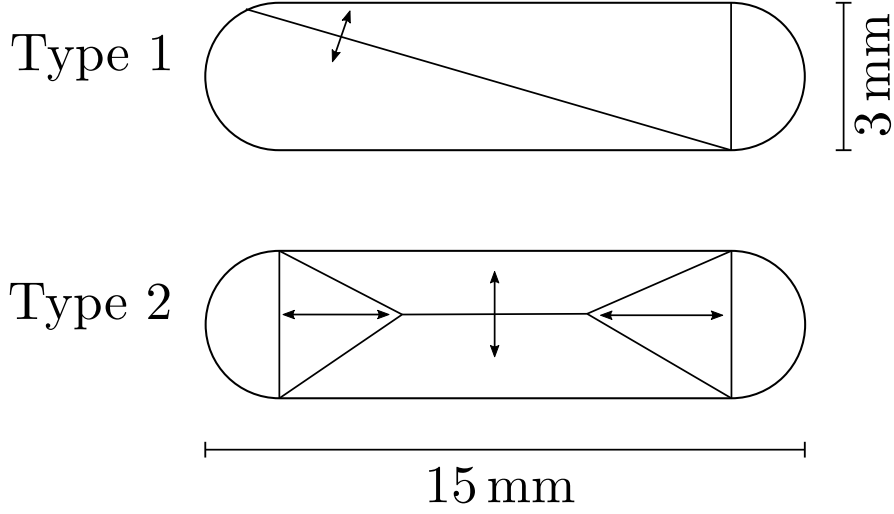


Figure 2.3.: Schematic of the faceted probe surfaces. Arrows indicate the directions of variation to achieve the desired probe surface field incidence angles. Type one (top) used for locations with field incidence $\gamma = [0, 3]^\circ$, type two (bottom) for locations with $\gamma = [-3, 3]^\circ$. Figure from Reference [41].

2.2.2. Cabling

Each tip is contacted with 2 wires. This sets up two circuits for a 4-terminal measurement, both closed through the plasma, with the vessel wall as reference ground. The bias voltage on the probe can be measured in a high-ohmic circuit, unperturbed by the current flowing in the other, low-ohmic circuit for current measurement.

Cables used inside the vessel must be compatible with both the stresses of that environment and the requirements of the Langmuir probe. Due to the size of the probe tips and expected plasma parameters, continuous current on the order of one ampere are expected, though they can be higher transiently. To measure I_{sat} to within 5% the probe must be negatively biased to at least $3T_e/e$. Sensible and feasible for us was a range of 200 V. To transmit fluctuations, the cable should have little damping up to a multiple of the sampling frequency of 500 kHz. The ultra high vacuum conditions in the vessel (1×10^{-7} mbar) require the use of insulation materials that will not release volatile compounds. A cable must thus furthermore be

compatible with high temperatures. To achieve this vacuum the machine is 'baked', i. e. heated to 150 °C, for a period of two weeks. Directly behind the divertor targets, temperatures during operation can exceed those during baking. Finally, though most of the electron cyclotron resonance heating (ECRH) radiation is absorbed by the plasma, some stray power is present everywhere in the machine where the microwaves with wavelength 2 mm can diffuse. Cabling must therefore have a reflective shield to not absorb and be heated by this stray radiation.

For these first 2 m from the probe a custom made twisted pair cable was used, consisting of two wires sleeved in a ceramic fabric mesh in a 3 mm copper tube. Through a connector box on the divertor frame, these could be plugged into a corresponding connector during the installation of the divertor. From here the in-vessel cabling was realised with commercially available, Kapton-insulated twisted pair cable, with the bundle of all LP cables guided and shielded by a copper pipe. Outside the vessel the pairs for each probe connect to a patch field. For the 70 m from here to the electronics rack either a 50-core twisted pair cable or individual 50 Ω coaxial cables can be selected. The 50-core cable was used for the 'conventional', slow measurement electronics whereas the coaxial cable was used for two experimental fast measurement and bias drive systems which will be briefly described at the end of the next section. Such a patch field existed for the UD and LD separately and the cables were grounded here. The boxes are in good electrical contact with the vessel and the targets.

2.2.3. Electronics

The established system, running routinely to diagnose the plasma, which we will refer to as conventional Langmuir probe (CLP), was previously used on the poloidal probe array of WEGA. It consists of eight measurement cards with eight channels respectively, each able to measure voltage or current. For this purpose a channels circuitry can be jumpered to use a 100/1 divider or a shunt resistor and differential amplifier to produce a signal proportional to voltage or current respectively. This is then digitised by a National Instruments 6033 analog-to-digital converter (ADC). The electronics of each channel are protected by a ESKA 522.517 fuse rated for 1 A and 250 V. We must correct for multiple types of error introduced by the CLP measurement cards, which we will describe later in this section.

These relate to the finite common noise rejection of the differential amplifier and the resistance of the printed circuit board (PCB) traces. The system was calibrated by a set of 1 k Ω or 10 k Ω test resistors. As the calibration currents thus generated were much smaller than the typical experimental ones, a correspondingly larger shunt resistor had to be used to test the linear response of the differential amplifiers over their entire input range. For this purpose and to accommodate different probe sizes and thus collected currents, shunt resistor values of 0.1 Ω , 1 Ω , 10 Ω and 100 Ω can be selected by a jumper. Through the power supply of the amplifiers the system has a second ground connection in the electronics rack, some 70 m from the torus. Because fluctuations on the ground loop established by these two connections were a concern, the voltage difference between them was recorded and found to be small, <1 V.

The bias voltage drive for the CLP system is provided by a combination of KEPCO 400-M bipolar and Phoenix Trio-48DC power supplies. Because each KEPCO can supply at most 4 A, the probes were split into four groups with one supply circuit each. The ten probes on Finger 3 of the UD and LD formed two such groups, a selection on both Fingers 4 a third and the eight probes in the TDUSE a fourth. Bias waveforms could be selected individually for each group. In practice, the settings for groups 1,2 and 4 were the same: They were swept with 500 Hz, a peak-to-peak amplitude of 100 V and an offset of -80 V. The probes of group 3 were kept at a constant bias of -180 V, recording ion saturation current. The remaining probes, also on Fingers 4 of UD and LD were unbiased, recording floating potential, or connected to the fast electronic systems introduced later in this section. Due to fluctuations, the 4 A maximum per group was sometimes intermittently exceeded, resulting in a reduction of the bias voltage amplitude.

Since there were in total 48 probes plus the two ground voltage difference monitors, the 64 measurement channels were not sufficient to record current and voltage on each probe. Instead the loop resistance of the cables was measured (16 Ω) and the output voltage of the power supplies recorded. Knowing the current for each probe, a correction could be calculated by $U_{\text{corr}} = R_{\text{cable}} * I_{\text{probe}}$ and applied to the output voltage to get the applied voltage at the tip for each probe. We verified this indirect measurement by a direct one on multiple probes.

Three corrections of the current measurements were necessary: common-mode correction, capacitance correction and shared-track correction.

The current measurement circuits used small shunt resistor for two reasons: Firstly, the differential amplifier (DAmp) detecting the voltage drop across it has an input range of -10 to 10 V and both saturates and may be damaged outside of it. Secondly, we do not want to influence the resistance of the LP circuit with a large shunt value. Using therefore a small resistance implies measuring a small voltage difference across the shunt relative to the large probe bias voltage, i. e. relative to laboratory ground. This requires a DAmp with a high common mode rejection ratio (CMRR), the inverse amplification of voltages present on both input terminals. The amplifier used (Analog Devices AD629) has a CMRR of 95 dB according to the data sheet, however this value could not be achieved in practice because of the periphery of the integrated circuit (IC). We observe therefore whenever the swept V_{LP} is applied an oscillating current proportional to the bias voltage, but shifted in phase. Amplitude and phase can be measured in phases without plasma, before and after each discharge. This phase shift is due to a superposition of the 'common mode current' with the capacitive current generated predominantly in the cable. This current can be calculated by $I_{cap} = C \frac{dV}{dt}$ where I_{cap} is the capacitive current, C the total capacitance and V the bias voltage. Because we use a single frequency sinusoidal sweep, I_{cap} is offset in time by $\frac{T}{4}$ or $\frac{\pi}{2}$ in phase, resulting in the observed shift. The magnitude of the phase shift depends on the relative amplitude of the two correction currents. We fit the total pre-plasma current with a factor and time offset applied to the bias voltage. It matches well with the expectation from the individual measurement of common mode rejection ratio (about 60 dB) and cable capacitance (20.0 ± 0.5) nF. This correction is applied to the entire current time trace. This method is relatively insensitive to variations of the sweep frequency or amplitude. After the correction there is still a detectable current without a plasma, containing components resonant to the sweep frequency, but it is no longer sinusoidal and much weaker at an amplitude of <5 mA.

A further correction is necessary due to the PCB circuitry. The voltage drop is not measured directly at the shunt resistor terminals but rather between the probe-side circuit track and the measurement card ground. The connection from the ground-side terminal to that common ground is shared by all channels. Because the track has a finite resistance itself, this implies that the signal on each channel also depends on the current in other channels

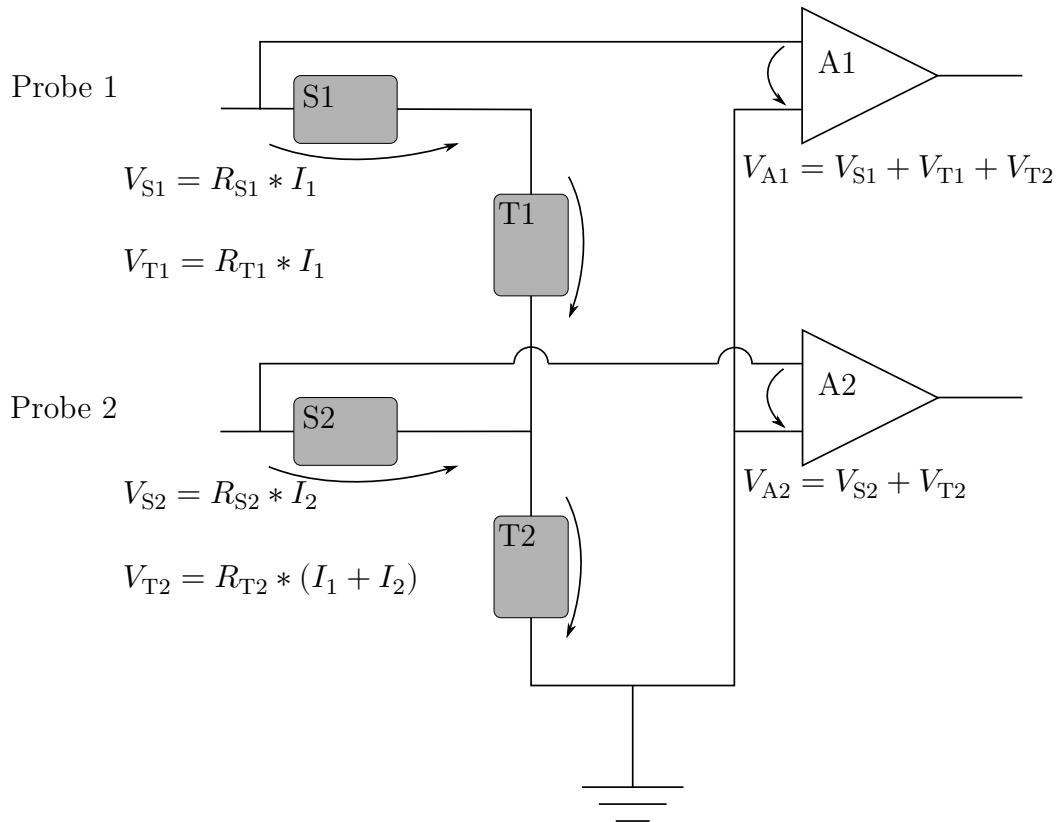


Figure 2.4.: Simplified scheme of the measurement card circuit. Only connections for 2 of the 8 channels are shown. **A**, **S**, and **T** for amplifiers, shunts, and tracks respectively, **V**, **I**, and **R** for voltages, currents and resistances. Arrows indicate voltage differences.

across the shared track segments. This is illustrated in Figure 2.4. From the circuit it becomes clear how the signal of each channel is composed and which correction must therefore be applied to disentangle the contributions of different channels. The matrix equation below shows how the currents and resistances contribute to the detected voltages, by inverting it we thus

obtain the desired probe currents.

$$\begin{pmatrix} R_{S1} + R_{J1} \\ R_{S2} + R_{J2} \\ R_{S3} + R_{J3} \\ R_{S4} + R_{J4} \\ R_{S5} + R_{J5} \\ R_{S6} + R_{J6} \\ R_{S7} + R_{J7} \\ R_{S8} + R_{J8} \end{pmatrix} * \mathbb{I}_8 + \begin{bmatrix} R_{\Sigma T1} & R_{\Sigma T2} & \dots & R_{\Sigma T8} \\ R_{\Sigma T2} & R_{\Sigma T2} & \dots & R_{\Sigma T8} \\ \vdots & \vdots & \ddots & \vdots \\ R_{\Sigma T8} & R_{\Sigma T8} & \dots & R_{\Sigma T8} \end{bmatrix} * \begin{bmatrix} I_1 \\ I_2 \\ I_3 \\ I_4 \\ I_5 \\ I_6 \\ I_7 \\ I_8 \end{bmatrix} = \begin{bmatrix} V_{A1} \\ V_{A2} \\ V_{A3} \\ V_{A4} \\ V_{A5} \\ V_{A6} \\ V_{A7} \\ V_{A8} \end{bmatrix} \quad (2.1)$$

Here \mathbb{I}_8 is an 8×8 identity matrix, I_i and V_{Ai} are respectively the current and voltage on channel i , R_{Si} is the shunt resistance used on that channel and $R_{\Sigma Ti}$ is the total resistance from that channel to ground ($R_{\Sigma n} = \sum_{i=n}^{i=8} R_{Ti}$). Additionally R_{Si} , must be corrected by the resistance of the jumper R_J selecting the shunt value which contributes another $\approx (110 \pm 30) \text{ m}\Omega$. The resistances of these track segments were both measured individually and determined by calibrating each channel with the aforementioned test resistors. To minimise how much correction would be necessary, we connected probes with high expected currents (near the pumping gap) to channels with little influence on others, i.e. higher channel number and greater proximity to the common ground. Typically channels 1-3 of each card were used for voltage and channels 5-8 for current measurements.

To correctly label the digital levels recorded by the ADCs and store all associated settings such as sweep frequency, a computer-readable system of configuration storage was necessary. This was programmed in `Java` in the form of a settings manager which created objects representing the entire configuration state of the diagnostic and stored it in the archive. This included the correct attribution of channel number on the measurement cards to probe tips and the jumper settings of those channels. In a second step, an independent `Datasource` program used this information to retrieve the ADC readings, scale them to obtain physically meaningful quantities (V_{LP} & I_{LP}), apply the necessary corrections and finally write the results back to new archive locations. This ensures that the entire path of the data analysis can be reconstructed, modified and rerun should we become aware of errors. The previous system of human-readable records of the settings

was not suitable for analysing the wealth of data gathered in the passed and future OPs. Further analysis code could use either the stored raw data in the archive or directly communicate with the data source.

2.3. Langmuir models

To gain useful information from LPs, we need a measurement model, by which we mean an equation that relates the parameters of interest to the raw measurements.

The difficulty of describing, comparing and using models stems in part from the diverse uses of the word. What constitutes a model is a matter of debate both between practitioners and philosophers of science [49, 50]. One approach is that models are constructs fulfilling different functions: to represent, illustrate, simplify and explain the 'essence', the 'important bits' of reality and observations [51]. Another is to loosely and empirically group models under labels such as those given in Table 2.1.

Table 2.1.: Loosely defined types of models from Reference [49]. LPs models are mixtures of different types, containing elements of simplification, phenomenological model and approximation.

Type	Description	Examples
Hypothesis	"Could be true"	Rutherford and Thomson atom models
Phenomenological model	"Behaves as if ..."	Ptolomaic epicycle planetary model
Approximation	Works given a scale ordering	Linear response (Hooke's law), perfect gas
Simplification	Omit some features for clarity	Van-der-Waals potential, Nuclear shell model
Instructive model	Gives insight	Mean free path, nuclear drop model
Analogy	Some common features	Ising model
Gedankenexperiment	To disprove a hypothesis	Carnot cycle

These groupings are not well separated and as we will see, LP models combine elements of multiple groups.

A related question to what a model is and what its functions may be is how to compare, rank and evaluate them. We think models should be

fundamental using the true, underlying physics reasons and first principles;

simple intellectually easy to grasp; and

accurate conforming to observations within given boundaries.

The first of these criteria implies a preference for models that are instantiations of theories over phenomenological models. The second means that we will use analytical models rather than numerical ones whose behaviour we can not intuitively predict. The third is the most quantitative one and will be the method of comparison between the models the first two criteria restrict us to.

Finally, because we are seeking a measurement model, we have an additional requirement with respect to the models in Table 2.1: The terms and parameters of the model must be sufficiently independent or orthogonal in their effect to be inferred from the raw data. For a model $z = ax + by$ where z is measured, x, y controllable and a, b to be inferred, this is perfectly possible. For a model $z = ax + bx^2$ less so and for $z = ax + bx$ it is impossible. So even if the last might be the most accurate explanatory model, it would not be suitable for a measurement of a, b .

2.3.1. Simple Langmuir model (SL) derivation

To derive the basic Langmuir model (SL), which will be the starting point of our discussion, we need two relations, one for the ion and one for the electron flux. The situation we consider will be that of an object in contact with a dense plasma with isothermal electrons and ions at rest (non-drifting). Dense implies that the characteristic Debye length λ_D is much shorter than the dimensions of our probe \mathbf{d} and that sufficient collisions occur to ensure that energy distributions are Maxwellian. Isothermal implies that the characteristic temperatures T_e and T_i are similar. Because electrons are lighter than ions, they move faster such that the random, one-directional

Maxwellian flux

$$\Gamma_{\text{Maxwell}}^{1\text{D}} = \frac{1}{4}n\bar{c} = \frac{1}{4}n\sqrt{\frac{8T}{\pi m}} \quad (2.2)$$

is much greater for electrons. $\bar{c}(T, m)$ is the average velocity of Maxwell-distributed particles. This will cause the object to charge up negatively, until sufficient electrons are electrostatically repelled. Charge perturbations are screened by a so called 'sheath' with a thickness of a few λ_D , the boundary of which we will consider frequently and label sheath edge (SE). Such a negatively charged object will act as a perfect sink for ions, which will thus travel towards it at the plasma sound speed c_s [52]. The first of the two relations we require is thus

$$\Gamma_i = n_{\text{SE}}c_s. \quad (2.3)$$

The density of electrons within the sheath is lower than in the bulk plasma, so even though there can be no discrete transition, we can define the sheath as the region within which quasi-neutrality is violated. Analogous to the population of two energy states, some electrons out of the statistical ensemble overcome the potential difference between the plasma and the object, such that just as in that case, the density there is given by a Boltzmann factor dependent on the potential difference δV and T_e :

$$n_e^{\text{surf}} = n_e^{\text{SE}} \exp\left(\frac{-e\delta V}{T_e}\right). \quad (2.4)$$

Here, as in the entire document, we take T to have units of energy, conveniently eV [53]. These energies are related to temperatures by the Boltzmann constant k_B . The electron flux to our object surface, and second relation we will require, is thus

$$\Gamma_e = \frac{1}{4}n_e^{\text{surf}}\bar{c}_e = \frac{1}{4}n_e^{\text{SE}} \exp\left(\frac{-e\delta V}{T_e}\right)\bar{c}_e. \quad (2.5)$$

We will define V_f as the δV necessary to shield sufficient electrons such that the net current at the surface is zero. In the case of singly charged hydrogen

ions:

$$\Gamma_i = \Gamma_e \quad (2.6a)$$

$$n_{\text{SE}}c_s = \frac{1}{4}n_e^{\text{SE}} \exp \frac{-e\delta V}{T_e} \bar{c}_e \quad (2.6b)$$

$$\bar{c}_e = 4c_s \exp \frac{eV_f}{T_e}. \quad (2.6c)$$

Because the different speed of electrons and ions was the reason for the surface charging up, it is intuitive that V_f should link \bar{c}_e and c_s .

If we now consider what the current density to an arbitrarily negatively charged surface at potential V should be, we combine Equation (2.3) and Equation (2.5) and use Equation (2.6c) to substitute for \bar{c}_e .

$$j = e(\Gamma_i - \Gamma_e) \quad (2.7a)$$

$$= e \left(n_{\text{SE}}c_s - \frac{1}{4}n_e^{\text{SE}} \exp \frac{-eV}{T_e} \bar{c}_e \right) \quad (2.7b)$$

$$= en_{\text{eSE}}c_s \left(1 - \exp \frac{eV_f}{T_e} \exp \frac{-eV}{T_e} \right) \quad (2.7c)$$

$$j = en_{\text{eSE}}c_s \left(1 - \exp \frac{-e(V - V_f)}{T_e} \right) \quad (2.7d)$$

Multiplying Equation (2.7d) by the appropriate area, we get the current I_{LP} we expect to flow to an object, negatively biased with respect to the bulk plasma. Varying the applied voltage $V = V_{\text{LP}}$, we can infer the parameters n_e , T_e and V_f and thus have a Langmuir probe model. For very negative $V_{\text{LP}} - V_f > -5T_e$, the exponential term becomes negligible and saturation is reached at $j_{\text{sat}} = en_{\text{eSE}}c_s$. The ion sound speed used in this and the above expressions is given by

$$c_s = \sqrt{\frac{ZT_e + \gamma_i T_i}{m_i}} \quad (2.8)$$

where Z is the average ion charge and γ_i is the ion adiabatic coefficient. We will explain our choices for the values of these auxiliary parameters in Section 2.4.

This derivation does not account for an electron saturation current $I_{e,\text{sat}}$, which flows when the probe is biased strongly positive. Since it now acts as a perfect electron sink, those particles reach $c_{\text{sound},e}$ at the SE, which is a factor m_i/m_e larger than c_s . $I_{e,\text{sat}}$ is in theory therefore so large that it would heat the probe (see Chapter 3) and require a different layout of electronics. It is in practice avoided by not biasing the probe far into the positive branch, and therefore also not considered in the SL.

Expansions of this very condensed derivation can be found in References [53–56].

2.3.2. Motivation for expansion to advanced models

The extensive consideration of LP models is motivated by the observations of OP 1.2a: In this campaign, the LPs showed high temperatures, even in apparently detached scenarios with strong convective heat flux reduction. Furthermore, there seemed to be an artificial lower T_e limit of approximately 10 eV that was never undercut. Examining the IV-characteristics, non-saturation of the supposed ion saturation current I_{sat} was clearly visible. This was thought to be the main reason for the overestimated T_e and could be phenomenologically addressed by subtracting a linear correction, but not resolved to our satisfaction [57]. Upon detailed inspection it also became clear that the electron current was saturating at a much lower level than expected from theory. As noted in those publications, we were well aware of the issues of low-incidence angle and flush mounted probes in other devices, as well as of the existence and use of other models [58]. These could however not be directly applied where codes were available to us, or reproduced where they were not. It was therefore necessary to disassemble existing models to the point where we could understand their components, adjust them to the situations of W7-X, reassemble them with all their auxiliary assumptions and information and implement them in a suitable code.

The three areas where models differ are outlined in the following sections.

2.3.3. Consideration of sheath

We have already seen that to go from intermediate I_{sat} to inferred n_e , we require the probe collection area A_{coll} . In a strong magnetic field ions are tightly bound to field lines (FLs), by which we mean $\rho_i \ll \mathbf{d}$. A_{coll} is

therefore in first approximation equal to A_{proj} , the area of the projection of the probe onto the field. In the extreme case of a flush mounted probe, whose normal vector \hat{n}_p is perpendicular to the field, it is clear that the sheath that extends from the probe surface will contribute to A_{coll} . For specific probe shapes this effect has been analytically calculated or modelled, such as for spherical, cylindrical [59] and rectangular, flush mounted probes [40]. For generic probe shapes such as ours, the approach by Tsui *et al.* [60] is easy to implement: Considering a rounded probe shape, the most significant contribution to A_{coll} will be made by the sheath where $\hat{n}_p \perp \hat{b}$ whereas the sheath where $\hat{n}_p \parallel \hat{b}$ contributes nothing. Only from FLs passing through the sheath, but not striking A_{proj} do we need to account for additional ions. For rounded probes, the condition $\hat{n}_p \perp \hat{b}$ is true along the line of furthest extent of A_{proj} , its perimeter P_{proj} . Even on probes with polygonal faces the edge of the plasma-wetted area is in reality, on a small scale rounded. We therefore use P_{proj} also for such probes and calculate the effective collection area as

$$A_{\text{coll}} = A_{\text{proj}} + P_{\text{proj}} * l_{\text{sheath}} \quad (2.9)$$

where l_{sheath} is the sheath thickness. We call this the perimeter sheath expansion model (PSE).

The situation for our probes is shown in Figure 2.5. For small field incidence angles, or equivalently large angles between \hat{n}_p and \hat{b} , the difference between extending the sheath along \hat{n}_p (from the surface) or simply perpendicular to $\hat{l}_p \times \hat{b}$ (from the perimeter), where \hat{l}_p is the tangent vector along the curve P_{proj} , is small.

Not the entire perimeter should be counted when determining the length along which the sheath can extend. As we can see in Figure 2.5, along the lower half of the perimeter the vector $\hat{l}_p \times \hat{b}$ pierces into the target. Since the sheath can't extend there, we use half the geometric P_{proj} in our calculation of A_{coll} .

A further consideration is whether the sheath can extend parallel to the target. Far away from the probe we would expect electric fields to be perpendicular to the target, but the modification in the vicinity of the probe might be strong. This question was inconclusively examined by Bergmann [61] and Weinlich *et al.* [62], we follow Tsui *et al.* in treating target-parallel and perpendicular direction equally.

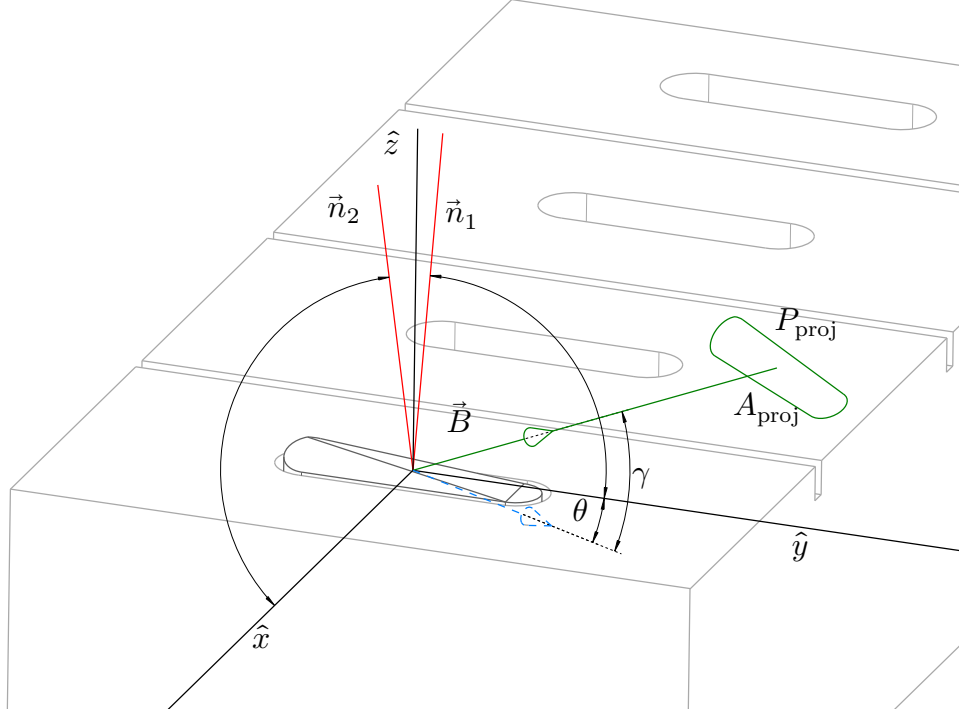


Figure 2.5.: Schematic view of our LPs with definitions of vectors, angles, areas and projections. Target finger is cut along the surface castellations. $\hat{x}, \hat{y}, \hat{z}$ are axes aligned with the probe and normal vector of the target. γ is the polar angle of the magnetic field vector \vec{B} shown in green, with its projection onto the surface in dashed blue, θ the azimuthal angle of the long probe major axis \hat{y} with the field projection. \vec{n}_1 and \vec{n}_2 are the normal vectors of the probe facets. As indicated by the arcs, each lies in a plane defined by \hat{z} and one other axis. γ and therefore also A_{proj} is exaggerated for better readability. Figure from Reference [41].

Finally we must consider that when V_{LP} is positive, the sheath in front of the probe will be smaller than that before the target. Consequently, the target sheath shadows the probe, reducing A_{proj} . Since the target is grounded, its sheath thickness is only dependent on V_p . Equation (2.9) is

thus corrected to

$$A_{\text{coll}} = A_{\text{proj}} + P_{\text{proj}}^{\text{eff}} * l_{\text{sheath}}^{\text{probe}} - P_{\text{proj}}^{\text{shadow}} * l_{\text{sheath}}^{\text{wall}} \quad (2.10)$$

$$A_{\text{coll}} = A_{\text{proj}} + \frac{P_{\text{proj}}}{2} * (l_{\text{sheath}}^{\text{probe}} - l_{\text{sheath}}^{\text{wall}}) \quad (2.11)$$

because as elaborated above in our case the segments defined by the lower and upper edge of the probe are approximately the same length.

In reality, the sheath will form a smooth surface, without hard edges or transitions, such that accounting for details of the geometry only superficially improve the quality of the model [63]. We expect some adjustment of P_{proj} to be necessary for optimal matching, similar to the model correction factor α used by Weinlich *et al.* [40].

Crucial for the calculation of the corrections to A_{coll} is the sheath thickness l_{sheath} . Frequently this is obtained from the Child-Langmuir law for space-charge limited current by assuming negligible electron density inside the sheath. Comparison with analytic solutions for simple geometries such as by Laframboise shows the approximation is accurate to within 10 % [64]. This thickness is given by

$$l_{\text{CL}} = c\lambda_{\text{D}} \left(\frac{e\Delta V_{\text{sheath}}}{T_{\text{e}}} \right)^{\frac{3}{4}} \text{ for } \Delta V_{\text{sheath}} > 0 \quad (2.12)$$

with $c = 0.8$ and λ_{D} the Debye length[65]. We follow Tsui *et al.* in estimating ΔV_{sheath} by

$$\Delta V_{\text{sheath}} = V_{\text{p}} - V_{\text{bias}} \quad (2.13a)$$

$$V_{\text{p}} = V_{\text{f}} + \frac{\Lambda T_{\text{e}}}{e} \quad (2.13b)$$

$$\Lambda = 2.5 \text{ and } c = 1. \quad (2.13c)$$

Using $\Lambda = 2.5$ here effectively neglects the magnetic sheath we will discuss below and $c = 1$ simplifies the Child-Langmuir expression and accounts for reported deviations from it [66, 67].

2.3.4. Consideration of magnetic pre-sheath

If $\rho_{\text{i}} \ll \mathbf{d}$, the ion flow is essentially one-dimensional only along the field. At non-perpendicular incidence of the particles onto the sheath, a pre-sheath is necessary to deflect ions such that their surface normal velocity

component fulfils the Bohm criterion ($v_{\text{SE}} = c_s$) [68]. This magnetic presheath is associated with a potential and through the Boltzmann factor consequently a density reduction. Weinlich *et al.* consider both the change in incidence angle [62] and the refraction of plasma and associated change in λ_D . In Reference [40], accounting for an electric field at the SE leads to a different formulation for the sheath thickness, given in Equation (2.14a). Using the notation of Weinlich *et al.*, l_{WC} is the sheath thickness, ψ the field incidence angle to the surface normal, Φ labels potentials and prime denotes derivatives w.r.t. distance from the wall or probe. Note that ψ in this notation corresponds to $90^\circ - \gamma$ in ours.

$$l_{\text{WC}} = \frac{l_{\text{norm}}}{12} [(\phi'_{\text{pr}}{}^3 - \phi'_{\text{w}}{}^3) + 3(4 - \phi'_{\text{SE}}{}^2)(\phi'_{\text{pr}} - \phi'_{\text{w}})] \quad (2.14a)$$

$$l_{\text{norm}} \approx \frac{\lambda_D}{2\sqrt{\cos \psi}} \quad (2.14b)$$

$$\phi'_{\text{w|pr}} = \sqrt{4\sqrt{1 + \phi_{\text{w|pr}}} - (4 - \phi_{\text{SE}}^2)} \text{ for } \phi_{\text{w|pr}} > 0 \quad (2.14c)$$

$$\phi_{\text{w|pr}} \approx -\frac{2e(\Phi_{\text{w|pr}} - \Phi_{\text{me}})}{T_e} + 2 \ln(2 \cos \psi) \quad (2.14d)$$

$$\phi'_{\text{SE}} \approx -\frac{\lambda_D \ln(2 \cos \psi)}{\rho_s \sqrt{\cos \psi}} \quad (2.14e)$$

Dimensionless potentials are referenced to the (Debye) sheath edge and normalised by the ion kinetic energy there divided by charge.

$$\phi = -\frac{\Phi - \Phi_{\text{SE}}}{\Phi_{\text{norm}}} \text{ where } \Phi_{\text{norm}} = \frac{m_i v_{\text{SE}}^2}{2Ze}. \quad (2.15)$$

Subscripts *me*, *De*, *w* and *pr* refer to values at the magnetic sheath edge, Debye sheath (SE), wall around the probe and probe itself respectively. $\rho_s = \frac{m_i c_s}{\sqrt{2Z|\vec{B}|}}$ is the ion Larmor radius at sound speed. By assuming that $T_e = T_{i,\text{me}}$, $Z = 1$, $\psi \geq 80^\circ$ and ions at the sheath edge are mono-energetic^I the equations can be simplified. Where these assumptions were used, it is shown by a "≈" symbol. This expression is consistent with the Child-Langmuir

^IThe mean is significantly greater than the spread of the ion velocity distribution. [40]

law in its region of validity: Under the assumptions of normal incidence and cold ions, a series expansion of l_{WC} recovers the $\propto V^{\frac{3}{4}}$ scaling of l_{CL} .

As might be expected with a discrete separation of a continuous potential drop and transition from quasi-neutral plasma to low- n_e sheath, how that entire potential drop is divided between the different regimes is subject to extended discussions [56]. We follow Weinlich *et al.* by using $\Lambda = 3$ in Equation (2.13b) for the calculation of l_{WC} , the approximate value for hydrogen plasmas.

Sheath thickness predicted by the two models differs by a factor of 2-2.5 depending on the conditions, as is shown in Figure 2.6. This difference manifests in the different predicted slopes of the IV-characteristic ion-current branch.

It can be explained by the different scaling of two effects with incidence angle ψ in the Weinlich-Carlson sheath expansion model (WSE). Firstly, n_e being reduced in the magnetic pre-sheath increases λ_D at the SE, scaling as $\cos(\psi^{-1/2})$. Secondly, since the total sheath potential drop $V_p - V_{\text{LP}}$ is now divided onto two domains, the Debye sheath drop is lower and its thickness reduced, scaling as $\ln[\cos(\psi)]$. This explains the behaviour at strong probe bias. Panel (b) of Figure 2.6 shows the effects at small positive V_{LP} , namely a constant offset δl_{min} corresponding to the pre-sheath thickness and an offset δV_{min} of the minimum V_{LP} for which a Debye sheath forms.

Since for our faceted probes there is no unique incidence angle, we calculate an average across all faces, weighted by the projected area of each face as

$$\gamma = \sum_{i=0}^{n_{\text{faces}}} \frac{\gamma_i * A_{\text{proj},i}}{A_{\text{proj}}}. \quad (2.16)$$

2.3.5. Consideration of current return path

Particles flowing predominantly along the FLs has an additional consequence of restricting the volume from which they can reach the probe. We may imagine tracing the projection of the probe away from it along the field to create the source volume. Considering diffusion, primarily through turbulence, the source volume will widen forming a cone, with the probe at its tip and an opening angle determined by the relative speeds of parallel and perpendicular particle transport. If the particle number in that volume is small, the

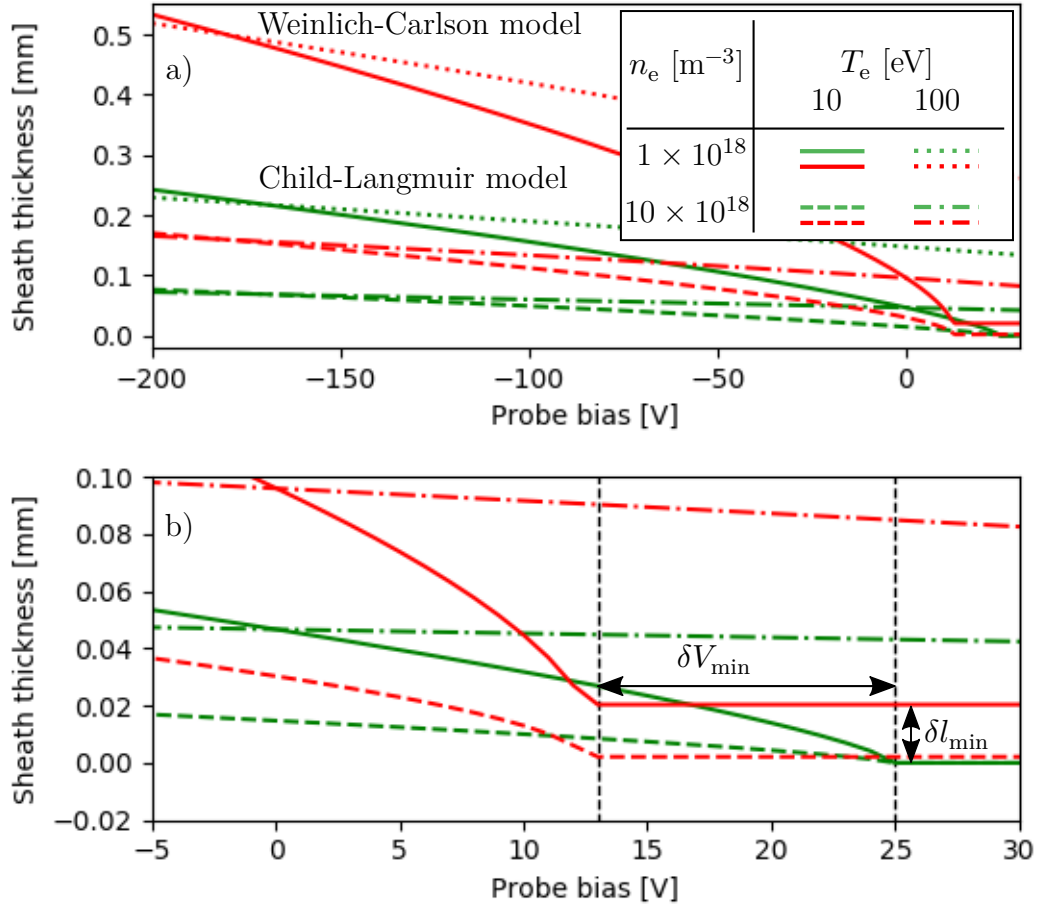


Figure 2.6.: Absolute sheath thickness in front of probe for Child-Langmuir (green) and Weinlich-Carlson (red) models at different conditions. Shadowing of the probe by the target is not considered. For the calculation V_f is taken to be zero. Figure from Reference [41].

probe may deplete the flux tube or must draw current from the intersection of the flux tube with other elements. This is of practical importance particularly in the electron branch, where large currents ($I_{e,\text{sat}} \approx \sqrt{\frac{m_i}{m_e}} I_{\text{sat}} \approx 50 I_{\text{sat}}$) may be drawn. Reduction of this ratio has long been observed and cited as a reason for not sweeping into the electron current branch [55]. As we will see however, strongly reduced ratios of $\frac{I_{e,\text{sat}}}{I_{\text{sat}}} = \kappa$ can have an impact on the inference of T_e even when substantial positive V_{LP} is avoided. If current is drawn from another element, the system resembles a double probe [69] and should be modelled as such, with the current ratio κ equal to the area ratio β . This approach, which we will call virtual asymmetric double probe, is followed for example by Monk *et al.* [70] and Weinlich *et al.*.

Measurements particularly on flush or shallow incidence angle probes show the acute necessity to consider reductions of κ [71]. It has been shown experimentally and through theoretical arguments [72] that the current is drawn from the immediate vicinity of the probe with a return current fall-off length $\mathcal{O}(4mm)$, not along a long flux tube. This implies that even probes with non-overlapping projections may influence each other if, through cross-field transport, current is drawn from one to another. We see evidence of this in Figure 2.7, showing the swept V_{LP} of probe UD7 on Finger 3 and V_f recorded by probe UD17 on the adjacent Finger 4. Although the projections of the probes do not overlap, UD17 is grounded and thus separated from the power supply and the measurements are made on different electronics cards, there is clearly a correlated perturbation of V_f . This observation matches the expectation of the asymmetric double probe model: Whenever UD7 is positively biased and drawing an electron current, $V_{f,17}$ increases to compensate. A similar, though less clear behaviour is observed on the I_{sat} probes on Finger 4. A density perturbation is not visible at greater distances, for example in the spectrum of the H_α spectrometer photo-multiplier tube (PMT) 28 with a sight line through the same island the probes contact.

Combining the options above we can construct six models, summarised in Table 2.2. We will refer to the current predicted by a model, given V_{LP} and parameter values, as model current I_{mod} .

Table 2.2.: Langmuir Models compared in this thesis, grouped by their sheath model and use of double probe characteristic.

	Single Probe	Double Probe
No sheath expansion	SL	DSL
Child-Langmuir Sheath	PSE	DPSE
Weinlich-Carlson Sheath	WSE	DWSE

2.4. Considerations for evaluation

Langmuir models make predictions for the IV-characteristic in stationary plasma conditions. For slowly varying bulk plasma parameters, we can approximate values as constant if sweeps are sufficiently fast. Fluctuations of the parameters significantly faster than the sweep period can in general not be resolved. We will assume the inferred parameters for one sweep period are the average of the varying parameters, even though this might not be strictly correct [73]. A sinusoidal density variation resonant with f_{sweep} for instance would create a bimodal scatter in measured I_{sat} values, whereas bursts of dense plasma reaching the probe, for instance in the form of blobs, would create an asymmetric distribution. The optimal fluctuation power spectrum would thus have a deep trough around the sweep frequency, such that slower variations can be resolved and faster ones smoothed. Particularly modes at only slightly higher frequencies than the sweep might systematically distort the characteristics, by for instance always contributing positively to $I_{e,\text{sat}}$.

Unfortunately, such a trough does not exist, as can be seen from the spectra of LP signals and H_α -Spectrometer (H_α -S) signals in Figure 2.7.

Dividing the sampled time trace into sweeps is trivial in theory, but not in practice. Every half-period of the voltage sweep from one extreme of V_{LP} to the other provides a full IV-characteristic. In principle one could fit only parts of the IV-characteristic to gain a higher resolution, but at the cost of a great deal of accuracy, as for instance T_e is by construction very hard to estimate from the I_{sat} branch. The practical difficulties come from the need to use the real, discretely sampled V_{LP} signal to get the best known applied voltage for each I_{LP} sample. That real V_{LP} signal, though in principle an amplified version of a pure 500 Hz sinusoid, is in practice subject to noise, fluctuations of generator output power and frequency drift. Multiple approaches were tried and implemented as `data_slicer` classes to

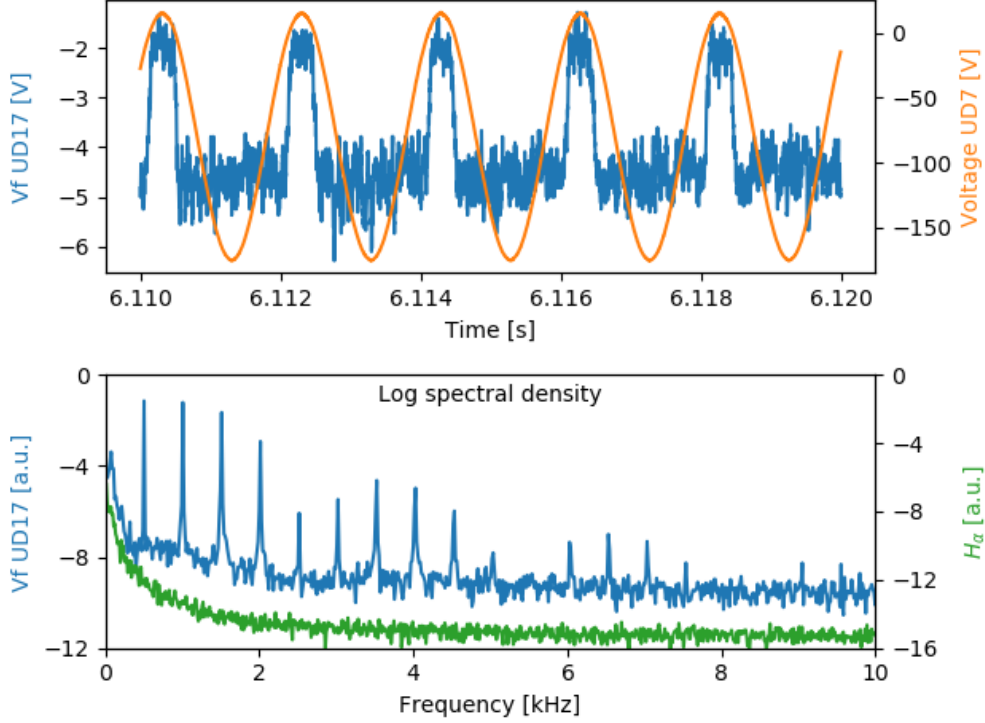


Figure 2.7.: Influence range of swept probes. Top panel shows the short range influence of swept probe UD7 on the adjacent V_f probe UD17, revealing that electron currents are drawn cross-field from the vicinity according to the double probe model. Bottom panel shows spectra of H_α signal from PMT28 and UD17. Peaks at harmonics of f_{sweep} are visible in the V_f spectrum on a monotonic baseline, comparable with the monotonic H_α spectrum. There is no fluctuation frequency minimum. The absence of peaks in the H_α signal suggests that there is little to no long-range influence. Figure from Reference [41].

separate signals before fitting. The implementation as classes enables the indexing of results by the employed `data_slicer` for later comparison and reproducibility. The different approaches are listed in Table 2.3.

Table 2.3.: Different slicers developed to separate V_{LP} time trace for IV-characteristic fitting.

Approach	Name	Problem
Slice the signal into even length segments (discarding the end)	Slicer	Segments not aligned with extrema of V_{LP} .
Add an offset to the segment indices	OffsetSlicer	Must be determined by hand, sweep period not necessarily an integer multiple of the sample period.
Fit a sinusoid in parameters frequency, phase, amplitude and V_{LP} offset, determine segment indices closest to extrema	VmaxFitSlicer	Drifts in frequency prevent fit.
Separate V_{LP} into groups at Voltage threshold, drop small groups, find middle index of large ones, segment signal there	VmaxClusterSlicer	Unequal length segments inconvenient, though unavoidable considering frequency drift.

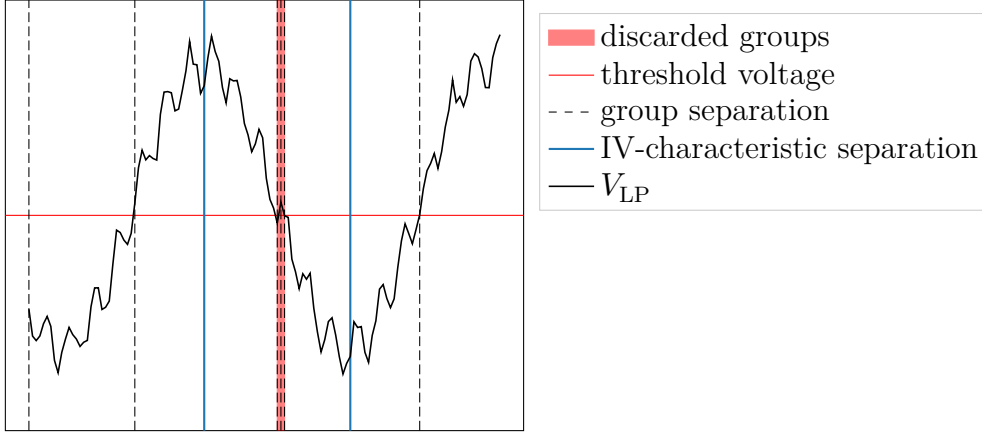


Figure 2.8.: Scheme of the mechanism of IV-characteristic separation with `VmaxClusterSlicer`. V_{LP} fluctuations exaggerated. First and last sweep discarded to avoid edge effects, typically outside of heating phase.

The `VmaxClusterSlicer` approach listed last was used for all investigations reported in this thesis. Only the minimum segment length must be specified, typically chosen was $0.4 \frac{f_{\text{sample}}}{f_{\text{sweep}}} = 400$ samples. A schematic clarifying the operation of this slicer is shown in Figure 2.8.

Despite having ensured that each IV-characteristic is long enough, fits to individual segment can fail and return implausible or very uncertain parameter values. In investigations where the full time scale is not required we drop such values and average over subsequent parameters to obtain a more easily readable signal. Others frequently fit a single IV-characteristic and thus set of parameters to observed data from multiple sweep periods [40]. We compared different methods in our Paper [41] and quote the relevant section here for the reader’s convenience.

”To obtain the evolution of the plasma quantities on time scales significantly below the sweep frequencies, several approaches are possible:

1. Analysis of every half sweep, averaging of the obtained model parameters p over N half sweeps, denoted $\langle p^{(1/2)} \rangle_N$.
2. Simultaneous analysis of N adjacent half sweeps, assuming constant

model parameters for all these sweeps, denoted $p(N/2)$.

3. Averaging over the raw data of N half sweeps — this can be executed by defining voltage intervals of the sweep voltage and averaging over all current values for each voltage interval; the probe model is then applied to the one resulting characteristic. This is denoted $p(\langle N/2 \rangle)$.

We compare the effect of these three averaging methods with $N = 10$ for one fixed probe model (DWSE) in Figure 2.9. The comparison is performed for three time intervals of 0.2 s within W7-X discharge 20180814.007. The three time intervals differ significantly in plasma density and temperature in front of the divertor and in the level of fluctuations. For the first averaging method, we exclude results of half sweeps with the uncertainty of T_e above 50 eV or $T_e > 250$ eV, indicating too strong fluctuations during the half sweep. We use LS fitting for all three methods. We note from this comparison that the resulting plasma parameters on the time scale of 5 times the sweep period do not differ significantly between the three averaging methods. Small systematic differences are visible for some plasma parameters, however not in the same direction under all discharge conditions.”

Throughout this work we use $Z = 1$ and $\gamma_i = 3$ and $T_i = T_e$, which we will justify in the following.

In principle I_{sat} is related to n_e by Z_{av} , the average ion charge. This quantity is in practice unavailable and can not be replaced by Z_{eff} , the effective ion charge, which weighs ion species according to their radiation intensity and thus emphasises heavy, strongly charged ions. Since Z is a linear scaling factor, if a measurement should at a later time become available, n_e values can be easily corrected. The ion species used in W7-X was hydrogen, with the exception of few helium discharges not part of this work. c_s at the sheath in a mixed species plasma seems to be a single velocity (rather than a different one for each species) [74] and consistent with the ion acoustic wave velocity

$$c_s \approx c_{\text{IAW}} = \sqrt{\sum_s \frac{n_{i,s} T_i}{n_e m_{i,s}}}, \quad (2.17)$$

where s indicates the species.

Riemann has shown that an ion adiabatic coefficient of $\gamma_i = 3$ is necessary at the sheath edge for kinetic and fluid treatment to be reconciled [52]. This is confirmed experimentally by Lunt *et al.* [75].

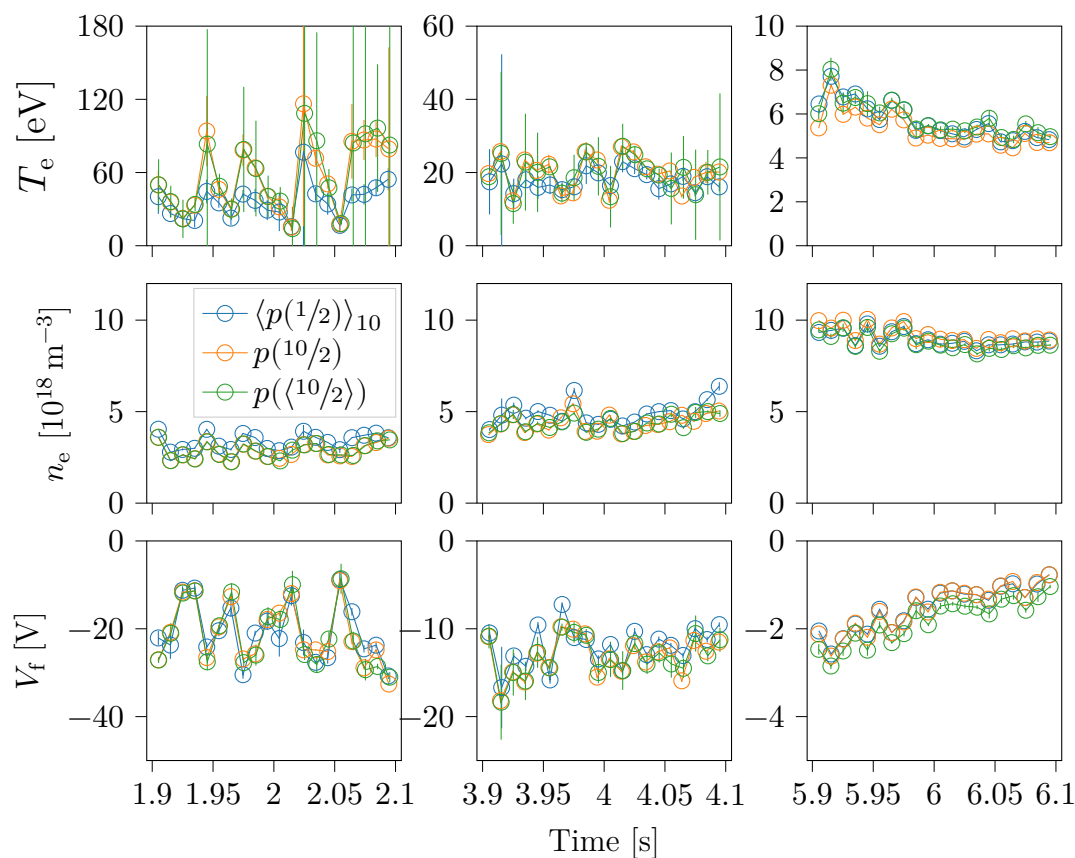


Figure 2.9.: Comparison of averaging methods for three time intervals (in columns) and different LP parameters (in rows). Uncertainties indicated as delivered by LS routine, see Section 2.5. Half-sweep fits $p^{(1/2)}$ with $\sigma_{T_e} > 50$ eV or $T_e > 250$ eV excluded from average. Figure from Reference [41].

In the core of W7-X, due to electron heating and turbulent losses, $T_i < T_e$, whereas in the edge, where we measure, $T_i = T_e$ is commonly assumed [76]. While the effect of a deviation would be marginal for the shape of the characteristic, the density would be influenced through the $\gamma_i T_i$ dependence of c_s .

For both methods we will employ to fit characteristics and obtain para-

Table 2.4.: Constraints, initial values and prior distributions for inference with LS and Bayesian methods.

Name	Initial	Min	Max	Prior
T_e [eV]	5	1	500	$\mathcal{U}(1, 500)$
n_i [10^{18} m^{-3}]	0.1	1×10^{-5}	100	$\mathcal{U}(1 \times 10^{-5}, 100)$
V_f [V]	0	-100	25	$\mathcal{U}(-100, 25)$
β_{DP}	5	1	50	$\mathcal{N}(\mu = 4, \sigma = 4) \in [1, 50]$

eters, LS and Bayesian inference, we require constraints on the parameters. The meaning and necessity of these constraints differ between the two models: For LS, constraints and initial values are necessary to speed up convergence and prevent unphysical results, but as we will see below they violate the assumptions of some methods based on LS fitting. For Bayesian inference, prior distributions of likely parameter values are central to the logic and represent our state of knowledge *prior* to taking the data into account. Here the focus must be to prevent biasing our results by making too strong assumptions on the possible outcomes. Table 2.4 lists the constraints, initial values and distributions used in both cases and for all models. The only change is the use of a truncated normal prior for the area ratio β_{DP} which restricts it more strongly to the range that is both physically plausible and theoretically expected [62]. It also approximates the distribution of β_{DP} obtained in unbiased LS fitting. The constraints on V_f were chosen to restrict it to within the V_{bias} range to assist LS convergence and should be reviewed when independent measurements become available.

2.5. Parameter uncertainty estimation

Uncertainties of parameters in our models can be inferred by considering the vicinity of the minimum of the sum of squared residuals (SSR).

If that region can be approximated by a multi-variate normal, it can be shown that parameter variances are given by the diagonal elements of the covariance matrix D . [77]

$$D = \sigma^2(\nabla^2 f(m, \vec{p}))^{-1} \quad (2.18)$$

The off-diagonal elements give the covariances. ∇^2 signifies the second or-

der derivatives w.r.t. all parameters, or Hessian matrix. The contours of constant SSR are ellipsoids. In the `symfit` package, parameter uncertainties are estimated in this way, because it leverages the symbolic representation of models to analytically compute the derivatives.

This simplified formulation is correct if all measurement points are independent and identically distributed (iid), in which case the maximum likelihood $\mathcal{L} \propto \chi^2$, where χ^2 is a weighted SSR we will introduce later, and the model is linear and unconstrained. Our data and model do not fulfil those requirements, so it is clear that the uncertainties generated by this method could not be strictly correct. In practice, the reported uncertainties were implausibly small, necessitating a more general approach. In hindsight, the effect of model non-linearity might have been overlooked had we not obtained implausible errors by neglecting the fluctuation error when determining σ in Equation (2.18).

To exemplarily show the effect of the deviations from the assumptions, we evaluate SSR on a grid around the optimum. Contours of $\chi_{\min}^2 + 1$ in projections onto the plane of two parameters let us read off the 'one σ '-level uncertainty in those parameters. Here, SSR is not correctly normalised such that it is not equal to χ^2 and the levels are arbitrary, but the distribution is representative. The example in Figure 2.10 shows that these contours are not ellipses, as expected for a non-linear, constrained model.

This evaluation of SSR on a grid is computationally very expensive as it scales exponentially with the number of dimensions. To feasibly tackle this type of problem Monte Carlo (MC) methods are typically used. The LS approach we discussed above is the simplified case of the more general Max- \mathcal{L} method, which does not require Gaussian errors and linear models. Max- \mathcal{L} in turn is a special case of inference using Bayesian analysis, which furthermore allows for parameter restrictions and previous knowledge to be incorporated in the form of *priors*. Bayesian inference is at the core of the *Minerva* project for scientific modelling and inference [78].

Bayes' formula [79],

$$\underbrace{P(F|D)}_{\text{posterior}} = \frac{\overbrace{P(D|F)}^{\text{likelihood}} \overbrace{P(F)}^{\text{prior}}}{\underbrace{P(D)}_{\text{evidence}}}, \quad (2.19)$$

is used to infer the posterior distribution of the parameters \mathbf{F} given the

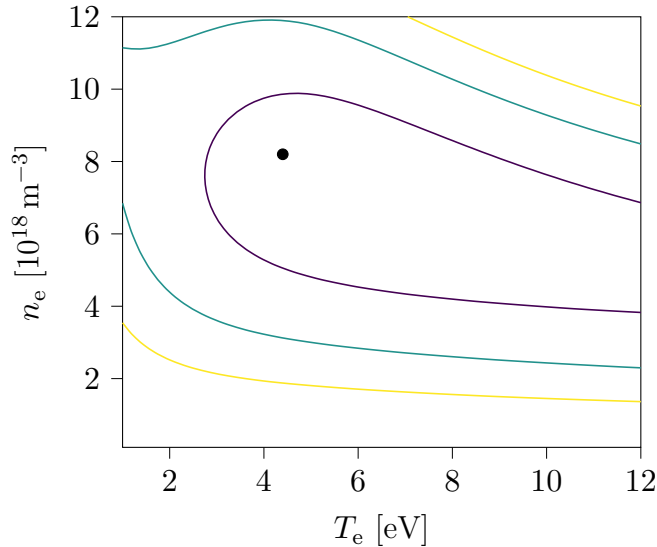


Figure 2.10.: Contours of SSR from grid evaluation in a slice through the optimal V_f and β_{DP} values of double Weinlich-Carlson sheath expansion model (DWSE) evaluated for probe UD10 at $t = 6.15$ s of 20180814.007. Because the model is not linear and unconstrained, the contours are not ellipses.

data **D**.

The central idea of **Minerva** is that in fusion experiments the same quantity is often measured by different diagnostics or required as an input to the inference. Examples include the core density being both measured by interferometry and Thomson scattering, or the magnetic field required in the mapping of electron cyclotron emission (ECE) spectroscopy and Stark effect measurements. To visualise, connect and implement all these mutual dependencies, Bayesian graphical models or networks are constructed. The LP diagnostic network built by us is shown in Figure 2.11. This model can be integrated with other W7-X diagnostics and elements, in particular the prediction node, can be extracted and shared with other facilities such as Joint European Torus (JET) or Mega-Ampere Spherical Tokamak (MAST) where **MINERVA** is also used [80, 81], standardising analysis and enabling objective comparison of results.

For all distributions in Equation (2.19) to be probability density functions

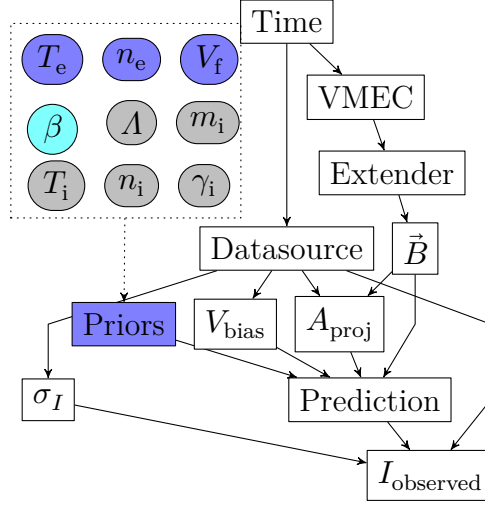


Figure 2.11.: The directed acyclic graph shows the simplified MINERVA forward model for the LP. Rectangular nodes indicate deterministic nodes, nodes with a rounded rectangular shape are probabilistic nodes. The prediction node allows to choose which equations are used to calculate the predicted current, cf. Table 2.2. A blue background indicates that the free parameter is always active, cyan that the free parameter is active for some of the available calculations in the prediction node, and grey indicates that, for now, these probabilistic nodes are not independently varied.

(PDFs) they must integrate to unity, and the normalisation by the evidence is necessary. The same is true if models are to be compared. To find optimal parameters values and uncertainties however, only the shape of the posterior distribution is needed and the scaling is irrelevant. The posterior distribution is therefore approximated by a histogram of MC samples generated by the Metropolis-Hastings algorithm (MHA). Each sample is a vector of parameters \vec{p} from which we can re-calculate I_{mod} , shown in Figure 2.12.

The full posterior distribution is difficult to visualise because it has dimensions equal to the rank of \vec{p} . We inspect projections in two dimensions, in which other dimensions are marginalised out by integration. An example of such a projection of the posterior is Figure 2.13. This approximation of the posterior could be generated in $\mathcal{O}(10^4)$ iteration steps, on a total timescale of one second. To ensure that the vicinity of the MAP is sampled,

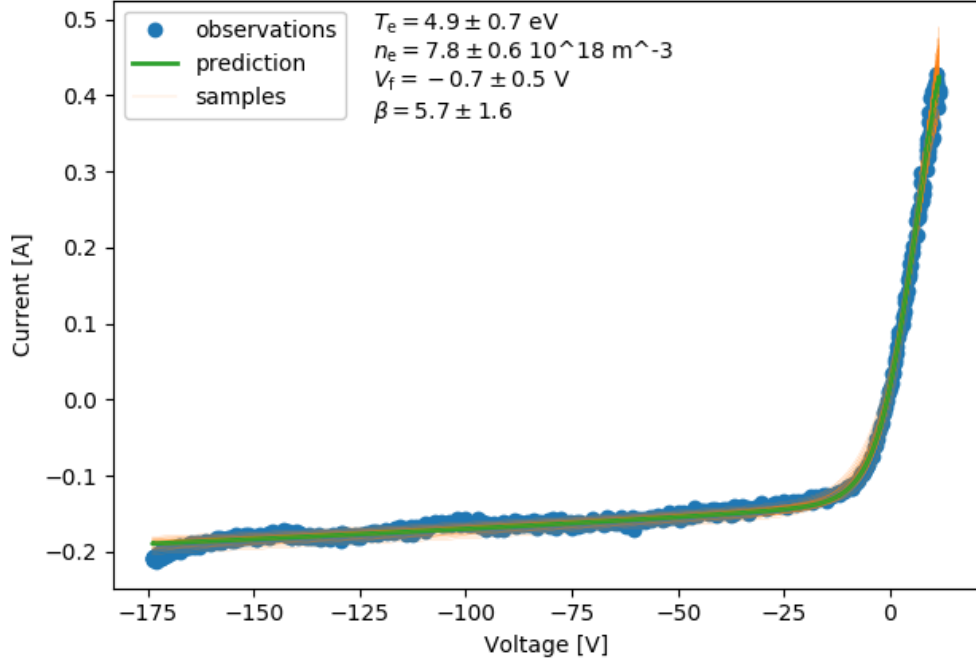


Figure 2.12.: Exemplary IV-characteristic from *Minerva* implementation of LP analysis. Observed data in blue, maximum a posteriori (MAP) values and predicted I_{mod} green, I_{mod} for parameters sampled from the posterior distribution orange. Calculated using DWSE model and same data as Figure 2.16. UD10 in experiment 20180814.007, $t = 6.115$ s

we first find this point by the Hooke and Jeeves algorithm and, furthermore, let the Markov chain Monte Carlo (MCMC) procedure at the core of the MHA 'burn-in' for non-recorded $\mathcal{O}(10^3)$ iteration steps to leave potential low-density regions.

The two-dimensional posterior projections can be further marginalised to one dimension, as for T_e in Figure 2.14.

The posterior is the final result of the inference, but contains more information than is required in practice. Often, we are content with a value and a symmetric confidence interval estimate. To obtain this, we calculate the centre of mass and standard deviation of the 1-D posterior, effectively approximating it by a Gaussian. This is permissible because the distributions generally are close to unimodal, as in the example above.

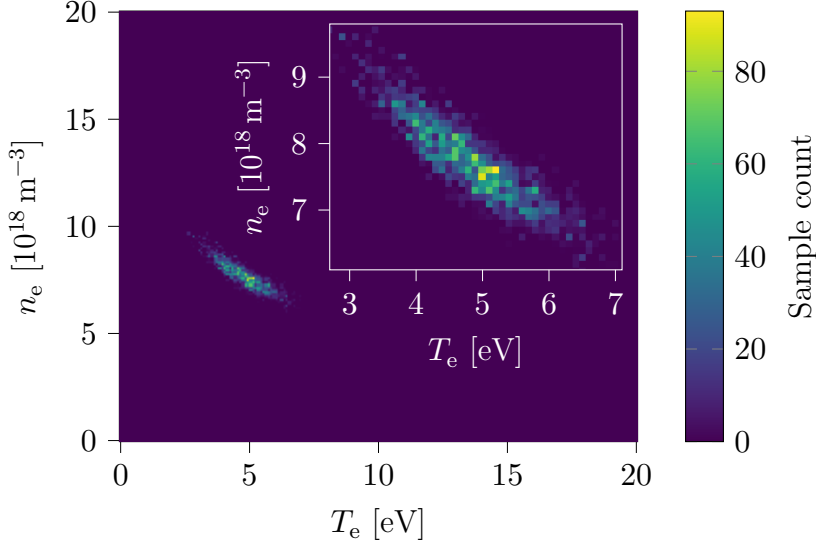


Figure 2.13.: Histogram of samples drawn from the posterior in T_e and n_e . The MHA sampling scheme ensures that the counts are proportional to the posterior probability such that the histogram is a discretised approximation. UD10 in experiment 20180814.007, $t = 6.115$ s.

The last step however seems to negate some of the benefit of using Bayesian inference over LS minimisation. It is a practical consideration due to different requirements on the form of the solution. The value and uncertainty generated by reducing the data are plausible, easily understood, and can be stored compactly. For the integration of LPs with other diagnostics, it is faster to rerun the inference procedure and access the full posterior sample distribution than to store and retrieve a representative number of samples or higher order statistical moments. Even though posterior samples and projections are not saved for each probe and sweep, doing so at regular intervals gives insight and understanding useful for interpretation of the normal parameter estimates. An example of this is the computation of the Pearson sample correlation coefficient r_{xy} in Section 3.3.

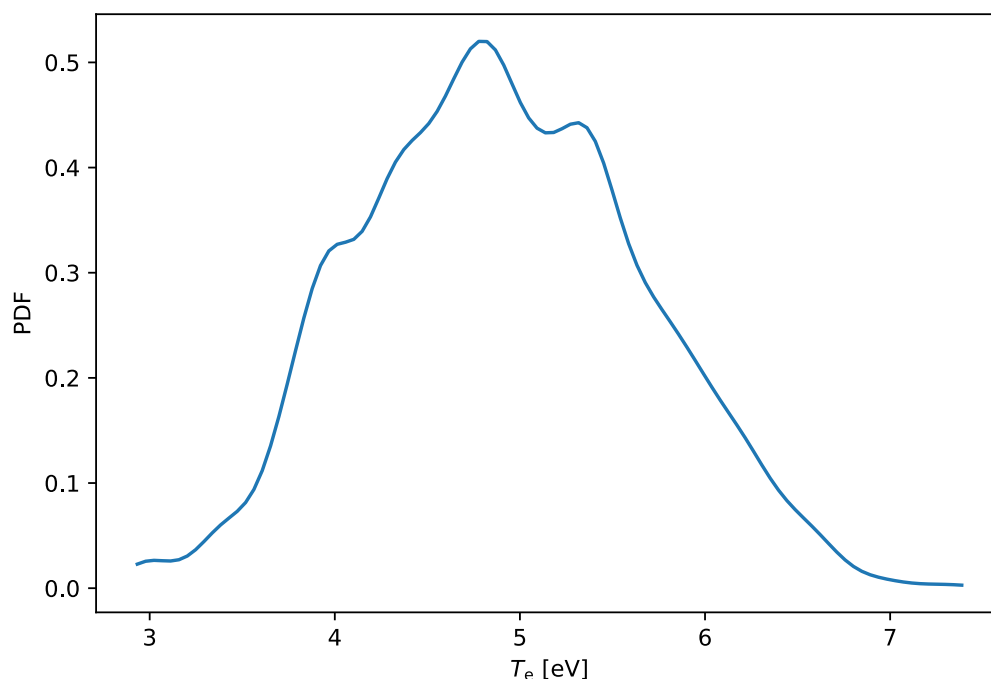


Figure 2.14.: 1-D posterior projection of T_e . Histogram smoothed by kernel density estimate (KDE) [82, 83] with Scott’s window. UD10 in experiment 20180814.007, $t = 6.115$ s.

2.6. Comparison of models

In the literature we surveyed, in particular References [40, 60, 84], models are proposed and exemplarily shown to work better than the SL model, but not directly compared to each other in specific cases with different conditions. Our plan was, thus, to select models based on the first and second criteria in Section 2.3, test and rank them according to the third criterion, and select the best performing one. We were not interested in accurately parametrising the IV-characteristic, which might have been achieved with a phenomenological model (possibly performing better on the ‘accurate’ criterion) to store and reproduce $I - V$ data in a compact form. We seek only to use an accurate fit as empirical evidence that the model captures the essential physics. A fundamental model accurately fitting the observed data gives us confidence that the inferred parameters are correct, especially

if it is capable of doing so in a wide range of conditions. A simple model we intuitively understand, which exhibits this robustness, allows to run the parameter inference unsupervised and confidently use its results.

2.6.1. χ^2 method

To optimise the parameters of a fit and to compare the fit quality of the different models, we will use the χ^2 (pronounced 'chi-square') method.

The statistical quantity χ^2 is defined as

$$\chi^2 = \sum_{i=1}^N \frac{(m_i - \mu_i)^2}{\sigma_i^2} \quad (2.20)$$

where m_i are N independent measurements, σ_i^2 their Gaussian variances and μ_i the predictions of a model. The squared residuals $m_i - \mu_i$ in the numerator of Equation (2.20) are the *observed* deviations from the model, whereas the variances are the *expected* deviation. If each m_i is indeed drawn from a normal distribution with mean and variance μ_i and σ^2 , each term in the sum should on average contribute 1, such that $\chi^2 = N$. If χ^2 is larger than N , either the observed deviations are larger, indicating that the predictions μ_i were incorrect, or the true variances were larger than expected. Conversely, if χ^2 is smaller than N , the predictions must have fitted the observations more closely than was to be expected given the variances, which consequently might have been overestimated. If we want to discriminate between prediction qualities of different models, we will need a consistent and independent method of finding the variances.

Another way of using χ^2 is to find the optimal predictions μ_i . This is especially relevant if they are generated by a model f , taking parameters \vec{p} and independent variable x such that $f(\vec{p}, x_i) = \mu_i$. Optimal \vec{p} for the specific model can now be found by minimising χ^2 . The variances take on the function of weights, emphasising or de-emphasising deviations at specific positions (or indices) x_i . With equal weights, χ^2 reduces to the least-squares method.

Applying this to our case, the role of different quantities are as follows:

- I_{LP} are the measurements m_i .
- V_{LP} are the positions x_i .

- Langmuir models (SL, PSE, etc.) are the prediction models f .
- Inferred quantities $T_e, n_e, V_f, \beta_{\text{DP}}$ are the model parameters \vec{p} .
- Model currents I_{mod} are the predictions μ .

Calculating the residuals is straight forward. To find optimal values of the inferred quantities this is sufficient, but to obtain comparable χ^2 values we have to think more carefully about the expected deviations. These stem from four sources,

model error due to the model not being able to fit the data for any reasonable parameters (the quantity we want to compare between models),

fluctuation error due to plasma fluctuations,

measurement error due to the instrumentation and external influences,

parameter error due to sub-optimal choice of parameters.

Measurement error can be estimated by calibration and propagated from known uncertainties such as guaranteed precisions of resistors. Parameter error should be reduced to zero after a successful run of the LS optimisation for each model. Note that this is not the uncertainty of each parameter, or the difference between the inferred and 'true' value^{II}, but the additional term added to the square sum of the residuals if \vec{p} is changed from the minimum. Fluctuation error is our term for those deviations from the IV-characteristic prescribed by a model which are due to real plasma effects, larger than the measurement error (and thus not attributable to it) and which can not be described by any model assuming static conditions for the duration of a sweep.

To compare model errors, we require a normalisation that considers only the three other types.

^{II}in as much as there can be a true value of a parameter for a physical model of the plasma

2.6.2. Normalisation of residuals

Because the model error is in most cases smaller than fluctuation and measurement error, we will need to combine many χ^2 to see an appreciable difference. It is therefore important to have a generic way of determining expected deviations as we will have to apply it to many characteristics. This method must be independent of the Langmuir models to not bias the comparison towards one of them.

The measurement error in I_{LP} due to uncertain shunt resistor voltage scales linearly with the magnitude of I_{LP} and is small, since precision components were used. More substantial is the common mode noise remaining after the correction and other effects we attribute to the cables and electronics. These can be estimated through error propagation and calibration and are modelled sufficiently well by a constant error contribution of less than 5 mA.

This is small compared to the observed fast time scale deviations from any model characteristic. These fluctuation error grows stronger or weaker throughout the discharge, varying with heating power, ndl and P_{rad} . We can see the changing magnitude of fluctuations also in the signals of the fixed-voltage I_{sat} and floating V_f probes. Stronger fluctuations do not necessarily correlate with stronger currents, for instance in high T_e and low n_e conditions, such that a relative error is not a satisfactory model. As mentioned above, there is no minimum in the signal frequency spectrum where the threshold of a simple cut-off filter could be set. More advanced filter designs may be possible, but would have to retain all features relevant to the Langmuir models, progressively dampening higher modes.

We choose a kernel approach for a physics independent, phenomenological model of the expected error σ_I . A schematic illustrating the steps of the method is shown in Figure 2.15. Approximating any IV-characteristic by linear segments, we subtract from I_{LP} data in small time segments (each associated with a voltage interval) a line of best fit and calculate the standard deviation of the remainder. To capture the long-scale time variation, this is done simultaneously for several adjacent half-profiles. By reshaping the time series of I_{LP} into a $n * m$ matrix, where n is the number of sweeps and m the number of samples per sweep, we can employ fast kernel algorithms from image processing. The kernel was moved across the matrix, performing the operation at each point and thus obtaining σ_I for the entire time trace.

Whereas in attempts to model the error by a constant and factor proportional to I_{LP} the parameters had to be estimated anew for each experiment, probe and time segment, a kernel size of 5 sweeps by 31 samples provided good results for all inspected data without manual adjustment.

With this expected deviation estimate, we can calculate χ^2 for each IV-characteristic. Because of our non-standard method, we do not expect χ^2 to be exactly N even for the ideal model. While models are comparable amongst each other in this way, the values should not be directly compared with those in other publications using different error methods. Consequently, $\chi^2 < N$ does not necessarily imply over-fitting.

2.6.3. Normalisation of χ^2

Now appropriately normalised, each residual sample of an ideal model should add one to χ^2 . To compare fit quality between multiple models, we need to account for the different number of degrees of freedom. χ_ν^2 is the normalised quantity defined by

$$\chi_\nu^2 = \frac{\chi^2}{\nu} = \frac{\chi^2}{N - k} \quad (2.21)$$

where N is the number of samples, k the number of constraints and ν the effective degree of freedom.

For linear models k is equal to the number of parameters n_p , but as Andrae *et al.* [77, 85] points out, this is not true for non-linear models, for which k cannot generally be determined and only constrained to $k \in [0, n_p]$. Every potential problem of χ_ν^2 comparison, for instance because of the difficulty or impossibility of determining k , brought up in these references applies to our case, but we argue for each one that it is mitigated. Parameter constraints (or more generally priors) make models non-linear, but we use the same constraints on the parameters in all models, so this should affect all similarly. Parameters influence each other, such as n_e reduces the effects of other parameters dynamically, but for all models in the same way. The number of constraints $k \in [0, n_p]$ for non-linear models, but as all LP models are approximately exponential k is likely similar. Even if it were different, given that $N \approx 500$, variations of $k \in [4, 0]$ only have an effect of $< 1\%$.

We use $\nu = N - 3$ for all single probe models and $\nu = N - 4$ for double probe models to calculate χ_ν^2 for each sweep. Separating the calculation by

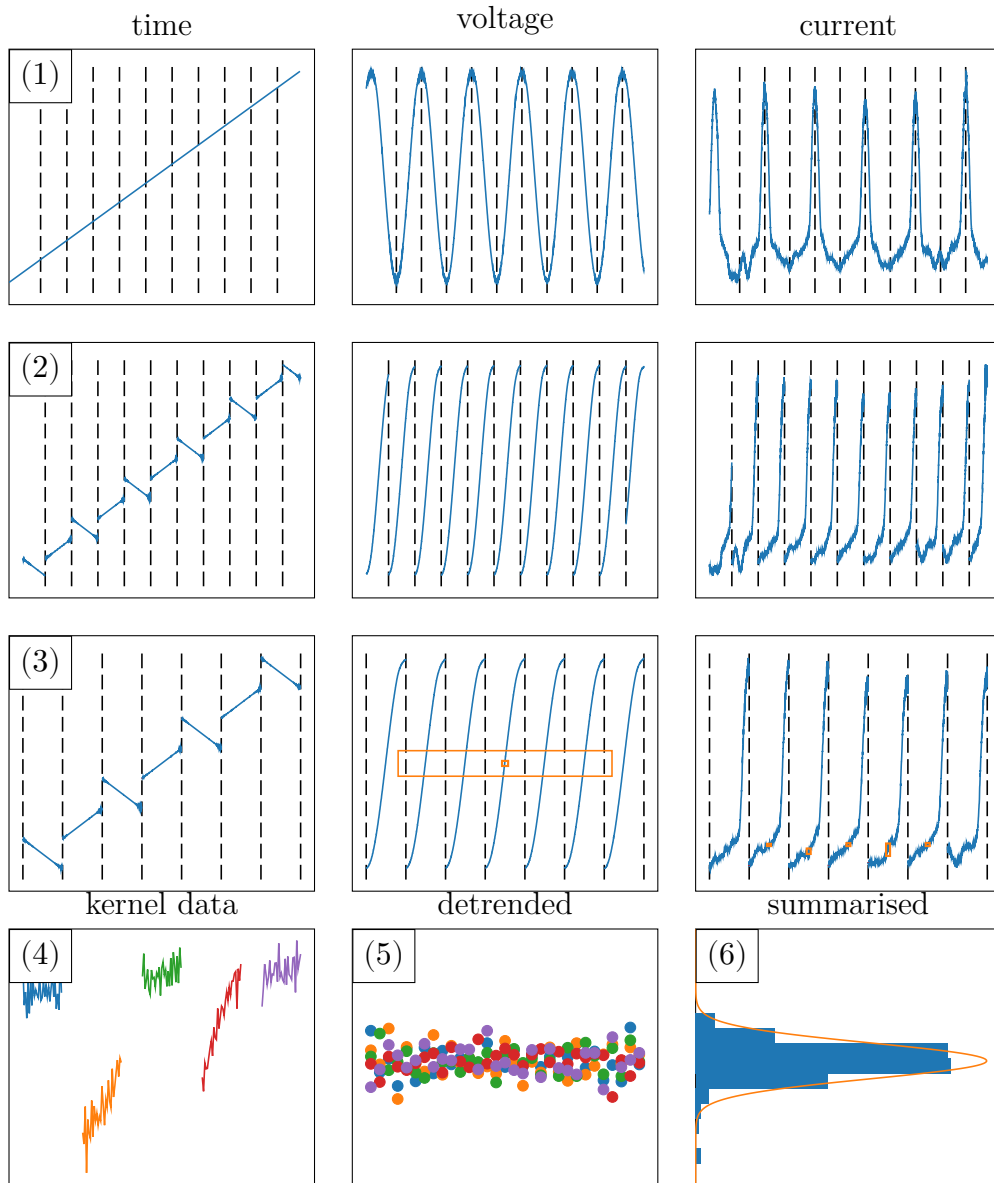


Figure 2.15.: Schematic illustrating the algorithm to determine expected error σ_I . (1) Time, V_{LP} , and I_{LP} data shown in columns is segmented using the `VmaxClusterSlicer` (Section 2.4, Figure 2.8). First and last segment are discarded. (2) Each segment is sorted according to V_{LP} . All are truncated to the shortest length among them. Data can now be represented as array. (3) A $n * m$ kernel ($\#sweeps * \#samples$) shown in orange sweeps over the array, selecting data. (4) Selected data for one time point t_i at centre of kernel. (5) Data is linearly detrended. (6) ⁶⁷ Standard deviation gives σ_I for t_i . Finally σ_I is extended to restore each segment to its original length and brought into chronological order.

Table 2.5.: Parameter values of fits in Figure 2.16 during strong edge radiation regime. Standard error given in brackets.

	T_e [eV]	n_e [$10^{18}m^{-3}$]	V_f [V]	β	χ^2_ν
SL	13.1(0.2)	6.3(0.04)	-1.5(0.2)	-	10.7
PSE	12.0(0.1)	5.9(0.03)	-1.3(0.1)	-	6.3
WSE	10.5(0.1)	5.4(0.03)	-1.2(0.1)	-	5.1
DSL	9.0(0.4)	7.5(0.1)	-1.0(0.1)	5.8(0.6)	13.3
DPSE	7.2(0.2)	7.5(0.09)	-0.6(0.1)	4.9(0.2)	6.2
DWSE	5.9(0.1)	7.1(0.05)	-0.4(0.07)	4.9(0.1)	1.7

sweep was done out of convenience, combining the data of n_s sweeps with m_i samples each would have simply increased χ^2 and ν to $\nu = \sum_i^{n_s} m_i - n_s * k$.

χ^2 is the expectation value of the χ^2 -distribution. For large N this tends towards a normal, so we must take into account a standard deviation of $\sqrt{2/\nu}$ when comparing two χ^2_ν values.

2.6.4. Results

A first example of LS fits is shown in Figure 2.16. All panels show the same data in black, model characteristics are drawn as coloured lines. The top row (Panels **a** & **b**) contains the full bias range, the middle row (**c** & **d**) a zoom on the ion current branch and the bottom row (**e** & **f**) a zoom on the electron current branch. Characteristic functions for all models are overlaid, with single probe models in the left column (**a,c** & **e**) and virtual double probe models in the right column (**b,d** & **f**). The necessity to account for sheath expansion to explain the non-saturation of the ion current can be clearly seen in Panels **c** & **d**, as well as the WSE model's good match with the data. The bottom row supports the virtual double probe hypothesis, showing excellent agreement of data and characteristics. We conclude that in this specific example, the DWSE model can best fit the I-V characteristic. This is supported quantitatively by the value of χ^2_ν obtained for each model given in Table 2.5.

The parameter values of the different models given in the caption vary significantly, especially the temperature. Trends in this variation clearly originate in the shape of the characteristics: Panel **c** shows how the transition point from electron current modelled by an exponential to the almost

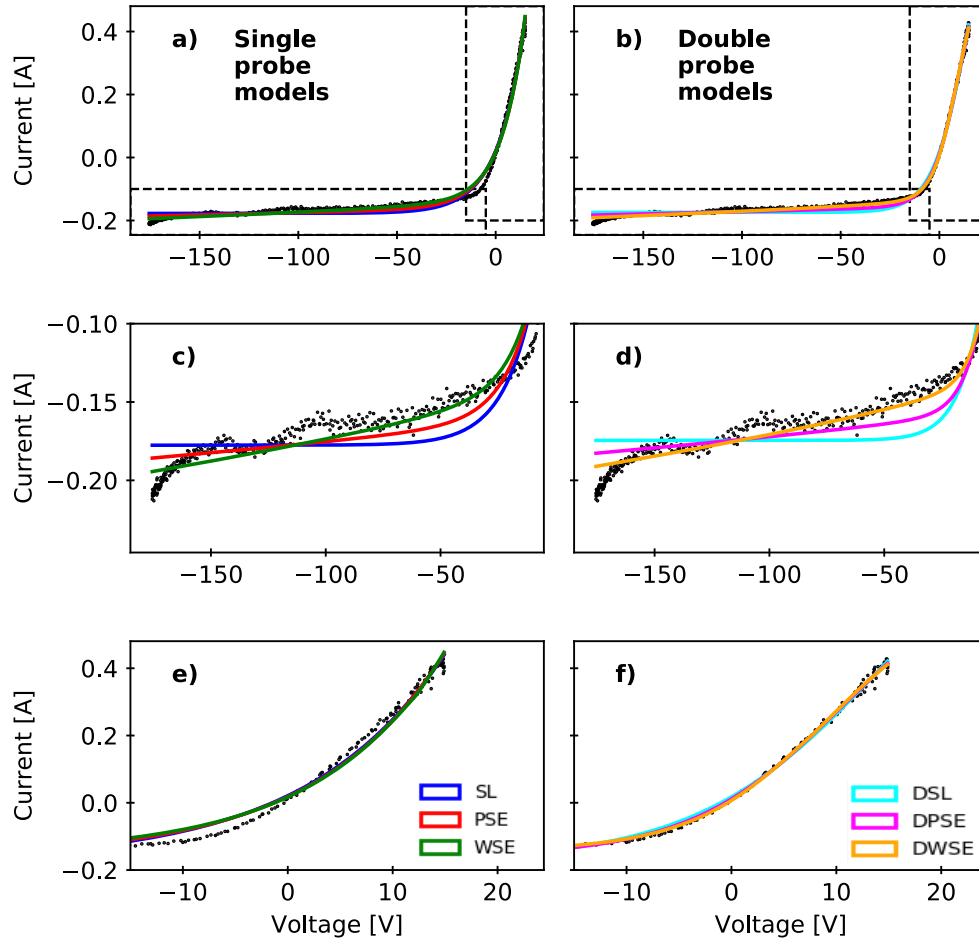


Figure 2.16.: Example I-V plots showing all six models from Table 2.2, overlaid over the same raw data in all panels. Left column (Panels **a,c** & **e**) single probe models, right column (Panels **b,d** & **f**) double probe models. Overview of entire data range in top row (Panels **a** & **b**), zoom on ion-current dominated region in middle row (Panels **c** & **d**), electron-current dominated region in bottom row (Panels **e** & **f**). Parameter values of fits in Table 2.5. Data from probe UD10, experiment 20180814.007, $t=6.115$ s. Strong edge radiation regime. Figure from Reference [41].

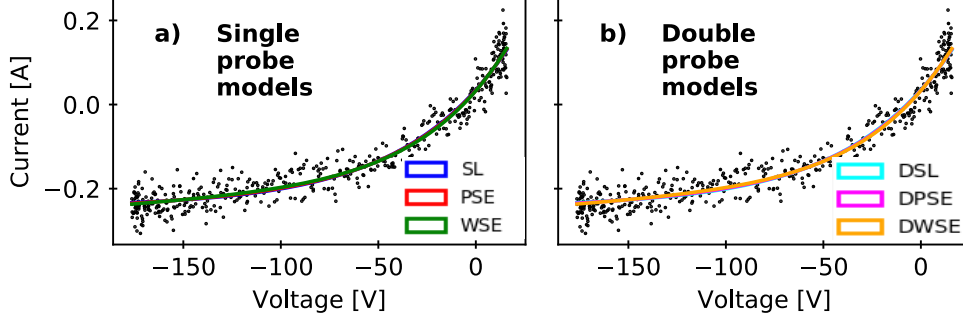


Figure 2.17.: Example I-V plots showing all six models from Table 2.2, overlaid over the same raw data in all panels. Single probe models in Panel **a**, double probe models in Panel **b**. Parameter values of fits in Table 2.6. Data from probe UD10, experiment 20180814.007, $t = 1.847$ s. Attached divertor operation. Figure from Reference [41].

Table 2.6.: Parameter values of fits in Figure 2.17 during attached divertor operation. Standard error given in brackets.

	T_e [eV]	n_e [$10^{18} m^{-3}$]	V_f [V]	β	I_{sat}
SL	54(2)	4.3(0.1)	-7.1(0.5)	-	0.149(0.003)
PSE	47(2)	4.1(0.1)	-6.8(0.5)	-	0.132(0.003)
WSE	38(1)	3.7(0.1)	-6.5(0.5)	-	0.107(0.003)
DSL	53(2)	4.3(0.1)	-7.2(0.5)	50(43)	0.147(0.003)
DPSE	46(2)	4.1(0.1)	-6.9(0.5)	50(45)	0.131(0.003)
DWSE	37(1)	3.7(0.1)	-6.6(0.5)	50(48)	0.106(0.003)

linear trend for the non-saturating ion current shifts further to positive V_{bias} going from SL to PSE to WSE. This increases the inferred growth rate of the exponential and therefore reduces the temperature. Simultaneously it reduces the ion-saturation current at zero sheath expansion, reducing the inferred density.

The saturation of the electron current requires the single probe models to assume a more shallow gradient near V_f , again reducing growth rate and thus increasing temperature.

For higher temperatures and lower densities we see the differences between

models much less clearly, as shown in a second example in Figure 2.17. The horizontal extent of the characteristic increases with temperature, which at fixed V_{bias} range means we do not reach saturated ion or electron currents. All models can fit the data equally well; χ_{ν}^2 lies in the range of 0.241 to 0.248. The inferred parameters however still vary strongly because the models interpret the data differently: again the PSE and WSE models shift the transition from ion current to electron current dominated branches and can match the data by assuming lower temperatures. This is illustrated by I_{sat} calculated for zero sheath expansion or $A_{\text{coll}} = A_{\text{proj}}$ shown in Table 2.6 for each model, which marks this transition. β cannot be determined from the data, the fitter therefore assumes the maximum value and correctly reports a large uncertainty. Note that this is matched by the small variation in the parameter values inferred by the single and double probe values.

Armed with a consistent method, we can calculate χ_{ν}^2 for many IV-characteristics and models, which we have done for UD10 of discharge 20180814.007. An overview of that discharge is shown in Figure 2.18. Line-integrated density $nd\ell$ was ramped up starting at 3 s, resulting in decreasing core temperatures, increasing radiation fraction f_{rad} and ultimately collapse of the discharge. We divide the data in two parts at 5.5 s, approximately coinciding with $f_{\text{rad}} = 0.5$. In Figure 2.19, histograms of the χ_{ν}^2 values for each model are shown. All data are from probe UD10 and evaluated for IV-characteristic half-profiles, i. e. at a time resolution of 1 kHz. The bin widths are 0.4 for $\chi_{\nu}^2 \in [0, 4]$ and 1 above, such that the uncertainty of χ_{ν}^2 is always much smaller than the bin width. A logarithmic scale for the χ_{ν}^2 values of the later half of the discharge was necessary because these characteristics are quite calm, such that σ is small and residuals are scaled up considerably. Even for the best performing model there are instances of $\chi_{\nu}^2 > 10$, but an overwhelming majority clusters around unity. As explained above, our unconventional expected error scaling means that $\chi_{\nu}^2 < 1$ does not necessarily imply overfitting, but more likely and overestimation of the error. This is in line with our results for single IV-characteristics and shows that, with some care to outliers and from among the tested models, the DWSE model can be applied most generally and its results trusted.

In the next chapters, we will compare these trusted results to other diagnostics, as outlined in Figure 1.7.

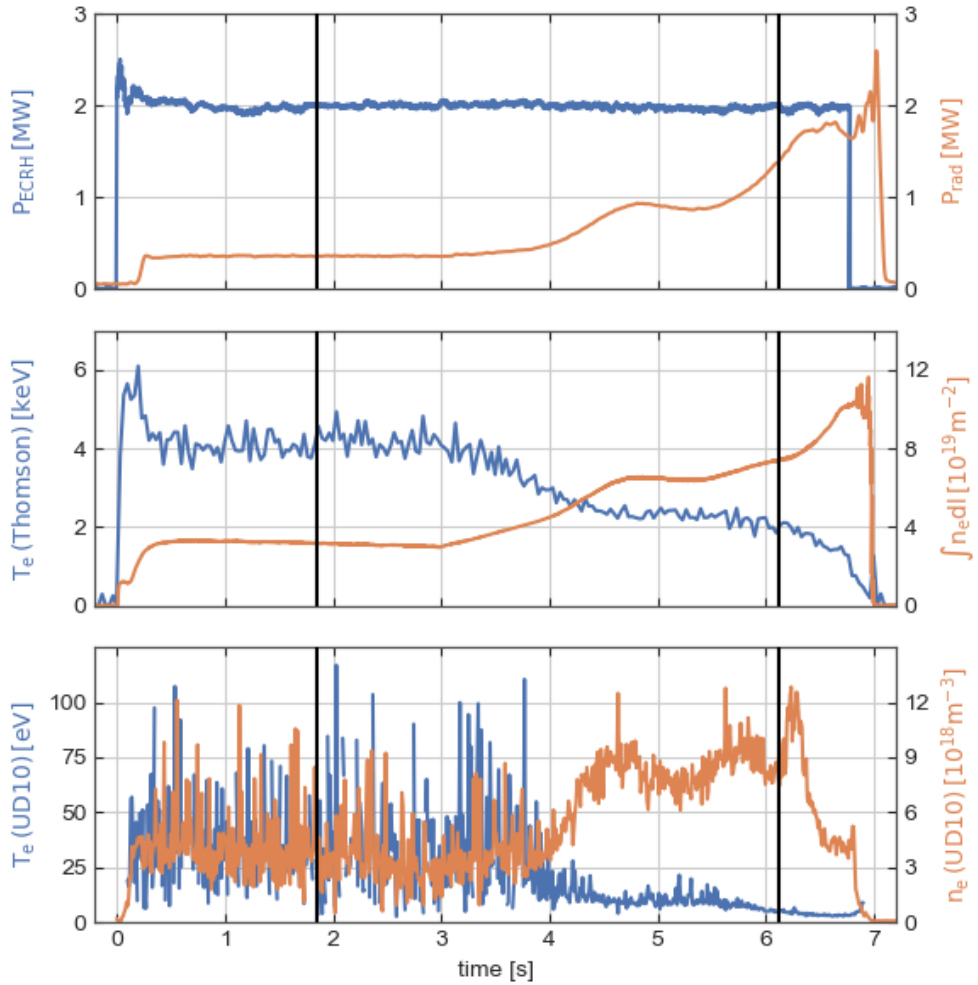


Figure 2.18.: Overview of discharge 20180814.007. Top panel shows time traces of the input ECRH power[86] in blue and radiative losses P_{rad} measured by the bolometers[87] in orange. Middle panel shows time traces of core electron temperature measured by Thomson scattering volume 2[88, 89] in blue and line integrated density from the dispersion interferometry system[90] in orange. Bottom panel shows time traces of temperature and density measured by Langmuir probe UD10 in blue and orange respectively. The Langmuir data are averaged with $N = 25$ and fits with temperature uncertainties $\sigma_{T_e} > 50 \text{ eV}$ or $T_e > 250 \text{ eV}$ are excluded. Black vertical lines indicate the times used for Figure 2.17 (1.847 s) and Figure 2.16 (6.115 s).

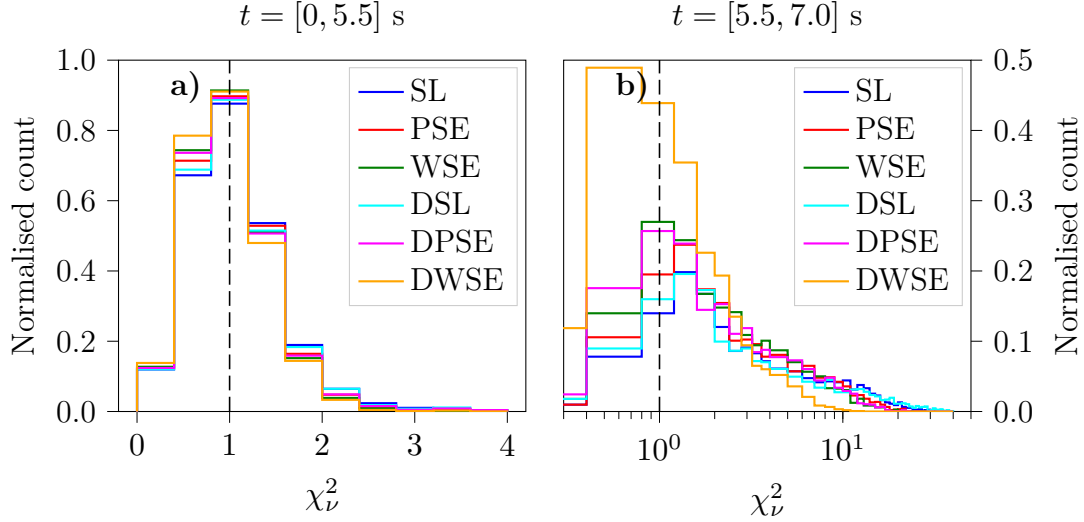


Figure 2.19.: Histogram of χ^2_ν values for IV-characteristics in the indicated time windows, colour coded by Langmuir model. The distributions in the left panel (a), during the low-radiation phase, are very similar for all models. The distributions in the right panel (b), during the high-radiation phase, show a clear advantage of DWSE over the other models.

2.6.5. Avenues for extension of work

Other ways to compare the models include Kolmogorov–Smirnov (KS) testing of residuals and Bayesian model comparison. The KS test determines whether samples are drawn from the same distribution as a reference distribution. This can be used to see if the normalised residuals are Gaussian-distributed with mean zero and standard deviation one [77]. It avoids the difficulty in determining the correct degree of freedom for χ^2 .

Having implemented the models in the MINERVA framework also opens the possibility of marginalising both data and parameters and calculating the probability of each model given the data. A Bayes factor determined this way could give some idea of the relative qualities of different models [79]. More involved would be determining the evidence for each model to normalise the resultant distributions and ensure they are actually probabilities. This would permit using an optimal mixture model, with each prediction weighted by the

probability of the model. Determining the evidence is normally problematic (hence the importance of the MHA in parameter determination which does not require it), but might be feasible in the comparatively low-dimensionality parameter space of the Langmuir models.

While it is of course permissible to test a representative dataset, the empirical strength of our findings would be improved by adding data from other probes and discharges. This would allow to more clearly delineate the conditions under which one model is superior to another than the $f_{\text{rad}} > 0.5$ condition we used. With the wealth of data that is available from OP 1.2, even in attached plasma conditions significant differences in model quality might become visible.

A better tool to experimentally investigate IV-characteristic in the presence of fluctuations might be a multi-pin probe like in Reference [91] in a homogenous plasma. By biasing each tip to a single voltage, no sweep is necessary and the temporal resolution can be greatly increased. Since the distance between tips can not be made too small, this would only be valid if the background and fluctuation spatial scale was greater than the tip distances.

The model could be further refined by constraining the time variation of the parameters. Currently each sweep is analysed independently, making large fluctuations of the parameters possible. A model incorporation a maximum rate of frequency of change would constrain this, but might be negatively impacted by individual outliers, excursions or problems of the inference. Ideally, in a plasma in which $f_{\text{sweep}} \gg \tau_Q$, where Q is any inferred quantity and τ_Q the characteristic scale of variation, $Q(t)$ could be fitted by continuous, smooth, piecewise splines described by a set of spline parameters $S(t)$. We could then in one step solve for all the spline parameters simultaneously, increasing the number of variables, but effectively enforcing stricter priors. The same approach is conceivable in the spatial dimension, though it may be difficult to know the scale of change δ_P and achieve the required probe spacing $d_{\text{probe}} \ll \delta_P$.

3

Heat flux comparison

3.1. Introduction

The sheath transmission coefficient γ_s relates the Langmuir probes (LPs) measurements of electrical current onto, and temperature at, a plasma facing component (PFC), to the heat flux there. It is of interest for simulations aiming to predict heat fluxes from plasma parameters at the edge [92]. Here we use γ_s primarily to cross-validate LPs results with the Infrared-Camera (IRC) system by determining it empirically. We will therefore not compare in detail the various theories striving to derive values of γ_s but focus on the predicted dependencies. Similar measurements of γ_s have been conducted on a number of machines: ASDEX Upgrade (AUG), Joint European Torus (JET), Doublet III-D (DIII-D), Japan Torus-60 (JT-60), Tungsten Environment in Steady-state Tokamak (formerly Tore Supra) (WEST), Texas Tokamak (TEXT) and Tokamak à configuration variable (TCV) cited in references [92, 93] and reproduced in Table 3.1. As possible reasons for the large spread of values the authors cite different PFC materials and compositions. Previous studies at Wendelstein 7-X (W7-X) which have compared LPs and IRCs, such as those by Hammond *et al.* [43] and Niemann *et al.* [94], used $\gamma_s \approx 4$ to match their measurements. Note that there is wide scatter in the values, and, consequently, also the groups of Marki *et al.* and Marsen *et al.* focus on dependencies and error analysis.

Even a pure repetition of this analysis is of importance for W7-X because the specific surface material and composition might make γ_s deviate from the value predicted from theory. Anticipating the largest source of uncertainty

Table 3.1.: Experimental values of γ_s on other experiments [93]. The range refers to values reported at different parameters and conditions.

Experiment	Range of γ_s
AUG	[3, 8]
JET	[2, 8]
DIII-D	[2, 4]
JT-60	[2, 20]
TEXT	≈ 5
WEST	[2, 11]
TCV	[4, 8]

to be systematic errors of the LPs, we pay particular attention to the correct handling of uncertainties throughout all analysis steps.

3.2. Theory

To obtain an expected value of γ_s we follow the derivation in reference [56].

Each particle contacting the wall will transfer a part of its energy to it. The energy flux, or, equivalently, heat convection q out of a plasma onto the surface, is given by

$$q = \gamma_s T_e \Gamma \quad (3.1)$$

where Γ is the particle flux at the surface and T_e the energy corresponding to the Boltzmann constant k_B times the electron temperature. Everywhere in the text mean particle energies for species s will be denoted T_s and have units of eV. The sheath transmission coefficient γ_s by definition accounts for all details of the energy transfer process. Using the sheath model introduced below to gain an intuitive understanding first, we will then consider additional sophistications and effects.

The sheath in front of a material surface is the region within which quasi-neutrality is violated. It must therefore have dimensions on the order of the Debye length λ_D . This is sufficiently small to justify the assumption that no collisions occur within it. Extending this to neutrals implies that there are also no particle sources in the sheath. Total energy and particle fluxes at the sheath edge (SE), are therefore equal to those at the surface. But

whereas the ion flux is at both locations directed only at the surface, where all ions get absorbed, the electron flux at the SE has a large component directed towards the surface and an only marginally smaller one away from it, missing the high energy electrons able to overcome the sheath potential. That potential adjusts itself precisely such that no net current flows.

Throughout the sheath up until the wall, the electron velocity distribution can be close to equilibrium and thus Maxwellian, but the electron density is reduced by the Boltzmann factor.

$$f_e(\vec{v}) = f_{\text{MAX}}(T_e, m_e, \vec{v}) \quad (3.2)$$

$$n_e(x) = n_{\text{SE}} \exp\left(\frac{eV(x) - eV_{\text{SE}}}{T_e}\right) \quad (3.3)$$

In using the particle flux at the surface Γ , we already account for the reduction in density and will obtain the correct heat flux q with an energy per electron unchanged from the SE to the surface.

The heat flux due to random motion of Maxwellian-distributed particles of species s in one direction d (for example towards the surface) is

$$q_d = 2T_s \Gamma_d. \quad (3.4)$$

Both directions perpendicular to d contribute $\frac{1}{2}T_s$ due to their kinetic energy alone. Along d however the increment is

$$\partial q_d = \frac{1}{2} m \vec{v}^2 \partial \Gamma_d \quad (3.5)$$

where

$$\partial \Gamma_d = v_d f_{\text{MAX}}(\vec{v}) d\vec{v}. \quad (3.6)$$

The term of order v_d^3 integrates to $1T_s$, resulting in the sum of $2T_s$ in Equation (3.4) above.

γ_s^e , the heat transmission coefficient due to electrons, would thus simply be 2 (cf. Equation (3.1) and Equation (3.4)), but must be corrected for two effects: Reflection of a fraction f_e^{R} of electrons and secondary electron emission (SEE) due to electron impact. Notably, the first considers 'elastic' collisions in which no energy is deposited, while the second accounts for

emission of cold electrons which must overcome the materials work function E_W .

Reflection simply reduces the total and therefore also net electron current. The correction for material work function is mostly omitted in the literature. For Carbon with $E_W = 4.6 \text{ eV}$ and $\delta_e \lesssim 0.5$ it becomes significant only for $T_e < 10 \text{ eV}$. The emitted electrons are assumed to be cold such that no additional term must be added to E_W in Equation (3.10b). SEE by ion impact is insignificant for ion energies below 1 keV [56].

Considering the ions next, their particle flux in absence of sources in the sheath is the same at the SE and the surface, as stated before. This flux must, for the unbiased wall, balance the electron flux. The ion velocity distribution is more complex than that of the electrons, with multiple effects influencing the heat flux:

1. The average velocity of the distribution,
2. the shape of the distribution and thus random flux towards the surface and
3. the acceleration due to the sheath potential drop.

The first point is addressed by Bohm's criterion that the average ion velocity perpendicular to the surface must be greater than the ion sound speed. The second point is analogous to our above considerations of the electron heat flux, but whereas the electron velocity distribution is known to be a truncated Maxwellian, ion velocity distribution at the sheath depends, amongst other factors, on collisions. Different ion velocity distribution models arrive at values for γ_s^i in the range of [1.5, 3], with 2.5 being a representative estimate [56, p.633]. This figure is normalised to ion temperature and accounts for the two first points. Because parameters such as the reflection coefficient and atomic processes depend sensitively on the ion energy, different distributions with the same average velocity can result in different heat fluxes. The third point is the most straight forward: ion energy is increased by the potential drop, the magnitude of which can be derived from the requirement of equal currents at V_f .

To derive an estimate of γ_s we will account for electron and ion current and heat flux densities. A scheme is shown in Figure 3.1. The current densities

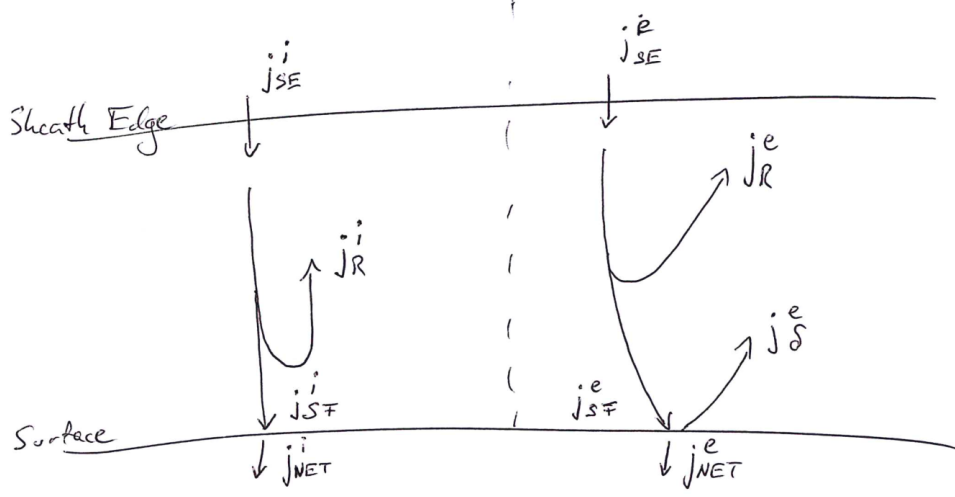


Figure 3.1.: Scheme of sheath current densities.

are defined as follows:

$$\begin{aligned}
 j_{SE}^i &= en_{SE}c_s && \text{Bohm criterion (3.7a)} \\
 j_R^i &= f_R^i j_{SE}^i && \text{Reflected ions (3.7b)} \\
 j_{SF}^i &= (1 - f_R^i) j_{SE}^i && \text{Impacting surface (3.7c)} \\
 j_{NET}^i &= (1 - f_R^i) j_{SE}^i && \text{Identical (3.7d)} \\
 &&& (3.7e) \\
 j_{SE}^e &= -1/4 en_{SE} \bar{c}_e && \text{1D Maxwellian flux (3.7f)} \\
 j_R^e &= f_R^e j_{SE}^e && \text{Reflected electrons (3.7g)} \\
 j_{SF}^e &= (1 - f_R^e) j_{SE}^e \exp\left(\frac{eV_f}{T_e}\right) && \text{Reduced by Boltzmann factor (3.7h)} \\
 j_\delta^e &= \delta_e j_{SF}^e && \text{SEE current density (3.7i)} \\
 j_{NET}^e &= (1 - \delta_e) j_{SF}^e && \text{Impacting surface (3.7j)}
 \end{aligned}$$

For floating conditions,

$$j_{NET}^i + j_{NET}^e = 0. \quad (3.8)$$

We derive the ion heat flux in terms of j_{SE}^i :

$$q_{NET}^i = (2.5T_i + \text{Integral of velocity distribution}) \quad (3.9a)$$

$$- eV_f)j_{NET}^i/e \quad \text{Acceleration by sheath potential} \quad (3.9b)$$

$$= (1 - f_R^i)(2.5T_i - eV_f)j_{SE}^i/e \quad (3.9c)$$

And the electron heat flux, also in terms of j_{SE}^i :

$$q_{SF}^e = 2T_e j_{SF}^e/e \quad \text{Integral of velocity distribution} \quad (3.10a)$$

$$q_\delta^e = \delta_e E_W j_{SF}^e/e \quad \text{SEE Work function} \quad (3.10b)$$

$$q_{NET}^e = q_{SF}^e - q_\delta^e = (2T_e - \delta_e E_W)j_{SF}^e/e \quad (3.10c)$$

$$= \frac{1}{1 - \delta_e} (2T_e - \delta_e E_W)j_{NET}^e/e \quad \text{Substituting } j_{NET}^e \quad (3.10d)$$

$$= \frac{1}{1 - \delta_e} (2T_e - \delta_e E_W)j_{NET}^i/e \quad \text{Using } V_f \text{ Equation (3.8)} \quad (3.10e)$$

$$= \frac{1 - f_R^i}{1 - \delta_e} (2T_e - \delta_e E_W)j_{SE}^i/e \quad \text{Substituting } j_{NET}^i \quad (3.10f)$$

Note here that the electrons reaching the *surface* heat it and may subsequently be re-emitted, cooling it. Reflected electrons never contribute heat or current density.

Adding ion and electron heat flux

$$q = q_{NET}^e + q_{NET}^i \quad (3.11a)$$

$$q = (1 - f_R^i)(2.5T_i - eV_f)j_{SE}^i/e + \frac{1 - f_R^i}{1 - \delta_e} (2T_e - \delta_e E_W)j_{SE}^i/e \quad (3.11b)$$

Calculating γ_s by normalising to $T_e j_{SE}^i/e$:

$$\gamma_s = \frac{q}{T_e j_{SE}^i/e} = (1 - f_R^i) \left(2.5 \frac{T_i}{T_e} - e \frac{V_f}{T_e} \right) + \frac{1 - f_R^i}{1 - \delta_e} \left(2 - \frac{\delta_e E_W}{T_e} \right) \quad (3.12)$$

Note that even the electron contribution is attenuated by the ion reflection coefficient and the electron reflection coefficient does not appear. This is because we do not need Equation (3.7h) since we substitute j_{NET}^e . Physically the reason is that electron reflection reduces both the current and heat flux

density linearly, so it should not appear in the quotient. As we will see, f_R^e does appear in the expression for V_f .

$$j_{\text{NET}}^i = j_{\text{NET}}^e \quad (3.13a)$$

$$(1 - f_R^i)j_{\text{SE}}^i = (1 - \delta_e)(1 - f_R^e)j_{\text{SE}}^e \exp\left(\frac{eV_f}{T_e}\right) \quad (3.13b)$$

$$(1 - f_R^i)en_{\text{SE}}c_s = 1/4en_{\text{SE}}\bar{c}_e(1 - \delta_e)(1 - f_R^e) \exp\left(\frac{eV_f}{T_e}\right) \quad (3.13c)$$

$$\frac{eV_f}{T_e} = \ln\left(\frac{4(1 - f_R^i)}{(1 - \delta_e)(1 - f_R^e)} \frac{c_s}{\bar{c}_e}\right) \quad (3.13d)$$

$$\frac{c_s}{\bar{c}_e} = \sqrt{\frac{T_e + \gamma_i T_i}{8T_e} \frac{\pi m_e}{m_i}} \quad (3.13e)$$

$$\frac{eV_f}{T_e} = \frac{1}{2} \ln \left[2\pi \frac{m_e}{m_i} \left(1 + \frac{\gamma_i T_i}{T_e}\right) \left(\frac{1 - f_R^i}{(1 - f_R^e)(1 - \delta_e)}\right)^2 \right] \quad (3.13f)$$

$$\approx -1.9 \quad (3.13g)$$

Energy equal to $e|V_f|$ is effectively transferred from electron to ion heat flux in the sheath by reducing the electron *density* and increasing the ion *energy*. The approximate value is calculated under the assumption of $Z_{\text{av}} = 1$, $T_i/T_e = 1$, $\gamma_i = 3$ and $\delta_e = 0.25$. For other ion charges n_{SE} , which is taken to be the electron density, must be corrected by a factor $1/Z_{\text{av}}$ in j_{NET}^i which will consequently also appear in the argument of the logarithm. The floating potential thus adapts to the electron reflection coefficient. This makes physical sense: If many electrons are reflected, a smaller potential is necessary to maintain equality of ion and electron current densities.

These expressions deviate from Reference [56]. In the case of γ_s (Equation (3.12), cf. Equation (3.22)) this may be because f_R^e is considered throughout rather than being introduced *ad hoc*. In the case of V_f (Equation (3.13f), cf. Equation (3.21)) f_R^i and f_R^e are in many cases similar or neglected all together, so the effect may have been omitted. Furthermore there is no pre-sheath contribution to γ_s . The effect of the pre-sheath is to accelerate ions to c_s , which we account for, and to slightly reduce the particle densities from n_0 to n_{SE} , which we have also considered.

We make no claim however that this is now a complete, correct theory.

The expressions for current densities at the SE are derived from fluid theory with only limited validity inside the sheath. The ion heat flux coefficient of 2.5 is an average of the velocity distribution integrals of multiple kinetic theories. The expressions were only re-derived from a complete account of fluxes, but under the same model assumptions and uncertainties.

We must further consider that

- Ions and electrons recombine to atoms, releasing their ionisation energy E_i
- These atoms may recombine to molecules on the surface, releasing their dissociation energy E_d , or be reflected with coefficient $f_{R,n}$.

These effects have a strong temperature dependence, and should in principle be accounted for using Boltzmann factors, we will approximate this to first order in T_e . Only recombination to ground state hydrogen and H_2 will be considered.

In principle all the introduced coefficients are dependent on particle energy, impact angle and material surface properties, but with the exception of δ_e we neglect this and use constant values. This is necessary because we do not know the precise surface composition and roughness and justified because they play a relatively minor role [95]. We will therefore use constant values for pure graphite, integrated over all incidence angles.

δ_e has a strong energy dependence, empirically parametrised by

$$\delta_e = \delta_e^{\max} 2.72^2 \frac{T_e}{T_e^{\max}} \exp\left(-2\sqrt{\frac{T_e}{T_e^{\max}}}\right). \quad (3.14)$$

Here δ_e^{\max} is the maximum emission coefficient, which is of order unity, but can be above for many metals. T_e^{\max} is the temperature at which maximum emission is achieved.

Taking everything above into consideration, the total sheath transmission coefficient is then

$$\gamma_s \approx (1 - f_R^i) \left(2.5 \frac{T_i}{T_e} - e \frac{V_f}{T_e}\right) + \frac{1 - f_R^i}{1 - \delta_e} \left(2 - \frac{\delta_e E_W}{T_e}\right) + \frac{E_i}{T_e} + \frac{E_d}{2T_e} (1 - f_{R,n}) \quad (3.15)$$

Table 3.2.: Constants for calculation of γ_s for Graphite and Hydrogen from Reference [95]

δ_{\max}	$T_{e,\max}$	$f_{R,i}$	$f_{R,e}$	$f_{R,n}$	E_w	E_i	E_d
1	300 eV	0.1	0.08	0.25	4.6 eV	13.6 eV	4.5 eV

Using the values for Graphite and Hydrogen from Langley *et al.* [95], given in Table 3.2, we calculate the expected γ_s and show its dependence on T_e in Figure 3.2. Multiple features can be distinguished:

- Sharp increase for low temperatures due to constant contributions of atomic and molecular recombination energies.
- Slow increase for high temperatures due to increase of SEE, up to infinity at $T_e^{\max} = 300$ eV (not shown).
- Constant value in the range 15 to 35 eV.
- γ_s offset depending on T_i/T_e ratio.
- γ_s offset between Stangeby's expression and ours, mainly due to pre-sheath contribution.

With the exception of the first, all these features lie either well within the error bounds of experimental values from our and other studies, or outside the region for which data exists. The theory will only guide our expectation, we will not be able to support or refute parameter or dependency choices and values.

Next, we will determine the experimental γ_s by calculating the quotient of q_{IR} and $T_e \Gamma_{LP}$, the particle flux derived from the Langmuir probes. Consider first the available measurements and their limitations.

3.3. LP measurement of heat flux

As was introduced above, the parallel heat flux to a surface in terms of plasma quantities is

$$q_{\parallel} = \gamma_s e n_e T_e c_s. \quad (3.16)$$

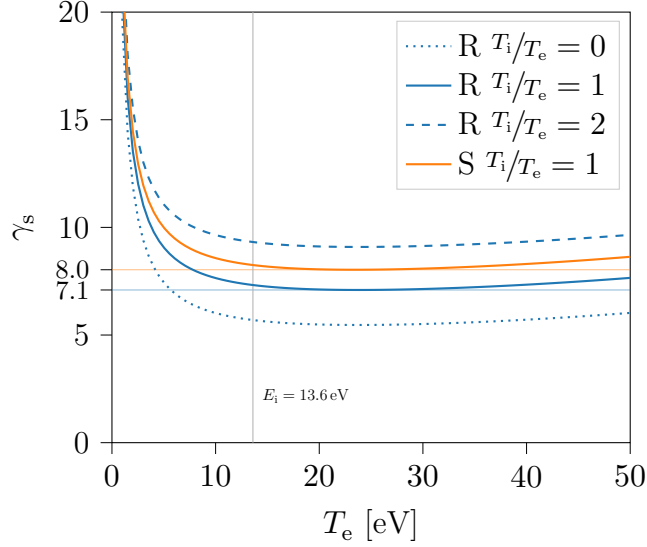


Figure 3.2.: Expected value of γ_s using values from Table 3.2. R indicates our Equation (3.15), S Stangeby's Equation (3.22).

LPs provide the required values, and we inferred them in our previous analysis in Chapter 2. Where there are uncertainties of the appropriate values of additional parameters, γ_i , Z_{av} and m_i in c_s , these do not affect us here, because they merely change the value of n_e , retracing the process by which we initially obtained it from j_{sat} . Using the same values, we thus undo any errors we may have introduced then, though systematic errors in the determination of T_e and j_{sat} would of course still be relevant. We prefer to express results in terms of plasma quantities rather than intermediate LP ones for clarity, physical understanding and comparability.

The wall surfaces are tilted with respect to the magnetic field to limit the heat flux, so q_{\parallel} is attenuated by a factor $\sin(\alpha + \alpha_{CF})$ where α is the angle of the surface and field and α_{CF} an effective angle modelling the contribution of cross field transport. Because $\alpha < 2^\circ$ for much of the divertor surface and the PFC design is predicated on the reduction of q by target inclination, it is important we consider this additional contributions precisely. This angle is defined by decomposing of the total flux into parallel and perpendicular component as shown in Figure 3.3. A different low order approximation to account for cross field transport is made in field line

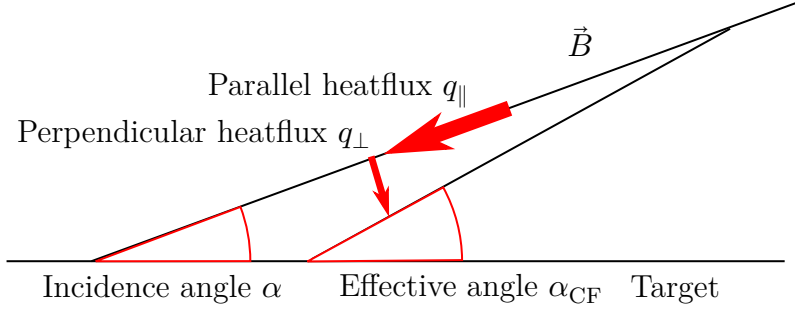


Figure 3.3.: Definition of α_{CF}

diffusion (FLD) simulations. These are used extensively and successfully at W7-X to predict heat load patterns on PFCs [76, 96]. Because FLD simulates single particle transport rather than energy, those studies effectively assume the perpendicular heat transport coefficient $\xi_{\perp} \approx D_{\perp}$.

The field line tracing (FLT) implements a random walk with steps along the field and a dispersion of points perpendicular to the field. Quoting directly from Reference [97]: 'The parameters to describe the process are: perpendicular diffusion coefficient D_{\perp} , mean free path λ , and velocity v . The *transport* steps are performed after a random length x with the distribution:

$$p(x) = \frac{1}{\lambda} \exp\left(\frac{-x}{\lambda}\right). \quad (3.17)$$

The direction of the steps is uniform in the plane perpendicular to the field, while the step size r is uniform in the interval

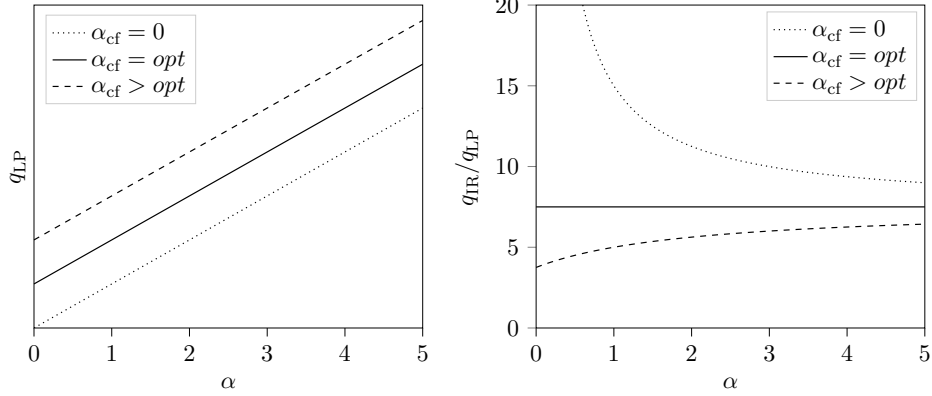
$$r \in \left[0, \sqrt{\frac{12D_{\perp}\lambda}{v}}\right] \quad (3.18)$$

so as to average to the correct 2d diffusion.' From the expectation values of these step sizes, λ and $\frac{1}{2}\sqrt{\frac{3D_{\perp}\lambda}{v}}$ for parallel and perpendicular direction respectively, we can calculate

$$\tan \alpha_{CF} = \frac{1}{2} \sqrt{\frac{3D_{\perp}}{\lambda v}}. \quad (3.19)$$

Table 3.3.: Typical values for FLD calculations and α_{CF}

D_{\perp}	λ	$v = c_s(T_e = 100 \text{ eV}, \gamma_i = 1)$	α_{CF}
$1 \text{ m}^2 \text{ s}^{-1}$	10 cm	$1.5 \times 10^5 \text{ m s}^{-1}$	0.4°


Figure 3.4.: Schematic of effect on γ_s if an effective cross field angle α_{CF} is not considered. *opt* is the optimal value of α_{CF} that best models the turbulent transport.

Typically used values, reported in Reference [76], are given in Table 3.3. The velocity is herein calculated as $v = c_s$ with $\gamma_i = 1$ and $T_i = T_e = 100 \text{ eV}$. The function of λ is that of a numerical control parameter, controlling the runtime and accuracy of the code rather than retaining its physical meaning of the mean free path length λ_{mfp} . It is chosen to be small compared to the typical connection length L_c . Simulations which account for heat and particle transport separately, such as those reported on by Schmitz *et al.* [98], often use $\xi_{\perp} + 3D_{\perp}$, but with $D_{\perp} = 0.5 \text{ m}^2 \text{ s}^{-1}$. Underestimating the added contribution of α_{CF} will lead to a $1/\alpha$ dependence of γ_s as shown in Figure 3.4. α_{CF} was not considered in the evaluation of the LPs. This is principally due to the fact that the probe tips were designed such that the area-weighted average of impact angle γ is never below 3° for any configuration. In the case of the 'standard' magnetic configuration in the centre of accessible space (EIM) it is for each probe $>5^\circ$. An increase by 0.4° is thus an effect smaller than 10%. Finally cross-field transport would only affect n_e , not the shape of the Current-Voltage characteristic (IV-characteristic) and thus not the

double probe area ratio β or T_e . q is proportional to $n_e T_e^{3/2}$, further reducing the relative importance of errors in n_e .

In Section 2.5 we argued it was sufficient to save only the mean and variance of the inferred kernel density estimates (KDEs) [82, 83] of n_e and T_e . To justify the use of separate Gaussian estimates of n_e and T_e to determine q_{LP} , we compare that approach to the more correct one of sampling from the joint posterior distribution and building q_{LP} from these using a KDE approach. As an example, we use the time point discussed in detail in Section 2.5 and specifically the joint posterior of n_e and T_e shown in Figure 2.13. In Figure 3.5 results of three methods are compared:

- Gaussian constructed from $\mu_q^{\text{LP}} = q_{\text{LP}}(\langle n_e \rangle, \langle T_e \rangle)$ and $\sigma_q^2 = \left(\frac{\partial q_{\text{LP}}}{\partial T_e} \right)^2 + \left(\frac{\partial q_{\text{LP}}}{\partial n_e} \right)^2$, i. e. the uncorrelated Gaussian error propagation. $\langle x \rangle$ denotes the mean. We will denote this method $\mathcal{N}(T_e)\mathcal{N}(n_e)$.
- Distribution constructed by KDE with Gaussian kernel and bandwidth determined by Scott's rule [99] from q_{LP} samples generated by $q_{\text{LP},i} = q_{\text{LP}}(n_{e,i}, T_{e,i})$ i. e. heat flux individually for each sample of the joint posterior. We will denote this method KDE.
- Gaussian constructed from $\mu_q^{\text{LP}} = q_{\text{LP}}(\langle n_e \rangle, \langle T_e \rangle)$ and $\sigma_q^2 = \left(\frac{\partial q_{\text{LP}}}{\partial T_e} \right)^2 + \left(\frac{\partial q_{\text{LP}}}{\partial n_e} \right)^2 + 2\rho_{T_e, n_e} \sigma_{T_e} \sigma_{n_e} \frac{\partial q_{\text{LP}}}{\partial T_e} \frac{\partial q_{\text{LP}}}{\partial n_e}$, i. e. the Gaussian error propagation corrected for correlation. $\rho_{T_e, n_e} \in [-1, +1]$ is the Pearson sample correlation coefficient r_{xy} . We will denote this method $\mathcal{N}(T_e, n_e)$.

We find that when using the correlation-corrected Gaussian error propagation with $\rho_{T_e, n_e} = -0.85$, the KDE result can be very well approximated. The strong correlation coefficient is expected and the resulting small uncertainty in Γ and q_{LP} unsurprising if we consider that Γ is proportional to the quantity physically measured by the LPs whereas n_e and T_e are only inferred. We thus proceed to use the correlation-corrected method to determine q_{LP} and Γ_{LP} , effectively modelling the joint posterior of (T_e, n_e) as a bi-variate Gaussian.

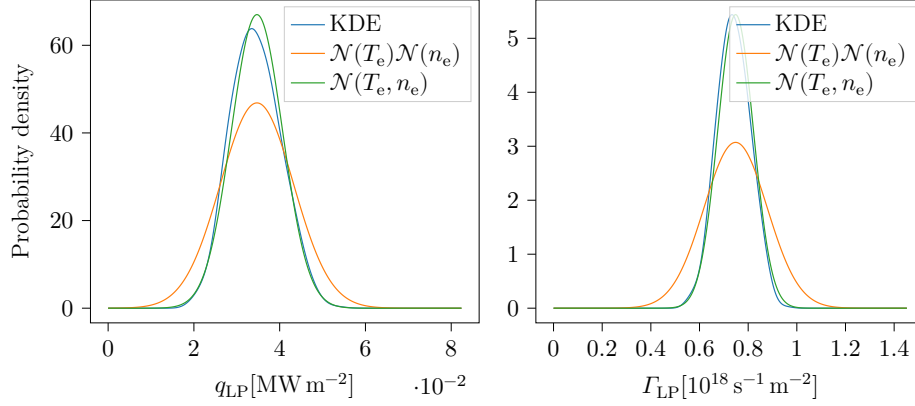


Figure 3.5.: probability density functions (PDFs) of Γ in the left panel and q_{LP} in the right, calculated from the Markov chain Monte Carlo (MCMC) samples of P10, 20180814.007, $t = 6.115$. The curves correspond to different methods of propagating the measurement error, as described in the text.

3.4. IR measurements of heat flux in W7-X

Infrared-Cameras (IRCs) measure the radiation from a body’s surface, using either a charge-coupled device (CCD) chip sensitive to long wavelengths or an array of micro-bolometers. The radiation can be associated with a temperature using the Rayleigh-Jeans law for long wavelengths and hot bodies or Planck’s law in other conditions. The accuracy at low temperatures is reduced because the total emitted power scales with frequency squared. This can be compensated by a longer exposure time, introducing a trade-off between temperature and time resolution. The specific software used by the W7-X IRCs does not allow for an automatic adjustment of the exposure time. Because the IR system has a safety relevant monitoring responsibility, the exposure time was generally set according to the maximal expected heat flux. This imposes a lower measurable limit of temperature [45].

An increase of the surface temperature must be due to a heat flux from the plasma greater than its temperature-dependent radiation balance. With knowledge of the heat conductivity and radiative properties, especially the emissivity of the body surface, codes such as Thermal Energy onto Divertor (THEODOR) [100] can calculate the heat flux. THEODOR solves the heat

diffusion equation on a grid using finite element methods. An important source of error in the heat flux determination is the change of emissivity. This can occur through a modification of the surface roughness or a build-up of deposition layers. By calculating the emissivity during the pre- and post-discharge phase, when the plasma heat flux is known to be zero, these effects are corrected for. The conduction to other connected components plays a negligible role as the operation phase (OP) 1.2 discharges were too short and the heat capacity of the test divertor unit (TDU) too large to significantly heat it beyond the surface layer and at the support structure. In the future this effect will remain irrelevant because the active cooling will maintain low temperatures of the support structure. Systematic errors in the high heatflux divertor (HHFD) system might be introduced by the coolant calorimetry.

Especially at low temperatures, noise is interpreted by THEODOR as fluctuations of the temperature, and, accordingly, fluctuating, occasionally negative heat fluxes. The level of these heat flux fluctuations, again during the pre- and post-discharge phase, are taken as uncertainties of q_{IR} . During OP 1.2 this uncertainty was determined to be 150 kW m^{-2} . Above $\approx 200 \text{ kW m}^{-2}$ we can reasonably assume that the PDF of a single q_{IR} measurement is Gaussian with the value as mean and the given uncertainty as variance, below that heat flux threshold a more detailed consideration would be necessary to determine the PDF.

3.5. Calculation of sheath transmission coefficient

To calculate γ_s , we unify the data grid of the LP and IRC measurements. As detailed in Chapter 2 Section 2.2, the two swept LPs arrays are situated on the Upper divertor (UD) and Lower divertor (LD) of module 5. The probes are spaced along one divertor finger by 25 mm, thus roughly at constant toroidal and radial, but varying poloidal location. For this purpose of using plasma parameters, they are sampled at 500 Hz. IRCs cover all ten divertor modules, however the camera observing the LD had optical and calibration issues throughout OP 1.2 and its data will not be used here. The resolution varies over the field of view, on poloidal profiles parallel and adjacent to

the probes it is 3 mm. For the reasons cited above, the time resolution of the IRCs was set to 100 Hz. We select pixels of the q_{IR} profile closest to the probes and average q_{LP} over time segments in between IRC frames, corresponding to the camera's exposure time. Thus we will obtain a value for γ_{s} at each point of the grid and can later correlate these individually with other properties such as incidence angle at the location, or averages of measurements and plasma parameters in each grid cell such as $\langle q_{\text{IR}} \rangle$ or $\langle T_{\text{e}} \rangle$. We call this the unified grid to distinguish it from each diagnostic's full resolution grid. This procedure, and the analysis in this section in general, is done using the python package `xarray` [101, 102].

Because our experimental data exhibits large uncertainties, it is important we also consider the uncertainty of our empirical estimate of γ_{s} . Using the (correlation-corrected) Gaussian estimates for the KDEs of T_{e} and n_{e} , their product q_{LP} too will have a Gaussian uncertainty distribution. The uncertainty $\sigma_{\text{q}}^{\text{IR}} = 150 \text{ kW m}^{-2}$ is also assumed to be Gaussian, if the value is far enough above the lower measurement threshold. Generally, the quotient γ_{s} will be a Cauchy distribution with undefined mean and variance, inconvenient for our aim of comparing it to the expected value and propagating these first two distribution moments through our code. This arises from the obvious difficulty of dividing distributions that overlap or have non-zero value at zero. If the distributions in numerator and denominator are peaked far from zero, typically with a coefficient of determination

$$\delta = \frac{\mu}{\sigma} \tag{3.20}$$

greater than 10, we can use the well-known propagation of uncorrelated errors to obtain value and standard error of γ_{s} [103]. In our case this, however, requires $q_{\text{IR}} \geq 10 * \sigma_{\text{q}}^{\text{IR}} = 1.5 \text{ MW m}^{-2}$ which is rarely observed. Marsaglia [104] introduced a more sophisticated formula allowing parameters of Gaussian approximations to ratio distributions of normals to be obtained, requiring that the coefficient of determination of the denominator be greater than 4 and that of the numerator less than 2.5. In our case this implies $\delta_{\text{q}}^{\text{LP}} > 4$ and $\delta_{\text{q}}^{\text{IR}} < 2.5$. Under these conditions, the Cauchy distribution becomes very similar to a Gaussian. Both requirements can be relaxed if the denominator never becomes negative, which is the case here. If the same is true of the numerator, the ratio distribution is unimodal, itself non-negative and skewed positive. Requiring that $\delta_{\text{q}}^{\text{LP}} > 4$, we can use Marsaglia's estimates

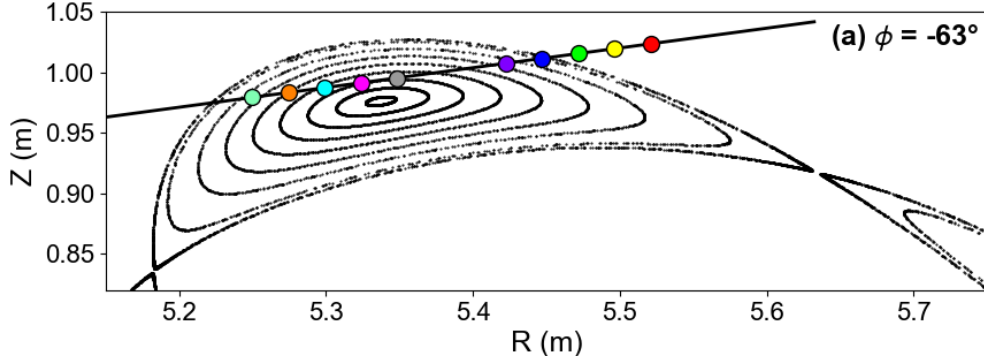


Figure 3.6.: Poincaré plot at the cross section of the UD probes showing the intersection of the island with the target plate in DBM configuration. Plot adapted from Reference [43].

and obtain a normal approximation for γ_s and thus value and variance. Note that the real upper uncertainty bound will be higher due to the skew. We will require $\delta_q^{\text{IR}} \geq 2$ to ensure normality of the q_{IR} distribution.

To display γ_s and other quantities, accounting for the uncertainties, KDEs are used: From each pair $(\gamma_s, \sigma_\gamma)$, a normal is generated from which we sample. A smoothed histogram of these samples gives a compact, faithful and generic representation of the spread of results.

To get a representative dataset with high and low values of heat flux, discharges in the low iota magnetic configuration (DBM) configuration will be analysed. In these the strike line is located on the horizontal target, further from the pumping gap than in the EIM configuration and thus better covered by the probe array, as shown in Figure 3.6.

3.6. Results

We will first exemplarily investigate the results for γ_s and its dependencies for a single discharge and then whether the picture changes if data from different discharges is combined.

For discharge 20181004.048 an overview is shown in Figure 3.7. It can be described roughly in four phases:

[0, 1.5] s Start-up with increasing $\int n_e dl$, low P_{rad} and Probe UD5 measuring

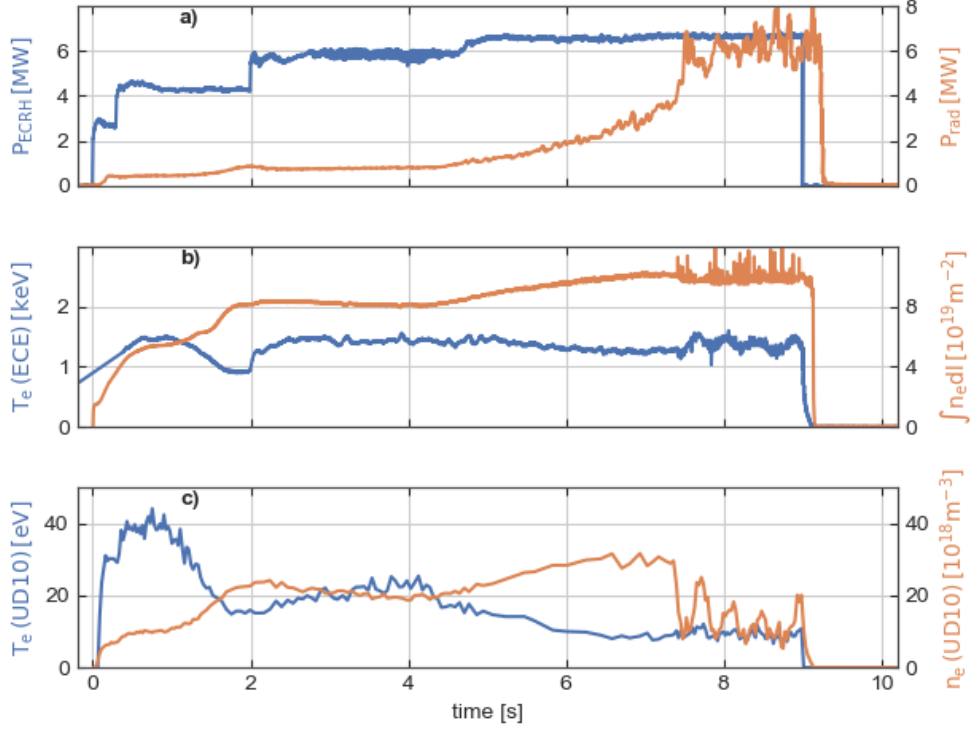


Figure 3.7.: Overview of discharge 20181004.048. Panel **a** shows time traces of the input electron cyclotron resonance heating (ECRH) power [86] in blue and radiative losses P_{rad} measured by the bolometers [87] in orange. Panel **b** shows time traces of core electron temperature measured by electron cyclotron emission (ECE) channel 13 [105] in blue and line integrated density from the dispersion interferometry system [90] in orange. Panel **c** shows time traces of temperature and density measured by Langmuir probe UD5 in blue and orange respectively. The Langmuir data are averaged with $N = 25$ and fits with temperature uncertainties $\sigma_{T_e} > 50 \text{ eV}$ or $T_e > 250 \text{ eV}$ are excluded.

Table 3.4.: Measurements of γ_s determined from the probability density shown in Figure 3.13. The maximum a posteriori (MAP) is the most likely value.

MAP	σ^-	σ^+	$\int_{\sigma^-}^{\sigma^+} p(\gamma_s)$
6.5	2.9	12.3	0.68

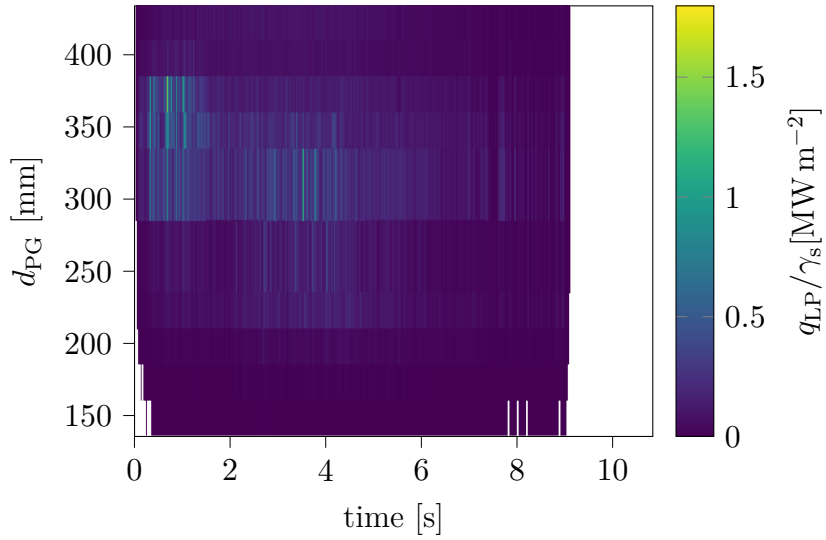


Figure 3.8.: q_{LP}/γ_s poloidal profile over time. d_{PG} is the distance to the pumping gap along the target finger. Time is relative to the beginning of ECRH.

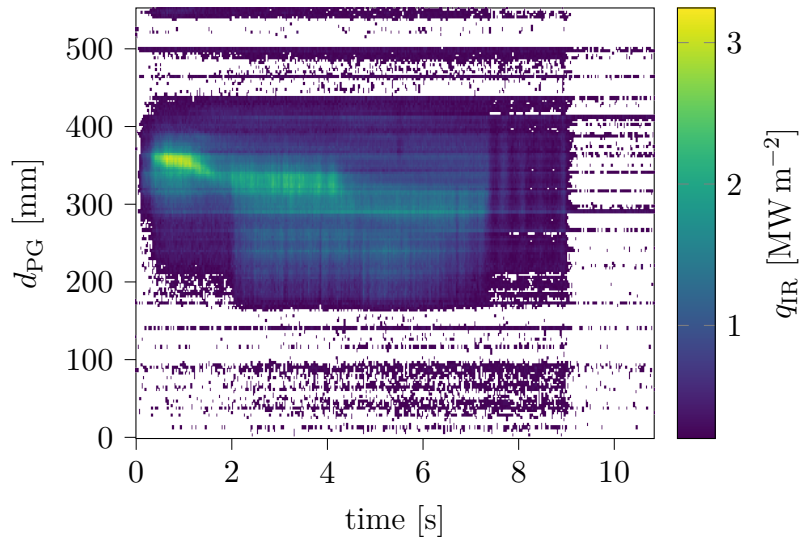


Figure 3.9.: q_{IR} poloidal profile adjacent to probes over time.

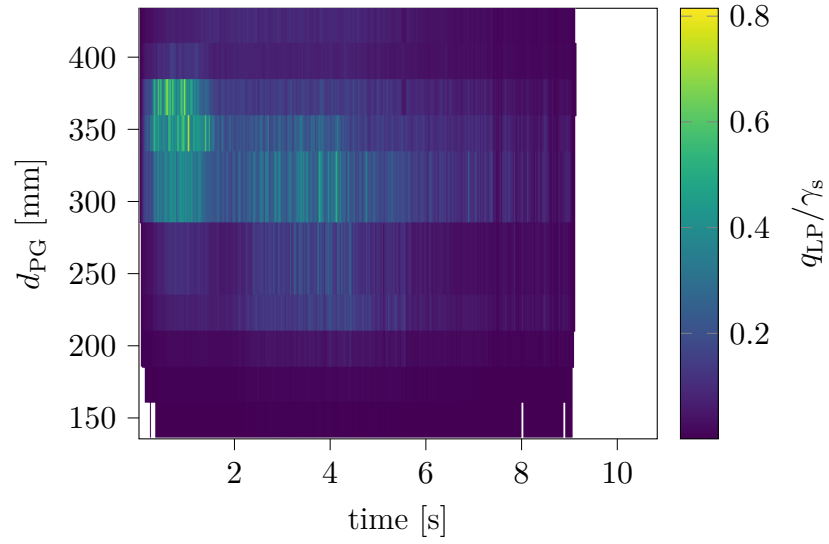


Figure 3.10.: q_{LP}/γ_s poloidal profile of the probes over time on the unified grid.

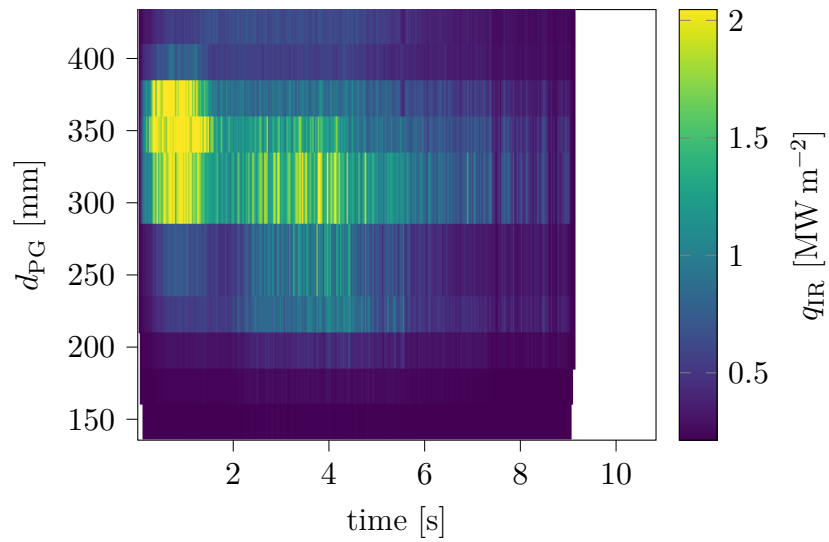


Figure 3.11.: q_{IR} poloidal profile adjacent to probes over time on the unified grid.

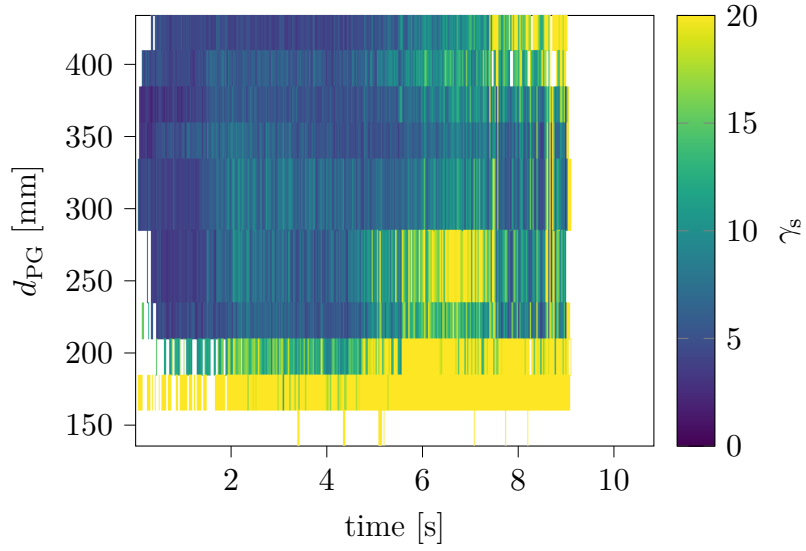


Figure 3.12.: γ_s over time at each probe position.

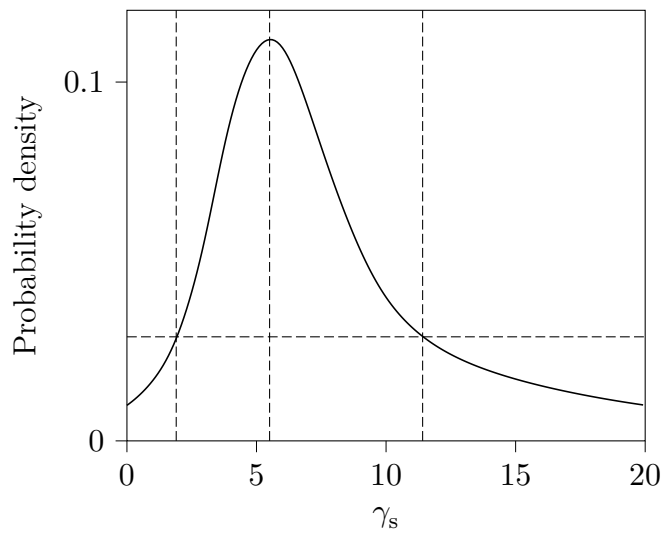


Figure 3.13.: Probability density obtained through KDE of γ_s .

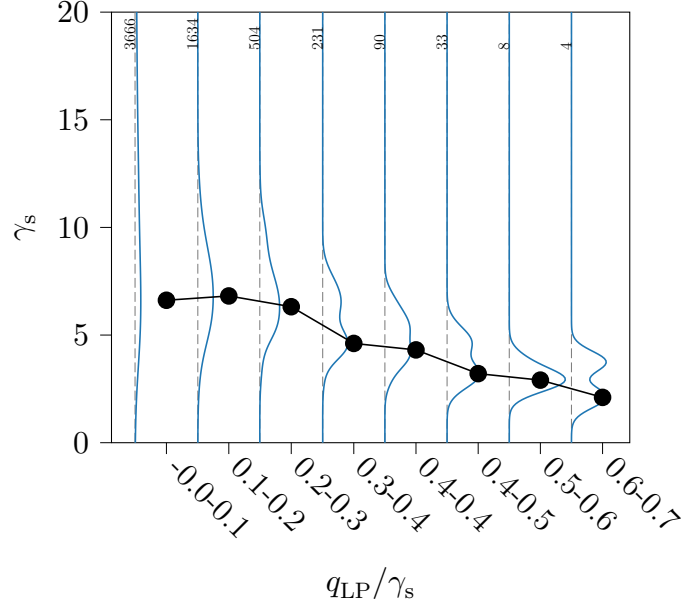


Figure 3.14.: KDEs of γ_s calculated for (q_{IR}, q_{LP}) value pairs with range of binned q_{LP} indicated on the abscissa. MAP shown in black, numbers indicate the counts in each bin.

comparatively high T_e and low n_e .

[1.5, 4.5] s Constant $\int n_e dl$, low P_{rad} and Probe UD5 measuring intermediate T_e and n_e .

[4.5, 7.5] s Slowly increasing $\int n_e dl$, strongly increasing P_{rad} due to radiation-controlled feedback fuelling by the Helium beam spectroscopy (HeBS) system. Probe UD5 measuring increasing n_e and decreasing T_e .

[7.5, 9] s Almost complete power dissipation by radiation, fluctuating $\int n_e dl$ and P_{rad} . UD5 T_e low, n_e fluctuating strongly.

q_{LP}/γ_s and q_{IR} are shown at their full data resolutions in Figure 3.8 and Figure 3.9 respectively. In Figure 3.10 and Figure 3.11 the averaged heat fluxes are shown on the unified grid as defined in the previous section. From these, γ_s is calculated and shown in Figure 3.12, but without knowing the displayed values' uncertainty and aggregating the values, it is hard to draw

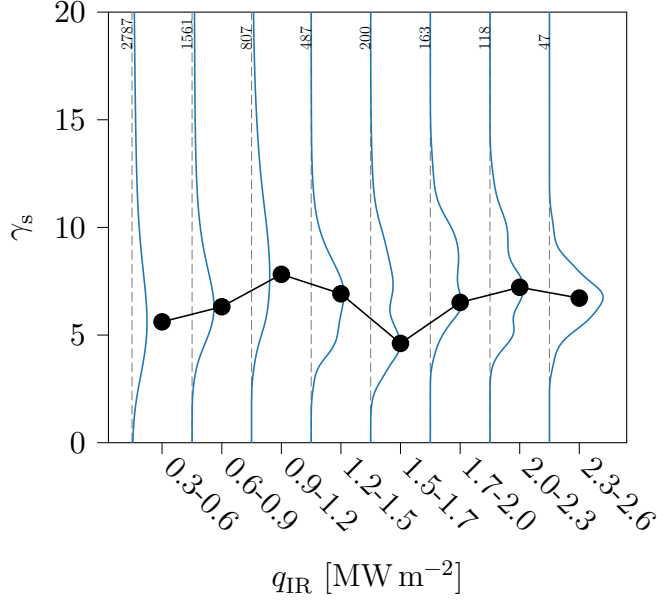


Figure 3.15.: KDEs of γ_s calculated for $(q_{\text{IR}}, q_{\text{LP}})$ value pairs with range of binned q_{IR} indicated on the abscissa. MAP shown in black, numbers indicate the counts in each bin.

conclusions from this graph. The PDF, obtained through KDE, of these results is shown in Figure 3.13, from which we can determine the MAP and highest density interval (HDI) given in Table 3.4. The expected value from Figure 3.2 is some $\approx 15\%$ higher than the most probable value, but well within the error bounds. The quoted error correspond to the HDI [106], selected such that $\approx 68\%$ of the probability mass of the PDF fall within the interval and no value outside of the interval is more likely than any within it. This makes the bounds and mode comparable to a Gaussian estimate of γ_s parametrised by (μ, σ) . μ is in both cases the mode (most likely value) and the interval $[\sigma^-, \sigma^+]$ encompass $\approx 68\%$ of the probability mass. Our distribution does of course not possess the additional properties of the unimodal, symmetric Gaussian of μ also being the mean and $\sigma^- = \sigma^+$.

Referring back to Figure 3.2 a possible explanation of the observed value of $\gamma_s \approx 6.5$ would be a much lower T_i , but such far reaching conclusions should not be drawn before the potential issues of the raw measurements are resolved. Marsen *et al.* observed γ_s decreasing in high-recycling condi-

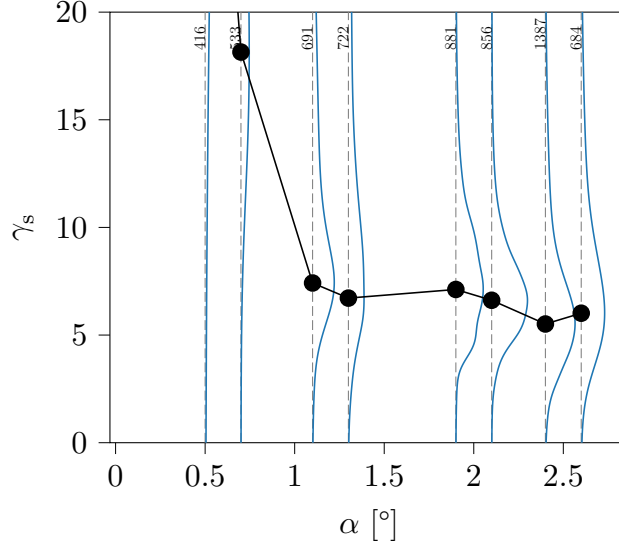


Figure 3.16.: KDEs of γ_s calculated for each probe and separately and ordered by angles. Compare with expectations of Figure 3.4. MAP shown in black, numbers indicate the counts in each bin.

tions [92], possibly attributable to an overestimation of T_e . This occurred at $\Gamma_{\parallel} > 2 \times 10^{24} \text{ m}^{-2} \text{ s}^{-1}$ and $T_e < 15 \text{ eV}$, a quadrant of parameter space we also reach in the discharge under consideration. γ_s calculated from those data points has a slightly higher MAP at ≈ 7.8 , in line with the observed correlations of T_e and n_e we will present below. In comparison to JET, the target density at W7-X scales more weakly with the upstream density, so that high-recycling conditions are not reached to the same degree (though more than in Wendelstein 7-AS (W7-AS)). The reason is thought to be stronger pressure and momentum transport losses. Consequently, lower densities and higher temperatures are also evident in the absence of higher order lines of the Hydrogen Balmer series in the observed spectra, which would be indicative of recombination [107].

In Section 3.2 and Section 3.3 we elaborated that two dependencies of γ_s are expected, on T_e and on incidence angle α , provided our initial guess of α_{CF} is not optimal.

γ_s evaluated for different T_e intervals can be seen in Figure 3.17 and shows the expected $1/T_e$ dependence, but also a linear trend of decreasing γ_s

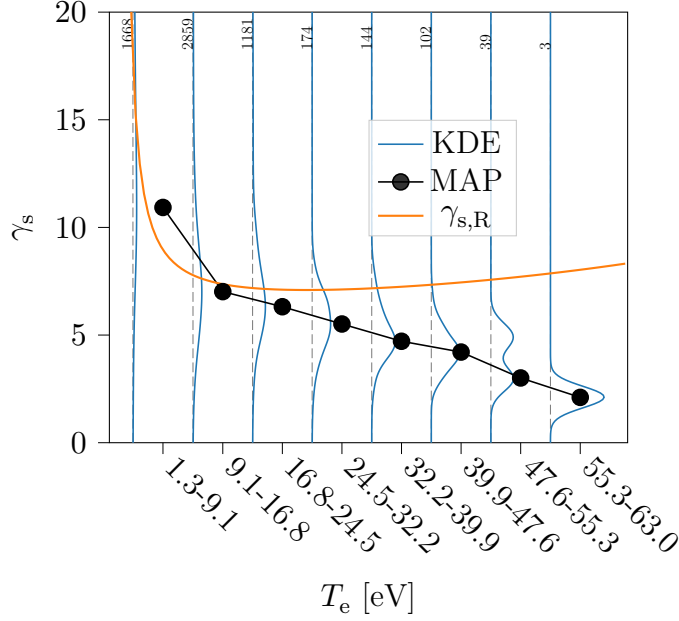


Figure 3.17.: KDEs of γ_s calculated for $(q_{\text{IR}}, T_e, n_e)$ value sets with range of binned T_e indicated on the abscissa. Compare with expectations of Figure 3.2 shown in orange. MAP shown in black, numbers indicate the counts in each bin.

with increasing temperature to below the level of 7.5, without the expected saturation. It should be noted that the determination of γ_s is very uncertain at low T_e , resulting in an extremely spread out PDF and only very data are available at high T_e .

The trend of $\gamma_s(\alpha)$ in Figure 3.16 seems to indicate we underestimated α_{CF} , but again we note that for the smaller angles the determination of γ_s is very uncertain. In the DBM configuration, the positions furthest from the strikeline and consequently with the lowest heat flux, namely the probe positions close to the pumping gap, are also those with the lowest incidence angles (cf. Figure 3.6 and Figure A.1 in Appendix). It is therefore not discernable in this configuration whether the correlation with angle implies causation or is due to this co-variance.

Throughout the discharge there is an evolution of most probable γ_s values (Figure 3.19). Quite clearly the time intervals and γ_s distributions correspond

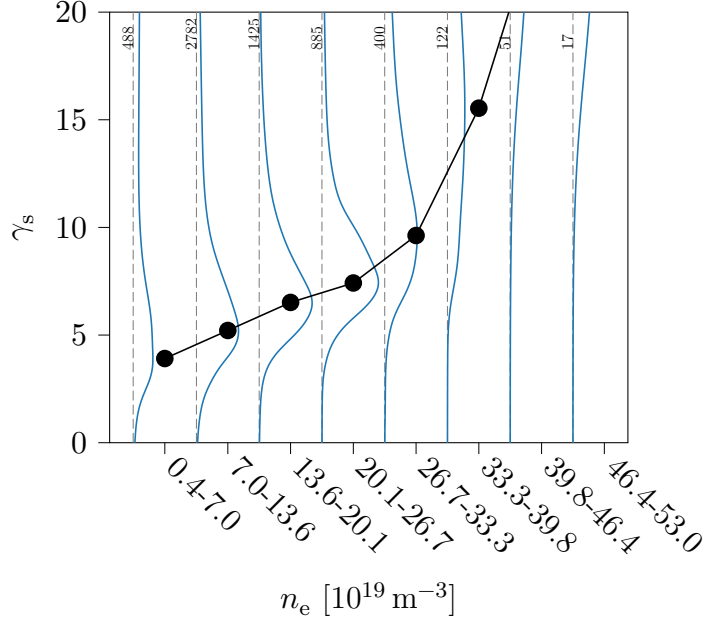


Figure 3.18.: KDEs of γ_s calculated for $(q_{\text{IR}}, T_e, n_e)$ value sets with range of binned n_e indicated on the abscissa. MAP shown in black, numbers indicate the counts in each bin.

to the discharge phases outlined above, with consistently low γ_s in the first, intermediate values in the second and highly uncertain determination in the latter two. Accurately attributing contributions of systematic errors in the measurements and real physical effects, such as through particle momentum loss in highly radiative regimes [92], is challenging and will not be conclusively resolved here. Multidimensional regression techniques to find a power law or linear combination of variables to model the dependency, as in Reference [94] or used in confinement time scaling [108], could be attempted, but will not by themselves offer physical explanations. We will investigate below the dependency on individual parameters to gain an understanding and provide a basis for further studies.

There is no obvious dependence on q_{IR} discernable in Figure 3.15, which might otherwise indicate a systematic deviation of the inferred heat fluxes. The bins are chosen such that $w_{\text{bin}} \approx 2\sigma_q^{\text{IR}}$. Even the results in the lowest value bin are still reasonably clear and well resolved. This indicates that the

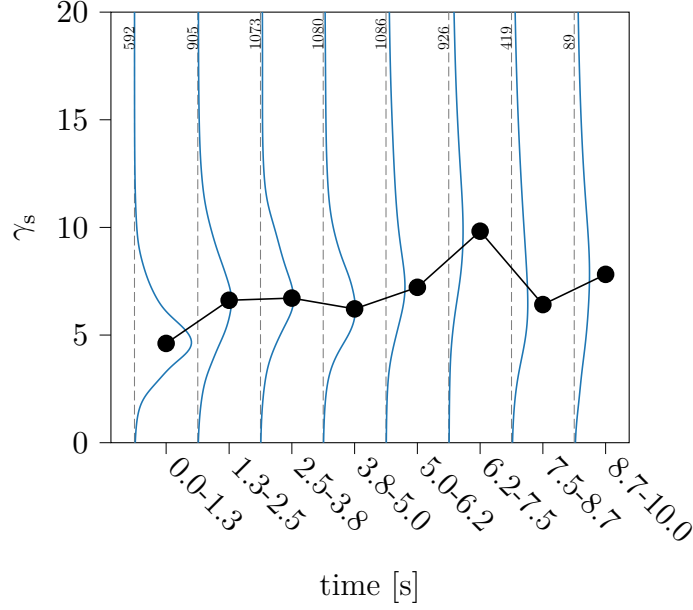


Figure 3.19.: KDEs of γ_s calculated for $(q_{\text{IR}}(t), q_{\text{LP}}(t))$ value pairs in 7 time segments of the discharge. MAP shown in black, numbers indicate the counts in each bin.

lower limit on q_{IR} we chose was appropriate.

The same can not be said for $\gamma_s(q_{\text{LP}})$, shown in Figure 3.14, which shows a downward tendency. Higher heat fluxes appear to be systematically overestimated relative to q_{IR} . To check whether this is purely due to the previously determined behaviour of $\gamma_s(T_e)$, we examine $\gamma_s(n_e)$ in Figure 3.18. In the region in which results are reliable and sufficient data exists, we observe a positive correlation. This effect should in principle compensate the negative slope of the T_e dependence, if n_e and T_e are generally positively correlated. From the discharge overview in Figure 3.7, however, we know that for most of the discharge, $t = [1, 7]$ s, the opposite is true and n_e & T_e are anti-correlated. We will see in Figure 3.20 that significant heat fluxes are observed in this discharge also for very asymmetric combinations of (T_e, n_e) . The presence of a trend in $\gamma_s(q_{\text{LP}})$ despite the anti-correlation might either be due to the principally stronger dependence of q_{LP} on T_e (power of $\frac{3}{2}$ rather than power of 1 for n_e) or a consequence of the co-dependence of the

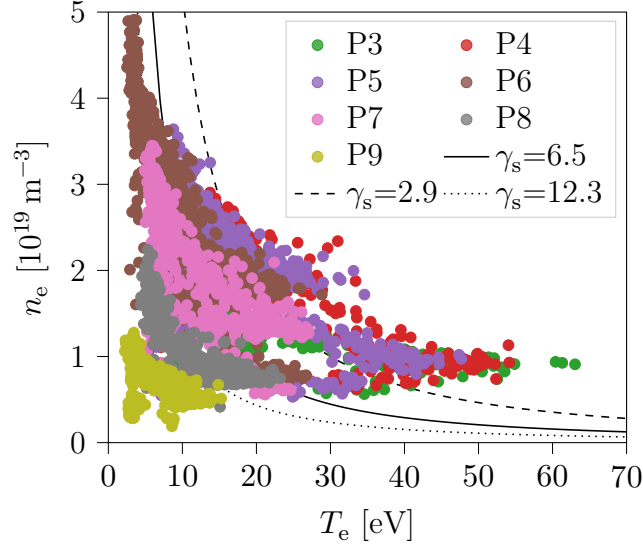


Figure 3.20.: Value pairs of (n_e, T_e) for which q_{IR} corresponds to $q_{\parallel} \in [10, 20] \text{ MW m}^{-2}$ for different probes. Expected values for specific γ_s shown as lines. Note that expected γ_s values were derived from the full dataset and are thus not expected to match the subset of points perfectly.

inferred (T_e, n_e) value pairs (see Section 3.3). The two explanations may be distinguishable using additional information of the Γ comparison in the following chapter with different exponents of T_e and n_e ($\Gamma \propto T_e^{1/2}$ whereas $q_{\text{LP}} \propto T_e^{3/2}$).

For given $(q_{\text{IR}}, \gamma_s, \alpha)$ with uncertainties we can calculate the (T_e, n_e) value band compatible with that observation. To show these bands simultaneously and in a comparable way for all probes, despite the different field-target inclination angles α at their positions, rather than q_{IR} we select a value of q_{\parallel} to group the data by. The average inclination angle in the DBM configuration is $\langle \alpha \rangle \approx 2^\circ$, such that $q_{\text{IR}} = (0.50 \pm 0.15) \text{ MW m}^{-2}$ corresponds to $q_{\parallel} \approx (15.0 \pm 4.5) \text{ MW m}^{-2}$. From our data we select positions and times where q_{\parallel} fall in this interval, and plot the corresponding (T_e, n_e) pairs. This reverts the procedure for determining γ_s and ensures internal consistency. Figure 3.20 shows three notable deviations from the expected behaviour:

- Lower than predicted T_e at high n_e

- Higher than predicted n_e at high T_e
- P9 not following the trend but deviating significantly from it

The first two points suggest a systematic correlation of the T_e and n_e values, in addition to the correlation of the uncertainties, as we already noted above on the discharge evolution. They also show again the behaviour we noted earlier in Figure 3.17 and Figure 3.18, namely of trending towards lower values of γ_s (dashed line) and higher values of γ_s (dotted line) for T_e and n_e respectively. The last point might be explained by a relatively stronger cross field diffusion at these positions, which are deep in the private flux region near the pumping gap (Figure 3.6). For all three cases, we must consider that by selecting individual value pairs with a binary condition (inside or outside of $[10, 20] \text{ MW m}^{-2}$), we may be getting an unrepresentative sample, potentially even only outliers of the distribution of value pairs for each probe. The error bars on the samples are not shown, but were checked and are too small to account for the deviation, as is expected given that only pairs with $\delta_{T_e}, \delta_{n_e} > 4$ were considered.

3.7. Summary

The sheath transmission coefficient γ_s describes how much energy is transferred per particle in plasma impinging on a surface. We have measured it empirically in Wendelstein 7-X (W7-X) by comparing the results of the Langmuir probes (LPs) with those of the Infrared-Camera (IRC) and found that we could reproduce the value expected from sheath theory within error bounds. The probable range we were able to restrict γ_s to matches that found in other experiments. Dependencies of γ_s were studied in detail to better understand systematic deviations of the LP measurements. While our observations do not match the theoretical expectation under all conditions, the agreement is robust enough to support the claim that the LP heat flux measurements are consistent with those of the IRC.

To disentangle the correlations between incidence angle and heat flux, future studies should merge the data set of this discharge with those of several others. This extension can also clarify if any of the observed correlations are due to a specific behaviour of the discharge investigated, such as the combination of core density and radiated power fraction.

3.8. Appendix

Stangeby's expression for V_f :

$$\frac{eV_f}{T_e} = \frac{1}{2} \ln \left[\left(2\pi \frac{m_e}{m_i} \right) \left(1 + \frac{T_i}{T_e} \right) (1 - \delta_e)^{-2} \right]. \quad (3.21)$$

Stangeby's expression for γ_s :

$$\gamma_s \approx \left[2.5 \frac{T_i}{T_e} - \frac{eV_f}{T_e} \right] (1 - f_R^i) + \frac{2}{1 - \delta_e} (1 - f_R^e) + \frac{1}{T_e} (eV_{PS} + E_i + E_d(1 - f_R^n)). \quad (3.22)$$

V_{PS} is the pre-sheath voltage. To fulfil Bohm's criterion, a pre-sheath must accelerate the ions, thus analogously transferring energy equal to

$$|eV_{ps}| = \ln(2)T_e. \quad (3.23)$$

The energy transferred in the pre-sheath eV_{ps} will at most be $\approx 0.7T_e$ but a reduced average value of $\approx 0.5T_e$ is more realistic, since some ions are 'born' from neutral within the pre-sheath [56, p.648]. This term makes up about half the difference between Stangeby's formulation and ours.

4

Particle flux comparison

4.1. Introduction

In addition to heat the divertor must remove particles. The particle flux Γ can be measured by Langmuir probes (LPs) through the ion saturation current I_{sat} , divided by the average charge of the ions Z_{av}

$$\Gamma = \frac{j_{\text{sat}}}{Z_{\text{av}}}. \quad (4.1)$$

Particles reaching the wall of the device are neutralised and either reflected themselves or release other neutrals from the wall. This process is called recycling and the ratio of outgoing ion flux (from the point of view of the plasma) and incoming neutral flux is the recycling ratio f_{rec} . For Wendelstein 7-X (W7-X) it is estimated that the steady state, machine global, f_{rec} is close to unity [109].

This incoming neutral flux can be measured by the emission radiating from it at specific wavelengths, when particles are excited through collisions in the plasma [110]. Once these neutrals are ionised, they cease to radiate at this specific wavelength. The photon-efficiency for a specific wavelength thus depends on the relative likelihood of excitation, de-excitation via emission of a photon at that wavelength, and ionisation. It counts photons per ionisation. The likelihood of these processes in turn depend on plasma parameters and can be looked up in databases such as Atomic Data and Analysis Structure (ADAS).

The inverse photon-efficiency S/XB (counting ionisation per photon) [111] is defined such that

$$\Gamma * f_{\text{rec}} = \Gamma_n = \text{S/XB} * \Phi_\alpha. \quad (4.2)$$

A high S/XB implies that neutrals are rapidly ionised, for example because the plasma density is high and there are many collisions, and thus have little opportunity to radiate. Because of this, each photon is indicative of many neutrals, and the photon count must consequently be amplified by the large S/XB value. A low value, potentially even below one in a very low temperature environment, implies that each neutral can be excited and de-excite multiple times before it is ionised, and the photon flux must be scaled down. The dependency on T_e and n_e is shown in Figure 4.1.

By comparing Γ recorded by the LPs and the photon flux Φ_α seen by the H_α cameras we can get an independent estimate of the empirical, effective S/XB (S/XB_{eff}) coefficient.

Comparing this to tabulated theoretical S/XB from T_e, n_e lookup (S/XB_{th}) for plasma parameters obtained from measurement or simulations provides a consistency check that can reveal whether

- the tabulated values are correct,
- the plasma parameters are accurate, and
- the assumptions typically made in the evaluation are justified.

If all are, S/XB_{eff} ought to be equal to S/XB_{th} .

4.2. H_α -light observation

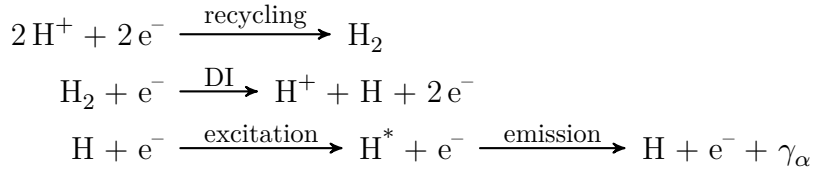
H_α emission in W7-X is monitored using a visible light camera system with appropriate interference filters [112]. Due to the use of wide-angle optics the spatial resolution on the surface varies, but is less than 10 mm on the horizontal target. The time resolution is 40 ms. Each camera has been calibrated with a light source of known intensity.

Unlike the Infrared (IR) emission from the target surface, H_α emission can originate from anywhere along the camera view-cone where sufficient

neutrals are present. Effects of plasma profiles, camera viewing angles, neutral reflection angles and ionisation mean free path length $\lambda_{\text{mfp},i}$ must thus be considered. For a detailed discussion see Reference [113].

Since the line of sight (LOS) passes through the edge of the plasma twice and through the core, there were concerns that the camera-side emission might significantly influence the total intensity, rather than the desired target-side emission. Investigations with Edge Monte Carlo 3D code coupled to the neutral transport code EIRENE (EMC3-Eirene) by Winters [114] showed this to be a negligible error for the Carbon emission, which similarly to the Hydrogen emission originates primarily from the plasma-target interaction. These were repeated by Kremeyer for Hydrogen with the same result (unpublished).

Hydrogen is not always released from the surface as atoms but may also occur as bound molecule. Depending on the dissociation and ionisation processes these molecules undergo, only a fraction of the incoming ions will at some point occur as neutral atoms able to be excited and emit H_α light. As an example, consider dissociative ionisation (DI) of molecular Hydrogen H_2 :



Clearly, because one Hydrogen atom is ionised immediately, only half as many H_α photons as expected are observed. This is corrected for with a molecular factor, which is typically taken as 2 [113]. It changes along the line of sight, depending on T_e and n_e .

4.3. S/XB derivation

There are multiple ways in which we can estimate S/XB.

- Ratio of Φ_α and Γ with $f_{\text{rec}} = 1$ (S/XB_{eff})
- S/XB_{th} lookup using (T_e, n_e) measured by LPs

- S/XB_{th} lookup using (T_e, n_e) measured by Helium beam spectroscopy (HeBS)
- S/XB_{th} lookup using (T_e, n_e) simulated by EMC3-Eirene, potentially matched to LP and HeBS results

The first method is valid if we ensure that the flux of neutrals into the viewing cone is approximately equal to the flux out of it. This requirement ensures that there is a fixed relation of Γ and neutron flux Γ_n for each considered volume. The cosine distribution of neutral release from the surface effectively acts to smear out the H $_{\alpha}$ emission with respect to Γ . We address this by selecting region of interest (ROI) from the camera image covering the tiles surrounding the LP tips because we estimate the $\lambda_{\text{mfp},i}$ to be similar in size to the divertor tiles. We assume $Z_{\text{av}} = 1$ to determine Γ .

For the second method, LPs provide only a single value of temperature and density rather than those along the LOS necessary for integrating over space. S/XB increases near-exponentially for n_e greater than about $1 \times 10^{19} \text{ m}^{-3}$. The dependency on T_e is strongest in the region of 10 to 30 eV, but small relative to the n_e dependency. This is shown in Figure 4.1. Using a constant value for the plasma parameters is thus especially problematic if they vary in or across these bounds.

For the third and fourth method, we must define an integration volume. This can be estimated by $\lambda_{\text{mfp},i}$ using the set of plasma parameters on the surface, or more correctly obtained by integrating the ionisation probability over radial plasma profiles until it reaches some reasonably high level. The HeBS measurement is not sensitive below 10 eV, such that the profile is frequently truncated above the target, potentially not capturing part of the emission region.

We will focus on the first two methods and compare them with the others where data is available. Despite the flaws of LP-derived S/XB_{th}, comparing it to S/XB_{eff} can reveal how far plasma parameters at the excitation location differ from the surface and potentially whether other effects play a role.

The procedure will be much the same as in Chapter 3. The measurement floor of the H $_{\alpha}$ cameras is far below the typical signal level, with a determination factor $\delta_{\alpha} = 40$, such that the division of two uncertain quantities does not pose a problem. j_{sat} is determined from inferred T_e and n_e , but its consistency can be checked by examining the Current-Voltage characteristic (IV-characteristic).

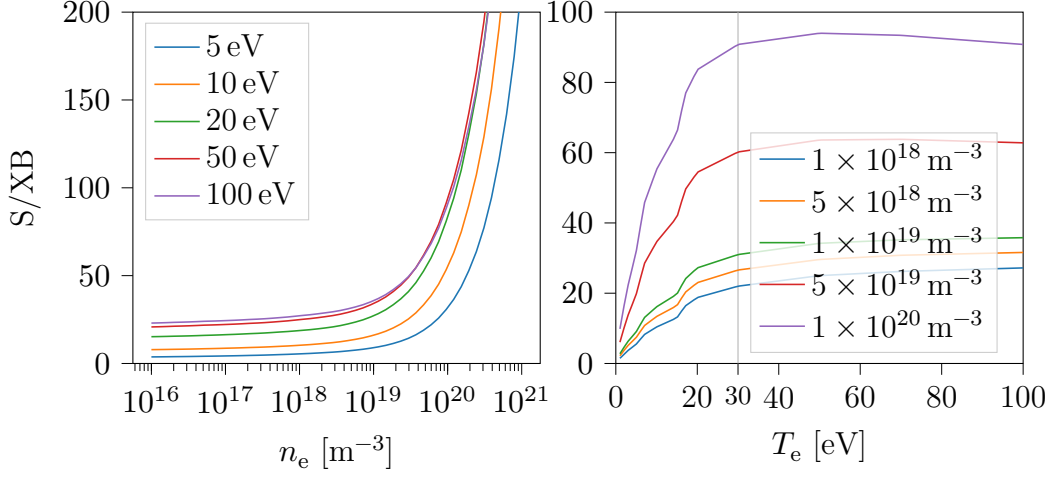


Figure 4.1.: S/XB_{th} dependency on T_e and n_e . Molecular correction $f_{mol} = 2$ included.

4.4. Results

We will examine two discharges, 20181010.010 with low line-integrated density ndl and attached divertor conditions, and 20180814.025 with high ndl and increasing radiated power fraction f_{rad} . Both were run in the 'standard' magnetic configuration in the centre of accessible space (EIM). Figure 4.2 shows a Poincaré plot of the intersection of the island with the target at the toroidal location of the LPs in that configuration.

4.4.1. Low-density discharge 20181010.010

An overview of the first investigated discharge is shown in Figure 4.3. Due to ndl in the range of 6×10^{19} to $8 \times 10^{19} m^{-2}$, the radiated power fraction f_{rad} stays below 25%. The particle flux and plasma temperature at the target are fairly constant throughout, despite the SL shift due to rising I_{tor} . Three gas puffs, at approximately 3s, 3.5s and 4s raise the density and lower the core temperature, though the stored energy remains constant.

Using the same techniques as in Chapter 3 we unify the full resolution grids of Φ_α (Figure 4.4) and Γ (Figure 4.5).

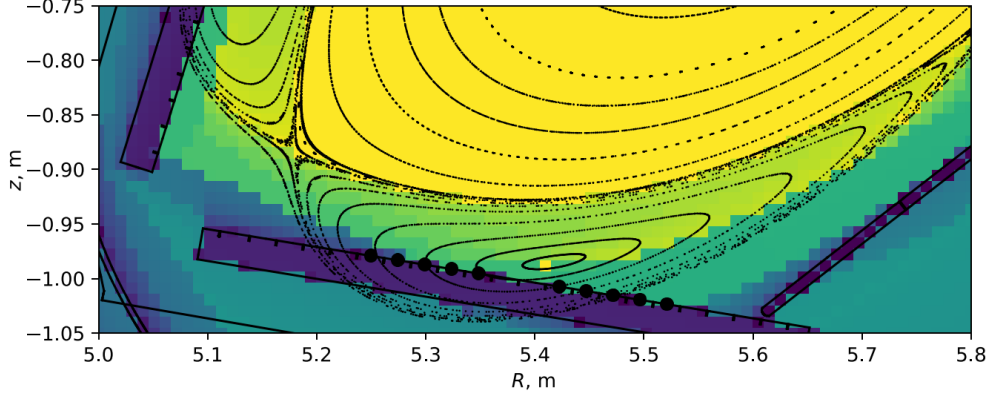


Figure 4.2.: Poincaré plot of the Lower divertor (LD) island-target intersection at the LPs location. Components and probes outlines in black, colour indicates connection length on logarithmic scale. The island o-point is at a major radius $R \approx 5.4$ m, above the gap between probe LD5 and LD6. The strike line (SL) is located at $R \approx 5.2$ m, outside the LP array. Neglecting drifts, the situation is symmetric to the Upper divertor (UD).

At each point of the unified grid, we can now calculate S/XB_{eff} , which is shown in Figure 4.6. Since unlike the γ_s , S/XB does assume a single value, but rather depends sensitively on both T_e , n_e , we need always compare it to S/XB_{th} as a reference point. Figure 4.7 therefore shows the time evolution of S/XB_{eff} and S/XB_{th} , using the LP inferred values at that position and time. Clearly there is a large difference between the two quantities, with the level of discrepancy varying strongly by location. To better distinguish trends in the data, we calculate the mode (most common value) of each time trace and scale the secondary ordinate with S/XB_{th} by the ratio of the two. This is shown in Figure 4.8. As evident by the overlap of the time traces, in this discharge with stationary heating power but increasing density, a single factor can adequately describe the deviation of S/XB_{eff} from S/XB_{th} . This factor is lowest for probes 8, 7 and 6 and increases strongly with increasing distance to the Pumping Gap (PG). Referring back to Figure 4.2, this correlates with the distance of the island and last closed flux surface (LCFS) from those probes. As we noted before, we expect the radiation location to be above the target, with the plasma parameters at the probes

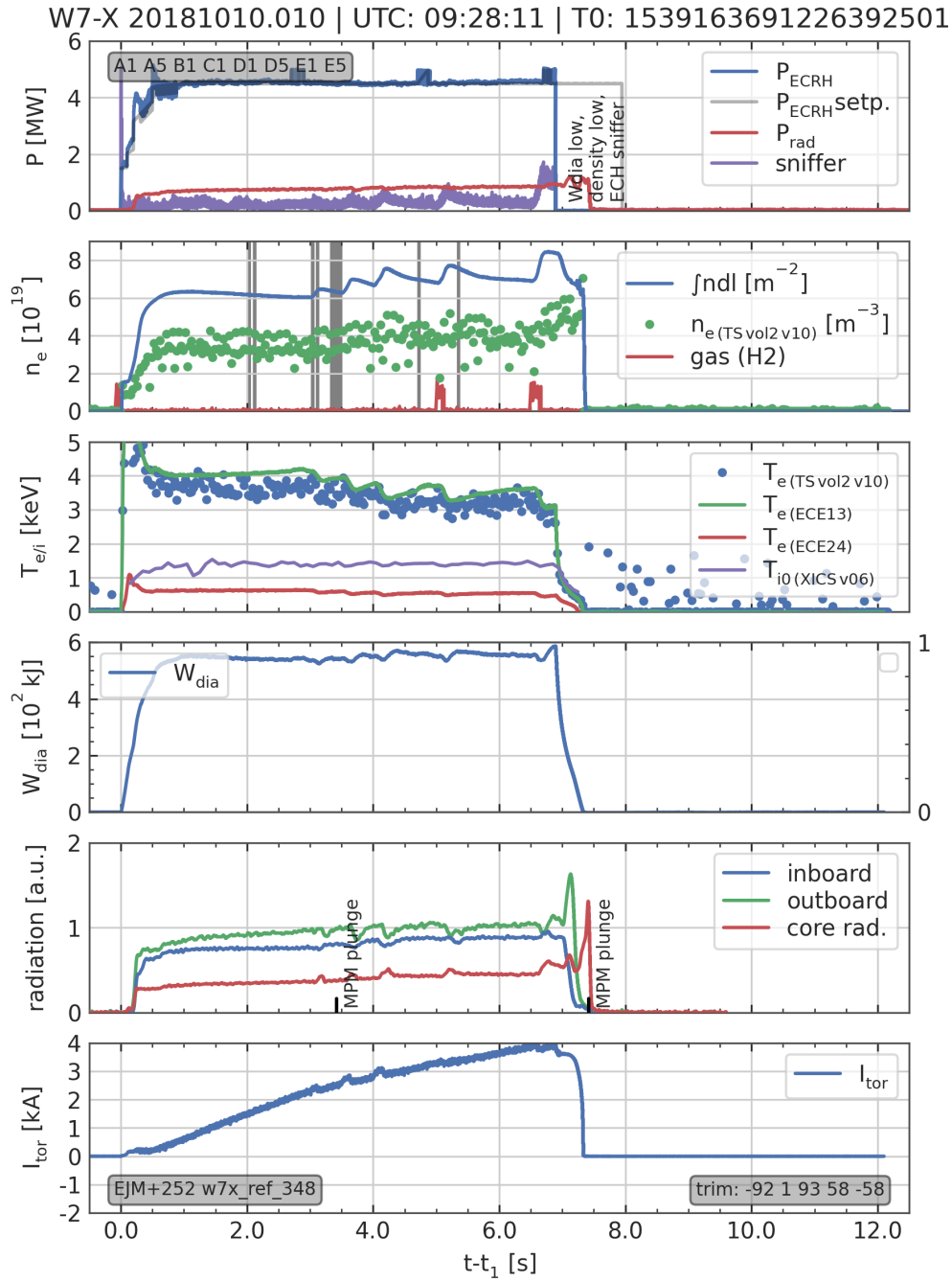


Figure 4.3.: Overview of discharge 20181010.010. References as in Figure 3.7.

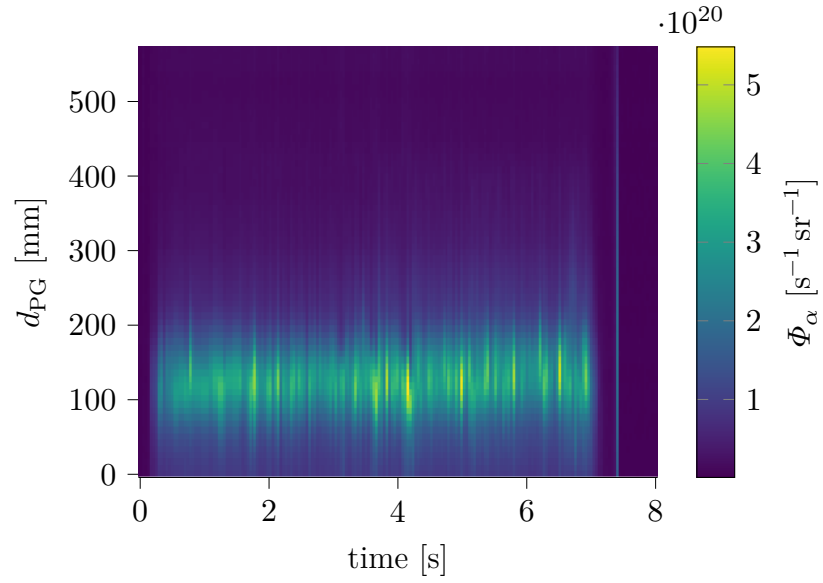


Figure 4.4.: H_α -Camera (H_α -C) data of 20181010.010 at native resolution.

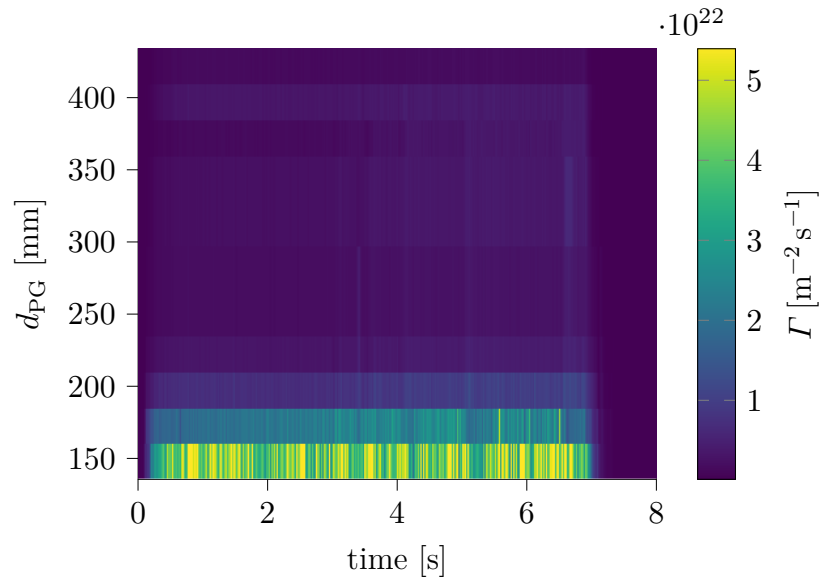


Figure 4.5.: Γ_{LP} data of 20181010.010 at native resolution. Probe 5 is missing due to a processing error.

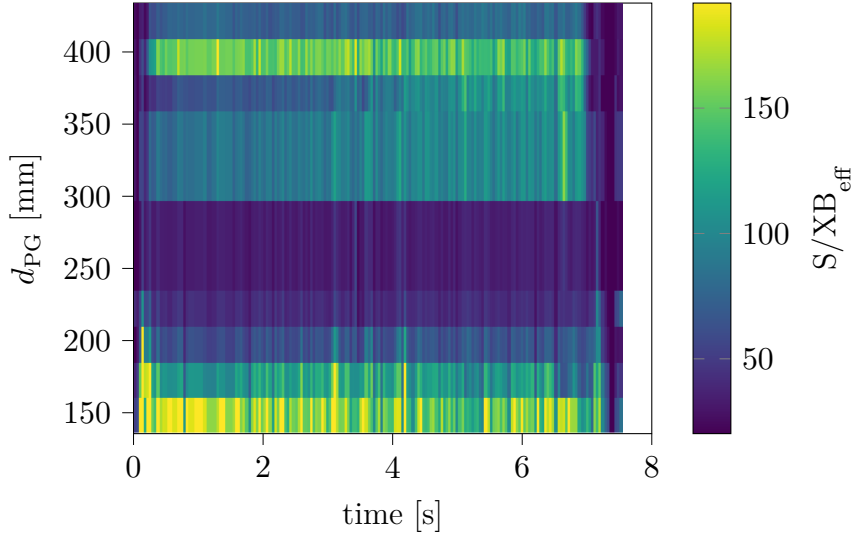


Figure 4.6.: S/XB_{eff} for discharge 20181010.010. Values in the 2nd and 98th percentile omitted for clarity.

being less relevant, the further away excitation occurs. We therefore suggest a discrepancy factor f_{prof} , defined as

$$f_{\text{prof}} = \frac{S/XB_{\text{eff}}}{S/XB_{\text{th}}}, \quad (4.3)$$

which we hypothesise is primarily related to the plasma parameter profiles.

Comparing the profiles of f_{prof} for discharges 20181010.010 and 20180814.025 (which we will discuss below) to the magnetic field topology in Figure 4.9 supports this hypothesis: f_{prof} differs markedly between either side of the o-point.

As conditions in the plasma edge do not significantly change throughout this discharge, with f_{rad} constant at a level below 25 %, it seems plausible that the radiation location stays the same and therefore also f_{prof} . Let us now apply this analysis to a discharge with greater variation in edge conditions.

4.4.2. High-density discharge 20180814.025

An overview of the discharge is shown in Figure 4.10. Through a steady

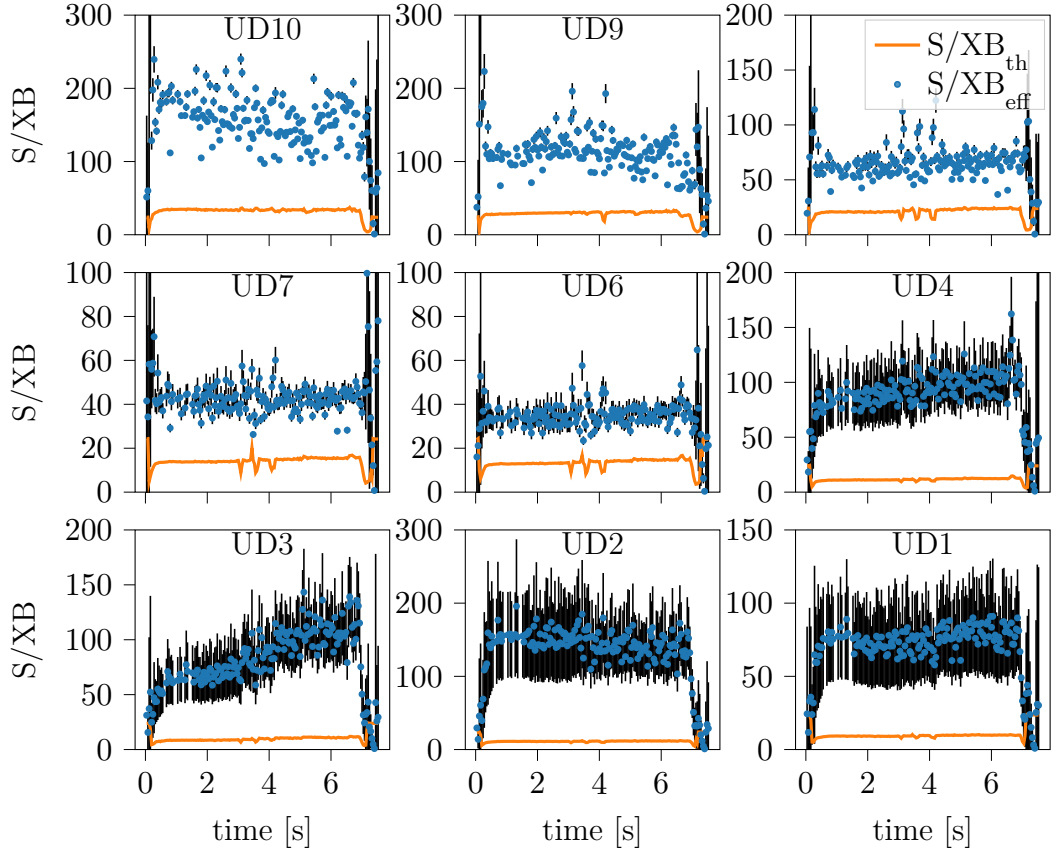


Figure 4.7.: S/XB_{eff} (blue) with error bars (black) and S/XB_{th} (orange) for each available UD probe of 20181010.010. S/XB_{th} is far below the observed S/XB_{eff} level, trends are not distinguishable. Note the different axis limits chosen for optimal readability.

density ramp to $ndl = 12 \times 10^{19} \text{ m}^{-2}$, the radiated power is increased until f_{rad} reaches approximately one. This causes a reduction of the particle and photon flux, particularly visible at $t = 6$ s in Figure 4.12 and Figure 4.11 respectively.

This reduction is however not homogenous across the profile, as we can see inspecting f_{prof} in Figure 4.13. The timetraces can be made to match with a single value of f_{prof} until approximately the interval [5, 6] s when the

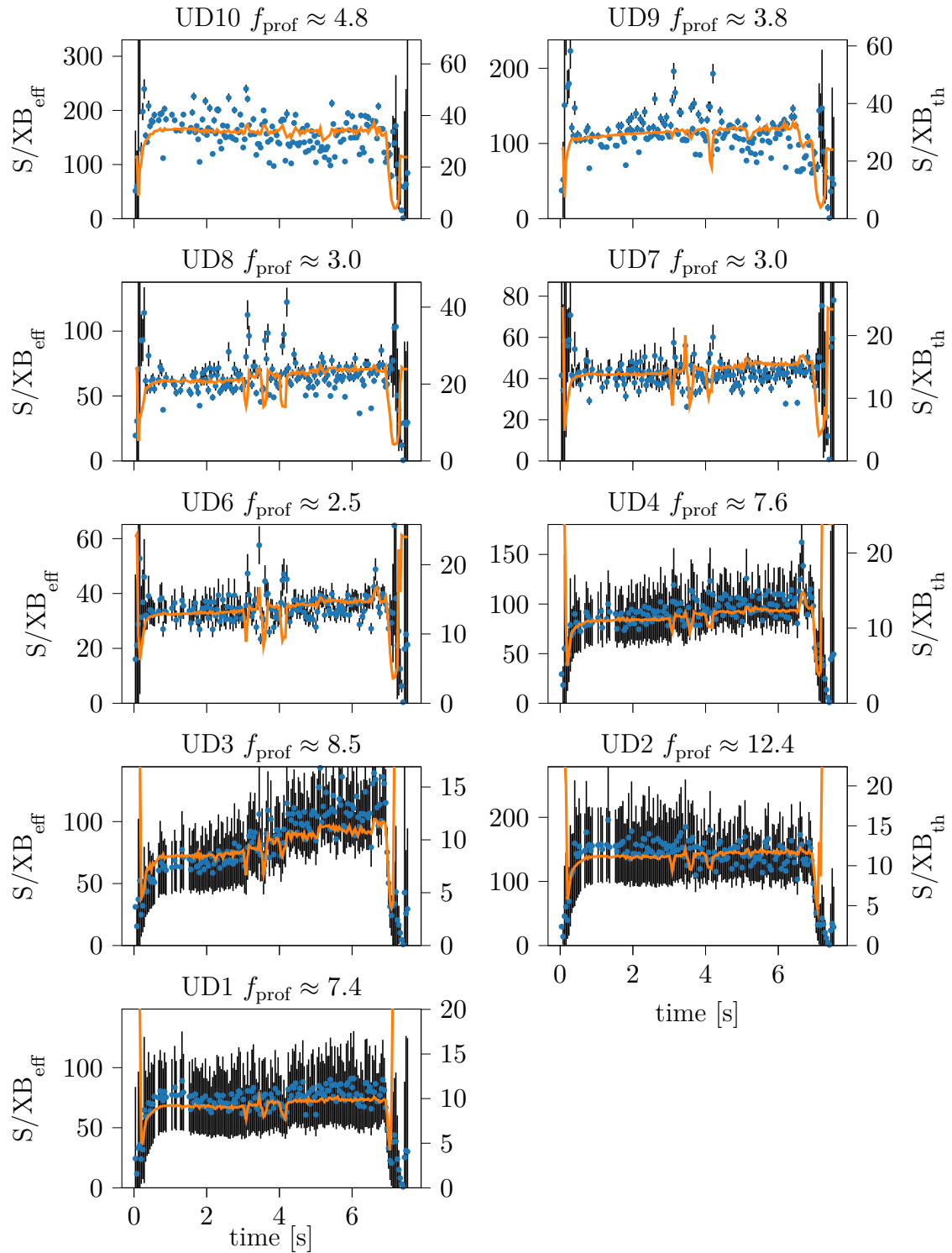


Figure 4.8.: S/XB_{eff} (blue) and S/XB_{th} (orange) for each available UD probe of 20181010.010. Axes are scaled by the most common f_{prof} value (see text).

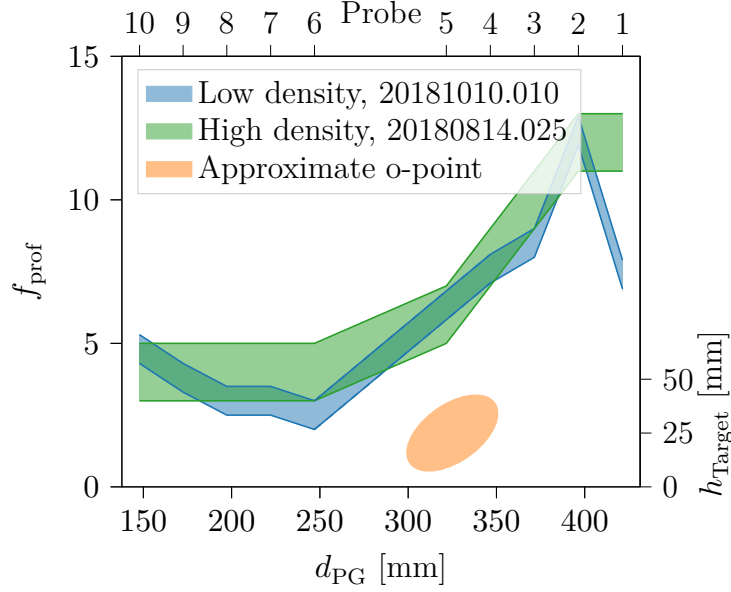


Figure 4.9.: Profiles of f_{prof} in the two examined discharges. Green and blue shaded regions show confidence intervals of f_{prof} with values on the left ordinate. Approximate position of the island o-point shown in orange, with height above target on the right ordinate. Probe 5 data interpolated for 20181010.010.

rapid change of f_{rad} occurs.

Investigating probe UD8 at 197.3 mm more closely (in Figure 4.14) we see that while Φ_α reduces fairly gradually starting at 5 s, Γ is at this time still rising. This is clearly due to the behaviour of n_e , as T_e drops almost linearly in the time window shown, whereas the density initially increases until 5.75 s and then drops rapidly. The reduction of Γ is driven mostly by this, evident by the similarity of the time traces and of course due to the $\sqrt{T_e}$ dependency. The discrepancy between S/XB_{eff} and S/XB_{th} is, however, not due to the reduction in Γ but rather the non-linear behaviour of $S/XB_{\text{th}}(T_e)$. This is illustrated in Figure 4.15, where the evolution of S/XB_{th} , if only one parameter changes and another is held constant, is examined.

An explanation for the empirical f_{prof} factor increasing is that T_e at the target drops in the non-linear range $[0, 30]$ eV whereas at the origin of the observed Φ_α , $T_e > 30$ eV and S/XB is thus insensitive. This decoupling

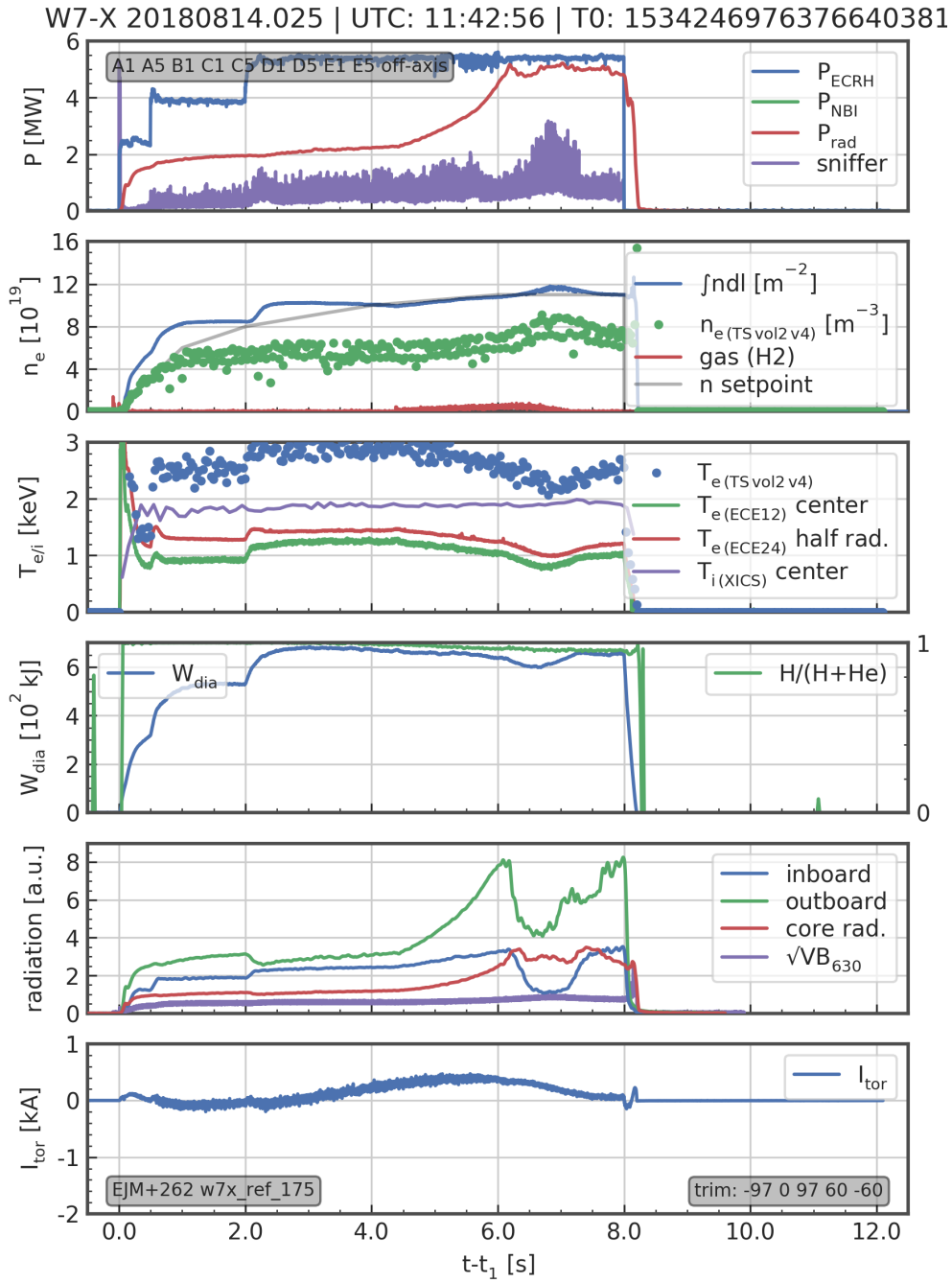


Figure 4.10.: Overview of discharge 20180814.025. References for data sources as in Figure 3.7.

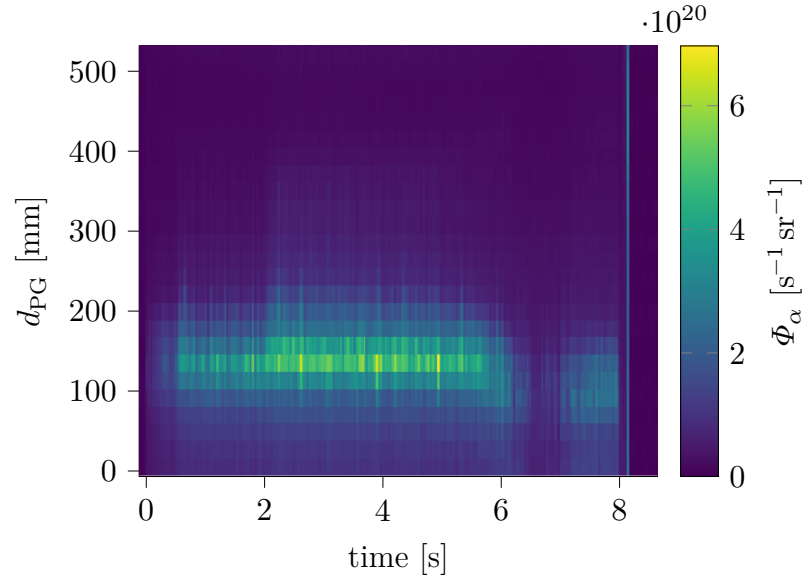


Figure 4.11.: H_α -C data of 20180814.025 at reduced spatial resolution.

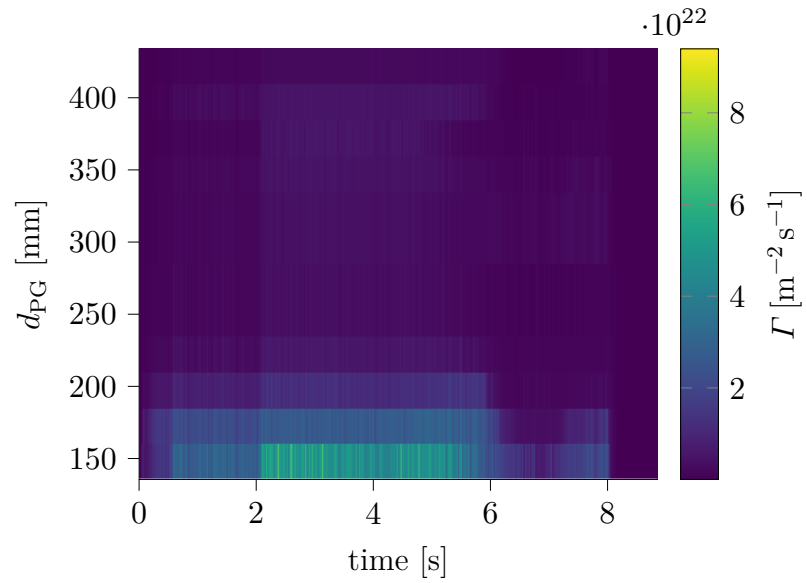


Figure 4.12.: Γ_{LP} data of 20180814.025 at native resolution.

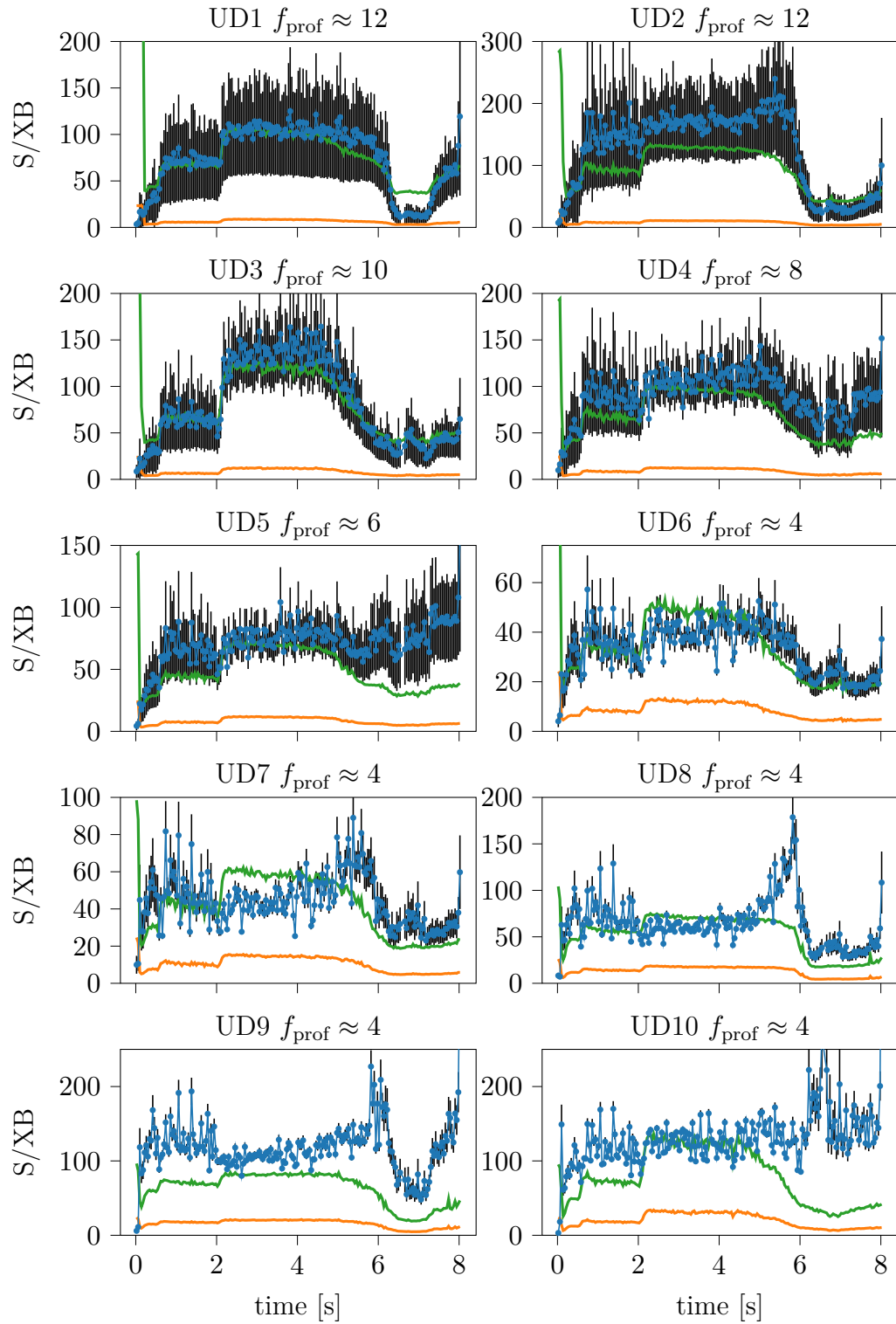


Figure 4.13.: S/XB_{eff} (blue), S/XB_{th} (orange) and approximate $f_{\text{prof}} * S/XB_{\text{th}}$ (green) for UDP1-10.

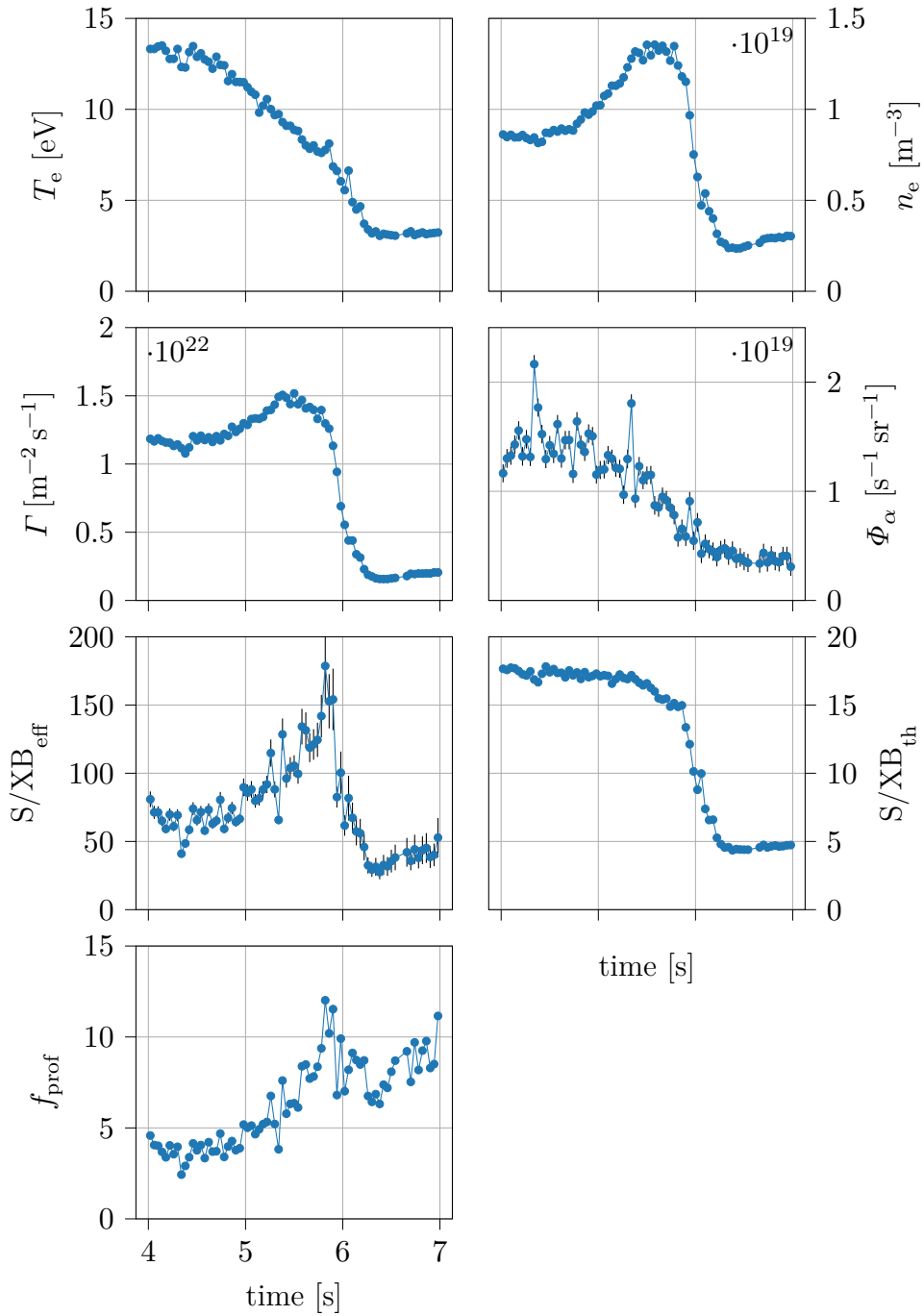


Figure 4.14.: Detail of particle flux transition of UD8. T_e drops continuously while n_e rises and falls. Γ approximately follows n_e , while Φ_α behaviour resembles T_e . S/XB_{eff} and S/XB_{th} evolve very differently.

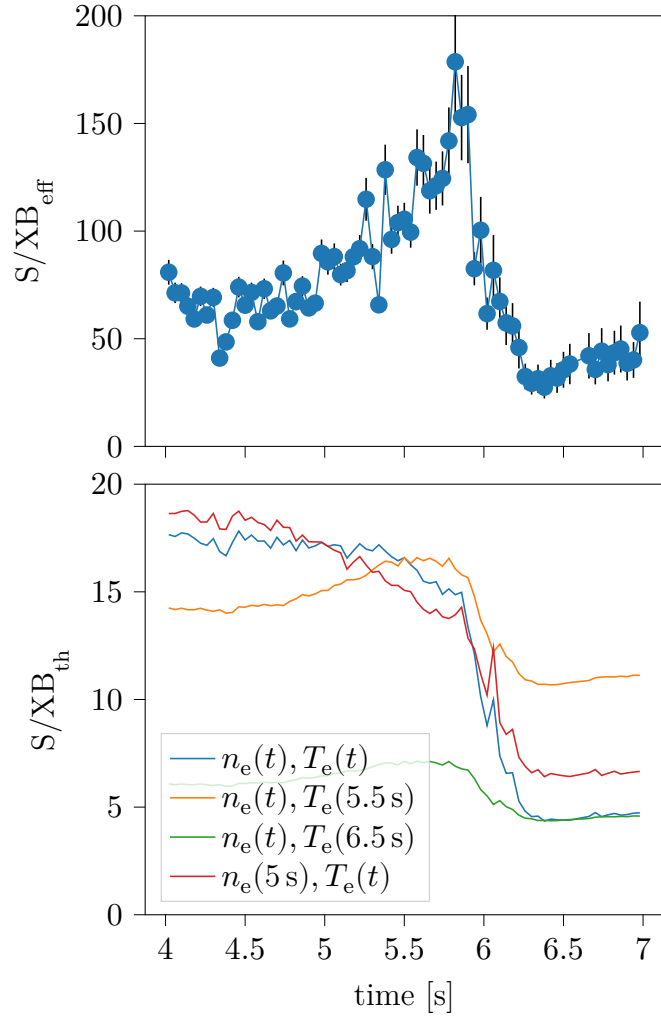


Figure 4.15.: Causes of f_{prof} time variation. Shown are S/XB_{th} using both time evolving parameters ($n_e(t), T_e(t)$) (blue) and hypothetical time traces if one parameter is fixed (red, orange, green). Most of the reduction of S/XB_{th} is due to non-linear response on temperature.

could be an indication of a detached plasma layer above the target.

4.5. Discussion

We have suggested the difference between S/XB_{eff} and S/XB_{th} may be at least partially explained by the varying profile of plasma quantities above the target and the LPs. If our initial argument that local ion flux must result in local photon flux is correct, the S/XB factor linking them must be explainable by the conditions somewhere along the H_α -C line of sight. The values of S/XB_{eff} are however not just high relative to S/XB_{th} as determined from the LP parameters, but require generally implausible parameters to be matched. A value of $S/XB \approx 200$ would imply $n_e \in [3 \times 10^{20}, 4 \times 10^{20}] \text{ m}^{-3}$ for $T_e < 200 \text{ eV}$. This is impossible given the line integrated density through the core ndl of $\mathcal{O}(10 \times 10^{19} \text{ m}^{-2})$. Higher temperatures have a negligible effect on S/XB_{th} . A scrape-off layer (SOL) profile reaching higher densities at an emission location further into the plasma can thus not be the full reason for the observations.

Possible reasons are a combination of 1. erroneous measurements, leading to an overestimation of S/XB_{eff} , 2. erroneous predictions of S/XB_{th} , causing us to doubt our measurements, or 3. incorrect assumptions. We will structure and discuss these below, with \nearrow signifying a quantity being 'too large' or overestimated and \searrow signifying it being 'too small' or underestimated:

1. $S/XB_{\text{eff}} \nearrow$ due to:
 - a) $\Gamma \nearrow$ because:
 - i. inferred $I_{\text{sat}} \nearrow$
 - ii. probe area \searrow
 - iii. $Z_{\text{av}} \searrow$
 - b) $\Phi_\alpha \searrow$ caused by:
 - i. calibration or saturation issues
 - ii. neutrals density $n_n \searrow$ because $f_{\text{rec}} < 1$
2. $S/XB_{\text{th}} \searrow$ because:
 - a) molecular factor $f_{\text{mol}} \searrow$

3. Wrong assumptions, such as:

a) local photon flux reflective of local ion flux

We will address each possible reason, and constrain what magnitude of error it might cause. Based on the best matching timetrace shown in Figure 4.8, a conservative estimate is for all effects to accumulate to a factor 2.5.

Addressing Item 1a and recalling

$$\Gamma = \frac{I_{\text{sat}}}{A_{\text{proj}} Z_{\text{av}}} \quad I_{\text{sat}} = A_{\text{coll}} e n_e \sqrt{T_e} c'_s, \quad (4.4)$$

where c'_s is a constant containing the dependencies on γ_i , T_i , etc., any of the terms may be a source of error.

Item 1(a)i: Depending on the model used for analysis, the inferred T_e and n_e can vary significantly, changing I_{sat} by up to 50 % (see Table 2.6 in Section 2.6.4). As is described in that chapter, the recorded IV-characteristics do not saturate, so I_{sat} can not be determined independently of the model inference. The values chosen for the factors in c'_s , can contribute a factor of 2. In EMC3-Eirene simulations to reproduce Φ_α , Feng for example uses a factor $\gamma_i = 1$ rather than our preferred value of $\gamma_i = 3$ (see Section 2.4). The analysis of the LPs was extensively checked, so an error of the required size seems unlikely.

Item 1(a)ii: The determination of the area relevant here does not depend on the Langmuir model, but only on the geometry of the probes. We are interested in the current density in the vicinity of the LP, so we use the determined plasma parameters and apply them in the calculation of the local Γ . While the magnetic field incidence angle plays a role for the projected area, and is simulated assuming a constant vacuum field, the probes tips were specifically designed such that the area A_{proj} was robust to small misalignments or incidence angle changes. An underestimate of A_{coll} relative to A_{proj} , through stronger sheath expansion, is conceivable.

Item 1(a)iii: Near the targets $Z_{\text{av}} > 1$, is certainly possible. To our best knowledge, values as high as 2 have not been reported.

Overall it can be said of Item 1a that we have shown in Chapter 3 heatflux measurements of the LPs and Infrared-Cameras (IRCs) to match within expectations. A systematic error of Γ of 2 or more would be hard to reconcile with this.

Item 1(b)i: Considering possible errors in the evaluation or calibration of the H_α -C is beyond the scope of this thesis. Further comparisons, by looking at Φ_α due to the injection of a known quantity of gas and comparison with H_γ observations, indicate that the H_α -C measurements are correct [115].

Item 1(b)ii: We have assumed $f_{\text{rec}} = 1$ and therefore a direct relation between the number and density of neutrals and ion flux. However that constraint was determined globally for the entire machine. There are likely local variations of f_{rec} , for instance due to depletion at frequently loaded regions of the targets, or through additional gas fuelling and released from heated plasma facing components (PFCs). These processes do occur, in these discharges specifically through the afore mentioned Hydrogen puffs and generally as shown by Reference [14]. This might reduce n_n , and therefore also the emission intensity.

Neutrals could also enter or leave the ROIs into areas with different neutral and/or ion fluxes. As the examined discharges are in the EIM configuration, the highest Γ at SL is not captured by the LPs. It depends on $\lambda_{\text{mfp},i}$ how far neutrals might smear out the spatial correlation of Γ and Φ_α . This question is being investigated using EMC3-Eirene by Feng *et al.*. Measurement of the neutral density is currently only accessible by pressure measurements at the machine midplane and below the divertor [14]. Preliminary analysis, using the methods of that reference shows that there is continuous outgassing of the wall throughout 20181010.010. Stronger gas release from those parts of the divertor that are weakly loaded and thus not 'cleaned', i. e. those further from the PG might explain the distribution of f_{prof} seen in Figure 4.9. Alternatively, a relatively homogenous contribution of additional neutrals would, through a constant offset, be most visible at locations of low Γ , also consistent with that observation. A Laser induced fluorescence (LIF) system is being developed for W7-X and could shed light on the neutral density and temperature above the divertor target [112].

Item 2a: We have applied $f_{\text{mol}} = 2$ everywhere, despite Reference [113] showing that it varies with r_{eff} and the contribution can be larger or smaller. The proximity of the relatively cold Carbon divertor might also lead to the formation of organic molecules with higher numbers of Hydrogen atoms. To explain a factor 2.5 difference however these would have to be present in a sufficiently high concentration which would have been recognised by the Diagnostic residual gas analyser (DRGA) system. Furthermore these molecules would need to ionise without intermediate neutral atomic hydrogen

stages to 'remove' neutrals from the emissive population.

Finally, a violation of the assumption Item 3a of local Φ_α being reflective of local Γ is a possible explanation. Our simple model of assuming full ionisation of neutrals within one $\lambda_{\text{mfp},i}$ may be insufficient.

4.6. Further work

Efforts have been made by a group of Kremeyer *et al.* to investigate this problem further with the analysis of additional discharges and diagnostics, dedicated EMC3-Eirene simulations and improved $\lambda_{\text{mfp},i}$ estimates from the divertor spectroscopy diagnostic and HeBS [115]. This effort is important in view of long pulse, gas balance steady state operation in fulfilment of W7-X goal of demonstrating Stellarator power plant viability for which recycling fluxes must be well understood. It also prepares for the challenging task of understanding gas and radiation balance after an envisioned upgrade of W7-X to a full metal machine with Tungsten PFCs.

A possible future project might be to use *Minerva*, with a more rigorous approach to the measurement network idea outlined in Chapter 1, to infer plasma parameters at the edge for the entire field of view of the IRC and H_α -C systems. Through the different T_e dependencies of q and Γ , as well as dependencies of γ_s and S/XB, together these diagnostics provide non-parallel constraints on the possible T_e and n_e at each point on the wall. Challenging is the smearing out of information contained in the Φ_α measurements by a kernel whose dimension depends on $\lambda_{\text{mfp},i}$, such that the resulting spatial resolution would necessarily be much coarser than that of either diagnostic. Additionally, LOS plasma and neutral profiles complicate the interpretation of Φ_α and changing plasma wall interaction (PWI) and thermal properties of wall components, as well as reflections, that of q_{IR} . This approach would likely need to be supplemented by EMC3-Eirene simulations and could be locally validated using the LPs, in the manner we started here. As a benefit it would offer a measurement coverage of the wall infeasible to match with LPs in a non-axisymmetric device.

Should the problem lie mainly with the LPs, this comparison would have achieved what it set out to do: to identify problems by verifying the consistency of overlapping measurements.

5

Langmuir probe measurements of plasma detachment in W7-X

The term detachment derives from the phenomenon that, given certain conditions, the heat and particle flux streaming towards a plasma facing component (PFC) does not reach it but is intercepted by a dense layer of gas. This layer radiates away much of the power which would otherwise impact the PFC, thus giving the appearance of a 'detached' glow above the target. Detachment is desirable because it strongly reduces the heat and particle flux impacting the target, otherwise foreseen to reach unsustainable levels in larger machines. In the case of heatflux, unsustainable implies exceeding the capacity for cooling, such that parts of the PFCs might melt or evaporate. Any particle flux will cause some erosion, so sustainability here implies a long timescale before limits of material damage and dust formation necessitating PFC replacement are reached. Because flux reduction is the sought after result, any edge regime achieving it is grouped under the label 'detachment', even if the physical processes causing it might differ or contribute to varying degrees. In addition to handling heat flux, pumping of neutrals and retention of impurities must be maintained. Therefore not all detached scenarios are equally favourable but instead multiple requirements must be considered.

To persistently reduce the power to the divertor at constant heating rate, energy must be dissipated through radiation and distributed over a much larger area, ideally the entire wall. The potential of spreading the heatflux in this way can be intuitively understood through the ratio of the wetted area in attached state of 1 m^2 [25] to the total first wall surface area of 223 m^2 [109].

Since we have rarely observed temperatures sufficiently low to allow volume recombination of hydrogen, the radiating species must be predominantly impurities such as carbon and oxygen. To generate a concentration of these impurity particles, they must be sputtered from the wall or injected. The number of sputtered particles is equal to the particle flux times the sputtering yield plus a contribution from fast exchange neutrals. The Langmuir probes (LPs) can contribute valuable information about the local ion flux Γ as well as the local temperature relevant for the sputtering yield. For a desired level of radiation, we need a) a certain concentration of radiators, and b) the right temperature, determining the radiation power $\frac{P_{\text{rad}}}{V * n_e * n_{\text{imp}}}(T_e)$.

In the experiments we describe, carbon is the main radiator, as expected considering the graphite PFCs. This was not the case pre-boronisation when oxygen was more important, as shown for instance by Zhang *et al.* [116][Fig.5]. After boronisation, oxygen and other impurity contributions were strongly reduced, see References [20][Fig.8] and [117][Fig.6,7]. This is further supported by the observations of the divertor spectroscopy which consistently shows a radiating carbon layer close to the divertor that detaches as the edge cools ([98][Fig.11] and [118][Fig.5]). It has not been possible so far to make an absolute radiation balance to attribute a power fraction to individual spectroscopic lines, though this is being planned by Krychowiak *et al.*. The carbon concentration measured by beam emission spectroscopy on the neutral beam injection (NBI) is consistent with Z_{eff} measurements, indicating that only trace amounts of (non-carbon) high-Z impurities are present in the plasma [119].

The radiation power of carbon decreases by two orders of magnitude from a maximum of $8 \times 10^{-32} \text{ W m}^3$ at 10 eV to a local minimum of $3 \times 10^{-34} \text{ W m}^3$ at 80 eV [120][Fig.12.3]. This corresponds to the typical temperature difference observed in the transition to detachment. The gradient of the radiation power has important implications for the stability of detachment, as a negative slope w. r. t. T_e as in the interval [10, 80] eV means that cooling begets more cooling and thus an unstable situation. A positive gradient as for [80, 110] eV on the other hand implies that an increase of T_e causes stronger radiation, more cooling, and stabilisation. Here, the LPs can contribute T_e data, however as we have seen the radiation is not generated directly at the surface. Possible causes of temperature reduction triggering strong radiation will be discussed in the examples below.

5.1. Outline

Developing a general theory of detachment in Wendelstein 7-X (W7-X) is far beyond the scope of this thesis. This ongoing process requires repeated and coordinated efforts at

- combining measurements of different quantities,
- checking and improving the consistency of independent measurements of the same quantity,
- simulating effects of changes in isolation and self-consistently,
- evaluating and describing experiments.

All these efforts will contribute to an increasingly wide, deep and robust understanding of the causes and effects of PFC heat flux reduction. The LPs can serve as one column supporting the overarching goal. We therefore will describe a database of observations and phenomenologically compare experiments, linking to plausible explanations and models as far as they are currently known and developed. Some of these discharges have been studied before and in many cases LP data was included in the publication of those studies [20, 98, 121]. We will describe LP measurements of different divertor regimes and then consider which mechanisms could lead to the observations, rather than positing a mechanism and looking for examples.

Our focus will be on the strike line (SL) due to it being the region of highest flux and therefore most critical to divertor operation. As mentioned in previous sections, the low iota magnetic configuration (DBM) configuration is best suited to investigations with the divertor LPs because the probe array covers the SL.

Another reason why a series of experiments will be described is that multiple operational strategies to achieve detachment were found during operation phase (OP) 1.2. This finding implies that the beneficial operating regime of detachment is a stable and natural state for the plasma to evolve to, rather than an extreme, unstable regime that can only be reached on specific paths and must be maintained through feedback control. This property makes it harder to describe a common principle, but is very promising for the outlook of island-diverted helical advanced stellarator (Helias) for the future. If this stability is both well understood and a consequence of

properties that can be retained in future machines, it would be a great advantage over competing designs.

The next Section 5.2 will introduce the key method used for the investigations in this chapter, parametric fits to the LP profiles. Section 5.4 will compare two discharges in detail to understand what machine-wide conditions cause a transition to a detached state in this case. Section 5.5 will further focus in on the key 200 ms of that transition. Section 5.6 attempts to identify the nature of fluctuations observed prior to and during that transition. Finally Section 5.7 considers a different discharge for which the cause of power detachment is more challenging to establish and the final state more unstable.

5.2. Reduction and parametrisation

To describe the wealth of available data succinctly, we parametrise them using an appropriate phenomenological model. In terms of the model qualities introduced in Section 2.3 we require simplicity and accuracy to reduce the amount of data while losing as little information as possible. The data in question are as before the LP inferred quantities, T_e , n_e and V_f , as well as the derived quantities, particle flux Γ , electron pressure p_e and heat flux q_{LP} and q_{IR} . These are available at ten positions, which can be described by a distance to the divertor pumping gap, and at a sampling rate of up to 1 kHz. In the spatial domain we want to preserve at least the following features of the SL:

- Amplitude, to monitor reduction or increase,
- Peak position, to follow for instance shifts caused by magnetic configuration changes,
- Width, to capture heat flux spreading.

The SL profile on the horizontal target is typically unimodal and asymmetric, so we will require an according function. Occasionally observed secondary peaks in the profile cannot be resolved sufficiently well by the LPs to distinguish and robustly fit them. While distribution functions such as a β or γ distribution can fit the profile well, their parameters are not intuitive and easy to interpret. The same is true for higher statistical moments of

the distribution such as skew and kurtosis, especially when these moments change in concert rather than isolation. These would be needed, however, in addition to mean and standard deviation to describe the data with sufficient accuracy.

We therefore choose a double gaussian (DG) or split normal distribution, described by

$$f(x; \mu, \sigma_1, \sigma_2) = \begin{cases} A \exp -\frac{(x-\mu)^2}{2\sigma_l^2} & \text{if } x < \mu \\ A \exp -\frac{(x-\mu)^2}{2\sigma_r^2} & \text{otherwise.} \end{cases} \quad (5.1)$$

The parameters $A_Q, \mu_Q, \sigma_{l,Q}, \sigma_{r,Q}$, where Q refers to any of the above listed LP inferred or derived quantities, fulfil our requirements and are intuitively interpretable while the functional form provides sufficient flexibility. The examples shown throughout this chapter suggest that profiles can, in most situations, be fitted well by this function (Figures 5.6, 5.7, 5.9, 5.12 and 5.16) and we understand the conditions under which the fit fails (Figure 5.11). We will therefore not evaluate the appropriateness of this chosen fit function in detail or do a rigorous evaluation of the fit quality.

The expected distribution of q_{LP} and Γ is an interesting and in our case unresolved question. For tokamaks it is typical to model the SL as parallel flux along the last closed flux surface (LCFS), spread by diffusive perpendicular transport and flux expansion [122]. This results in the poloidal distribution on the divertor being a normal distribution, convoluted with the upstream power decay profile. A similar analytical model is not applicable to island divertors because of the more complex topology.

In a second method which was developed, but ultimately not used, a DG fit is first performed to q_{IR} . We then select at each point throughout the discharge the probe closest to $\mu_{q_{\text{IR}}}$ as representative of the SL. An example illustrating the shortcomings of this method is given in Figure 5.1. Firstly, the DG fit must not fail because, for example, the assumption of a single peak in the profile is not fulfilled, or q_{IR} is below the noise level. Secondly, there must be a probe close enough to $\mu_{q_{\text{IR}}}$ for the representation to be accurate. Thirdly, the possibility of erratic jumping between different probe time traces makes the resultant reduction hard to interpret.

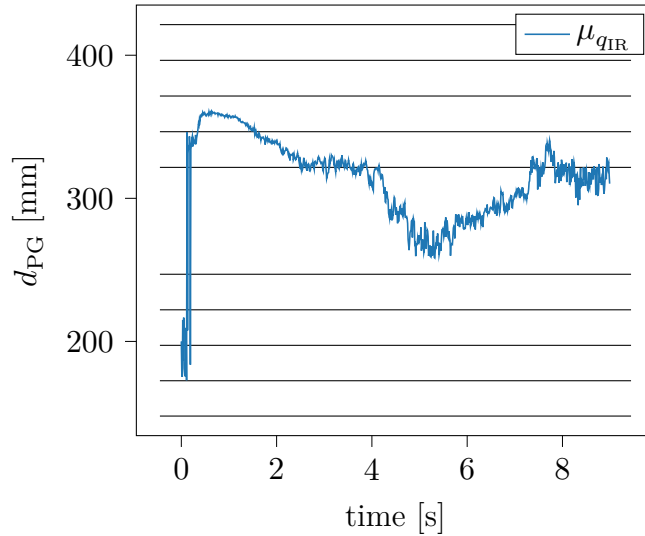


Figure 5.1.: The position of peak heat flux q_{IR} , as derived from fitting a DG to the Infrared (IR) data, is shown as a function of time. The positions of the Langmuir probes are shown as black lines. At each time point the closest probe to the SL can be selected as representative. The ambiguity in the phase from 4 to 7 s illustrates the problems of this probe selection method (see text).

5.3. SL position and movement

The coil system of W7-X in principle offers the possibility of continuously modifying the magnetic field by changing coil currents [123]. In practice, discretised points in this space were defined and a finite number of them used in experiments. Perturbative excursions from these configurations were made using the non-superconducting trim and control coils. While part of the optimisation goals of W7-X was to make the magnetic configurations stiff with respect to plasma pressure and profiles [124], the toroidal plasma current has a marked effect. This toroidal current I_{tor} consists of a bootstrap current I_{bs} , initially shielded by induced mirror currents in the conducting plasma, which decay on the approximately $10\text{ s } L/R$ timescale of plasma inductance L and resistance R . While quasi-isodynamicity of the magnetic field, which if fully achieved would preclude the existence of a bootstrap current I_{bs} , was another optimisation goal of W7-X, this could in practice

only be realised approximately on a single flux surface. A small, but non-zero, equilibrium I_{bs} remains [125]. Nonetheless, because of the low shear profile of ι , relatively small changes in the plasma current can modify the position of the edge island chain, to which the divertor is fitted. An increase of this current, typically on the order of a few kA, causes this island chain to shift inwards to smaller minor radii. This in turn moves the SL on the low iota horizontal target segment outwards in major radius, away from the pumping gap. We will not discuss the SL movement on other parts of the divertor here since Langmuir probes are only installed in this segment. As the SL is the region of greatest heat and particle flux, it is the prime concern for detachment. We would thus prefer to analyse discharges run in configurations in which the SL lies on the LP array, such as the low-iota configuration DBM. Depending on the physics under investigation, the most appropriate configurations were chosen for each series of experiments, e. g. configurations with different magnetic well depth for studies of passing and trapped particle fraction. Many diagnostics were adapted to the 'standard' magnetic configuration in the centre of accessible space (EIM), but due to the construction of the test divertor unit (TDU) this was not possible for the LPs (see Section 2.2). The EIM configuration was frequently used for plasma edge studies, so most detachment examples are from this configuration, in which the SL lies closer to the pumping gap, but not on the LP array. Fortunately for us, the equilibrium bootstrap current in EIM is comparably large because this configuration primarily targets low neoclassical transport, such that in longer discharges the SL is moved towards the LPs. By using the observations of the Infrared-Camera (IRC) system we can monitor this movement precisely and know the distance of the SL from the probes [126]. Unfortunately for us, the transition to detachment causes a reduction and possibly sign change of I_{bs} . Again I_{tor} changes slowly on the L/R timescale, presumably resulting through the same effects as described above in a slow SL shift towards the Pumping Gap (PG). This is much harder to monitor as in detachment the heatflux at the SL is often reduced below the IRC noise threshold of 150 kW m^{-2} (cf. Chapter 3). On timescales much shorter than L/R we can assume the magnetic separatrix strikepoint on the target to be unchanged and meaningfully compare measurements before and after the detachment transition.

Unpublished work by Dinklage shows that changes to the T_i and T_e profiles may be responsible for the reduction of the current during detachment.

Whether this is the full reason is not yet clear, because the electron cyclotron current drive (ECCD) contribution to I_{tor} is very challenging to calculate in high $nd\ell$ discharges. This is due to those discharges being heated by electron cyclotron resonance heating (ECRH) in O2 (second harmonic ordinary mode), which is not fully absorbed but converted to X2 (second harmonic extraordinary mode) and reflected multiple times, requiring power deposition calculations of the reflected beams. ECCD currents for all discharges are thus not readily available yet.

5.4. Inter-shot comparison of detachment

One broader goal of analysing individual detachment discharges is of course to understand the controllable discharge conditions that induce it, such as heating and fuelling level.

To better understand the transition into detachment we will follow Bacon's method^I, and compare the discharges 20181004.023 and 20181004.024. As shorthand in this chapter, we will label discharges 20181004.023 and 20181004.024 as D#23 and D#24 respectively. Both are in the DBM configuration and at comparable densities and heating power, but while the former did not detach, the latter did. Figure 5.2 shows the line integrated density measurement of the interferometer [90] $\int n_e d\ell := nd\ell$ of the first seconds of each discharge, as well as P_{ECRH} , P_{rad} and W_{dia} . We choose these discharges because they are in the low-iota configuration in which the LPs can resolve most of the SL profile.

The evolution of $nd\ell$ in both discharges is remarkably similar. n_e at the divertor is typically closely related to $n_{e,\text{lfs}}$ [128] whereas it is not necessarily closely related to $nd\ell$ which integrates over a potentially very different profile. In our case however, both discharges are in the same configuration, fuelled the same way and without pellets, and heated purely by ECRH. There is therefore little to suggest the profiles should differ much, since none of the factors are present that have been shown to strongly influence profiles in W7-X (NBI-heating, pellet fuelling, configuration change [129]).

^IFor understanding the phenomenon of heat, according to Strevens: '[First] assemble all positive instances of heat. [Second,] for each positive instance, find similar circumstances in which heat is absent. [Third,] assemble all the ways in which heat varies with other quantities.' [127]

The configuration of both discharges is modified by ECCD, but in the time window $t = [0, 3]$ s under consideration, the toroidal current $I_{\text{tor}} < 1$ kA, so the modification is small. As direct measurements of $n_{e,\text{lcf}}s$ are not continuously available, we use ndl as a proxy related by some unknown, constant profile factor.

The time traces of P_{ECRH} are identical but for a constant amplitude factor of 1.22. This will certainly affect the power balance of the discharge and thus detachment, but we will argue that the main reason is another.

Note that the level of P_{rad} in 20181004.024 (D#24) is hard to reconcile with the other observations. Despite P_{rad} exceeding P_{ECRH} by a factor of 3 in the window $[1.5, 2.7]$ s, ndl stays constant and W_{dia} is increasing. An explanation might be a problem in deriving P_{rad} from the measurements of the individual bolometry channels, for example due to a localised radiation zone directly in front of the horizontal bolometry camera from which this time trace is generated. Such radiation filaments are visible in camera images at the relevant time, such as in Figure 5.3, but appear only intermittently. The same calculation performed for the vertical bolometry camera shows the same behaviour, so this explanation would have to invoke two localised radiation zones at just the right locations. According to the diagnosticians the results look like there may be a radial offset of the tomography geometry, but this has been excluded by phantom reconstructions [130]. For now we assume P_{rad} to be scaled by some unknown factor in the mentioned time window.

Stored energy W_{dia} tracks ndl in both discharges, until during the transition into detachment of D#24 from $t = 1.3$ s to 1.5 s it reduces by about a third, whereafter during the detached phase, W_{dia} evolves at a lower level, but similarly in time, as D#23.

The IRC total divertor loads in Figure 5.4 shows clearly that there is a transition phase in D#24, followed by complete power detachment on all observed divertors, whereas D#23 stays attached.

To see this transition in the LP data, we will use the parameters of the DG fits. Due to the five-dimensional dataset (Table 5.1), we will not graph all the relationships at once. To concentrate on detachment, we will at first neglect the asymmetry between the upper and lower divertor, consider only the former and discuss how the latter differs at a later point in this thesis. The quantities are examined in the order q_{LP} , n_e , T_e to first establish contact to the q_{IR} data and then see how the heat flux profile and evolution come

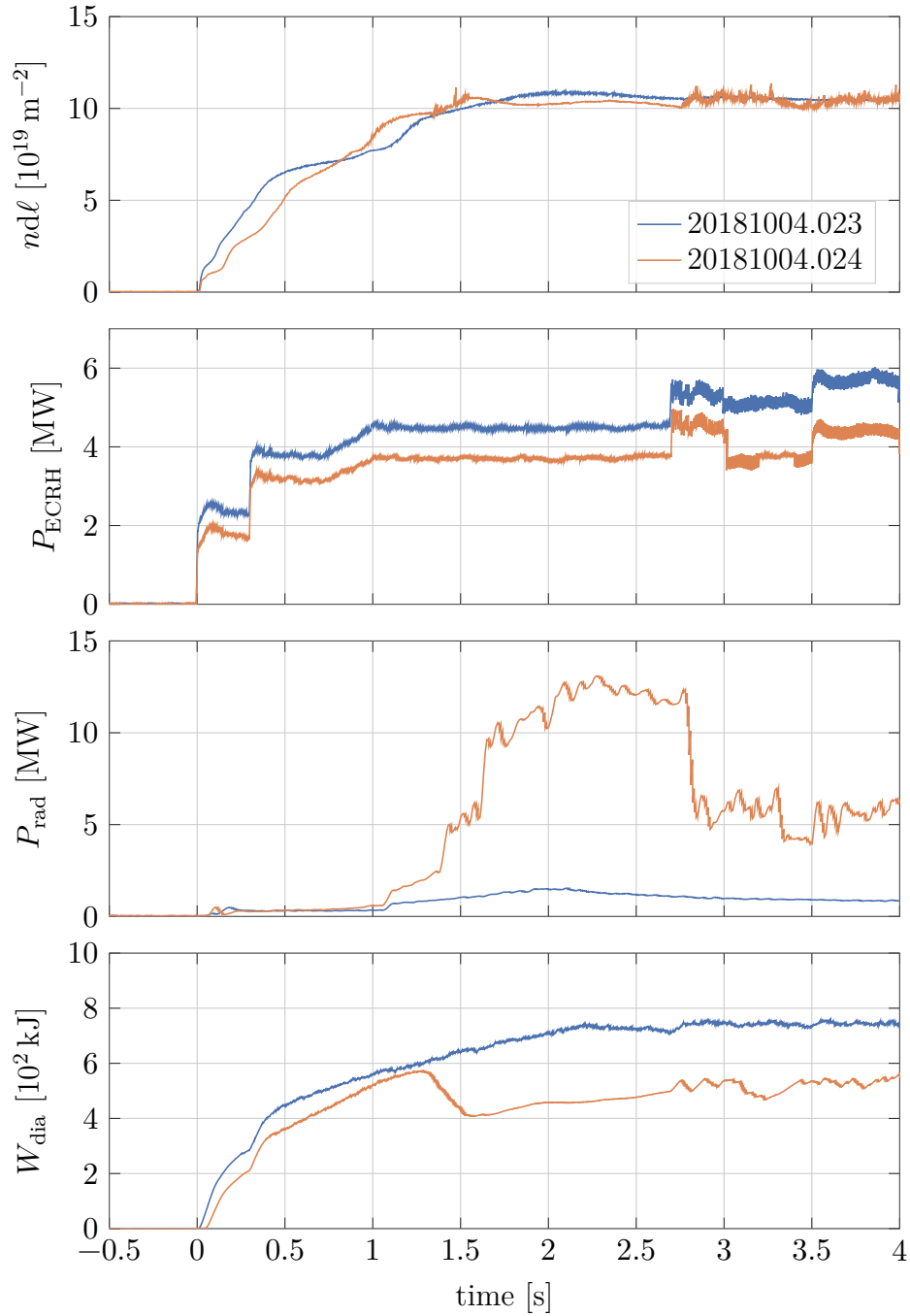


Figure 5.2.: Global plasma quantities for the first seconds of 20181004.023 (D#23) and D#24. P_{rad} in the former discharge is implausible, see text for discussion. The similarity of these global quantities across the two discharges (disregarding P_{rad}) contrasts with the differences shown in Figure 5.4.



Figure 5.3.: Visible spectrum camera frame from AEQ51 port onto half module 51 divertor in 20181004.024 at $t = 1.34$ s. Bright region at centre-right of image is the vertical divertor target. Radiation band extends further along field lines (FLs) beyond divertor to bottom-right of image. At centre-left, bands of radiation above the wall are visible. Black line in centre indicates profile analysed in Figure 5.13.

about. The time dimension has been smoothed by a centred rolling average over 10 samples.

Figure 5.5 shows, as expected, that the Upper divertor (UD) q_{LP} profiles are very similar in both discharges until the detachment transition. During the transition around 1.5 s, the fits become unreliable for D#24, but stabilise afterwards as can be seen in Figure 5.6. It is therefore clear that the SL broadens. Taking into account the correlation, the average sum of $\sigma_{l,q_{LP}}^{UD}$ and $\sigma_{r,q_{LP}}^{UD}$ increases by 50 % from (124 ± 13) mm in $t = [0.2, 1.2]$ s

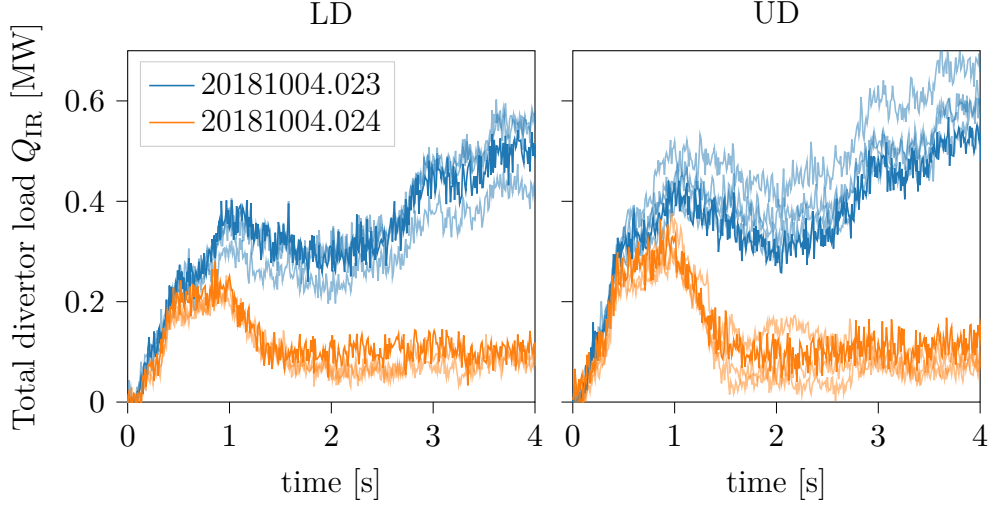


Figure 5.4.: Total divertor loads for the first seconds of D#23 and D#24. Time traces of module 3 are available for both UD and LD and highlighted, other available traces shown semi-transparent give an indication of variation.

Table 5.1.: DG fit dataset dimensions and coordinates.

Dimension	Coordinates
program	D#23, D#24
component	Upper divertor or Lower divertor
quantity	n_e, T_e, Γ, q_{LP}
DG parameter	$A, \mu, \sigma_l, \sigma_r$
time	$[0, 3]$ s (500 Hz)

to (180 ± 34) mm in $t = [1.6, 2.6]$ s. Profiles of q_{IR} at the same time points are shown for comparison in Figure 5.7. The fit parameters at $t = 1$ s are compared in Table 5.2 and match reasonably well. Differences in μ_q^{UD} and the similarity of $\sigma_{l,q_{IR}}^{UD} \approx \sigma_{r,q_{LP}}^{UD}$ & $\sigma_{l,q_{LP}}^{UD} \approx \sigma_{r,q_{IR}}^{UD}$ can be attributed to unphysical variations of the q_{IR} profile ($q_{IR} < 0$, poloidal fluctuations), non-monotonous LP values ($P7 > P6$), and possibly influence of incidence angle on γ_s (Chapter 3). At $t = 2$ s q_{IR} is below the measurement threshold, so no useful information can be extracted. This shows again the importance

Table 5.2.: Comparison of q_{IR} and q_{LP} fit parameters at $t = 1$ s in D#24.

Quantity	$A_q^{\text{UD}}[\text{MW}]$	$\mu_q^{\text{UD}}[\text{mm}]$	$\sigma_{l,q}^{\text{UD}}[\text{mm}]$	$\sigma_{r,q}^{\text{UD}}[\text{mm}]$
q_{LP}	0.89 ± 0.16	299 ± 19	62 ± 17	91 ± 14
q_{IR}	0.70 ± 0.02	325 ± 5	95 ± 5	65 ± 4

of the LP diagnostic for detachment studies.

Figure 5.8 shows the evolution of n_e . Notable are the steep drop in amplitude at $t = 1.3$ s and the almost constant profile parameters in the detachment phase. Relative to the attached phase, $\mu_{n_e}^{\text{UD}}$ is shifted towards the pumping gap and the profile becomes more skewed, with the already smaller $\sigma_{l,n_e}^{\text{UD}}$ further reduced and the larger $\sigma_{r,n_e}^{\text{UD}}$ increased. The total width increases slightly from ≈ 170 mm to ≈ 180 mm. Fits at 1 s and 2 s exemplifying this are shown in Figure 5.9.

Finally, Figure 5.10 shows the evolution of the T_e DG fit parameters. Notable is the strong skew of the profile with $\sigma_{r,T_e}^{\text{UD}}$ significantly greater than $\sigma_{r,n_e}^{\text{UD}}$ already in the attached phase of 20181004.24 and all of 20181004.23. In the detached phase, the fit routine fails, the reason for which is clear from Figure 5.11: the T_e profile changes shape and the DG distribution no longer describes the data well.

Asymmetries between the upper and lower divertors can be explained by drifts [43]. In D#24 these result in lower fluxes to the Lower divertor (LD) and modified profiles. Figure 5.12 show exemplarily for two time points the general trends present throughout the discharge. These are qualitatively compared through the fit parameters with the UD in Table 5.3.

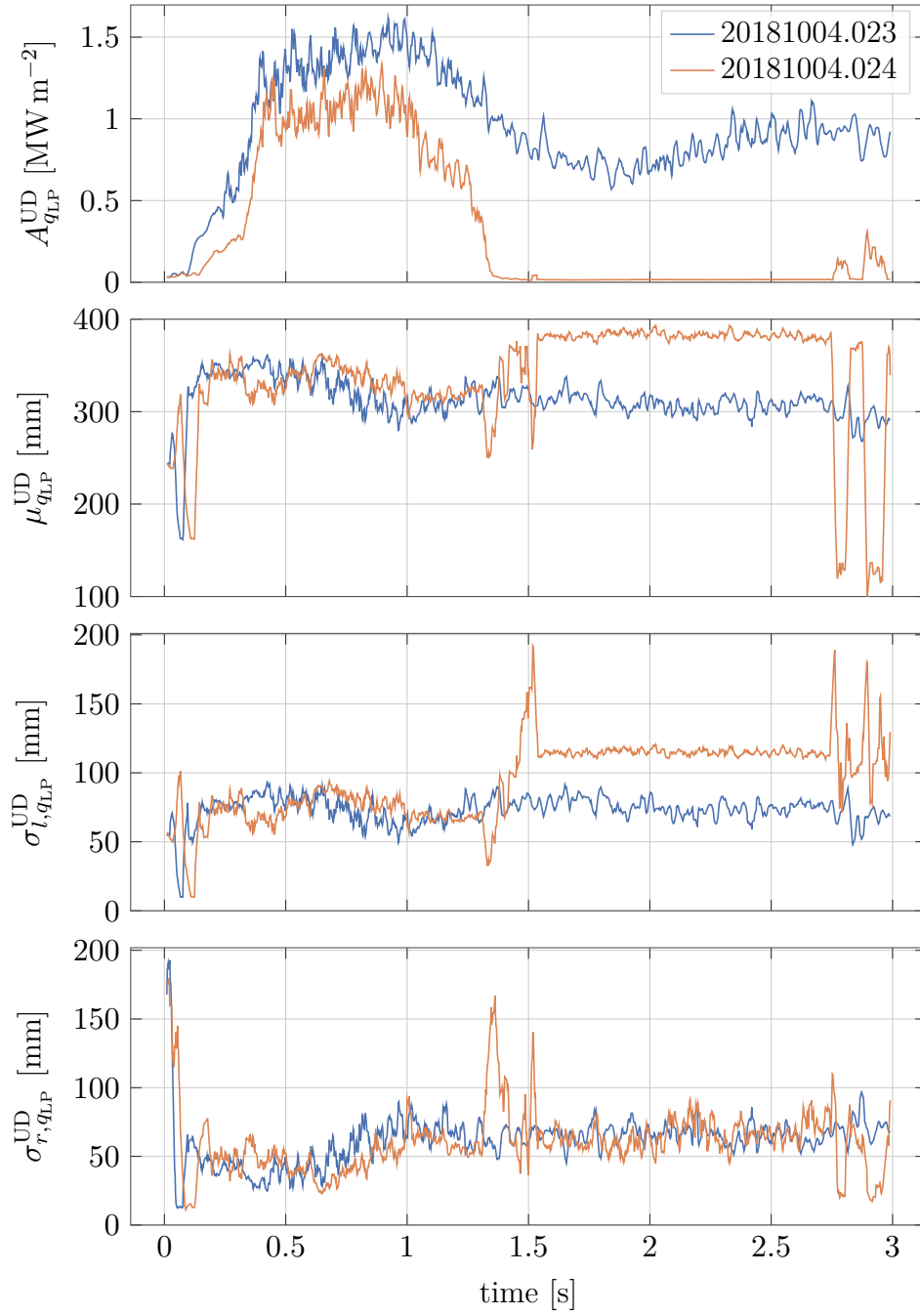


Figure 5.5.: Time evolution of DG profile parameters for q_{LP} (Langmuir-derived heat flux). Amplitude A calculated using $\gamma_s = 6.5$.

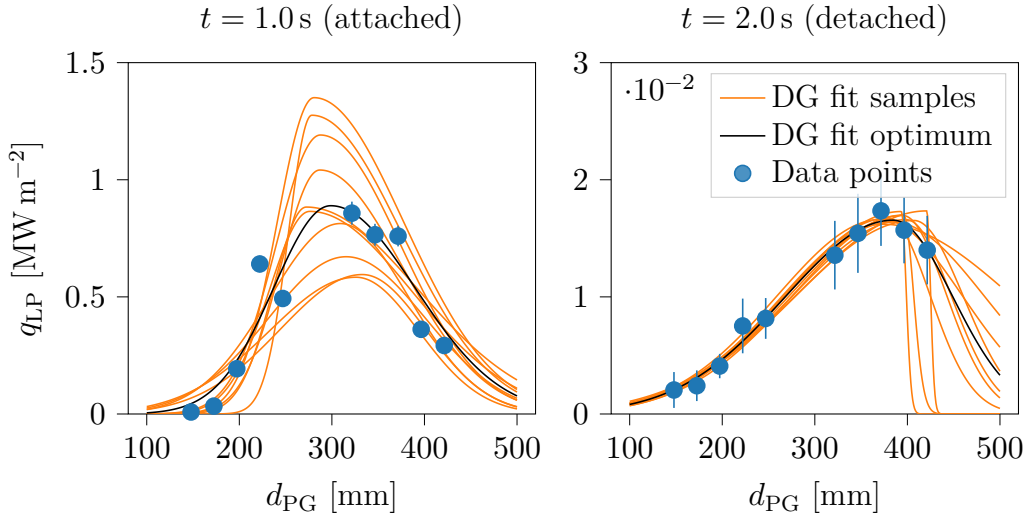


Figure 5.6.: Selected profiles of q_{LP} , UD, D#24. Note $\mathcal{O}(50)$ ordinate scale change.

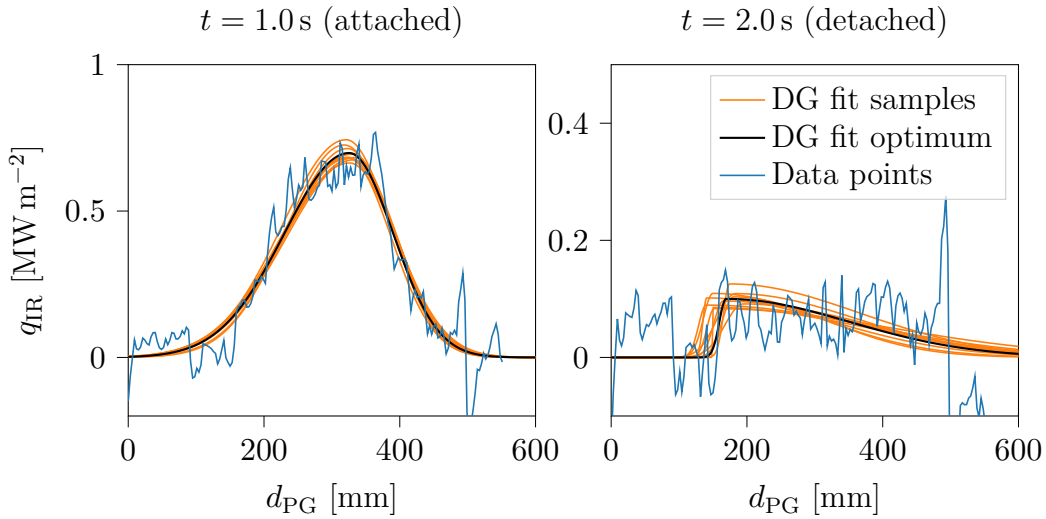


Figure 5.7.: Selected profiles of q_{IR} , UD, D#24.

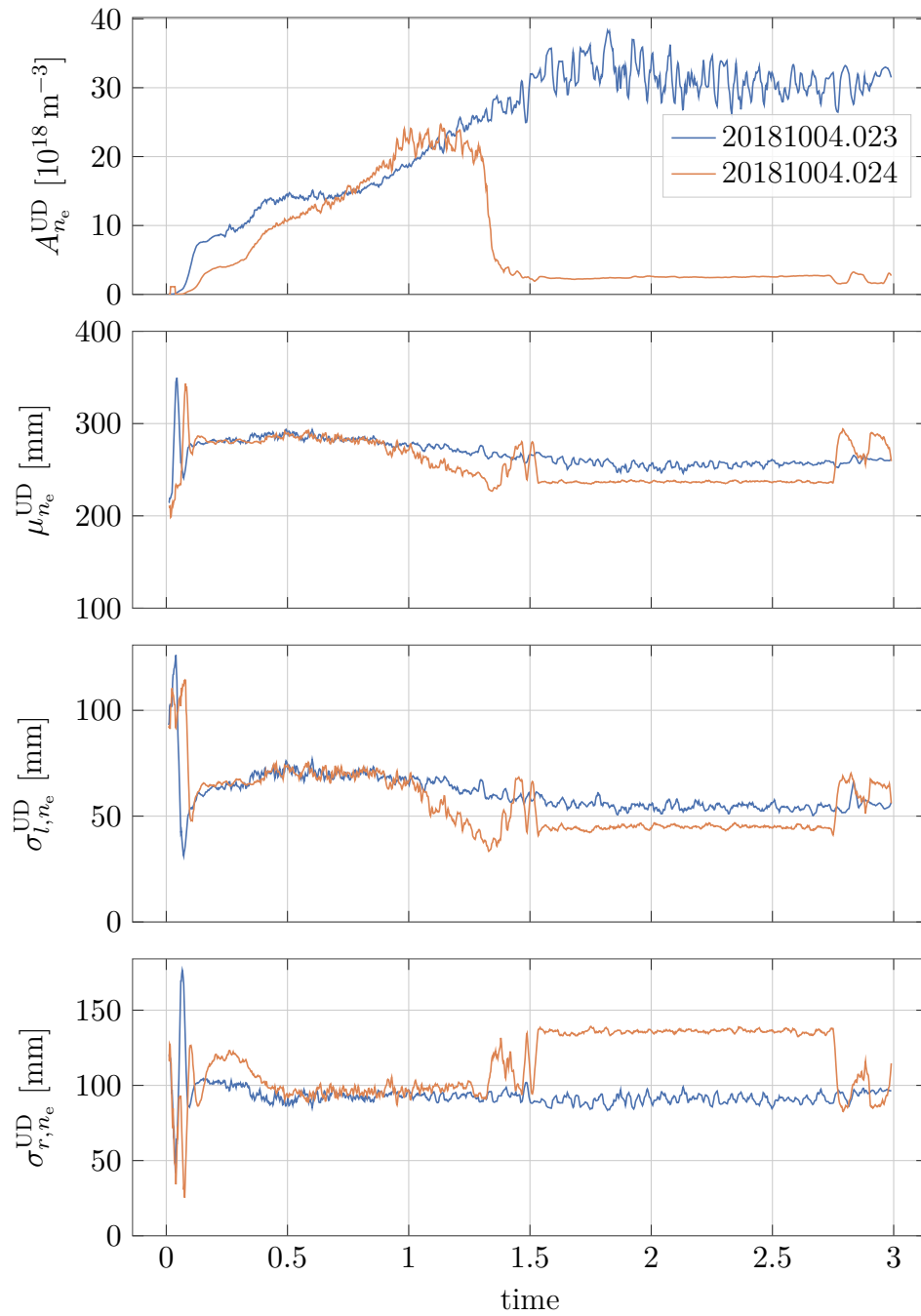


Figure 5.8.: Time evolution of DG profile parameters for Langmuir-derived n_e .

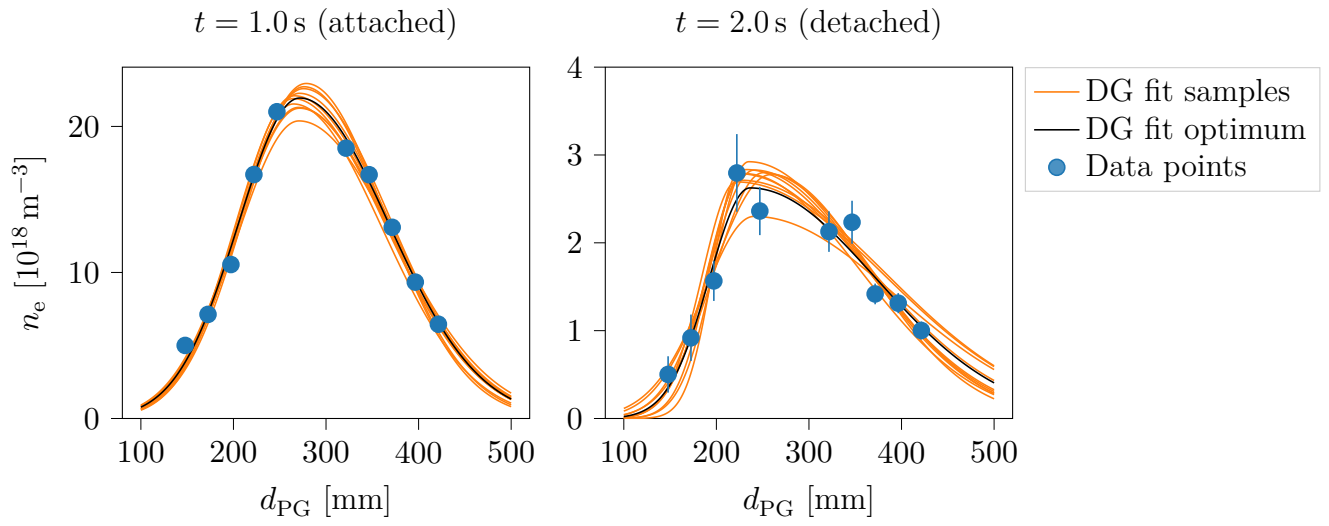


Figure 5.9.: Selected profiles of n_e , UD, D#24

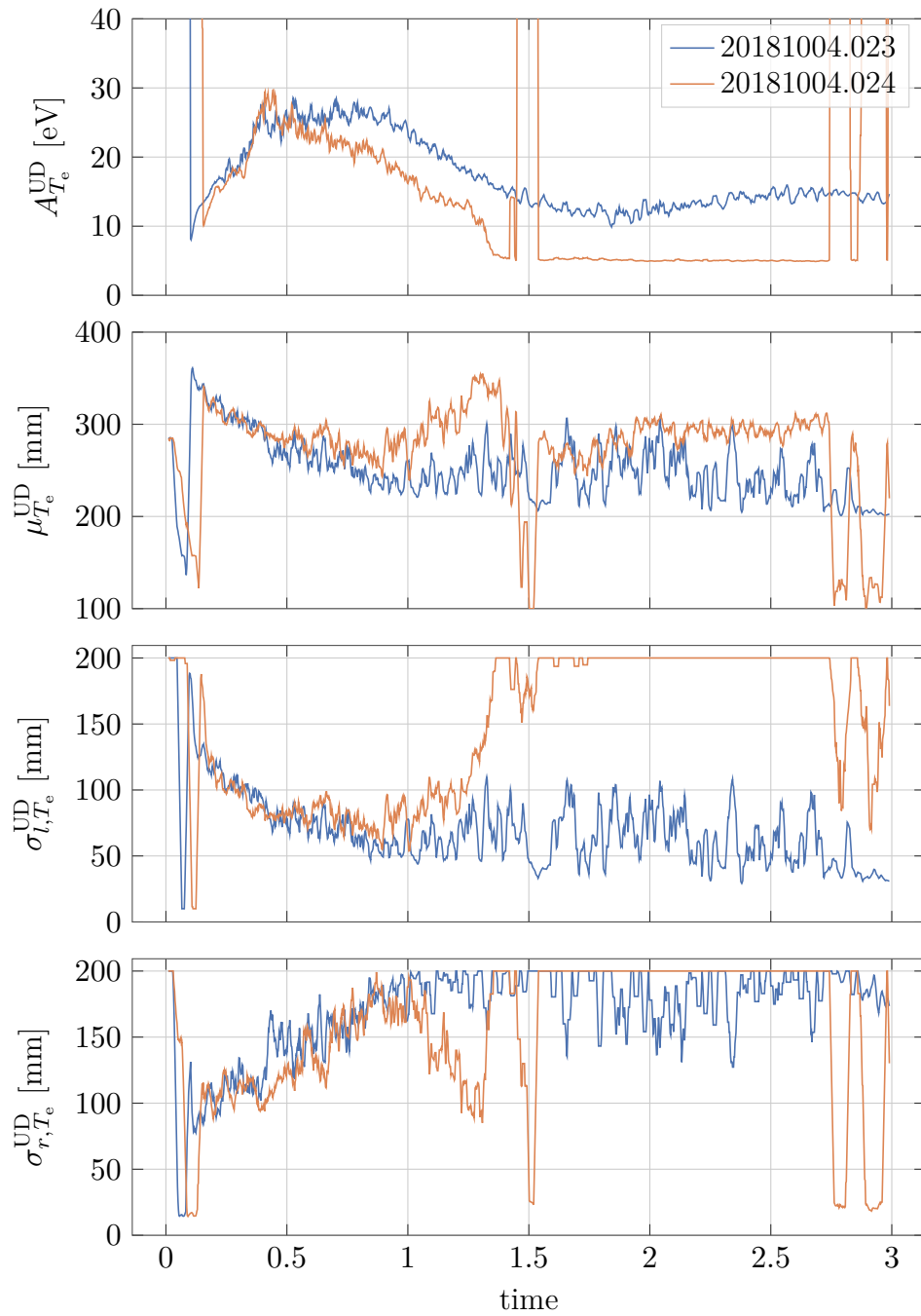


Figure 5.10.: Time evolution of DG profile parameters for Langmuir-derived T_e .

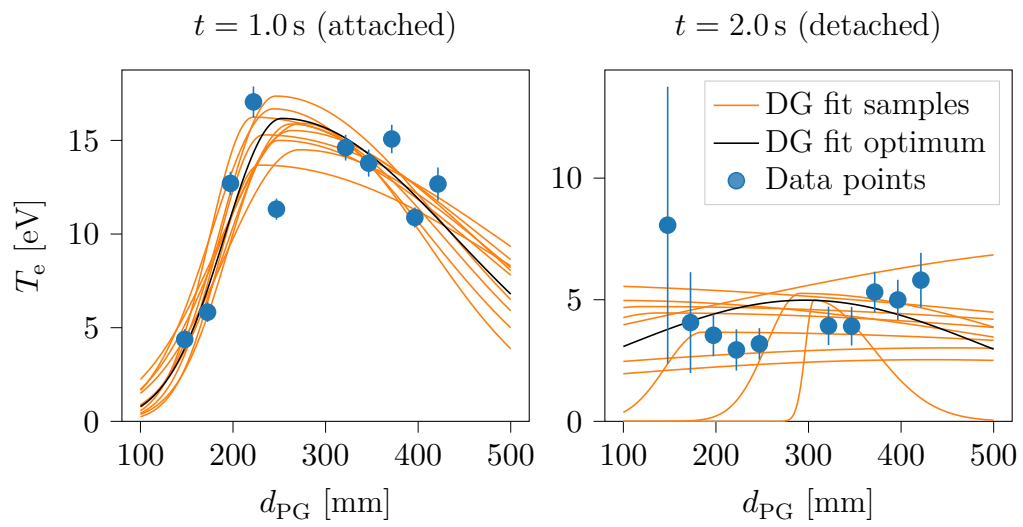


Figure 5.11.: Selected profiles of T_e , UD, D#24. Initial parameters assumed as optimal for $t = 2.0$ s because data distribution is not unimodal and fit fails.

Table 5.3.: Qualitative comparison of LD and UD DG fit parameters in D#24, describing the up-down asymmetry. Descriptions w. r. t. respective UD parameters of the same discharge.

Q	A_Q^{LD} [MW]	μ_Q^{LD} [mm]	σ_Q^{LD} [mm]
n_e	Lower during attached, equal in detached phase w. r. t. $A_{n_e}^{\text{UD}}$	Similar initially, shifted outwards with detachment	Larger and more equal σ_t^{LD} & σ_r^{LD} , i. e. broader and more symmetric profiles. Weakly reduced (more peaked) in detachment as opposed to broadened for UD
T_e	Lower during attached, similar in detached phase	Similar initially, shifted outwards with detachment	Larger and more equal initially, similarly ill-defined later
q_{LP}	Up to $\frac{2}{3}$ lower initially, equal in detached phase, fluctuating with $\lesssim 20$ Hz	Equal in attached phase, shifted inwards and significantly fluctuating later	Slightly larger and more unequal initially, 50% reduced w. r. t. $\sigma_{q_{\text{LP}}}^{\text{UD}}$ in detachment.

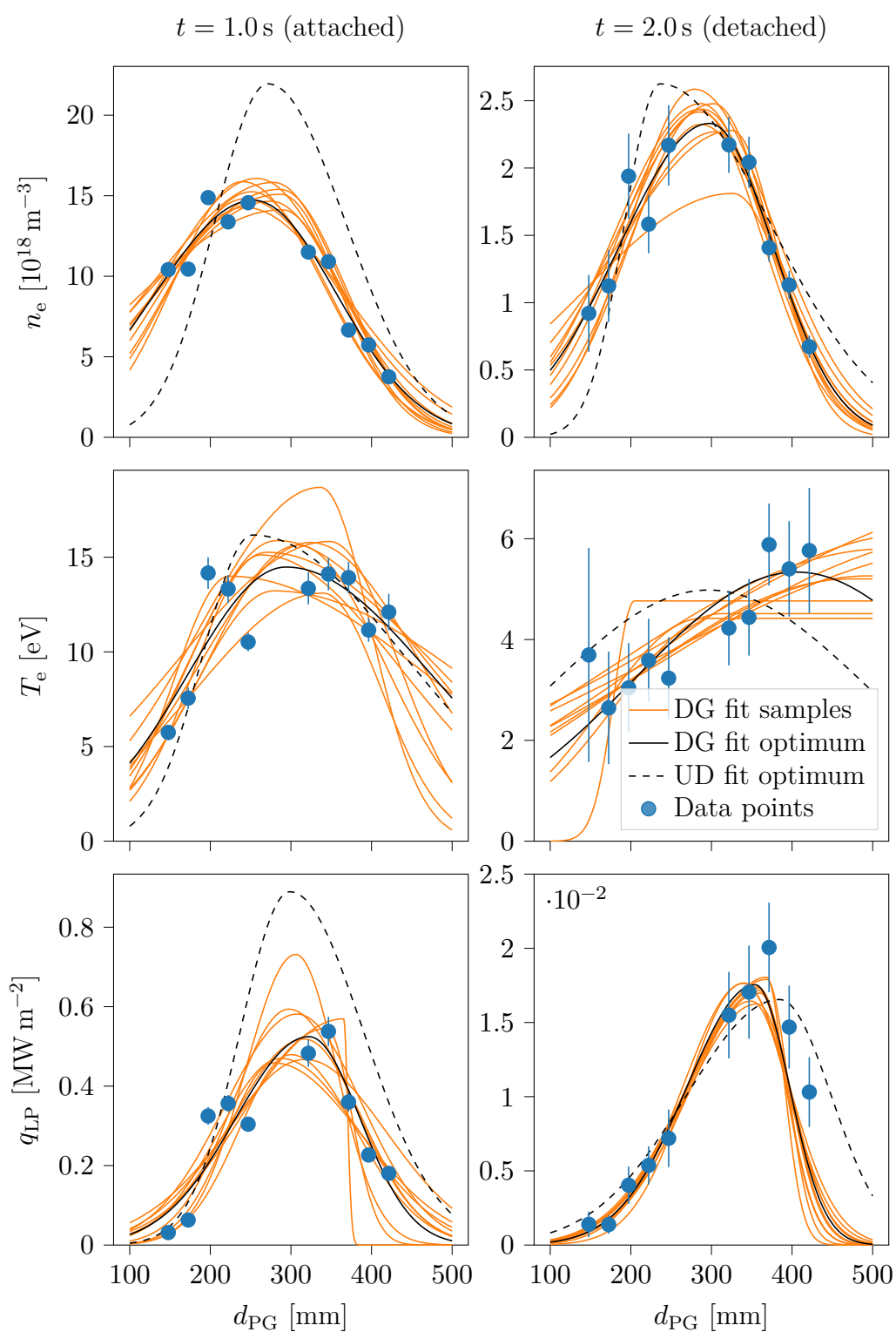
During the detachment phase, a radiation front moves inwards away from the wall which we can qualitatively see in Figure 5.13. Here, profiles along the line indicated in black in Figure 5.3 are shown. For a more quantitative assessment, profile diagnostics or tomographic reconstruction would be necessary.

Since $nd\ell$ is nearly identical for both discharges, P_{ECRH} only differs slightly and as we argued above the core profiles are likely very similar, what is the reason for the starkly different edge behaviour observed? The difference in P_{rad} , notwithstanding the uncertainty addressed above, is only a way to restate the same question as for the lack of other power exhaust channels, detachment is always accompanied by significant f_{rad} . (The converse isn't true, high f_{rad} does not always imply detachment).

Our hypothesis is that the difference is due to fuelling, which plays an important role in detachment at W7-X. We will therefore examine the gas balance of both discharges in Figure 5.14. The measurement and analysis methods were developed by Schlisio *et al.* in Reference [14]. In cooperation with the main author of that group, these methods were applied to D#23 and D#24, which had not previously been studied and the interpretation discussed.

For the particle balance, the neutral gas content of the vessel and the particles that become ionised and form the plasma play a relatively small role. From the gradient of the cumulated pumped number of particles we can infer that the neutral compression and therefore sub-divertor pressure of D#23 is higher, since the pumped flow depends only on this quantity and the (constant) pump speed. The discharges are set apart by the amount of gas that is fuelled to reach the desired $nd\ell$ level and how much of it is absorbed by the wall, i. e. their fuelling efficiency.

In the first discharge, in addition to the gas pre-fill, the wall releases gas until $t \approx 1$ s when, in order to increase $nd\ell$, the gas feedback system adds $\approx 24 \times 10^{20}$ H_2 molecules. About half of these are absorbed by the wall, which then slowly releases them throughout the discharge at a rate of $\approx 2 \times 10^{20} \text{ s}^{-1}$ (\dot{N}_{wall}). The pumps can sustain this, such that the plasma particle content stays constant and no further fuelling (\dot{N}_{fuel}) is required. An important factor in the rate of out-gassing is the wall temperature. Since this is elevated after the discharge at $t = 12$ s, out-gassing continues and the initial wall reservoir $N_{\text{wall},0}$ is depleted such that the relative stored inventory becomes negative.



148

Figure 5.12.: Selected profiles for LD data of D#24, comparing the attached and detached states. The T_e measurements in the detached state are too uncertain for a reliable DG fit. Note the $\mathcal{O}(40)$ scale change of the q_{LP} ordinate in last panel. UD fit optima are shown dashed for comparison.

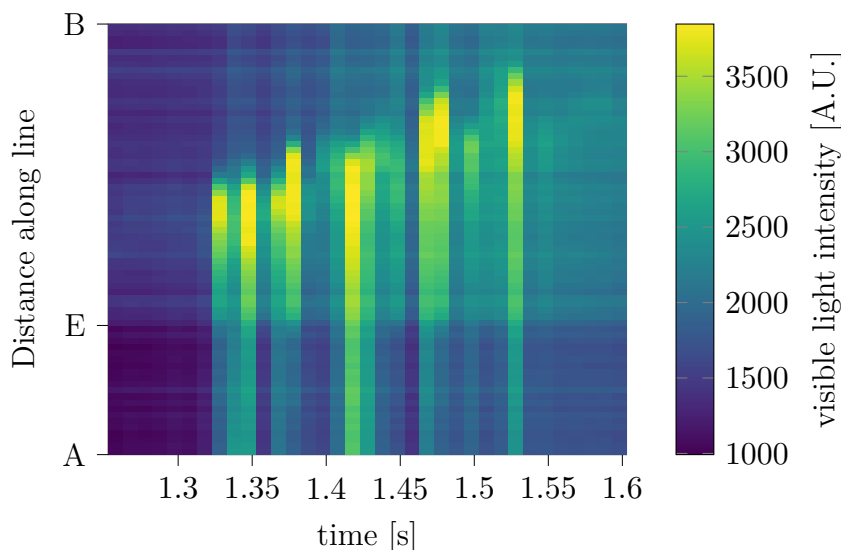


Figure 5.13.: Time evolution of total light intensity recorded by visible light camera along line indicated in black in Figure 5.3. That line and the ordinate in this plot roughly approximate a radial profile through the edge radiation above the inner wall. **E** marks the transition from short to long line of sight (LOS), with different background light intensity. Beginning at 1.33s during D#24, bands of radiation are visible in some frames. The maximum of light intensity, interpretable as a radiation front, shifts into the plasma until 1.53s.

In the second discharge, while the dynamic is similar, the relative wall inventory stays positive throughout. During the first $t = 2$ s, $\approx 60\%$ more fuelling is necessary to reach the same $nd\ell$ as in the previous discharge. As the neutral pressure and therefore particle inventory does not increase, the difference must be absorbed by the walls. These are at $t = 2$ s loaded with twice as many particles relative to the discharge start as in D#23. Outgassing is slower, at a rate of $\approx 8 \times 10^{19} \text{ s}^{-1}$, which leads to correspondingly lower sub-divertor pressure and thus pumping rate (\dot{N}_{pump}). At the end of ECRH the wall inventory is higher than at the start of the discharge.

Our interpretation is as follows: The wall absorbs more particles, possibly because it was depleted in the previous discharge, necessitating a higher fuelling rate. The increased fuelling rate cools the edge and leads to a higher

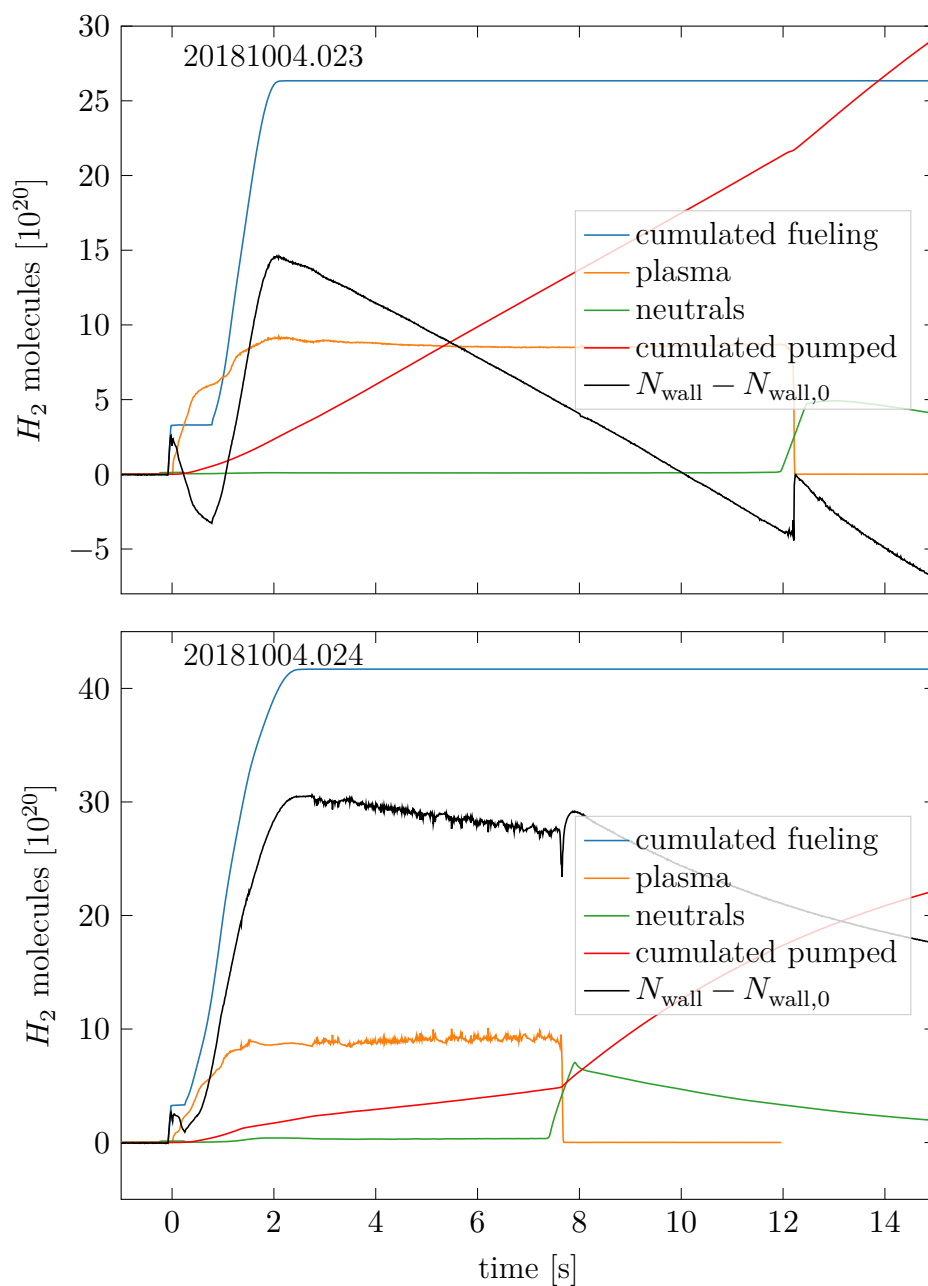


Figure 5.14.: Gas balance in terms of H_2 inventory. Neutral gas content and cumulative pumped derived from pressure gauges, plasma particle content from ndl , cumulative fuelled from flow and pressure sensors in fuelling system. Wall inventory difference relative to unknown $N_{\text{wall},0}$ inferred from other quantities. For detailed discussion see Reference [14]. Courtesy of Georg Schlisio.

f_{rad} . This in turn reduces the heat flux to the PFCs, resulting in lower temperatures. Gas release is therefore slower, such that the sub-divertor pressure remains low. Detachment is in this case a consequence of reduced fuelling efficiency.

A question that arises from this is on the role of pumping rate \dot{N}_{pump} , a parameter that was not independently experimentally varied. Would an increase of the divertor's pumping action cause more gas to be removed from the vessel, possibly reducing the wall inventory enough to change inter-discharge dynamics? This is challenging to study experimentally not only because the compression is a difficult to control parameter (though some influence is possible through SL movement [98]), but primarily because the wall inventory is only accessible through the balance of in- and out-fluxes. Any difference caused by a changed pumping rate would thus have to affect the vessel neutral pressure to be observable. This pressure is low and not accurately known, as it is measured by pressure gauges retracted far into ports. A more complete understanding of the inventory history of the wall would also be necessary, to move from a by-discharge relative wall inventory to a by-campaign relative wall inventory. The uncertainty in the wall inventory due to the unknown initial boundary condition would fade with each subsequent discharge, possibly enabling absolute statements about the depletion or loading state of the PFCs. Pumping speed, the other control parameter of pumping rate \dot{N}_{pump} , was not systematically varied during OP 1.2, but the installation of cryo-pumps in OP 2 will bring with it greater flexibility and maximal pumping speeds. This will enable further studies of the effect of the particle balance on detachment behaviour.

5.4.1. Open questions for further work

In the scope of this thesis, only ex-post reasoning for why a particular discharge detached was feasible. How can we predict whether a discharge will evolve to become detached and what are the general dynamics?

Evidently many variables can have similar values or be in similar states (same $nd\ell$, P_{ECRH} in both discharges, $\dot{N}_{\text{fuel}} = 0$, $\dot{N}_{\text{wall}} = -\dot{N}_{\text{pump}}$) while detachment is or is not observed. Suppose a 'detachment-determining' variable exists that we are either not measuring or, more likely, that is a non-linear combination and interaction of multiple quantities. If such a hypothetical variable is described by some differential equation, is there a continuum

of stable solutions (Case A), a single stable one that all discharges slowly converge to (Case B), or multiple distinct ones with a barriers between them (Case C)? The evidence of long, stable detachment [39] is compatible with all three: Control parameters were kept constant such that Case A can not be ruled out and there is no counter-example of a comparable attached discharge to rule out Case B. If Case C were closest to the truth, as suggested by our comparison of the two discharges above in which an initial difference (the wall reservoir $N_{\text{wall},0}$) influences the entire evolution despite otherwise similar parameters, the question becomes of what kind and magnitude the initial difference must be. A later impulse to the system can clearly overcome the barrier between states, as evidenced for example by the induced transition to detachment in impurity injection experiments [118]. Remarkable in this context is the 'stability' of the detached state against further transition to radiative collapse. Our exemplary investigations of discharges in this chapter attempt to understand this 'detachment-landscape' of stable valleys by describing empirical paths through it (individual discharges) and develop some of the tools for a more complete survey.

5.5. Transition into detachment

In addition to the discharge-level conditions for detachment, we are interested in the transition process itself and its timescale.

In Figure 5.15 we look at the transition into detachment of the UD in more detail at higher time resolution.

It is clear that the DG fits are only of limited usefulness in describing the LP profiles in detachment. Especially the very broad, occasionally concave, T_e profiles are a challenge because a more general fit form capable of approximating them well might generally be less stable. For this reason, when investigating the detachment transition in greater detail below, we will supplement A_Q by single probe traces.

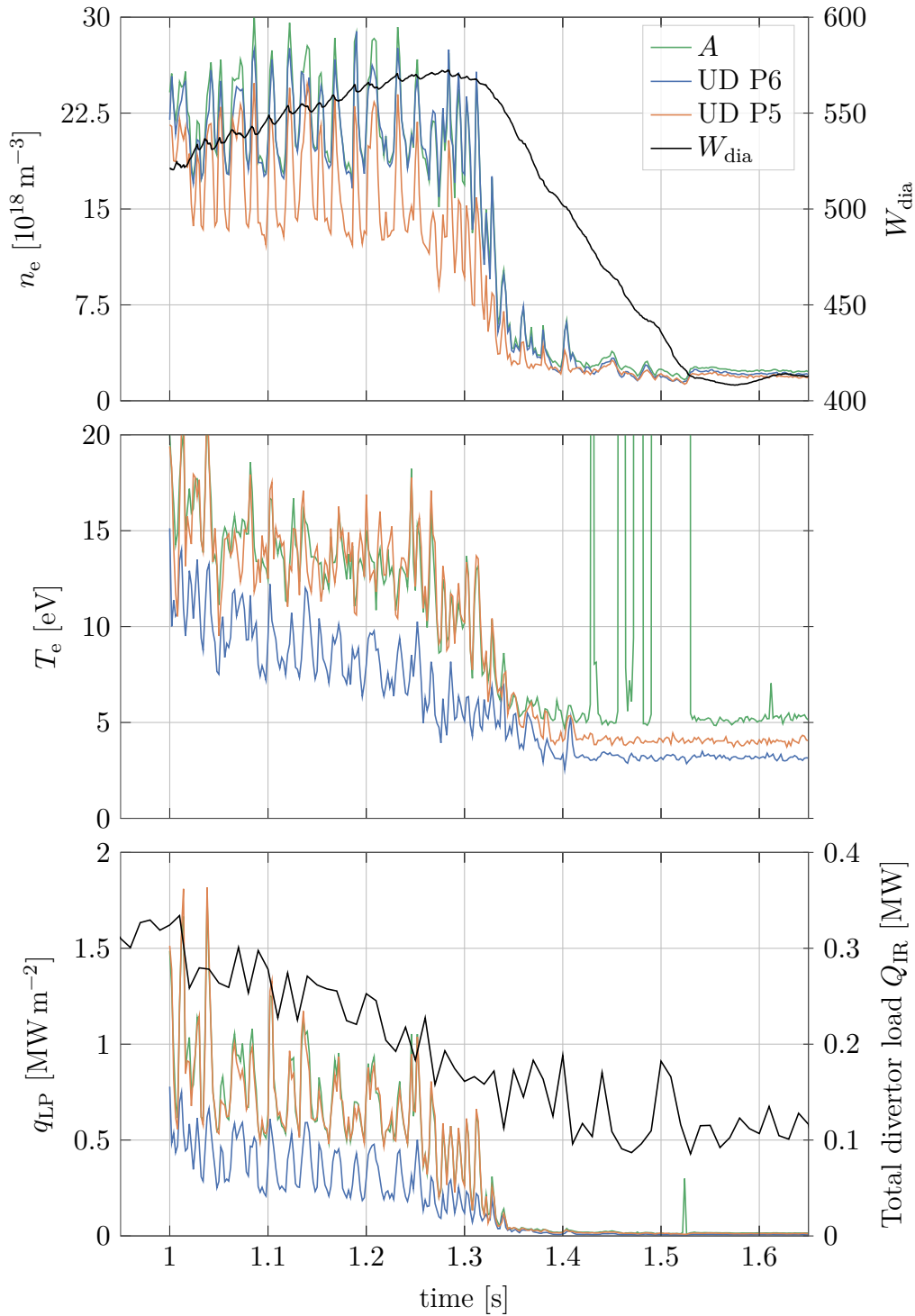
Despite the large fluctuations, it is clear that W_{dia} lags behind the reduction in T_e and consequently q_{LP} , as might be expected for a change starting at the edge and propagating inwards as profiles adjust. The sample frequency of the LPs, here $f_{\text{sweep}} = 500$ Hz, seems sufficient to resolve the detachment transition, which appears to be on a time scale of approximately 50 to 100 ms depending on if judged by the n_e or q_{LP} traces. This is

considerably shorter than the timescale of movement of the radiation front we may estimate from Figure 5.13. The evolution of q_{LP} is comparable to the total divertor load Q_{IR} reduction observed by the IRCs and shown in the bottom panel of Figure 5.15. (Note that the IRCs operate at a framerate of about 100 Hz and the Langmuir probes are thus much better suited to investigate the detachment transition.) This indicates that Q_{IR} is either dominated by, or homogeneously follows, the q at the SL. The former of these options is very likely, as by definition the SL is the region of greatest heat flux. The (non-exclusive) latter option matches at a very local space and short time scale the observation by IRCs of uniform detachment ('homogenous thermal unloading') across entire divertor modules and multiple seconds in Reference [98][Fig.3]. The saturation of $Q_{\text{IR}} > 0.1 \text{ MW}$ is due to the IRC noise threshold of 0.1 MW m^{-2} in combination with the wetted area of approximately 1 m^2 .

Note the similarity with the abrupt detachment transition of 20 180 814.025 in Figure 4.14, in which however we do not see fluctuations because the time traces shown are averaged to the H_α -Camera (H_α -C) frequency. This higher time resolution reveals coincident fluctuations of the LP quantities and sawtooth-like W_{dia} behaviour preceding the transition.

The widening gap between T_e of UD5 and UD6 for $t = [1, 1.25] \text{ s}$ is explained by a shift of the distribution peak, also evident in the movement of $\mu_{T_e}^{\text{UD}}$ in Figure 5.10 in the same interval. The modification of the profile during the detachment transition is perhaps best illustrated by a series of equidistant fits to q_{LP} in Figure 5.16.

A normalisation of the individual probe traces to $A_{q_{\text{LP}}}^{\text{UD}}$ shown in Figure 5.17, is more difficult to interpret, but offers an unparametrised view of the data. Each probe trace has been smoothed with a rolling average. The normalisation ensures that shape- and relation-information is preserved even though the amplitude changes dramatically. A shift of the SL manifests as a change of the order of the probes: When initially P5 has the highest flux and appears on top, its 'rank' reduces and finally P3 is most representative of the amplitude. The broadening of the SL can be inferred from the much closer grouping of all probes at the end of the time interval. While a spatial gradient spreads out the normalised values, a flat distribution would have them all converge.



154 **Figure 5.15.:** Transition into detachment of D#24 at full time resolution. Single probe traces near the SL shown to support DG fit results. Non-local measures of detachment transition on secondary ordinate in black.

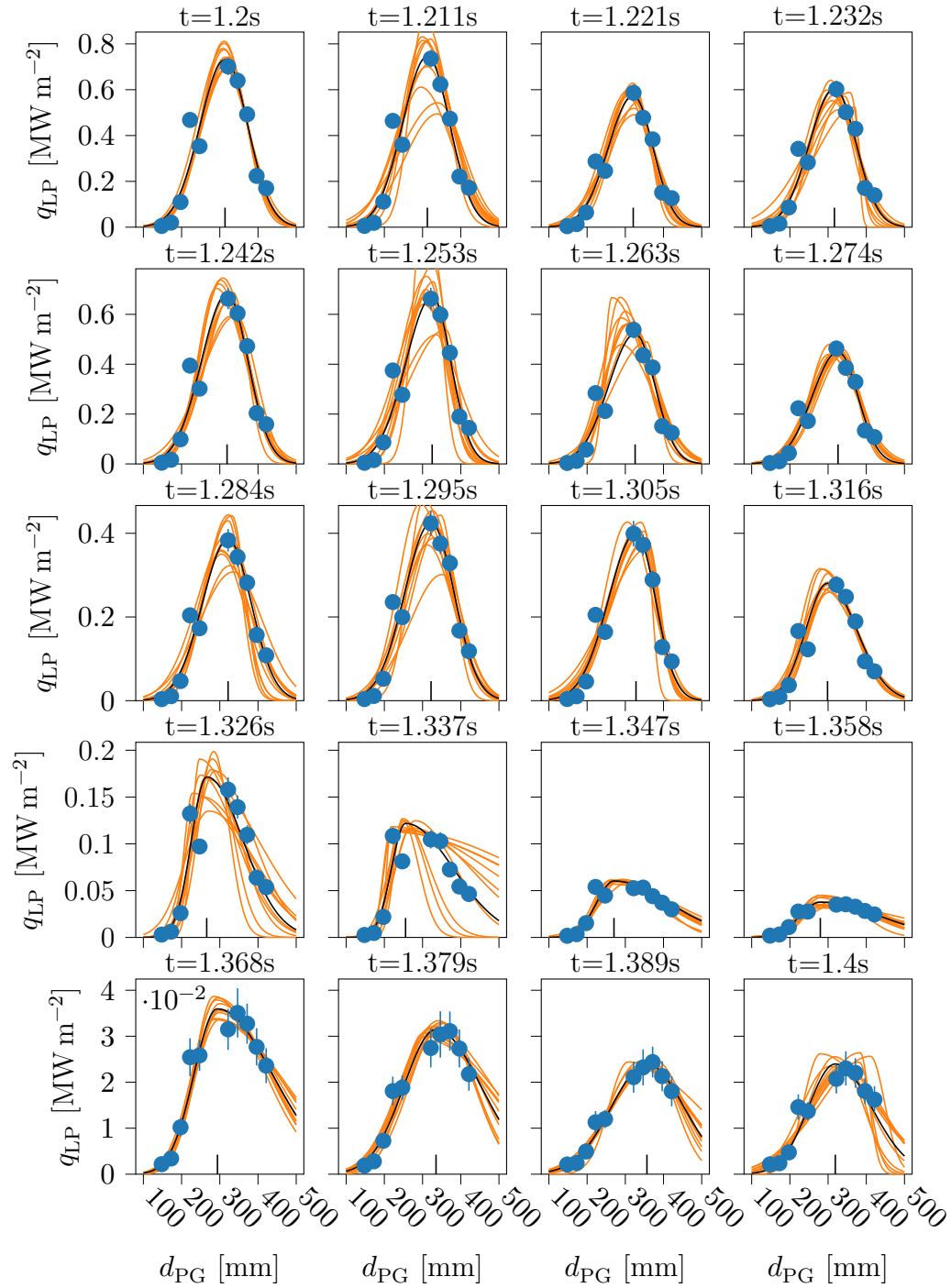


Figure 5.16.: DG fits to q_{LP} during the transition to detachment in D#24. Data in blue, optimal fit in black, samples of probable fits orange. Times as titles above each plot. Ordinates are on one scale for each row, showing the particularly fast reduction from 1.305 to 1.358 s. A vertical line marks the position of $\mu_{q_{LP}}^{UD}$ at each time.

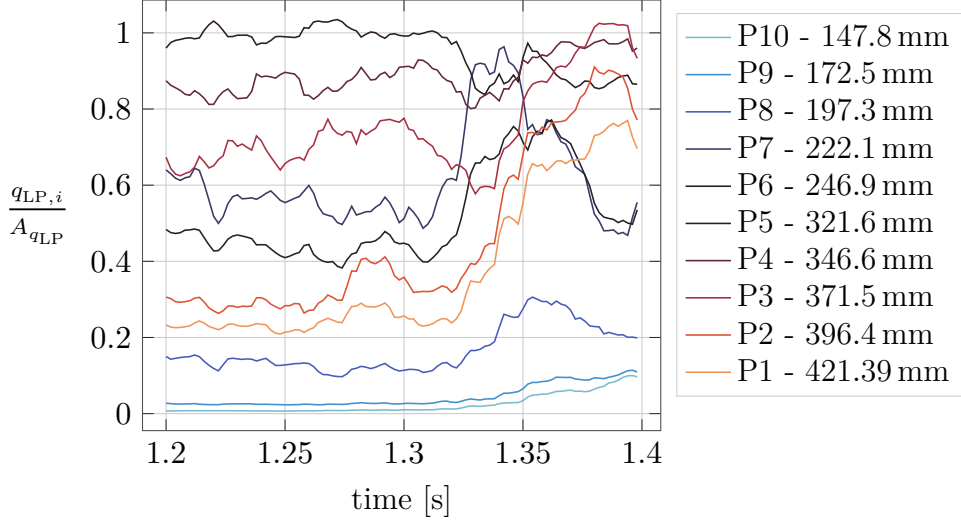


Figure 5.17.: Normalised q_{LP} probe traces during the transition to detachment in D#24. Each time trace is normalised to $A_{q_{LP}}^{UD}$, such that if $\mu_{q_{LP}}^{UD}$ perfectly coincides with the position of a probe, its normalised time trace is equal to 1. Colours are chosen such that the positions at the centre of the LP array and near the SL are dark, diverging to blue or red moving towards or away from the PG respectively. The data is smoothed with a rolling average.

5.6. Fluctuations prior to detachment transition

To investigate the nature of the fluctuations observed in the last section, we subtract a 100 sample (100 ms) centred rolling average from the n_e and T_e time traces. For each position, the remainders of this subtraction is normalised by its standard deviation.

The scatter of the normalised n_e and T_e remainders, \tilde{T}_e & \tilde{n}_e , in Figure 5.18 shows no clear correlation. If the fluctuations were radiation instabilities where reduced temperature causes recombination, extending from outside into the plasma, we would expect an anti-correlation of \tilde{T}_e & \tilde{n}_e . On the other hand fluctuations might be propagating from the hot and dense inside of the LCFS out into the cold and tenuous scrape-off layer (SOL). Such plasma blobs are studied in W7-X by Killer *et al.* [131] and Zoletnik *et al.* [132]. They are filamentary structures formed through different instability mechanisms

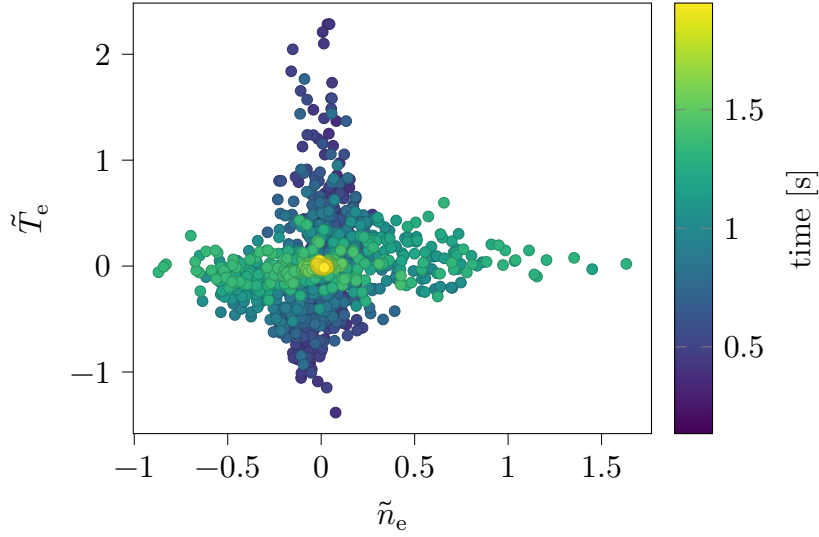


Figure 5.18.: Scatter of normalised T_e and n_e fluctuations for UD P6 in D#24. No clear correlation visible, points independently distributed along axes. Fluctuation strength separated in time with \tilde{T}_e phase (blue, $t < 0.8$ s), \tilde{n}_e phase (green, $0.8 \text{ s} < t < 1.6$ s) and calm detachment phase (yellow, $t > 1.6$ s).

which remain coherent as they drift. In these, \tilde{T}_e & \tilde{n}_e ought to be positively correlated. Observing no strong correlation means we cannot definitively attribute the fluctuations to either mechanism, although given the timescale and skew towards positive \tilde{T}_e & \tilde{n}_e excursions, filaments from inside the LCFS seem more plausible.

Rather than clearly aligned or anti-aligned, the fluctuations of n_e & T_e are temporally separated. This is reproduced in Figure 5.18 for UD Probe 6, with early data points (blue, $t < 0.8$ s) spread along the T_e axis and intermediate (green, $0.8 \text{ s} < t < 1.6$ s) ones along n_e . The last data points (yellow, $t > 1.6$ s) cluster at the origin as the fluctuations have died down. The sample Pearson correlation coefficient for this probe is $r_{xy} \approx 0.22$, indicating a weak positive correlation.

From the cross-correlation of different probe time traces, no delay between them can be detected, likely because the LP sweep resolution (1 kHz) is too low, meaning we can not determine which probe is contacted first.

The frequency of these fluctuations is lower than that of those reported

on by Zotelnik *et al.*, Ballinger *et al.* and Wurden *et al.* [132–134]. Future work should attempt to combine different time resolution diagnostics to study this phenomenon in more detail.

5.7. Unstable detachment

As a different example of discharge evolution, consider the discharge 20 181 004.048 we already looked at in a previous chapter (see Figure 3.7). When before we needed only a case where variations of Γ occur in DBM and are observed by the H_α -Cs, we now want to examine in more detail the reason and mechanism by which power detachment occurs.

In the first 4 s of this experiment, the ECRH power is stepped up to 6 MW, and then kept relatively constant. The gas fuelling system is programmed to raise the line-integrated density as measured by the interferometer ndl to $7 \times 10^{19} \text{ m}^{-2}$ by $t = 2.5 \text{ s}$ and then turn off. Starting at $t = 4 \text{ s}$ the Helium beam spectroscopy (HeBS) system takes over fuelling, further raising ndl to $1 \times 10^{20} \text{ m}^{-2}$ and maintain this value by feedback control of the gas input. Gas is injected from valve 4 in divertor module 51, where the UD LPs are situated.

The added fuelling causes, whether through a modification of profiles or by raising ndl , an increase of the radiated power fraction. The resulting reduction of heat load on the UD can be seen in Figure 3.9.

Control of the HeBS gas flow rate is achieved through the voltage applied to the piezoelectric valve. While a calibration of gas flow rates was done prior to OP 1.2, the predicted flow does not match the measured reduction in pressure, with a factor 2 systematic difference. We therefore show in Figure 5.19 the readily available applied voltage as a qualitative measure of gas flow. From $t = 6 \text{ s}$ until the end of the discharge, the valve is mostly fully open, but intermittently closes when ndl overshoots the feedback setpoint.

We will focus on the development of n_e at the divertor measured by the LPs. As we do not require the full LP time resolution of 1 kHz, we average in time over 100 adjacent values to obtain \bar{n}_e and use the standard deviation of these values as error of the new time trace. This gives a representative error estimate because fluctuation amplitude \tilde{n}_e typically exceeds parameter uncertainty σ_{n_e} . Because the heat flux profile shifts over the course of the discharge and becomes ill-defined in detachment, we can not for the entire

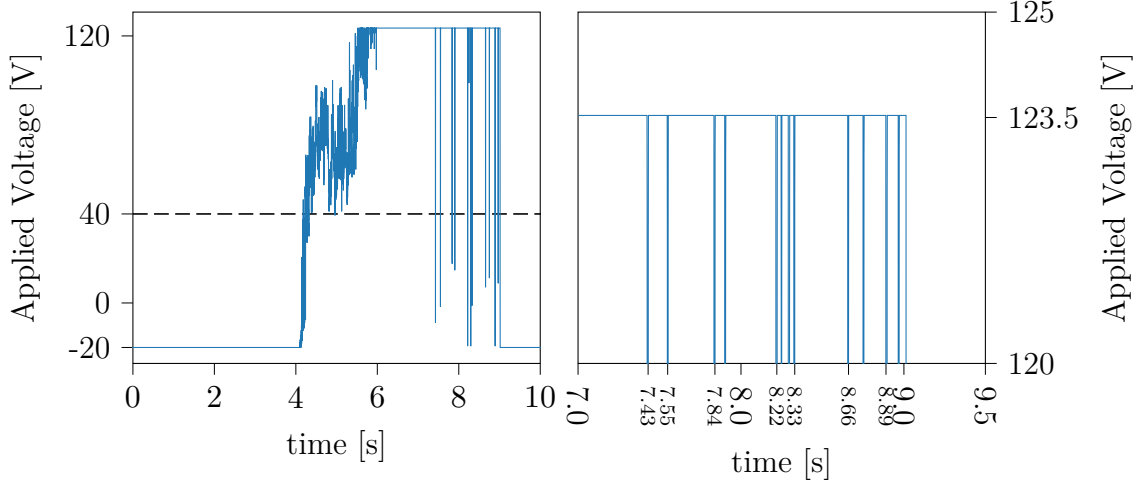


Figure 5.19.: Voltage applied to the HeBS valve 4. The dashed line indicates the threshold above which the valve is opened and gas streams in. Gas flow is not a linear function of applied voltage above the threshold.

duration use n_e of on specific probe to be representative of the SL. We therefore fit the LP quantity profiles by the DG distribution introduced above. The upper panel of Figure 5.20 shows the movement of μ_{n_e} on UD and LD throughout the discharge. The initial separation between $\mu_{n_e}^{\text{UD}}$ and $\mu_{n_e}^{\text{LD}}$, as well as the later convergence in the detached phase matches the observations by Hammond *et al.* [43]. We can conclude that drifts, magnetic field errors and target misalignments do not appear to play a discernable role after $t = 7$ s when $f_{\text{rad}} \approx 1$.

Noteworthy is the behaviour of A_{n_e} , shown in the lower panel of Figure 5.20. On the UD, where the HeBS valve through which gas is injected is located, n_e rises approximately linearly until 7 s before crashing sharply. Fluctuations afterwards correlate with intermittent closures of the valve, although the response is strongly spread out. On the LD, the rise of n_e stops earlier, peaking at approximately 6 s and shows much lower fluctuation amplitude afterwards.

Since reduction of n_e on LD occurs around $t = 6$ s, before the crash near the gas source at UD, this behaviour can not be explained by a propagation and diffusion of the crash event. Neither does it seem to be due to a T_e

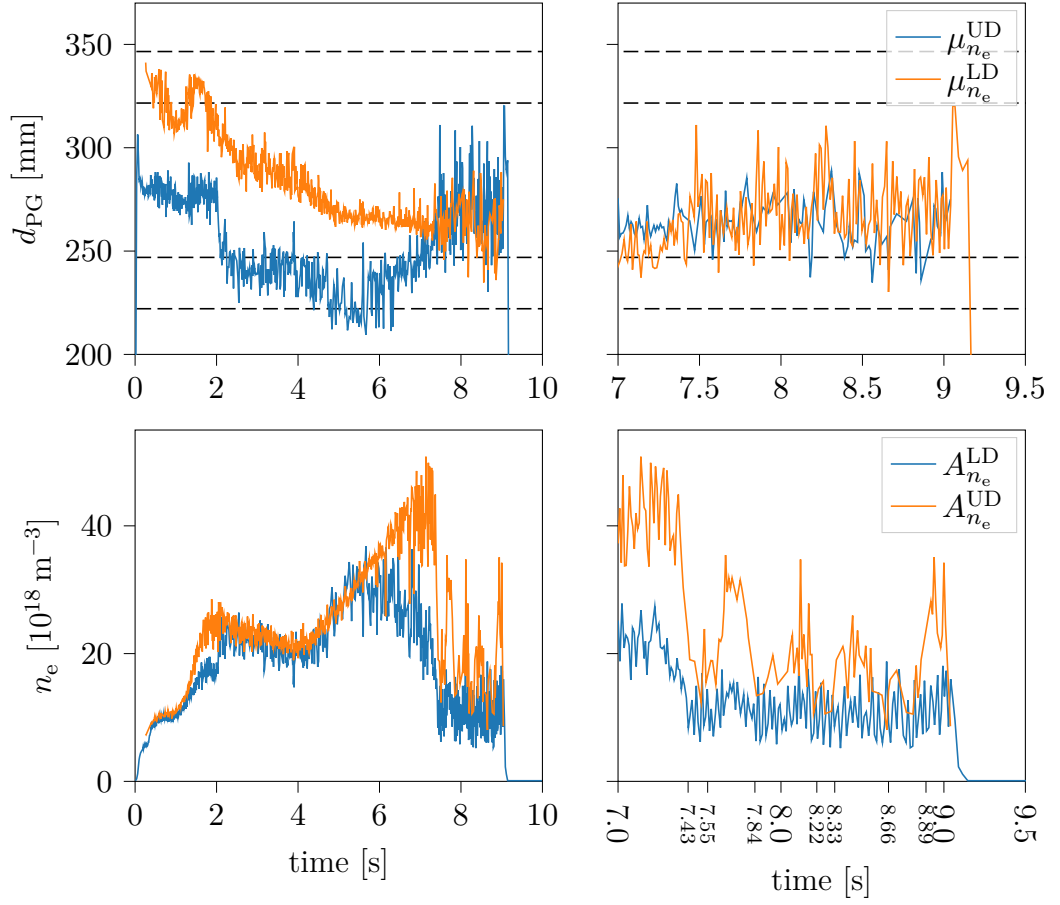


Figure 5.20.: Mode position μ_{n_e} and amplitude A_{n_e} of two-sided Gaussian fits to LP densities. Horizontal dashed lines indicate position of probes.

threshold effect, as A_{T_e} barely changes for $t > 6$ s (see Figure 5.21). Fits of the LD LPs are slightly less stable as probe LD9 had to be excluded from the analysis due to an error in the inference procedure.

A possible explanation is that there are two different relevant mechanisms: The LD detaches due to increasing ndl and P_{rad} , with the typical pattern of n_e initially tracking the rise ndl from $t = 4$ s to 6 s, whereupon f_{rad} becomes significant at a level of $\approx 1/3$ and n_e falls gradually. n_e at UD on the other hand is sustained by the local gas source, until this is switched off

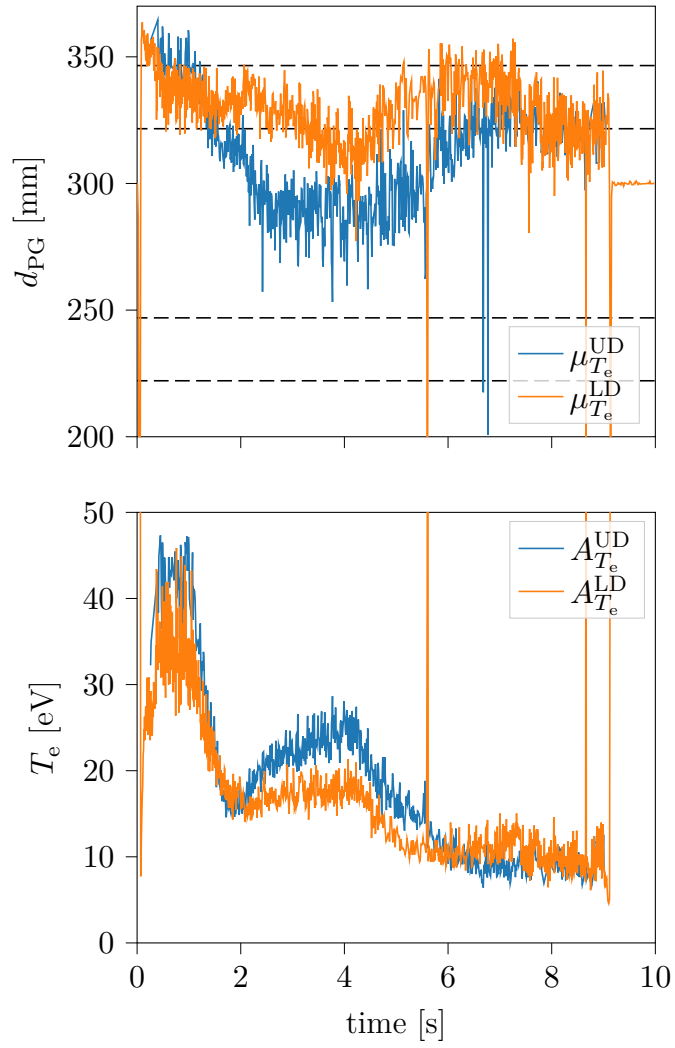


Figure 5.21.: Mode position μ_{T_e} and amplitude A_{T_e} of two-sided Gaussian fits to LP temperatures. Horizontal dashed lines indicate position of probes.

at 7.25 s and n_e crashes to match the LD level. Subsequent gas injections encounter a cold and relatively tenuous plasma, only ionize partially near the probes, and therefore have a weak and diffuse effect on measured n_e . At $T_e \approx 10$ eV the reduction from 50×10^{18} to $10 \times 10^{18} \text{ m}^{-3}$ corresponds to an increase of $\lambda_{\text{mfp}}^{\text{ion}}$ from approximately 3 to 14 cm, making distant ionisation plausible. This is of course only an indication as the relevant temperatures and densities are not those at the surface but those above it, but magnitude and trend nonetheless support this hypothesis.

This explanation is to be rejected for three reasons. Firstly, the time traces of voltage applied to the HeBS gas valve and $A_{n_e}^{\text{UD}}$ correlate, but the order does not match the proposed explanation above. The closure of the valve at $t = 7.43$ s occurs *after* the reduction of n_e , subsequent closures coincide with increases of n_e or have no effect. Secondly, the valve only closes for ≈ 10 ms, too short to explain the dip of n_e for $\mathcal{O}(200 \text{ ms})$. Thirdly, inspecting the heatflux profiles on all divertor units in Figure 5.22 we see that the up-down asymmetry we initially ascribed to the location of the fuelling valve is in fact present throughout the machine.

The sharp peaks in the ndl signal can be explained by the rotating bands (Figure 5.23) observed by the Event Detection Intelligent Camera (EDICAM) system [135]. These bands are regions of locally increased density which pass through the interferometry LOS. The ndl signal is fed to the HeBS gas injection feedback, which was set to average over seven 2 ms samples. This averaging explains why the majority of ndl peaks do not cause a closure of the gas valve, despite the control parameter derived from the interferometer signal temporarily exceeding the threshold value (Figure 5.24). The locally increased P_{rad} finally causes a reduction of heat and particle flux, mainly through a reduction of density (Figure 5.25).

A more plausible explanation is therefore a phenomenon that both causes the fluctuations of $A_{n_e}^{\text{UD}}$ and, by simultaneously affecting ndl , leads to a closing of the gas valve. This could be something similar to a multifaceted asymmetric radiation from the edge (MARFE) [136–138], a thermal edge instability occurring in tokamaks. A related phenomenon is the self-regulated plasma edge beneath the last-closed-flux-surface (Serpens) mode observed in large helical device (LHD) [139]. Possible MARFEs were previously observed and described in W7-X during the limiter campaign [140]. Comparing typical features listed in the references above in Table 5.4, we observe many also in discharge 20181004.048.

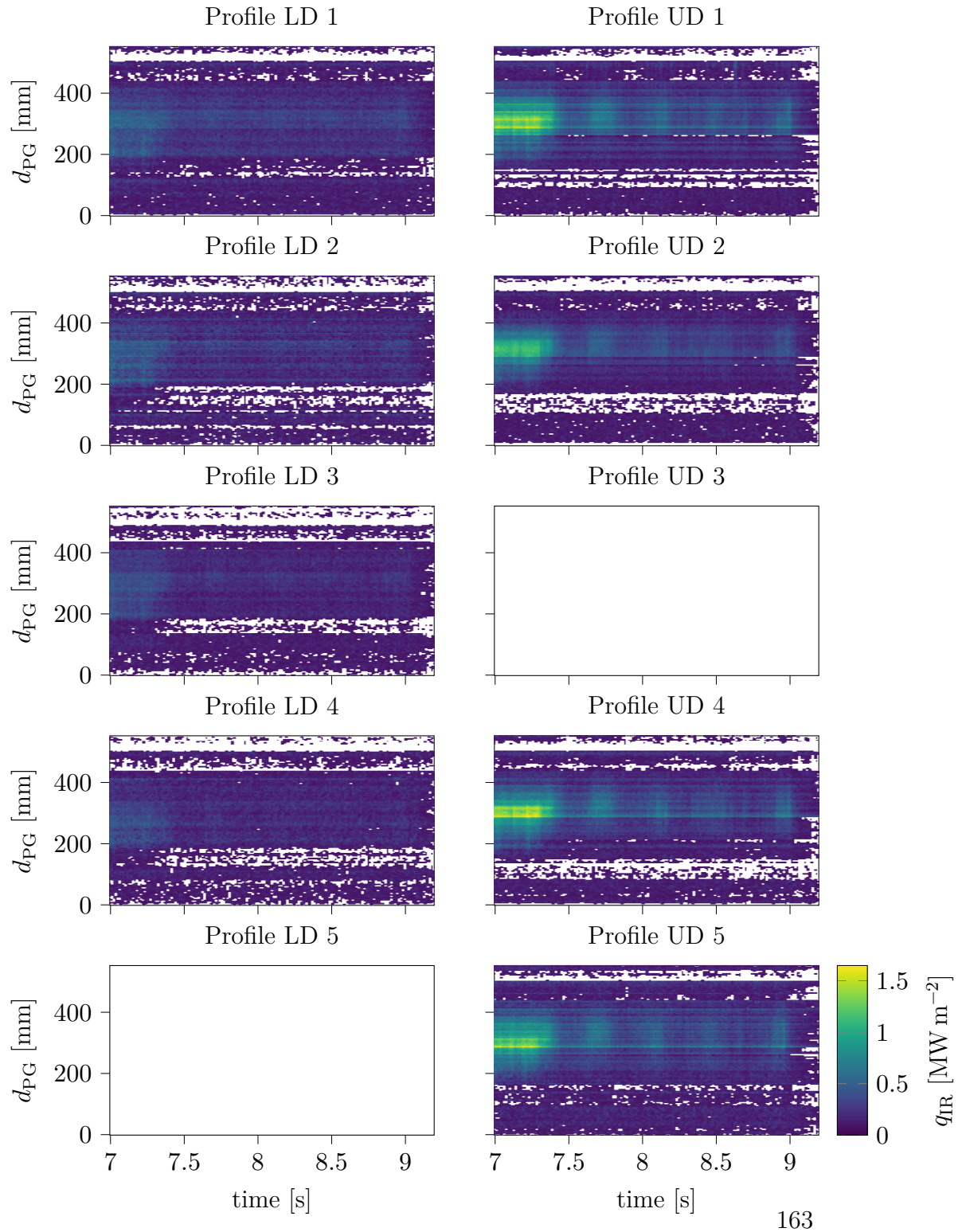


Figure 5.22.: Heatflux profile adjacent to LPs for all IRCs of 20181004.048. The number refers to the module. Data from cameras in modules 3 and 5 missing because of overheated charge-coupled device (CCD) chip and unavailable data from endoscopic camera respectively. Prominent up-down symmetry, no effect of fuelling in module 5 discernable.



Figure 5.23.: Visible spectrum camera frame from AEQ51 port onto half module 51 divertor in 20181004.048 at $t = 7.7$ s. Bright region at centre-right of image is the vertical divertor target. Radiation band extends further along FLs beyond divertor to bottom-right of image. At centre-left, bands of radiation above the wall are visible.

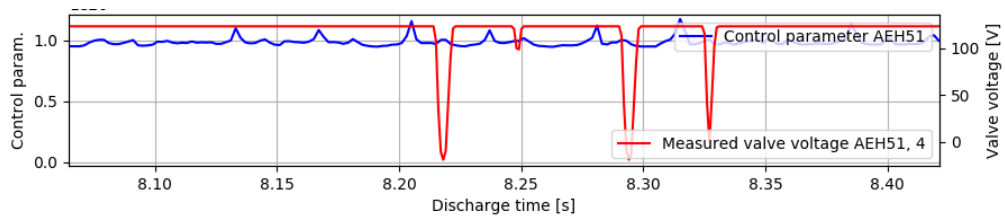


Figure 5.24.: ndl control parameter and feedback response voltage of HeBS showing delaying effect of rolling average.

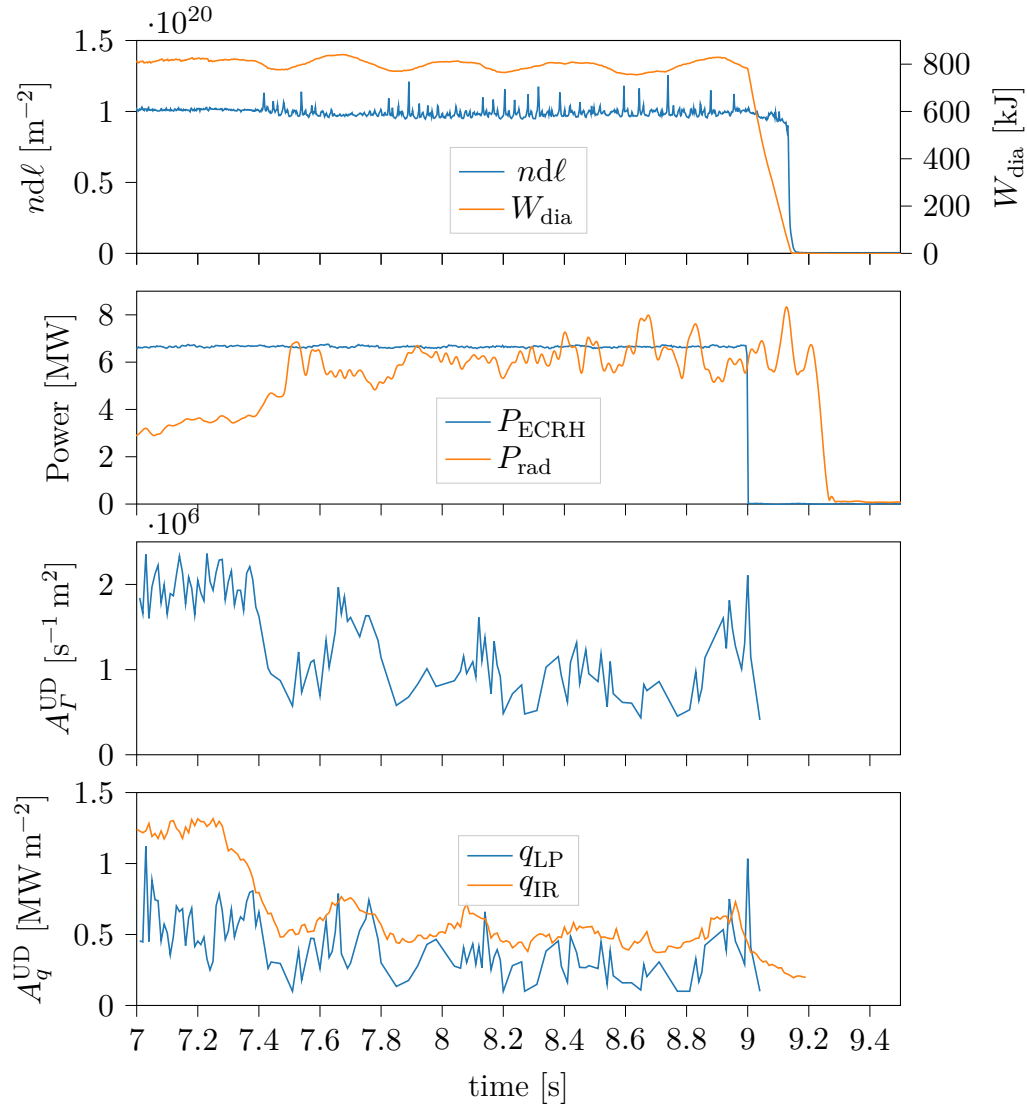


Figure 5.25.: Global measurements during fluctuating phase. Increase in P_{rad} corresponds to decrease of q and T . Top panel: $nd\ell$ measured by the interferometer showing spikes on an otherwise constant signal. W_{dia} approximately constant until ECRH is turned off. Second panel: Injected and radiated power showing $f_{\text{rad}} \approx 1$ with significant fluctuations. Third panel: A_T^{UD} . Fourth panel: LP A_q^{UD} measured by IRC and LPs with $\gamma_s = 6.5$.

Table 5.4.: MARFE features and observations.

Typical MARFE features	Observations in W7-X XP 20181004.048
Toroidally continuous structure	Effect on all UDs (Figure 5.22) and extended radiation bands (Figure 5.23).
Increases in local n_e	Sharp peaks in interferometer signal (Figure 5.25 top panel).
Increase of low- Z , low-state radiation	Broad peaks in bolometry signal (Figure 5.25 second panel), visible radiation confined to edge (Figure 5.23).
Increased edge n_e fluctuation amplitude	Fluctuation amplitude more than doubles (Figure 5.26).
Constant core conditions	Little variation of W_{dia} and constant baseline of ndl (Figure 5.25 top panel).
Decrease of local T_e	Not observed, T_e stays constant (Figure 5.21)

With the exception of the last item in Table 5.4, these observations constitutes strong evidence for the hypothesis that this discharge transitions into some MARFE-like state.

To further investigate this, relevant diagnostics such as the EDICAM and bolometry systems should be used to pinpoint the trajectory of individual radiation bands and correlate these with the LP time traces. In this way, low- and high-radiation regions can be mapped to T_e or n_e peaks.

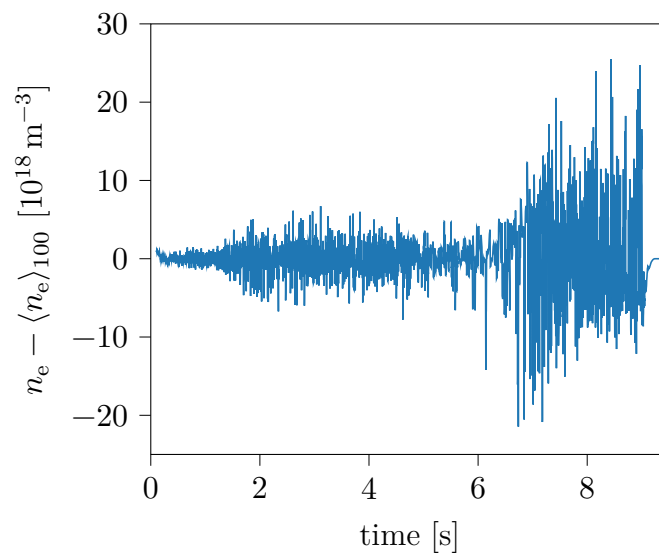


Figure 5.26.: n_e signal of UD6 after subtraction of 100 sample centred rolling average. Doubling of fluctuation amplitude after $t = 6.25$ s.

6

Summary

In this thesis, measurements made with Langmuir probes in the divertor of Wendelstein 7-X (W7-X) were thoroughly analysed, thereby characterising important plasma parameters and shedding light on fusion plasma edge processes.

The foundations are the evaluation of the Langmuir probes (LPs). They are deep by being based on physically explainable and understood models. One of these is the double Weinlich-Carlson sheath expansion model (DWSE) describing the magnetic and electrostatic sheath expansion around each probe and the restricted return current source. These cause a V_{LP} -dependent increase of the collected I_{sat} and reduction of $I_{e,sat}$. By automating the analysis process the foundations are widened: Through the implementation in the **Minerva** framework, results are consistently obtained without manual, expert intervention required and made available for all experiments for which raw data was collected. The robustness of the foundations has been ensured by testing large numbers of Current-Voltage characteristics (IV-characteristics) and comparing not only different models, but also algorithms for data segmentation, averaging and error estimation. A key result is shown in Figure 6.1: In cases when fit quality is distinguishable, there is a clear preference for the DWSE model. This is shown to generally be the case across many IV-characteristics in Figure 2.19. Table 6.1 shows that this model choice is important, as inferred parameters differ significantly even where there is no preference for a particular model.

The evaluation using Bayesian inference is the first of LPs in fusion plasmas. The modular implementation of models and evaluation offers not only the possibility of extension, but also reuse by the scientific community.

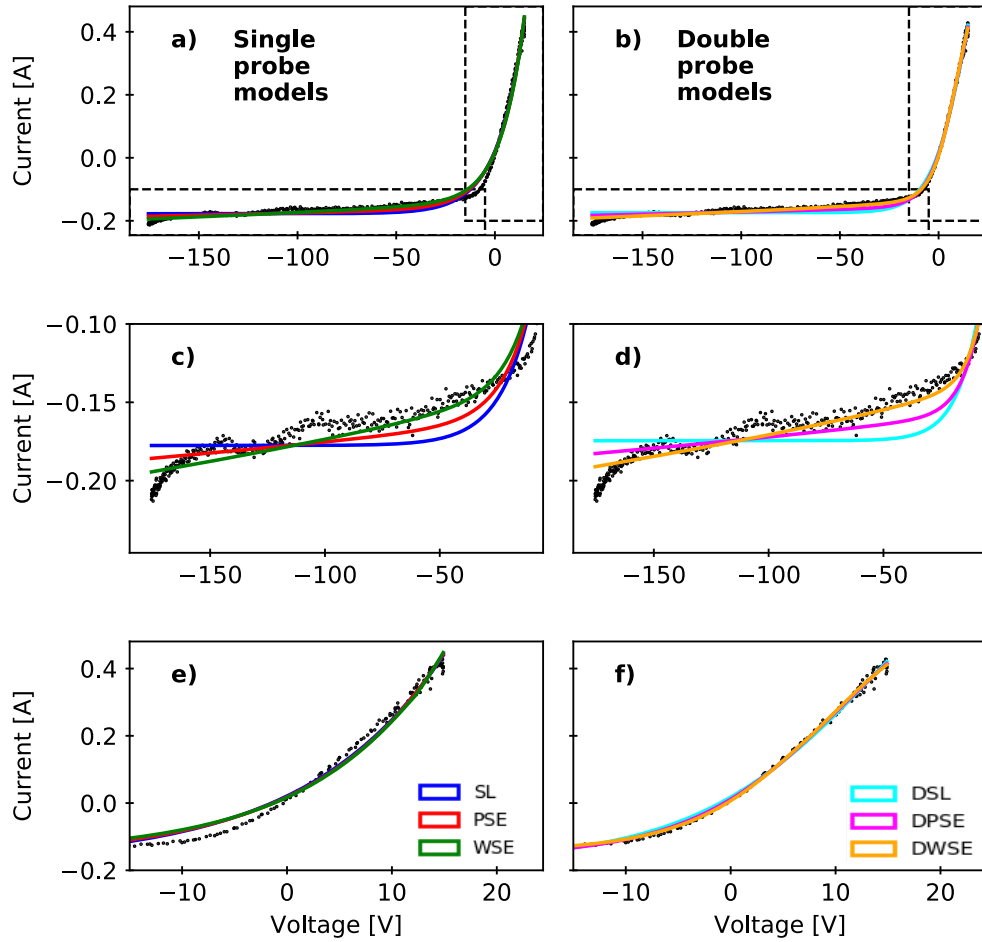


Figure 6.1.: Example I-V plots showing all six models from Table 2.2, overlaid over the same raw data in all panels. The DWSE model fits the data best. Parameter values of fits in Table 2.5. Data from probe UD10, experiment 20180814.007, $t=6.115$ s. Strong edge radiation regime.

Table 6.1.: Key result: Model choice matters even when all fit equally well. Parameter values for one IV-characteristic during attached divertor operation differ, even though χ^2_ν is between 0.241 and 0.248 for all.

	T_e [eV]	n_e [$10^{18}m^{-3}$]	V_f [V]	β
SL	54(2)	4.3(0.1)	-7.1(0.5)	-
PSE	47(2)	4.1(0.1)	-6.8(0.5)	-
WSE	38(1)	3.7(0.1)	-6.5(0.5)	-
DSL	53(2)	4.3(0.1)	-7.2(0.5)	50(43)
DPSE	46(2)	4.1(0.1)	-6.9(0.5)	50(45)
DWSE	37(1)	3.7(0.1)	-6.6(0.5)	50(48)

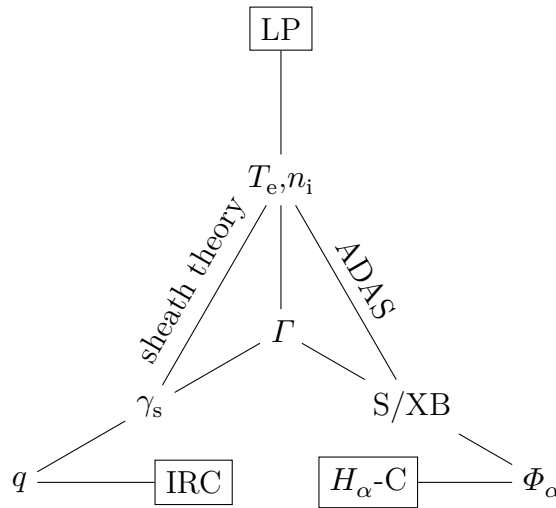


Figure 6.2.: Measurement network of heat flux q and particle flux Γ diagnostics. By comparing measurements discrepancies can be identified and intermediate factors determined.

The LP evaluation is reinforced by the comparison of calculated heat and particle fluxes with those measured by the Infrared-Camera (IRC) and H_α -Camera (H_α -C) systems. Through auxiliary assumptions and relations, more or less direct measurements of these quantities are connected in a measurement network shown in Figure 6.2. This network was realised through unifying data dimensions while preserving data attributes, such that operations could be performed on large amounts of data and dependencies

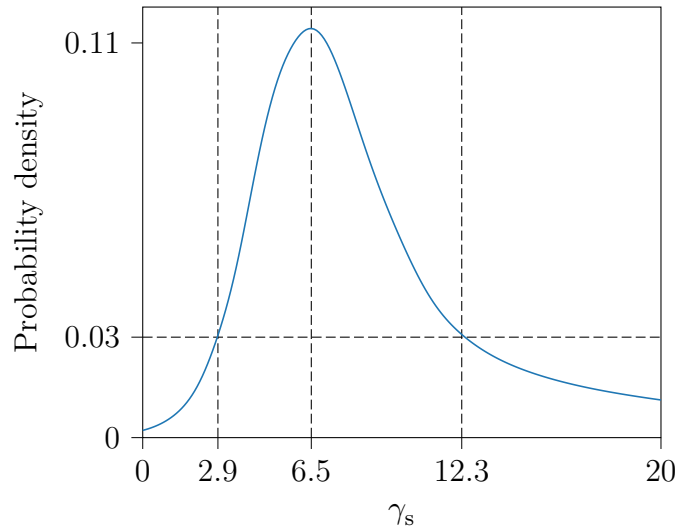


Figure 6.3.: Key result: Probability density function of γ_s . Most likely value is in agreement with theory and reported results from other experiments.

observed, in code that allows scaling the approach to additional discharges. Both comparisons succeeded in their aim to check consistency and identify inconsistencies, even if the sources of the latter could not be determined.

The first comparison showed good agreement with theoretical expectations and results from other, similar studies, culminating in the determination of the sheath transmission factor γ_s in Figure 6.3. Dependency studies clearly point at remaining problems, which should be further investigated using the established methods and inform trust intervals for the use of LP data.

The second comparison encountered major difficulties to reconcile the observations of particle flux diagnostics. A hypothesis was developed that differences may originate from separated measurement locations with varying plasma conditions. This is quantified and shown in Figure 6.4. This work is being actively continued and expanded by other researchers, as the scale of discrepancy was unexpected.

On the foundation of the LP data, a double gaussian (DG) fit method of parametrisation and data reduction was built to make it more easily understandable to and applicable for the W7-X team. The developed method can condense observations only accessible to the LPs such as T_e and n_e , as

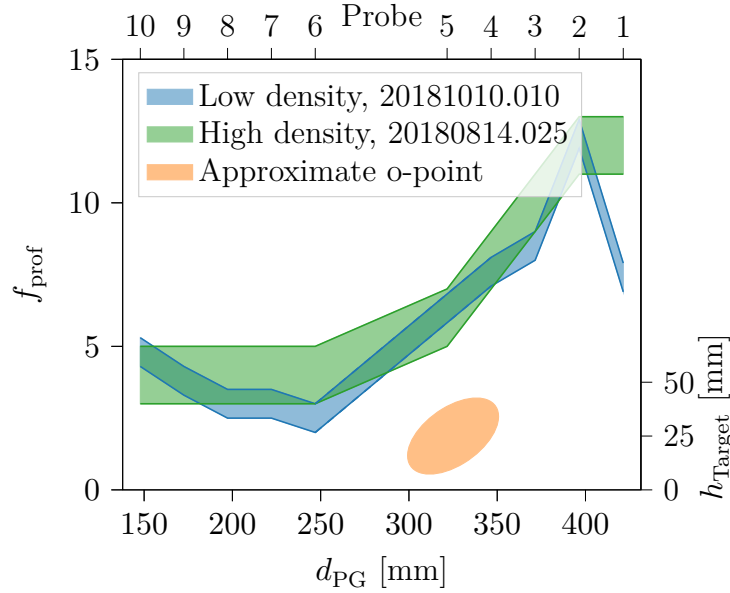


Figure 6.4.: Key result: Large discrepancy between measurements of particle flux and photon flux due to recycled neutrals, captured in the factor f_{prof} . Profiles of f_{prof} show a relation to island location.

well as supplement other diagnostics in parameter regions where they have low fidelity, as shown for the case of the IRC system in detached conditions in Figure 6.5. The parametrisation was used to support several aspects of the challenging and multi-faceted task to understand detachment in the W7-X island divertor in Chapter 5.

The questions of strike line (SL) broadening, drift-asymmetries and sequence of T_e and n_e reduction were examined and observations described. Detaching discharges were compared and reasons for differing evolution found in the state and behaviour of the wall gas reservoir. Though no definitive conclusions were reached, these observations can contribute to the evolving understanding of particle balance control, crucial for the further development of the helical advanced stellarator (Helias) line as a fusion reactor concept.

The full time resolution of the LP system was brought to bear on the question of the transition into detachment, in particular when comparing the LP data to other measures of the process. This revealed strong fluctuations

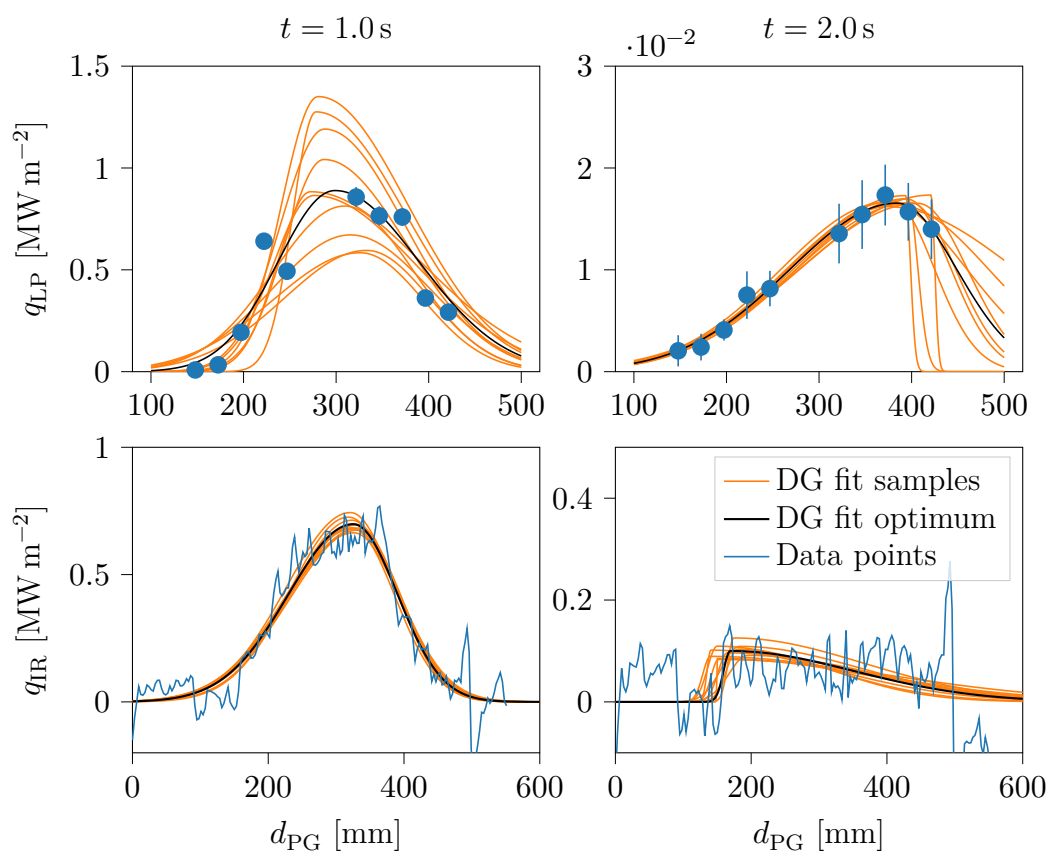


Figure 6.5.: Key results: Parametric fits of LP data can be compared to other diagnostics and supplement them where their fidelity is low. In this example LPs resolve the heat flux when it is below the IRC measurement threshold.

just prior to the rapid drop of heat flux, as shown in Figure 6.6.

An example of unstable detachment was examined and evidence in favour of and against the presence of multifaceted asymmetric radiation from the edges (MARFEs) phenomena gathered. Though much of it points towards a similarity of the processes responsible, the correlation of T_e and n_e shown in Figure 6.7 is inconclusive as to whether fluctuations transport cold plasma inwards to the core or hot plasma outwards.

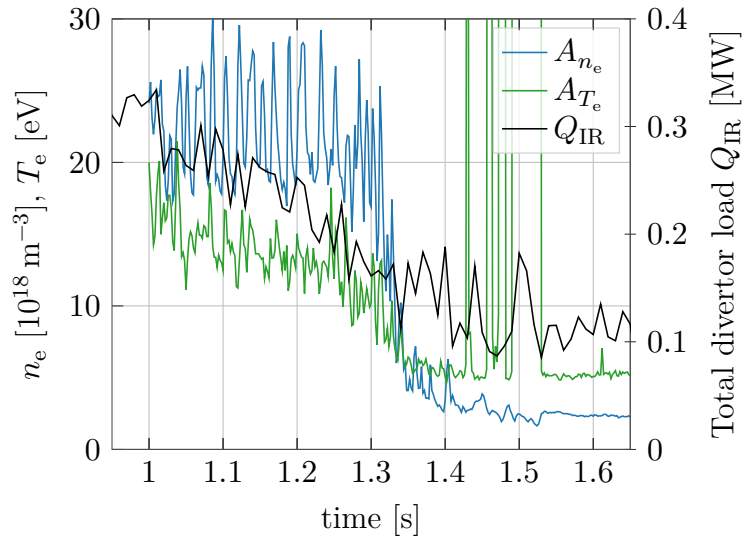


Figure 6.6.: The time resolution of the LPs reveals fluctuations prior to the detachment transition, particularly in n_e , which drops non-linearly compared to the gradual reduction in T_e .

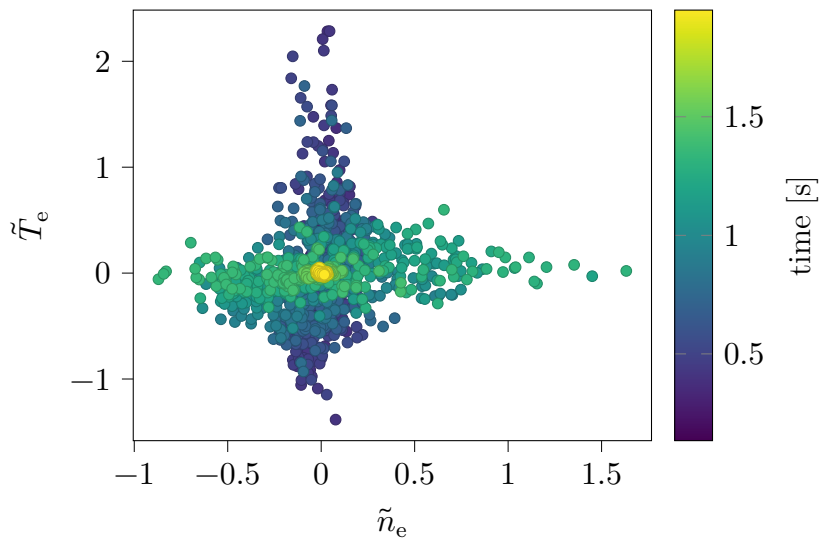


Figure 6.7.: During unstable detachment, scatter of normalised T_e and n_e fluctuations shows no correlation, only time dependence. This casts doubt on whether the observed phenomena are MARFES.

The next challenges will be to apply what has been learnt about LP models to the new operation phase (OP) 2 pop-up probes, using the established framework for further refinement. The consistency checks with other diagnostics should be followed up on to find the reason for discrepancies and their parametric dependencies. Consistent measurements of all aspects of divertor physics in W7-X should be the basis for the holistic understanding of detachment that is being pursued.

Bibliography

- [1] H.-S. BOSCH and G. HALE. »Improved formulas for fusion cross-sections and thermal reactivities«. In: *Nuclear Fusion*, Vol. 33.12 (1993), page 1919.
- [2] J. D. LAWSON. »Some Criteria for a Power Producing Thermo-nuclear Reactor«. In: *Proceedings of the Physical Society, Section B*, Vol. 70.1 (Jan. 1957), pages 6–10. DOI: 10.1088/0370-1301/70/1/303.
- [3] F. HERNÁNDEZ and P. PERESLAVTSEV. »First principles review of options for tritium breeder and neutron multiplier materials for breeding blankets in fusion reactors«. In: *Fusion Engineering and Design*, Vol. 137 (2018), pages 243–256. DOI: <https://doi.org/10.1016/j.fusengdes.2018.09.014>.
- [4] M. ASPLUND, N. GREVESSE and A. SAUVAL. »The new solar abundances - Part I: the observations«. In: *Communications in Asteroseismology*, Vol. 147 (2006), pages 76–79.
- [5] S. HUDSON et al. »Computation of multi-region relaxed magneto-hydrodynamic equilibria«. In: *Physics of Plasmas*, Vol. 19.11 (2012), page 112502.
- [6] P. HELANDER. »Theory of plasma confinement in non-axisymmetric magnetic fields«. In: *Reports on Progress in Physics*, Vol. 77.8 (2014), page 087001.
- [7] P. W. ANDERSON. *Basic notions of condensed matter physics*. CRC Press, 2018.
- [8] M. LANDREMAN and P. J. CATTO. »Omnigenity as generalized quasisymmetry«. In: *Physics of Plasmas*, Vol. 19.5 (2012), page 056103. DOI: 10.1063/1.3693187.

- [9] J. C. HILLESHEIM et al. »Stationary Zonal Flows during the Formation of the Edge Transport Barrier in the JET Tokamak«. In: *Physical Review Letters*, Vol. 116 (6 Feb. 2016), page 065002. DOI: 10.1103/PhysRevLett.116.065002.
- [10] L. SPITZER. »The Stellarator Concept«. In: *The Physics on Fluids*, Vol. 1 (1958). DOI: 10.1063/1.1705883.
- [11] G. BONGIOVÍ et al. »Assessment of potential heat flux overload of target and first wall components in Wendelstein 7-X finite-beta magnetic configurations and choice of locations for temperature monitoring«. In: *Fusion Engineering and Design*, Vol. 161 (2020), page 111902. DOI: <https://doi.org/10.1016/j.fusengdes.2020.111902>.
- [12] H. BOLT et al. »Plasma facing and high heat flux materials – needs for ITER and beyond«. In: *Journal of Nuclear Materials*, Vol. 307-311 (2002), pages 43–52. DOI: [https://doi.org/10.1016/S0022-3115\(02\)01175-3](https://doi.org/10.1016/S0022-3115(02)01175-3).
- [13] P. NORAJITRA et al. »Divertor conceptual designs for a fusion power plant«. In: *Fusion Engineering and Design*, Vol. 83.7 (2008). Proceedings of the Eight International Symposium of Fusion Nuclear Technology, pages 893–902. DOI: <https://doi.org/10.1016/j.fusengdes.2008.05.022>.
- [14] G. SCHLISIO et al. »The evolution of the bound particle reservoir in Wendelstein 7-X and its influence on plasma control«. In: *Nuclear Fusion*, (2020). DOI: <https://doi.org/10.1088/1741-4326/abd63f>.
- [15] A. LANGENBERG et al. »Charge-state independent anomalous transport for a wide range of different impurity species observed at Wendelstein 7-X«. In: *Physics of Plasmas*, Vol. 27.5 (2020), page 052510.
- [16] V. PERSEO et al. »Direct measurements of counter-streaming flows in a low-shear stellarator magnetic island topology«. In: *Nuclear Fusion*, Vol. 59.12 (2019), page 124003.

-
- [17] A. FIL et al. »Separating the roles of magnetic topology and neutral trapping in modifying the detachment threshold for TCV«. In: *Plasma Physics and Controlled Fusion*, Vol. 62.3 (Jan. 2020), page 035008. DOI: 10.1088/1361-6587/ab69bb.
- [18] T. PETRIE et al. »Effect of changes in separatrix magnetic geometry on divertor behaviour in DIII-D«. In: *Nuclear Fusion*, Vol. 53.11 (2013), page 113024.
- [19] W. MORRIS et al. »MAST upgrade divertor facility: a test bed for novel divertor solutions«. In: *IEEE Transactions on Plasma Science*, Vol. 46.5 (2018), pages 1217–1226.
- [20] T. S. PEDERSEN et al. »First divertor physics studies in Wendelstein 7-X«. In: *Nuclear Fusion*, Vol. 59.9 (2019), page 096014.
- [21] M. HIRSCH et al. »Major results from the stellarator Wendelstein 7-AS«. In: *Plasma Physics and Controlled Fusion*, Vol. 50.5 (2008), page 053001.
- [22] A. KOMORI et al. »Edge plasma control by local island divertor in LHD«. In: *Nuclear Fusion*, Vol. 45.8 (2005), page 837.
- [23] N. OHYABU et al. »The large helical device (LHD) helical divertor«. In: *Nuclear Fusion*, Vol. 34.3 (1994), page 387.
- [24] A. BADER et al. »HSX as an example of a resilient non-resonant divertor«. In: *Physics of Plasmas*, Vol. 24 (3 Mar. 2017), page 032506. DOI: 10.1063/1.4978494.
- [25] H. NIEMANN et al. »Large wetted areas of divertor power loads at Wendelstein 7-X«. In: *Nuclear Fusion*, Vol. 60.8 (2020), page 084003.
- [26] C. BEIDLER et al. »Physics and Engineering Design for Wendelstein VII-X«. In: *Fusion Technology*, Vol. 17.1 (Jan. 1990), pages 148–168. DOI: <https://doi.org/10.13182/FST90-A29178>.
- [27] T. KLINGER et al. »Overview of first Wendelstein 7-X high-performance operation«. In: *Nuclear Fusion*, Vol. 59.11 (2019), page 112004.
- [28] M. ENDLER et al. »Wendelstein 7-X on the path to long-pulse high-performance operation«. In: *SOFT2020 conference proceedings*, (Feb. 2021).

- [29] T. SUNN PEDERSEN et al. »First results from divertor operation in Wendelstein 7-X«. In: *Plasma Physics and Controlled Fusion*, Vol. 61.1 (Jan. 2019), page 014035. DOI: <https://doi.org/10.1088/1361-6587/aaec25>.
- [30] G. GRIEGER et al. »Physics optimization of stellarators«. In: *Physics of Fluids B: Plasma Physics*, Vol. 4.7 (July 1992), pages 2081–2091.
- [31] H.-S. BOSCH et al. »Technical challenges in the construction of the steady-state stellarator Wendelstein 7-X«. In: *Nuclear Fusion*, Vol. 53.12 (Dec. 2013), page 126001. DOI: <https://doi.org/10.1088/0029-5515/53/12/126001>.
- [32] J. GEIGER et al. »Aspects of steady-state operation of the Wendelstein 7-X stellarator«. In: *Plasma Physics and Controlled Fusion*, Vol. 55.1 (2012), page 014006.
- [33] V. ERCKMANN et al. »Electron Cyclotron Heating for W7-X: Physics and Technology«. In: *Fusion Science and Technology*, Vol. 52.2 (Aug. 2007). Edited by N. A. UCKAN and M. A. HENDERSON, pages 291–312. DOI: <https://doi.org/10.13182/FST07-A1508>.
- [34] G. GRIEGER et al. »Physics Studies for Helical-Axis Advanced Stellarators«. In: *Proceedings of the 12th Conference on Plasma Physics and Controlled Nuclear Fusion Research, Nice, France, 12–19 October 1988*. Vol. 2. paper IAEA-CN-50/C-1-4. International Atomic Energy Agency. IAEA, 1989, pages 369–387.
- [35] Y. FENG et al. »Comparison between stellarator and tokamak divertor transport«. In: *Plasma Physics and Controlled Fusion*, Vol. 53.2 (Feb. 2011). Special section on physics at the stellarator-tokamak interface, <http://stacks.iop.org/PPCF/53/024009>, page 024009.
- [36] H. RENNER et al. »Physical Aspects and Design of the Wendelstein 7-X Divertor«. In: *Fusion Science and Technology*, Vol. 46.2 (Sept. 2004). Edited by N. A. UCKAN, R. ANDREANI and Y. SHIMOMURA. Special Issue: Fourteenth International Stellarator Workshop (Part 2), Greifswald, Germany, September 22–26, 2003, pages 318–326.

-
- [37] J. BOSCARY et al. »Actively water-cooled plasma facing components of the Wendelstein 7-X stellarator«. In: *Fusion Science and Technology*, Vol. 64.2 (Aug. 2013). Edited by N. A. UCKAN, R. ANDREANI and Y. SHIMOMURA. Proceedings of the Twentieth Topical Meeting on the Technology of Fusion Energy (TOFE-2012) (Part 1), Nashville, Tennessee, August 27–31, 2012, pages 263–268. DOI: <https://doi.org/10.13182/FST12-499>.
- [38] A. PEACOCK et al. »Progress in the design and development of a test divertor (TDU) for the start of W7-X operation«. In: *Fusion Engineering and Design*, Vol. 84.7–11 (June 2009). Edited by H. ZOHM. Proceedings of the 25th Symposium on Fusion Technology (SOFT-25), Rostock, Germany, 15–19 September 2008, pages 1475–1478.
- [39] M. JAKUBOWSKI et al. »Heat and particle flux detachment with stable plasma conditions in the Wendelstein 7-X stellarator fusion experiment«. 2020. arXiv: 2001.02067 [physics.plasm-ph].
- [40] M. WEINLICH and A. CARLSON. »Flush mounted Langmuir probes in an oblique magnetic field«. In: *Physics of Plasmas*, Vol. 4.6 (1997), pages 2151–2160.
- [41] L. RUDISCHHAUSER et al. »The Langmuir probe system in the Wendelstein 7-X test divertor«. In: *Review of Scientific Instruments*, Vol. 91.6 (2020), page 063505.
- [42] T. S. PEDERSEN et al. »Confirmation of the topology of the Wendelstein 7-X magnetic field to better than 1:100,000«. In: *Nature Communications*, Vol. 7.1 (2016), pages 1–10.
- [43] K. HAMMOND et al. »Drift effects on W7-X divertor heat and particle fluxes«. In: *Plasma Physics and Controlled Fusion*, Vol. 61.12 (2019), page 125001.
- [44] S. A. LAZERSON et al. »Error fields in the Wendelstein 7-X stellarator«. In: *Plasma Physics and Controlled Fusion*, Vol. 60.12 (2018), page 124002.
- [45] M. JAKUBOWSKI et al. »Infrared imaging systems for wall protection in the W7-X stellarator«. In: *Review of Scientific Instruments*, Vol. 89.10 (2018), 10E116.

- [46] R. LAUBE et al. »Designs of Langmuir probes for W7-X«. In: *Fusion Engineering and Design*, Vol. 86.6-8 (2011), pages 1133–1136.
- [47] A. KUANG et al. »The flush-mounted rail Langmuir probe array designed for the Alcator C-Mod vertical target plate divertor«. In: *Review of Scientific Instruments*, Vol. 89.4 (2018), page 043512.
- [48] J. D. LORE et al. »Modeling and Preparation for Experimental Testing of Heat Fluxes on W7-X Divertor Scraper Elements«. In: *IEEE Transactions on Plasma Science*, Vol. 46.5 (2018), pages 1387–1392. DOI: 10.1109/TPS.2017.2780624.
- [49] R. PEIERLS. »Model-making in physics«. In: *Contemporary Physics*, Vol. 21.1 (1980), pages 3–17.
- [50] A. GELFERT. »Cultures of Modelling: Rudolf Peierls on ‘Model-Making in Physics’«. In: *Studia Metodologiczne*, Vol. 39 (2019), pages 49–71. DOI: 10.14746/sm.2019.39.2.
- [51] D. M. BAILER-JONES. »Scientists’ thoughts on scientific models«. In: *Perspectives on Science*, Vol. 10.3 (2002), pages 275–301.
- [52] K.-U. RIEMANN. »The Bohm criterion and sheath formation«. In: *Journal of Physics D: Applied Physics*, Vol. 24.4 (1991), page 493.
- [53] R. J. GOLDSTON. *Introduction to plasma physics*. CRC Press, 2020.
- [54] N. HERSHKOWITZ. »How Langmuir probes work«. In: *Plasma Diagnostics*, Vol. 1 (1989), pages 113–183.
- [55] I. H. HUTCHINSON. »Principles of Plasma Diagnostics«. In: *Plasma Physics and Controlled Fusion*, Vol. 44.12 (2002), page 2603.
- [56] P. C. STANGEBY. *The Plasma Boundary of Magnetic Fusion Devices*. 1st ed. Institute of Physics Publishing, 2000.
- [57] L. RUDISCHHAUSER et al. »Characterisation of power flux reduction in the Wendelstein 7-X divertor plasma with Langmuir probes«. In: *45th EPS Conference on Plasma Physics*. European Physical Society. 2018.
- [58] L. RUDISCHHAUSER et al. »Characterisation of the Wendelstein 7-X divertor plasma with Langmuir probes«. In: *Verhandlungen der Deutschen Physikalischen Gesellschaft*. Deutsche Physikalische Gesellschaft. 2018.

-
- [59] J. G. LAFRAMBOISE. *Theory of spherical and cylindrical Langmuir probes in a collisionless, Maxwellian plasma at rest*. Technical report. Toronto University Downsview (Ontario) Institute for Aerospace Studies, 1966.
- [60] C. TSUI et al. »Accounting for Debye sheath expansion for proud Langmuir probes in magnetic confinement fusion plasmas«. In: *Review of Scientific Instruments*, Vol. 89.1 (2018), page 013505.
- [61] A. BERGMANN. »Two-dimensional particle simulation of the current flow to a flush-mounted Langmuir probe in a strong oblique magnetic field«. In: *Physics of Plasmas*, Vol. 9.8 (2002), pages 3413–3420.
- [62] M. WEINLICH. *Elektrostatische Sonden in starken Magnetfeldern*. PhD thesis. Technical University of Munich, 1995.
- [63] V. ROZHANSKY, A. USHAKOV and S. VOSKOBOYNIKOV. »Electric fields and currents in front of a biased electrode (flush mounted probe) and the I-V characteristics of the electrode for various mechanisms of transverse conductivity«. In: *Nuclear Fusion*, Vol. 39.5 (1999), page 613.
- [64] I. HUTCHINSON. *Principles of Plasma Diagnostics*. 2nd ed. Cambridge University Press, 2002.
- [65] C. D. CHILD. »Discharge From Hot CaO«. In: *Physical Review (Series I)*, Vol. 32 (5 May 1911), pages 492–511. DOI: 10.1103/PhysRevSeriesI.32.492.
- [66] J. P. GUNN et al. »Flush-mounted Probes in the TdeV Tokamak: Theory and Experiment«. In: *Contributions to Plasma Physics*, Vol. 36.S1 (1996), pages 45–52. DOI: 10.1002/ctpp.19960360108.
- [67] A. PODOLNÍK et al. »Interpretation of flush-mounted probe current-voltage characteristics using four-parametric fits«. In: *Plasma Physics and Controlled Fusion*, Vol. 61.10 (Sept. 2019), page 105011. DOI: 10.1088/1361-6587/ab3de8.
- [68] R. CHODURA. »Plasma-wall transition in an oblique magnetic field«. In: *The Physics of Fluids*, Vol. 25.9 (1982), pages 1628–1633.
- [69] K. GUENTHER et al. »Characteristics of electric probes in the tokamak SOL: influences of the magnetic field«. In: *Journal of Nuclear Materials*, Vol. 176 (1990), pages 236–239.

- [70] R. MONK et al. »Interpretation of ion flux and electron temperature profiles at the JET divertor target during high recycling and detached discharges«. In: *Journal of Nuclear Materials*, Vol. 241 (1997), pages 396–401.
- [71] G. MATTHEWS et al. »Investigation of the fluxes to a surface at grazing angles of incidence in the tokamak boundary«. In: *Plasma Physics and Controlled Fusion*, Vol. 32.14 (1990), page 1301.
- [72] M. WEINLICH et al. »Return currents from a single probe in a magnetized plasma«. In: *Contributions to Plasma Physics*, Vol. 38.S1 (1998), pages 13–18.
- [73] K. MATSUMOTO and M. SATO. »Langmuir probe characteristic modulated with random fluctuations«. In: *Journal of Applied Physics*, Vol. 54.4 (1983), pages 1781–1786. DOI: 10.1063/1.332227.
- [74] D. LEE, N. HERSHKOWITZ and G. D. SEVERN. »Measurements of Ar⁺ and Xe⁺ velocities near the sheath boundary of Ar–Xe plasma using two diode lasers«. In: *Applied Physics Letters*, Vol. 91.4 (2007), page 041505. DOI: 10.1063/1.2760149.
- [75] T. LUNT, G. FUSSMANN and O. WALDMANN. »Experimental investigation of the plasma-wall transition«. In: *Physical Review Letters*, Vol. 100.17 (2008), page 175004.
- [76] D. BÖCKENHOFF, M. BLATZHEIM et al. »Application of improved analysis of convective heat loads on plasma facing components to Wendelstein 7-X«. In: *Nuclear Fusion*, Vol. 59.8 (2019), page 086031.
- [77] R. ANDRAE. »Error estimation in astronomy: A guide«. 2010. eprint: 1009.2755 (astro-ph).
- [78] J. SVENSSON and A. WERNER. »Large scale Bayesian data analysis for nuclear fusion experiments«. In: *2007 IEEE International Symposium on Intelligent Signal Processing*. IEEE. 2007, pages 1–6.
- [79] D. BÄTTIG. *Angewandte Datenanalyse*. 2nd ed. Springer Spectrum, 2017. DOI: 10.1007/978-3-662-54220-0.

-
- [80] J. SVENSSON et al. »Modelling of JET Diagnostics Using Bayesian Graphical Models«. In: *Contributions to Plasma Physics*, Vol. 51.23 (2011), pages 152–157. DOI: 10.1002/ctpp.201000058. eprint: <https://onlinelibrary.wiley.com/doi/pdf/10.1002/ctpp.201000058>.
- [81] M. HOLE et al. »The use of Bayesian inversion to resolve plasma equilibrium«. In: *Review of Scientific Instruments*, Vol. 81.10 (2010), 10E127.
- [82] E. PARZEN. »On Estimation of a Probability Density Function and Mode«. In: *The Annals of Mathematical Statistics*, Vol. 33.3 (Sept. 1962), pages 1065–1076. DOI: 10.1214/aoms/1177704472.
- [83] B. W. SILVERMAN. *Density Estimation for Statistics and Data Analysis*. 1st ed. Chapman & Hall/CRC Monographs on Statistics & Applied Probability. Taylor & Francis, 1986. URL: <https://www.crcpress.com/Density-Estimation-for-Statistics-and-Data-Analysis/Silverman/p/book/9780412246203>.
- [84] O. FÉVRIER et al. »Analysis of wall-embedded Langmuir probe signals in different conditions on the Tokamak à Configuration Variable«. In: *Review of Scientific Instruments*, Vol. 89.5 (2018), page 053502.
- [85] R. ANDRAE, T. SCHULZE-HARTUNG and P. MELCHIOR. »Dos and don'ts of reduced chi-squared«. 2010. arXiv: 1012.3754 [astro-ph].
- [86] T. STANGE et al. »Advanced electron cyclotron heating and current drive experiments on the stellarator Wendelstein 7-X«. In: *EPJ Web of Conferences*. Vol. 157. EDP Sciences. 2017, page 02008.
- [87] D. ZHANG et al. »Design criteria of the bolometer diagnostic for steady-state operation of the W7-X stellarator«. In: *Review of Scientific Instruments*, Vol. 81.10 (2010), 10E134.
- [88] E. PASCH et al. »The Thomson scattering system at Wendelstein 7-X«. In: *Review of Scientific Instruments*, Vol. 87.11 (2016), 11E729.
- [89] S. BOZHENKOV et al. »The Thomson scattering diagnostic at Wendelstein 7-X and its performance in the first operation phase«. In: *Journal of Instrumentation*, Vol. 12.10 (2017), P10004.

- [90] K. BRUNNER et al. »Real-time dispersion interferometry for density feedback in fusion devices«. In: *Journal of Instrumentation*, Vol. 13.09 (2018), P09002.
- [91] N. WILD, R. STENZEL and W. GEKELMAN. »Electron temperature measurements using a 12-channel array probe«. In: *Review of Scientific Instruments*, Vol. 54.8 (1983), pages 935–939.
- [92] S. MARSEN et al. »Experimental sheath heat transmission factors in diverted plasmas in JET«. In: *Journal of Nuclear Materials*, Vol. 438 (2013), S393–S396.
- [93] J. MARKI et al. »Sheath heat transmission factors on TCV«. In: *Journal of Nuclear Materials*, Vol. 363 (2007), pages 382–388.
- [94] H. NIEMANN et al. »Features of near and far scrape-off layer heat fluxes on the Wendelstein 7-X inboard limiters«. In: *Nuclear Fusion*, Vol. 60.1 (2019), page 016014.
- [95] R. A. LANGLEY et al. »Data compendium for plasma-surface interactions«. In: *Nuclear Fusion*, Vol. 24.S1 (1984), S9.
- [96] M. ENDLER et al. »Managing leading edges during assembly of the Wendelstein 7-X divertor«. In: *Plasma Physics and Controlled Fusion*, Vol. 61.2 (2018), page 025004.
- [97] S. A. BOZHENKOV et al. »Service oriented architecture for scientific analysis at W7-X. An example of a field line tracer«. In: *Fusion Engineering and Design*, Vol. 88.11 (2013), pages 2997–3006.
- [98] O. SCHMITZ et al. »Stable heat and particle flux detachment with efficient particle exhaust in the island divertor of Wendelstein 7-X«. In: *Nuclear Fusion*, (2020).
- [99] D. W. SCOTT. *Multivariate density estimation: theory, practice, and visualization*. John Wiley & Sons, 2015.
- [100] A. HERRMANN et al. »Energy flux to the ASDEX-Upgrade diverter plates determined by thermography and calorimetry«. In: *Plasma Physics and Controlled Fusion*, Vol. 37.1 (Jan. 1995), pages 17–29. DOI: 10.1088/0741-3335/37/1/002.

-
- [101] S. HOYER and J. HAMMAN. »xarray: N-D labeled arrays and datasets in Python«. In: *Journal of Open Research Software*, Vol. 5.1 (2017). DOI: 10.5334/jors.148.
- [102] S. HOYER, C. FITZGERALD, J. HAMMAN et al. *xarray: v0.8.0*. 2016. DOI: 10.5281/zenodo.59499.
- [103] E. DÍAZ-FRANCÉS and F. J. RUBIO. »On the existence of a normal approximation to the distribution of the ratio of two independent normal random variables«. In: *Statistical Papers*, Vol. 54.2 (2013), pages 309–323.
- [104] G. MARSAGLIA et al. »Ratios of normal variables«. In: *Journal of Statistical Software*, Vol. 16.4 (2006), pages 1–10.
- [105] M. HIRSCH et al. »ECE Diagnostic for the initial Operation of Wendelstein 7-X«. In: *EPJ Web of Conferences*. Vol. 203. EDP Sciences. 2019, page 03007.
- [106] J. KRUSCHKE. *Doing Bayesian data analysis: A tutorial with R, JAGS, and Stan*. Academic Press, 2014.
- [107] F. REIMOLD et al. »Experimental indications of high-recycling and the role of plasma pressure and power dissipation in the detachment evolution in W7-X«. In: *FEC2020*. Edited by IAEA. 2021.
- [108] H. YAMADA et al. »Characterization of energy confinement in net-current free plasmas using the extended International Stellarator Database«. In: *Nuclear Fusion*, Vol. 45.12 (2005), pages 1684–1693. DOI: 10.1088/0029-5515/45/12/024.
- [109] T. KREMEYER. *Particle Fueling and Exhaust in the Wendelstein 7-X Island Divertor*. The University of Wisconsin-Madison, 2019.
- [110] A. POSPIESZCZYK. *Diagnostics of edge plasmas by optical methods*. In: R. K. JANEV. *Atomic and Plasma-Material Interaction Processes In Controlled Thermonuclear Fusion*. Edited by H. W. DRAWIN. Amsterdam: Elsevier, 1993.
- [111] K. BEHRINGER et al. »Spectroscopic determination of impurity influx from localized surfaces«. In: *Plasma Physics and Controlled Fusion*, Vol. 31.14 (1989), page 2059.

- [112] R. KÖNIG et al. »The set of diagnostics for the first operation campaign of the Wendelstein 7-X stellarator«. In: *Journal of Instrumentation*, Vol. 10.10 (2015), P10002.
- [113] H. FRERICHS et al. »Synthetic plasma edge diagnostics for EMC3-EIRENE, highlighted for Wendelstein 7-X«. In: *Review of Scientific Instruments*, Vol. 87.11 (2016), page 11D441.
- [114] V. WINTERS. »EMC3-EIRENE simulation of first wall recycling fluxes and their relation to H-alpha spectroscopic signals«. In: *Plasma Physics and Controlled Fusion*, (2021). submitted.
- [115] T. KREMEYER et al. »Global particle balance to analyze fuelling, exhaust, recycling and particle confinement at Wendelstein 7-X«. In: *Nuclear Fusion*, (Feb. 2021).
- [116] D. ZHANG et al. »First Observation of a Stable Highly Dissipative Divertor Plasma Regime on the Wendelstein 7-X Stellarator«. In: *Physical Review Letters*, Vol. 123.2 (2019), page 025002.
- [117] S. SEREDA et al. »Impact of boronizations on impurity sources and performance in Wendelstein 7-X«. In: *Nuclear Fusion*, Vol. 60 (2020). DOI: <https://doi.org/10.1088/1741-4326/ab937b>.
- [118] F. EFFENBERG et al. »First demonstration of radiative power exhaust with impurity seeding in the island divertor at Wendelstein 7-X«. In: *Nuclear Fusion*, Vol. 59.10 (2019), page 106020.
- [119] O. FORD et al. »Charge exchange recombination spectroscopy at Wendelstein 7-X«. In: *Review of Scientific Instruments*, Vol. 91.2 (2020), page 023507.
- [120] R. SCHNEIDER. *Plasma edge physics for tokamaks*. Habilitation. University of Greifswald, 2001.
- [121] T. S. PEDERSEN et al. »First divertor physics studies in Wendelstein 7-X«. In: *Nuclear Fusion*, Vol. 59.9 (2019), page 096014.
- [122] A. U. TEAM et al. »Inter-ELM power decay length for JET and ASDEX Upgrade: measurement and comparison with heuristic drift-based model«. In: *Physical Review Letters*, Vol. 107.21 (2011), page 215001.

-
- [123] J. GEIGER et al. »Physics in the magnetic configuration space of W7-X«. In: *Plasma Physics and Controlled Fusion*, Vol. 57.1 (2014), page 014004.
- [124] W. LOTZ, J. NÜHRENBURG and C. SCHWAB. »Optimization, MHD mode and alpha particle confinement behaviour of Helias equilibria«. In: *Plasma Physics and Controlled Nuclear Fusion Research 1990. Volume 2*. 1991.
- [125] A. DINKLAGE et al. »Magnetic configuration effects on the Wendelstein 7-X stellarator«. In: *Nature Physics*, Vol. 14.8 (2018), pages 855–860.
- [126] Y. GAO et al. »Effects of toroidal plasma current on divertor power depositions on Wendelstein 7-X«. In: *Nuclear Fusion*, Vol. 59.10 (2019), page 106015.
- [127] M. STREVEVS. *The Knowledge Machine*. Liveright, 2020.
- [128] A. LOARTE et al. »Plasma detachment in JET Mark I divertor experiments«. In: *Nuclear Fusion*, Vol. 38.3 (1998), page 331.
- [129] J. BALDZUHN et al. »Enhanced energy confinement after series of pellets in Wendelstein 7-X«. In: *Plasma Physics and Controlled Fusion*, Vol. 62.5 (2020), page 055012.
- [130] P. HACKER. »Discussion on HEPP talk«. Private communication. Sept. 2020.
- [131] C. KILLER et al. »Plasma filaments in the scrape-off layer of Wendelstein 7-X«. In: *Plasma Physics and Controlled Fusion*, Vol. 62 (2020). DOI: <https://doi.org/10.1088/1361-6587/ab9313>.
- [132] S. ZOLETNIK et al. »Multi-diagnostic analysis of plasma filaments in the island divertor«. In: *Plasma Physics and Controlled Fusion*, Vol. 62.1 (2019), page 014017.
- [133] S. BALLINGER et al. »Fast camera imaging of plasmas in Alcator C-Mod and W7-X«. In: *Nuclear Materials and Energy*, Vol. 17 (2018), pages 269–273.
- [134] G. WURDEN et al. »Quasi-continuous low frequency edge fluctuations in the W7-X stellarator«. In: *45th EPS Conference on Plasma Physics*. European Physical Society. 2018.

- [135] T. SZEPESI et al. »Combining research with safety: Performance of the Wendelstein 7-X video diagnostic system«. In: *Fusion Engineering and Design*, Vol. 146 (2019), pages 874–877.
- [136] B. LIPSCHULTZ et al. »Marfe: an edge plasma phenomenon«. In: *Nuclear Fusion*, Vol. 24.8 (1984), page 977.
- [137] B. LIPSCHULTZ. »Review of MARFE phenomena in tokamaks«. In: *Journal of Nuclear Materials*, Vol. 145 (1987), pages 15–25.
- [138] J. WESSON and T. HENDER. »An extended treatment of MARFE stability«. In: *Nuclear Fusion*, Vol. 33.7 (1993), pages 1019–1024.
- [139] J. MIYAZAWA et al. »Density regimes of complete detachment and Serpens mode in LHD«. In: *Plasma and Fusion Research*, Vol. 1 (2006), pages 026–026.
- [140] U. WENZEL et al. »Observation of Marfes in the Wendelstein 7-X stellarator with inboard limiters«. In: *Nuclear Fusion*, Vol. 58.9 (2018), page 096025.

Acronyms

Acronym	Description
Databases	
ADAS	Atomic Data and Analysis Structure
Dynamical systems	
KAM	Kolmogorov–Arnold–Moser
Engineering	
ADC	analog-to-digital converter
CAD	computer-aided design
CCD	charge-coupled device
CMRR	common mode rejection ratio
DAmP	differential amplifier
EDICAM	Event Detection Intelligent Camera
IC	integrated circuit
LOS	line of sight
PCB	printed circuit board
PMT	photo-multiplier tube
ROI	region of interest
Gas Diagnostics	
DRGA	Diagnostic residual gas analyser
LIF	Laser induced fluorescence

Acronym	Description
General Physics	
IR	Infrared
Langmuir Probe Glossaries	
IV-characteristic	Current-Voltage characteristic
CLP	conventional Langmuir probe
DWSE	double Weinlich-Carlson sheath expansion model
PSE	perimeter sheath expansion model
SL	simple Langmuir model
WSE	Weinlich-Carlson sheath expansion model
Nuclear Fusion Experiments	
AUG	ASDEX Upgrade
DIII-D	Doublet III-D
Helias	helical advanced stellarator
HSX	Helically Symmetric Experiment
JET	Joint European Torus
JT-60	Japan Torus-60
LHD	large helical device
MAST	Mega-Ampere Spherical Tokamak
TCV	Tokamak à configuration variable
TEXT	Texas Tokamak
W7-AS	Wendelstein 7-AS
W7-X	Wendelstein 7-X
WEGA	Wendelstein Experiment in Greifswald für die Ausbildung
WEST	Tungsten Environment in Steady-state Tokamak (formerly Tore Supra)
Nuclear Fusion Machine Components	
HHFD	high heatflux divertor
LD	Lower divertor

Acronym	Description
NBI	neutral beam injection
PFC	plasma facing component
PG	Pumping Gap
TDU	test divertor unit
TDUSE	test divertor unit scraper element
TE	Target Element
UD	Upper divertor
Organisational	
OP	operation phase
Plasma Diagnostics	
H_{α} -C	H_{α} -Camera
H_{α} -S	H_{α} -Spectrometer
HeBS	Helium beam spectroscopy
IRC	Infrared-Camera
LP	Langmuir probe
Plasma Physics	
S/XB _{eff}	empirical, effective S/XB
S/XB _{th}	theoretical S/XB from T_e, n_e lookup
SEE	secondary electron emission
SE	sheath edge
ECCD	electron cyclotron current drive
ECE	electron cyclotron emission
ECRH	electron cyclotron resonance heating
FL	field line
ICRH	ion cyclotron radiation heating
MARFE	multifaceted asymmetric radiation from the edge
PWI	plasma wall interaction
Serpens	self-regulated plasma edge beneath the last-closed-flux-surface

Acronym	Description
SL	strike line
SOL	scrape-off layer
Plasma Physics Laboratories	
IPP	Max-Planck Institute for Plasma Physics
Plasma Theory	
LCFS	last closed flux surface
MHD	magnetohydrodynamic
Plasma Theory Codes	
EMC3-Eirene	Edge Monte Carlo 3D code coupled to the neutral transport code EIRENE
FLD	field line diffusion
FLT	field line tracing
THEODOR	Thermal Energy onto Divertor
Statistics	
DG	double gaussian
HDI	highest density interval
iid	independent and identically distributed
KDE	kernel density estimate
KS	Kolmogorov–Smirnov
LS	least-square
MAP	maximum a posteriori
Max- \mathcal{L}	maximum likelihood
MC	Monte Carlo
MCMC	Markov chain Monte Carlo
MHA	Metropolis-Hastings algorithm
PDF	probability density function
SSR	sum of squared residuals

W7-X Magnetic Configurations

Acronym	Description
DBM	low iota magnetic configuration
EIM	'standard' magnetic configuration in the centre of accessible space

List of Symbols

Symbol	Description	Unit
General physics quantities		
σ	Reaction cross-section	m
ρ	Larmor radius	m
Langmuir Probe Glossaries		
A_{coll}	Probe collection area	m ²
A_{proj}	Area of probe projection	m ²
P_{proj}	Perimeter of probe projection	m
f_{sweep}	Sweep frequency	Hz
β_{DP}	Double probe area ratio	
d	Probe size dimesion	m
I_{mod}	Model current	A
I_{LP}	Probe current	A
V_{LP}	Applied probe voltage	V
Nuclear Fusion Machine Components		
d_{PG}	Distance to PG	m

List of Symbols

Symbol	Description	Unit
Plasma physics quantities		
γ_i	Ion adiabatic coefficient	
S/XB	Ratio of ionisation, excitation and branching ratio. Inverse photons per neutral.	
I_{bs}	Bootstrap current	A
I_{tor}	Toroidal plasma current	A
ι	Rotational transform	
β	Plasma beta	
s	Shear, radial derivative of ι	
I_{sat}	Ion saturation current	A
$I_{e,sat}$	Electron saturation current	A
j_{sat}	Ion saturation current density	A m ⁻²
$nd\ell$	Line integrated density	m ⁻²
n_e	Electron density	m ⁻³
n_{imp}	Impurity density	m ⁻³
n_i	Ion density	m ⁻³
n_n	Neutral density	m ⁻³
W_{dia}	Diamagnetic energy	J
f_{prof}	S/XB correction factor	
Φ_α	H_α photon flux	s ⁻¹ sr
f_{rad}	Radiated power fraction	
f_{rec}	Fraction of ions recycled as neutrals at PFCs	
Z_{av}	Average ion charge	
Z_{eff}	Effective ion charge	

Symbol	Description	Unit
$\lambda_{\text{mfp},i}$	Mean free path length of ionisation	m
Γ	Particle flux	$\text{s}^{-1} \text{m}^{-2}$
V_{bias}	Bias voltage	V
V_{f}	Floating potential	V
V_{p}	Plasma potential	V
P_{ECRH}	ECRH Power	W
P_{rad}	Radiated power	W
q	Heat flux or heat load	MW m^{-2}
R	Major radius	m
ϵ	Aspect ratio	
ρ_i	Ion gyro (Lamor) radius	m
ϱ	Normalised minor radius	
r_{eff}	Effective minor radius	m
r	Minor radius	m
γ_{s}	Sheath transmission coefficient	
T_{e}	Electron temperature	eV
T_{i}	Ion temperature	eV
τ_{E}	Energy confinement time	s
c_{s}	Ion sound speed	m s^{-1}
v_{\perp}	Field-perpendicular velocity	m s^{-1}
H_{α}	Hydrogen α transition line, Balmer series transition $n = 3 \rightarrow n = 2$, 656.5 nm	nm

Statistics

r_{xy}	Pearson sample correlation coefficient
-----------------	--

List of Figures

1.1.	Binding energy per nucleon.	3
1.2.	Fusion cross sections of light-nuclei processes.	4
1.3.	Reactivity of the DT reaction.	5
1.4.	Schematic of nested toroidal flux surfaces.	9
1.5.	Schematic ι -profile of multiple devices over normalised radius. Strength of island resonances indicated on arbitrary scale by horizontal extent.	19
1.6.	Magnetic and vacuum system of W7-X torus.	21
1.7.	Measurement network of q and Γ diagnostics.	23
2.1.	View of one divertor module	28
2.2.	Probe numbering and naming of components.	29
2.3.	Schematic of the faceted probe surfaces.	31
2.4.	Simplified scheme of the measurement card circuit.	35
2.5.	Schematic view of our LPs with definitions	44
2.6.	Absolute sheath thickness in front of probe.	48
2.7.	Influence range of swept probes.	51
2.8.	Scheme of the mechanism of IV-characteristic separation with <code>VmaxClusterSlicer</code>	53
2.9.	Comparison of averaging methods	55
2.10.	Contours of sum of squared residuals (SSR) from grid evalu- ation.	58
2.11.	Minerva model for the LP diagnostic	59
2.12.	Exemplary IV-characteristic from <code>Minerva</code> implementation of LP analysis.	60
2.13.	Histogram of samples drawn from the posterior in T_e and n_e	61
2.14.	1-D posterior projection of T_e	62
2.15.	Schematic illustrating the algorithm to determine expected error σ_I	67

List of Figures

2.16. Example I-V plots showing all six models, strong edge radiation regime.	69
2.17. Example I-V plots showing all six models, attached divertor operation.	70
2.18. Overview of discharge 20180814.007.	72
2.19. Histogram of χ_ν^2 values for many IV-characteristics.	73
3.1. Scheme of sheath current densities.	79
3.2. Expected value of γ_s using values from Table 3.2. R indicates our Equation (3.15), S Stangeby's Equation (3.22).	84
3.3. Definition of α_{CF}	85
3.4. Schematic of γ_s angle dependence	86
3.5. Comparison of error propagation methods.	88
3.6. Poincaré plot at the cross section of the UD probes in DBM	91
3.7. Overview of discharge 20181004.048.	92
3.8. q_{LP}/γ_s poloidal profile over time.	93
3.9. q_{IR} poloidal profile adjacent to probes over time.	93
3.10. q_{LP}/γ_s poloidal profile of the probes over time on the unified grid.	94
3.11. q_{IR} poloidal profile adjacent to probes over time on the unified grid.	94
3.12. γ_s over time at each probe position.	95
3.13. Probability density obtained through kernel density estimate (KDE) [82, 83] of γ_s	95
3.14. γ_s - q_{LP} dependence	96
3.15. γ_s - q_{IR} dependence	97
3.16. γ_s - angle dependence	98
3.17. γ_s - T_e dependence	99
3.18. γ_s - n_e dependence	100
3.19. γ_s - time dependence	101
3.20. Consistency of data with γ_s	102
4.1. Theoretical S/XB from T_e, n_e lookup (S/XB_{th}) dependency on T_e and n_e	109
4.2. Poincaré plot of the Upper divertor (UD) island	110
4.3. Overview of discharge 20181010.010	111
4.4. H_α -C data of 20181010.010 at native resolution.	112

4.5.	Γ data of 20181010.010	112
4.6.	Empirical, effective S/XB (S/XB_{eff}) for discharge 20181010.010	113
4.7.	S/XB timetraces for 20181010.010	114
4.8.	f_{prof} for 20181010.010	115
4.9.	Profiles of f_{prof}	116
4.10.	Overview of discharge 20180814.025	117
4.11.	H_{α} -C data of 20180814.025 at reduced spatial resolution. . .	118
4.12.	Γ_{LP} data of 20180814.025 at native resolution.	118
4.13.	S/XB_{eff} (blue), S/XB_{th} (orange) and approximate f_{prof} * S/XB_{th} (green) for UDP1-10.	119
4.14.	Detail of particle flux transition of UD8.	120
4.15.	Causes of f_{prof} time variation.	121
5.1.	$\mu_{q_{\text{IR}}}$ of 20181004.048 illustrating problems of probe selection method.	132
5.2.	Global plasma quantities for 20181004.023 and 20181004.024.	136
5.3.	Visible spectrum image of radiation bands in 20181004.024.	137
5.4.	Total divertor loads for 20181004.023 and 20181004.024. . .	138
5.5.	q_{LP} profile parameters 20181004.023 & .024	140
5.6.	Selected q_{LP} profiles 20181004.024	141
5.7.	Selected q_{IR} profiles 20181004.024	141
5.8.	n_e profile parameters 20181004.023 & .024	142
5.9.	Selected n_e profiles 20181004.024	143
5.10.	T_e profile parameters 20181004.023 & .024	144
5.11.	Selected T_e profiles 20181004.024	145
5.12.	Lower divertor profiles	148
5.13.	Time evolution of qualitative edge radiation profile.	149
5.14.	Gas balance in terms of H_2 inventory.	150
5.15.	Transition into detachment of 20181004.024 at full time res- olution.	154
5.16.	q_{LP} profiles of detachment transition	155
5.17.	q_{LP} probe traces of detachment transition	156
5.18.	Scatter of normalised T_e and n_e fluctuations for UD6 in 20181004.024.	157
5.19.	Opening of Helium beam spectroscopy (HeBS) valve.	159
5.20.	μ_{n_e} and A_{n_e} 20181004.048	160
5.21.	μ_{T_e} and A_{T_e} 20181004.048	161

List of Figures

5.22. Heatflux profile adjacent to LPs for all IRCs.	163
5.23. Visible spectrum image of radiation bands in 20181004.048.	164
5.24. ndl control parameter and feedback response voltage of HeBS showing delaying effect of rolling average.	164
5.25. Increase in P_{rad} corresponds to decrease of q and Γ	165
5.26. n_e fluctuation amplitude 20181004.048	167
6.1. Key result: Example I-V plots showing superiority of DWSE model.	170
6.2. Measurement network of q and Γ diagnostics.	171
6.3. Key result: Probability density function of γ_s	172
6.4. Key result: Profiles of f_{prof}	173
6.5. Key results: DG fits of LP data	174
6.6. Fluctuations prior to the detachment transition observed.	175
6.7. Scatter of normalised T_e and n_e fluctuations.	175
A.1. Connection lengths and incidence angles for probes in DBM configuration. Adapted from [43]	207

List of Tables

1.1. Physical mechanisms of heat flux diffusion and corresponding divertor concept realisations.	18
2.1. Loosely defined types of models from Reference [49]. LPs models are mixtures of different types, containing elements of simplification, phenomenological model and approximation.	38
2.2. Langmuir Models compared in this thesis, grouped by their sheath model and use of double probe characteristic.	50
2.3. Different slicers developed to separate V_{LP} time trace for IV-characteristic fitting.	52
2.4. Constraints, initial values and prior distributions for inference with least-square (LS) and Bayesian methods.	56
2.5. Parameter values of fits in Figure 2.16 during strong edge radiation regime. Standard error given in brackets.	68
2.6. Parameter values of fits in Figure 2.17 during attached divertor operation. Standard error given in brackets.	70
3.1. Experimental values of γ_s on other experiments [93]. The range refers to values reported at different parameters and conditions.	76
3.2. Constants for calculation of γ_s for Graphite and Hydrogen from Reference [95]	83
3.3. Typical values for field line diffusion (FLD) calculations and α_{CF}	86
3.4. Measurements of γ_s determined from the probability density shown in Figure 3.13. The maximum a posteriori (MAP) is the most likely value.	92
5.1. DG fit dataset dimensions and coordinates.	138

List of Tables

5.2. Comparison of q_{IR} and q_{LP} fit parameters	139
5.3. Comparison of UD and Lower divertor (LD) DG fit parameters	146
5.4. MARFE features and observations.	166
6.1. Key result: Model choice matters even when all fit equally well.	171
A.1. Field vectors and target incidence angles on probes for dif- ferent configurations.	208
A.2. Probe positions and facet inclination angle.	209

A

Appendix

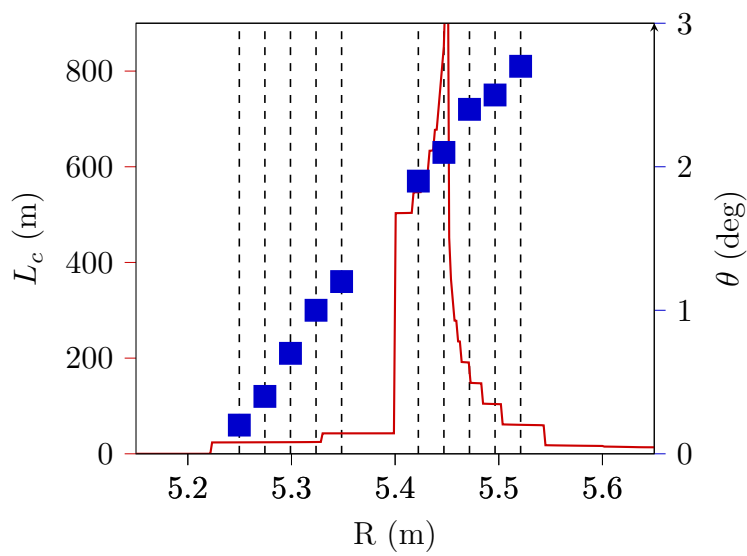


Figure A.1.: Connection lengths and incidence angles for probes in DBM configuration. Adapted from [43]

Table A.1.: Field vectors and target incidence angles on probes for different configurations.

C	N	EIM				DBM			
		B_x [T]	B_y [T]	B_z [T]	γ [°]	B_x [T]	B_y [T]	B_z [T]	γ [°]
LD	1	2.4043	-0.2797	0.1186	1.4	2.3780	-0.2678	0.1750	2.7
	2	2.4114	-0.2853	0.1073	1.2	2.3848	-0.2741	0.1643	2.5
	3	2.4191	-0.2913	0.0951	1.0	2.3921	-0.2809	0.1529	2.4
	4	2.4273	-0.2976	0.0823	0.8	2.3999	-0.2880	0.1409	2.1
	5	2.4359	-0.3044	0.0686	0.5	2.4082	-0.2955	0.1282	1.9
	6	2.4641	-0.3267	0.0238	-0.2	2.4351	-0.3201	0.0865	1.2
	7	2.4741	-0.3349	0.0076	-0.5	2.4447	-0.3291	0.0716	1.0
	8	2.4843	-0.3435	-0.0090	-0.8	2.4545	-0.3385	0.0562	0.7
	9	2.4948	-0.3526	-0.0262	-1.1	2.4644	-0.3484	0.0403	0.4
	10	2.5054	-0.3622	-0.0437	-1.4	2.4745	-0.3589	0.0241	0.2
	11	2.4317	-0.2578	0.1195	1.6	2.4077	-0.2466	0.1788	3.0
	12	2.4397	-0.2622	0.1100	1.4	2.4153	-0.2517	0.1697	2.8
	13	2.4482	-0.2670	0.0993	1.2	2.4234	-0.2573	0.1598	2.6
	14	2.4572	-0.2723	0.0877	1.0	2.4319	-0.2634	0.1489	2.4
	15	2.4667	-0.2780	0.0751	0.8	2.4409	-0.2699	0.1372	2.2
	16	2.4976	-0.2974	0.0320	-0.0	2.4704	-0.2917	0.0974	1.5
	17	2.5087	-0.3046	0.0160	-0.3	2.4810	-0.2998	0.0827	1.2
	18	2.5202	-0.3122	-0.0007	-0.6	2.4920	-0.3083	0.0673	0.9
	19	2.5321	-0.3202	-0.0181	-1.0	2.5033	-0.3173	0.0514	0.6
	20	2.5445	-0.3287	-0.0361	-1.3	2.5151	-0.3267	0.0349	0.3
UD	1	1.7807	1.6395	0.1186	-1.0	1.7664	1.6144	0.1750	-2.4
	2	1.7832	1.6482	0.1073	-1.3	1.7682	1.6235	0.1643	-2.6
	3	1.7859	1.6575	0.0951	-1.0	1.7701	1.6333	0.1529	-2.4
	4	1.7888	1.6675	0.0823	-0.7	1.7723	1.6436	0.1409	-2.1
	5	1.7918	1.6780	0.0686	-0.5	1.7746	1.6545	0.1281	-1.9
	6	1.8015	1.7126	0.0238	0.1	1.7819	1.6903	0.0865	-1.3
	7	1.8047	1.7251	0.0077	0.3	1.7844	1.7032	0.0716	-1.1
	8	1.8079	1.7382	-0.0091	0.7	1.7867	1.7166	0.0561	-0.7
	9	1.8111	1.7516	-0.0262	1.0	1.7889	1.7304	0.0403	-0.5
	10	1.8140	1.7656	-0.0437	1.5	1.7909	1.7448	0.0242	-0.1
	11	1.8157	1.6379	0.1195	-2.0	1.8029	1.6147	0.1788	-3.3
	12	1.8196	1.6461	0.1100	-1.3	1.8060	1.6233	0.1697	-2.7
	13	1.8237	1.6550	0.0993	-1.1	1.8093	1.6326	0.1598	-2.5
	14	1.8279	1.6646	0.0877	-1.3	1.8126	1.6425	0.1489	-2.7
	15	1.8322	1.6748	0.0751	-0.6	1.8161	1.6531	0.1372	-2.0
	16	1.8458	1.7086	0.0320	-0.1	1.8271	1.6881	0.0974	-1.6
	17	1.8505	1.7210	0.0160	0.2	1.8309	1.7008	0.0827	-1.3
	18	1.8554	1.7339	-0.0007	0.5	1.8348	1.7142	0.0673	-1.0
	19	1.8603	1.7474	-0.0181	1.0	1.8388	1.7281	0.0514	-0.6
	20	1.8653	1.7616	-0.0361	1.3	1.8427	1.7427	0.0349	-0.2

Table A.2.: Probe positions and facet inclination angle. Probes of type 1 only have two facets, probes of type 2 four facets. Front and back angles with \hat{y} direction, side angles with \hat{x} direction.

C	N	position [mm]			facet angles [°]			
		x	y	z	front	side	back	side
LD	1	865.719	-5452.778	-1023.417	13.6	3.4	-	-
	2	861.917	-5428.400	-1019.385	14.2	3.6	-	-
	3	858.116	-5404.021	-1015.353	14.8	3.8	-	-
	4	854.315	-5379.643	-1011.322	15.4	4.0	22.4	6.1
	5	850.514	-5355.265	-1007.290	16.1	4.2	21.2	5.8
	6	839.110	-5282.130	-995.197	18.1	5.0	17.4	5.0
	7	835.309	-5257.752	-991.166	18.7	5.2	16.1	4.7
	8	831.508	-5233.374	-987.135	19.4	5.5	14.8	4.4
	9	827.706	-5208.995	-983.104	20.0	5.8	13.5	4.1
	10	823.905	-5184.617	-979.074	20.7	6.1	12.2	3.7
	11	922.352	-5459.780	-1022.304	12.6	3.1	-	-
	12	918.333	-5435.426	-1018.337	13.2	3.3	-	-
	13	914.314	-5411.072	-1014.370	13.8	3.5	-	-
	14	910.295	-5386.719	-1010.403	14.5	3.7	-	-
	15	906.276	-5362.365	-1006.436	15.2	3.9	22.0	6.0
	16	894.220	-5289.303	-994.535	17.5	4.7	18.1	5.1
	17	890.201	-5264.949	-990.569	18.3	5.0	16.7	4.8
	18	886.182	-5240.595	-986.602	19.1	5.3	15.3	4.4
	19	882.164	-5216.241	-982.636	19.9	5.6	13.9	4.1
	20	878.145	-5191.887	-978.669	20.6	5.9	12.5	3.7
UD	1	2504.700	-4920.250	1023.425	15.3	3.8	-	-
	2	2493.425	-4898.300	1019.350	14.2	3.5	-	-
	3	2482.175	-4876.325	1015.350	14.6	3.7	-	-
	4	2470.900	-4854.375	1011.350	16.4	4.0	23.3	6.1
	5	2459.650	-4832.425	1007.275	15.2	4.3	19.6	5.8
	6	2425.900	-4766.550	995.200	18.0	4.9	18.1	5.1
	7	2414.650	-4744.600	991.200	17.5	5.1	16.2	4.9
	8	2403.400	-4722.625	987.100	20.2	5.5	15.6	4.4
	9	2392.150	-4700.675	983.100	18.8	5.8	12.9	4.1
	10	2380.900	-4678.725	979.100	21.9	6.2	12.4	3.6
	11	2462.975	-4959.200	1022.300	11.1	2.8	-	-
	12	2451.925	-4937.125	1018.350	14.0	3.4	-	-
	13	2440.850	-4915.075	1014.375	13.8	3.6	-	-
	14	2429.800	-4893.000	1010.400	12.5	3.4	-	-
	15	2418.725	-4870.950	1006.425	17.0	4.2	22.3	5.8 ²⁰⁹
	16	2385.525	-4804.750	994.500	18.0	4.6	19.7	5.2
	17	2374.475	-4782.675	990.600	18.4	4.9	17.5	4.9
	18	2363.400	-4760.625	986.600	18.1	5.2	15.3	4.6
	19	2352.325	-4738.550	982.625	21.0	5.6	14.5	4.1
	20	2341.275	-4716.475	978.675	21.3	6.0	12.5	3.6



Publications

As first author

- [1] L. RUDISCHHAUSER et al. »The Langmuir probe system in the Wendelstein 7-X test divertor«. In: *Review of Scientific Instruments*, Vol. 91.6 (2020), page 063505.

As coauthor

- [1] T. KREMEYER et al. »Global particle balance to analyze fuelling, exhaust, recycling and particle confinement at Wendelstein 7-X«. In: *Nuclear Fusion*, (Feb. 2021).
- [2] C. KILLER et al. »Plasma filaments in the scrape-off layer of wendelstein 7-X«. In: *Plasma Physics and Controlled Fusion*, Vol. 62 (2020). DOI: <https://doi.org/10.1088/1361-6587/ab9313>.
- [3] O. SCHMITZ et al. »Stable heat and particle flux detachment with efficient particle exhaust in the island divertor of Wendelstein 7-X«. In: *Nuclear Fusion*, (2020).
- [4] S. SEREDA et al. »Impact of boronizations on impurity sources and performance in Wendelstein 7-X«. In: *Nuclear Fusion*, Vol. 60 (2020). DOI: <https://doi.org/10.1088/1741-4326/ab937b>.
- [5] M. JAKUBOWSKI et al. »Heat and particle flux detachment with stable plasma conditions in the Wendelstein 7-X stellarator fusion experiment«. 2020. arXiv: 2001.02067 [physics.plasm-ph].

- [6] H. NIEMANN et al. »Features of near and far scrape-off layer heat fluxes on the Wendelstein 7-X inboard limiters«. In: *Nuclear Fusion*, Vol. 60.1 (2019), page 016014.
- [7] K. HAMMOND et al. »Drift effects on W7-X divertor heat and particle fluxes«. In: *Plasma Physics and Controlled Fusion*, Vol. 61.12 (2019), page 125001.
- [8] T. S. PEDERSEN et al. »First divertor physics studies in Wendelstein 7-X«. In: *Nuclear Fusion*, Vol. 59.9 (2019), page 096014.
- [9] A. DINKLAGE et al. »Magnetic configuration effects on the Wendelstein 7-X stellarator«. In: *Nature Physics*, Vol. 14.8 (2018), pages 855–860.



Acknowledgements

This work was not possible without the help of many people. I want to thank:

Thomas, for the optimism and drive he brings to projects and some important moments of encouragement and appreciation.

Michael, for all the advice, help, teaching, being available for questions, thoroughness and thoughtfulness.

Ken, for all the work on the Langmuir probes, without which I wouldn't have gotten half as far.

Daniel, for becoming one of my closest friends, but also for discussions, learning together, figuring things out on the whiteboard, helping with any kind of code and setting a high standard in methodicalness I try to hold myself to.

Boyd, for generously helping, and even changing his intercontinental travel plans to debug electronics for three days.

Peter, for his expertise in electronics and willingness to teach and explain.

Jörn, for letting me ineffectively mess about in his workshop and occupy space with half-understood test-setups.

Udo, for many enjoyable hours of pair programming and less enjoyable ones of debugging.

Jim, for many memorable moments in Greifswald and some intense fundamental discussions.

All fellow Greifswald PhDs, for helping each other out, building hats, and letting me serve as their representative.

All my colleagues, for being very welcoming, a great work environment, and many great parties.

The IPP, for enabling PhD work free from financial uncertainties and administrative hassles, ubiquitous elsewhere.

Finally Anke, for being relentlessly supportive while putting up with uncertain time plans and various emotions towards my work and this thesis.

Special thanks to Michael, Daniel and Anke for proofreading parts or all of what I've written.

This work has been carried out within the framework of the EUROfusion Consortium and has received funding from the Euratom research and training programme 2014-2018 and 2019-2020 under grant agreement No 633053. The views and opinions expressed herein do not necessarily reflect those of the European Commission.

Statutory declaration

Eigenständigkeitserklärung

Hiermit erkläre ich, dass diese Arbeit bisher von mir weder an der Mathematisch-Naturwissenschaftlichen Fakultät der Universität Greifswald noch einer anderen wissenschaftlichen Einrichtung zum Zwecke der Promotion eingereicht wurde. Ferner erkläre ich, dass ich diese Arbeit selbstständig verfasst und keine anderen als die darin angegebenen Hilfsmittel und Hilfen benutzt und keine Textabschnitte eines Dritten ohne Kennzeichnung übernommen habe.

Greifswald, 25.06.2021

LUKAS RUDISCHHAUSER